ANL-19/27 Vol.2
ISSN 1931-5007
June 2020

APS Science
2019 Volume 2

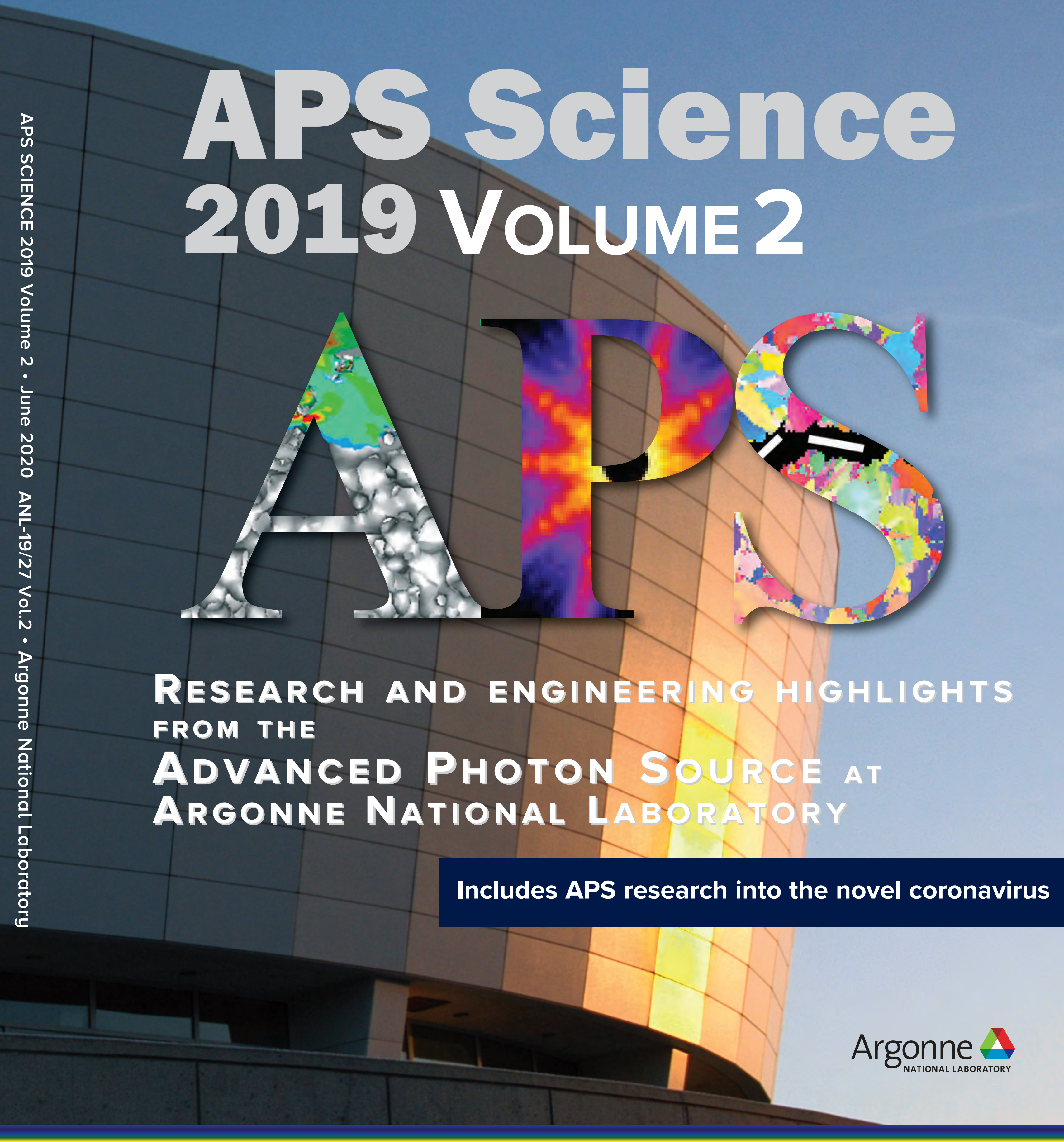

RESEARCH AND ENGINEERING HIGHLIGHTS
FROM THE
ADVANCED PHOTON SOURCE AT
ARGONNE NATIONAL LABORATORY

Includes APS research into the novel coronavirus

Argonne NATIONAL LABORATORY

APS SCIENCE 2019 Volume 2 • June 2020 ANL-19/27 Vol.2 • Argonne National Laboratory

ANL-19/27 Vol.2 • SSN 1931-5007 • June 2020

About Argonne National Laboratory
Argonne is a U.S. Department of Energy laboratory managed by UChicago Argonne, LLC
under contract DE-AC02-06CH11357. The Laboratory's main facility is outside Chicago, at 9700 South Cass Avenue, Lemont, Illinois 60439. For information about Argonne
and its pioneering science and technology programs, see www.anl.gov.

DOCUMENT AVAILABILITY
Online Access: U.S. Department of Energy (DOE) reports produced after 1991 and a growing number of pre-1991 documents are available free at OSTI.GOV (http://www.osti.gov/), a
service of the US Dept. of Energy's Office of Scientific and Technical Information.

Reports not in digital format may be purchased by the public from the National Technical Information Service (NTIS):U.S. Department of Commerce National Technical Information Service
5301 Shawnee Rd
Alexandria, VA 22312
www.ntis.gov
Phone: (800) 553-NTIS (6847) or (703) 605-6000
Fax: (703) 605-6900
Email: orders@ntis.gov

Reports not in digital format are available to DOE and DOE contractors from the Office of Scientific and Technical Information (OSTI):
U.S. Department of Energy
Office of Scientific and Technical Information
P.O. Box 62
Oak Ridge, TN 37831-0062
www.osti.gov
Phone: (865) 576-8401
Fax: (865) 576-5728
Email: reports@osti.gov

Disclaimer
This report was prepared as an account of work sponsored by an agency of the United States Government. Neither the United States Government nor any agency thereof, nor UChicago Argonne, LLC, nor any of their employees or officers, makes any warranty, express or implied, or assumes any legal liability or responsibility for the accuracy, completeness, or usefulness of any information, apparatus, product, or process disclosed, or represents that its use would not infringe privately owned rights. Reference herein to any specific commercial product, process, or service by trade name, trademark, manufacturer, or otherwise, does not necessarily constitute or imply its endorsement, recommendation, or favoring by the United States Government or any agency thereof. The views and opinions of document authors expressed herein do not necessarily state or reflect those of the United States Government or any agency thereof, Argonne National Laboratory, or UChicago Argonne, LLC.

On the cover: Background: The APS auditorium exterior at dusk.

ANL-19/27 Vol.2
ISSN 1931-5007
June 2020

APS Science
2019 VOLUME 2

RESEARCH AND ENGINEERING HIGHLIGHTS
FROM THE
ADVANCED PHOTON SOURCE AT
ARGONNE NATIONAL LABORATORY

Argonne is a U.S. Department of Energy (DOE) laboratory managed by UChicago Argonne, LLC.
The Advanced Photon Source is a DOE Office of Science user facility
operated for the DOE Office of Science by Argonne National Laboratory under Contract No. DE-AC02-06CH11357.

FOLLOW US: @advancedphoton LIKE US: Advanced Photon Source flickr: www.flickr.com/photos/97432701@N03/

Table of Contents

Table of Contents cont’d. on next page

“Table of Contents” cont’d. from previous page

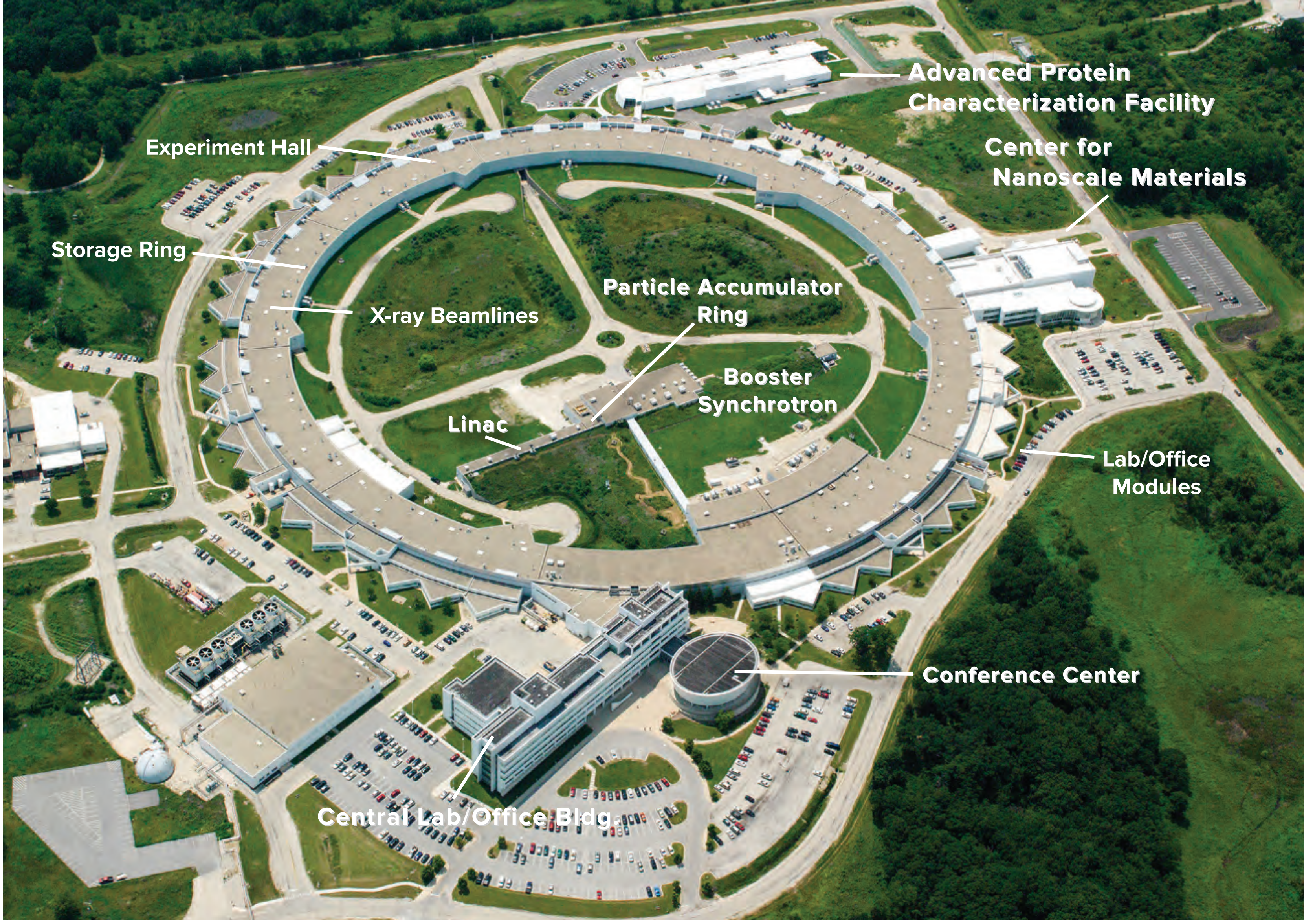

The Advanced Photon Source Facility at Argonne National Laboratory

The APS, a national synchrotron radiation research facility operated by UChicago Argonne, LLC, and Argonne National Laboratory for the U.S. Department of Energy (DOE) Office of Science-Basic Energy Sciences, Scientific User Facilities Division, provides this nation's brightest high-energy x-ray beams for science. Research by APS users extends from the center of the Earth to outer space, from new information on batteries, combustion engines and microcircuits, to new and improved pharmaceuticals, and nanotechnologies whose scale is measured in billionths of a meter. The APS helps researchers illuminate answers to the challenges of our high-tech world, from developing new forms of energy to sustaining our nation's technological and economic competitiveness to pushing back against the ravages of disease. Research at the APS promises to have far-reaching impact on our technology, our economy, our health, and fundamental knowledge of the materials that make up our world.

The APS occupies an 80-acre site on the Argonne campus, about 25 miles from downtown Chicago, Illinois. It shares a site with the Center for Nanoscale Materials and the Advanced Protein Characterization Facility.

For directions to Argonne, see https://www.anl.gov/visiting-argonne.

CONTACT US

For more information about the APS send an email to apsinfo@aps.anl.gov or write to APS Info, Bldg. 401, Rm. A4113, Argonne National Laboratory, 9700 S. Cass Ave., Lemont, IL 60439.

To order additional copies of this, or previous, issues of *APS Science* send email to apsinfo@aps.anl.gov.

To download PDF versions of *APS Science* back issues go to
www.aps.anl.gov/Science/APS-Science

Visit the APS on the Web at
www.aps.anl.gov

ARGONNE NATIONAL LABORATORY 400-AREA FACILITIES

ADVANCED PHOTON SOURCE

(Beamlines, Disciplines, and Source Configuration)

ADVANCED PROTEIN CHARACTERIZATION FACILITY

CENTER FOR NANOSCALE MATERIALS

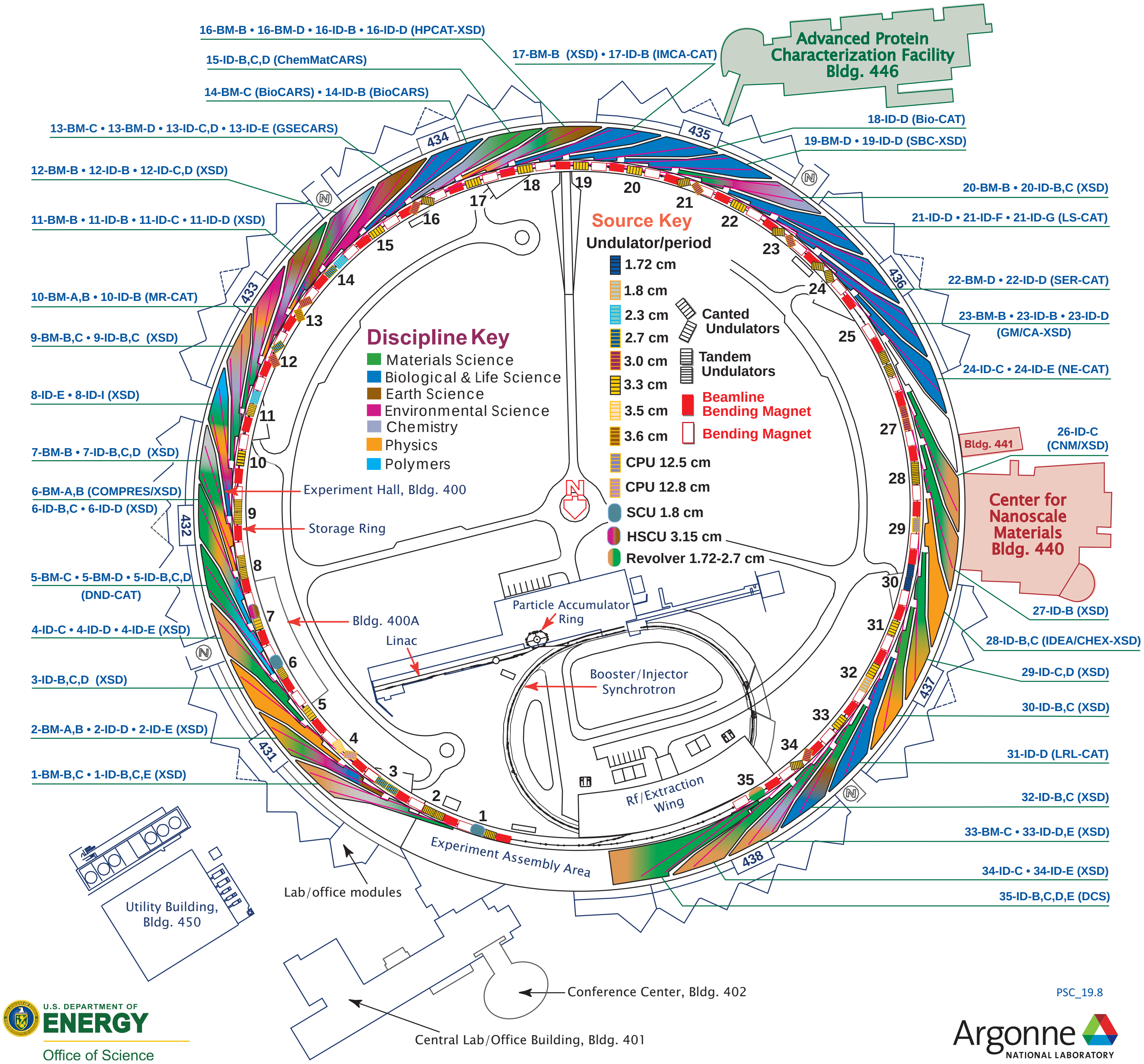

U.S. DEPARTMENT OF ENERGY
Office of Science

Argonne NATIONAL LABORATORY

APS sectors: At the APS, a "sector" comprises the radiation sources (one bending magnet and nominally one insertion device, although the number of insertion devices in the straight sections of the storage ring can vary) and the beamlines, enclosures, and instrumentation that are associated with a particular storage ring sector. The APS has 35 sectors dedicated to user science and experimental apparatus. X-ray Science Division (XSD) sectors comprise those beamlines operated by the APS. Collaborative access team (CAT) sectors comprise beamlines operated by independent groups made up of scientists from universities, industry, and/or research laboratories both federal and private.

APS BEAMLINES

Key: Beamline designation • Sector operator • Disciplines • Techniques • Radiation source energy • User access mode(s) • General-user status

1-BM-B,C • **X-ray Science Division (XSD)** • Materials science, physics • Optics testing, detector testing, topography, energy dispersive x-ray diffraction, white Laue single-crystal diffraction • 6-30 keV, 50-120 keV • On-site • Accepting general users

1-ID-B,C,E • XSD • Materials science, physics, chemistry • High-energy x-ray diffraction, tomography, small-angle x-ray scattering, fluorescence spectroscopy, pair distribution function, phase contrast imaging • 41-136 keV, 45-116 keV • On-site • Accepting general users

2-BM-A,B • XSD • Physics, life sciences, geoscience, materials science • Tomography, phase contrast imaging • 10-170 keV, 11-35 keV • On-site • Accepting general users

2-ID-D • XSD • Life sciences, materials science, environmental science • Microfluorescence (hard x-ray), micro x-ray absorption fine structure, nanoimaging, ptychography • 5-30 keV • On-site • Accepting general users

2-ID-E • XSD • Life sciences, environmental science, materials science • microfluorescence (hard x-ray), tomography • 7-10.5 keV, 11-17 keV • On-site • Accepting general users

3-ID-B,C,D • XSD • Physics, geoscience, life sciences, chemistry, materials science • Nuclear resonant scattering, inelastic x-ray scattering, high-pressure diamond anvil cell • 7-27 keV, 14.41-14.42 keV • On-site • Accepting general users

4-ID-C • XSD • Physics, materials science • Magnetic circular dichroism (soft x-ray), x-ray magnetic linear dichroism, x-ray photoemission spectroscopy, x-ray photoemission electron microscopy, anomalous and resonant scattering (soft x-ray) • 500-2800 eV • On-site • Accepting general users

4-ID-D • XSD • Physics, materials science • Anomalous and resonant scattering (hard x-ray), magnetic x-ray scattering, magnetic circular dichroism (hard x-ray) • 2.7-40 keV • On-site • Accepting general users

4-ID-E • XSD • Materials science, physics • Synchrotron x-ray scanning tunneling microscopy • 500-1800 eV • On-site • Accepting general users

5-BM-C • **DuPont-Northwestern-Dow Collaborative Access Team (DND-CAT)** • Materials science, polymer science • Powder diffraction, tomography, wide-angle x-ray scattering • 10-42 keV • On-site • Accepting general users

5-BM-D • DND-CAT • Materials science, polymer science, chemistry • X-ray absorption fine structure, high-energy x-ray diffraction, general diffraction • 4.5-25 keV, 4.5-80 keV • On-site • Accepting general users

5-ID-B,C,D • DND-CAT • Materials science, polymer science, chemistry • Powder diffraction, x-ray standing waves, x-ray optics development/techniques, small-angle x-ray scattering, surface diffraction, x-ray reflectivity, wide-angle x-ray scattering • 6-17.5 keV • On-site • Accepting general users

6-BM-A,B • **COMPRES/XSD** • Materials science, geoscience • Energy dispersive x-ray diffraction, high-pressure multi-anvil press • 20-200 keV • On-site • Accepting general users

6-ID-B,C • XSD • Physics, materials science • Magnetic x-ray scattering, anomalous and resonant scattering (hard x-ray), general diffraction, grazing incidence diffraction • 3.2-38 keV • On-site • Accepting general users

6-ID-D • XSD • Physics, materials science • Magnetic x-ray scattering, high-energy x-ray diffraction, powder diffraction, pair distribution function • 50-100 keV, 70-130 keV • On-site • Accepting general users

7-BM-B • XSD • Physics • Radiography, tomography, microfluorescence (hard x-ray) • 5-150 keV, 6-15 keV, 25-55 keV • On-site • Accepting general users

7-ID-B,C,D • XSD • Materials science, atomic physics, chemistry • Time-resolved x-ray scattering, time-resolved x-ray absorption fine structure, phase contrast imaging • 18 keV, 12-26 keV • On-site • Accepting general users

8-ID-E • XSD • Materials science, polymer science, physics • Grazing incidence small-angle scattering, x-ray photon correlation spectroscopy • 7.35-7.35 keV, 11-11 keV • On-site • Accepting general users

8-ID-I • XSD • Polymer science, materials science, physics • X-ray photon correlation spectroscopy, intensity fluctuation spectroscopy, small-angle x-ray scattering • 6-12.5 keV, 10.9-10.9 keV • On-site • Accepting general users

9-BM-B,C • XSD • Materials science, chemistry, environmental science • X-ray absorption fine structure, x-ray absorption near-edge structure • 2.1-25.2 keV • On-site • Accepting general users

9-ID-B,C • XSD • Chemistry, materials science, life sciences • Nano-imaging, microfluorescence (hard x-ray), coherent x-ray scattering (hard x-ray), ultra-small-angle x-ray scattering • 4.5-30 keV • On-site • Accepting general users

10-BM-A,B • **Materials Research (MR)-CAT** • Materials science, chemistry, environmental science, physics • X-ray absorption fine structure • 4-32 keV • On-site • Accepting general users

10-ID-B • MR-CAT • Materials science, environmental science, chemistry • X-ray absorption fine structure, time-resolved x-ray absorption fine structure, microfluorescence (hard x-ray) • 4.3-27 keV, 4.8-32 keV, 15-65 keV • On-site • Accepting general users

11-BM-B • XSD • Chemistry, materials science, physics • Powder diffraction • 22-33 keV • On-site, mail-in • Accepting general users

11-ID-B • XSD • Chemistry, environmental science, materials science • Pair distribution function, high-energy x-ray diffraction • 58.66 keV, 86.7 keV • On-site • Accepting general users

11-ID-C • XSD • Materials science, chemistry, physics • High-energy x-ray diffraction, diffuse x-ray scattering, pair distribution function • 105.6 keV • On-site • Accepting general users

11-ID-D • XSD • Chemistry, environmental science, materials science • Time-resolved x-ray absorption fine structure, time-resolved x-ray scattering • 6-25 keV • On-site • Accepting general users

12-BM-B • XSD • Materials science, polymer science, chemistry, physics, environmental science • X-ray absorption fine structure, small-angle x-ray scattering, wide-angle x-ray scattering • 4.5-30 keV, 10-40 keV • On-site • Accepting general users

12-ID-B • XSD • Chemistry, materials science, life sciences, polymer science, physics • Small-angle x-ray scattering, grazing incidence small-angle scattering, wide-angle x-ray scattering, grazing incidence diffraction • 7.9-14 keV • On-site • Accepting general users

12-ID-C,D • XSD • Chemistry, physics, materials science • Small-angle x-ray scattering, grazing incidence small-angle scattering, wide-angle x-ray scattering, surface diffraction • 4.5-40 keV • On-site • Accepting general users

13-BM-C • **GeoSoilEnviro Center for Advanced Radiation Sources (GSECARS)** • Geoscience, environmental science • Surface diffraction, high-pressure diamond anvil cell, single-crystal diffraction • 15-15 keV, 28.6-28.6 keV • On-site • Accepting general users

13-BM-D • GSECARS • Geoscience, environmental science • Tomography, high-pressure diamond anvil cell, high-pressure multi-anvil press • 4.5-80 keV • On-site • Accepting general users

13-ID-C,D • GSECARS • Geoscience, environmental science • Surface diffraction, microdiffraction, x-ray standing waves, x-ray absorption fine structure, resonant inelastic x-ray scattering, x-ray emission spectroscopy, high-pressure diamond anvil cell, high-pressure multi-anvil press • 4.9-45 keV, 10-75 keV • On-site • Accepting general users

13-ID-E • GSECARS • Geoscience, environmental science • Microfluorescence (hard x-ray), micro x-ray absorption fine structure, microdiffraction, fluorescence spectroscopy • 2.4-28 keV, 5.4-28 keV • On-site • Accepting general users

"APS Beamlines' cont'd. on next page

"APS Beamlines cont'd. from previous page

14-BM-C • **BioCARS** • Life sciences • Macromolecular crystallography, fiber diffraction, biohazards at the BSL2/3 level, subatomic (<0.85 Å) resolution, large unit cell crystallography • 8-14.9 keV • On-site • Accepting general users

14-ID-B • BioCARS • Life sciences, materials science, physics, chemistry • Time-resolved crystallography, time-resolved x-ray scattering, Laue crystallography, wide-angle x-ray scattering, biohazards at the BSL2/3 level, macromolecular crystallography • 7-19 keV • On site • Accepting general users

15-ID-B,C,D • **ChemMatCARS** • Materials science, chemistry • Anomalous and resonant scattering (hard x-ray), microdiffraction, high-pressure diamond anvil cell, single-crystal diffraction, liquid surface diffraction, x-ray reflectivity • 6-32 keV, 10-70 keV • On-site • Accepting general users

16-BM-B • **High Pressure (HP)CAT-XSD** • Materials science, geoscience, chemistry, physics • White Laue single-crystal diffraction, energy dispersive x-ray diffraction, phase contrast imaging, radiography, pair distribution function • 10-120 keV • On-site • Accepting general users

16-BM-D • HPCAT-XSD • Materials science, geoscience, chemistry, physics • Powder angular dispersive x-ray diffraction, single-crystal diffraction, x-ray absorption near-edge structure, x-ray absorption fine structure, tomography • 6-45 keV • On-site • Accepting general users

16-ID-B • HPCAT-XSD • Materials science, geoscience, chemistry, physics • Microdiffraction, single-crystal diffraction, high-pressure diamond anvil cell • 18-60 keV • On-site • Accepting general users

16-ID-D • HPCAT-XSD • Materials science, geoscience, chemistry, physics • Nuclear resonant scattering, inelastic x-ray scattering (1-eV resolution), x-ray emission spectroscopy, high-pressure diamond anvil cell • 5-37 keV, 14.41-14.42 keV • On-site • Accepting general users

17-BM-B • XSD • Chemistry, materials science • Powder diffraction, pair distribution function • 27-51 keV • On-site • Accepting general users

17-ID-B • **Industrial Macromolecular Crystallography Association (IMCA)-CAT** • Life sciences • Macromolecular crystallography, multi-wavelength anomalous dispersion, microbeam, single-wavelength anomalous dispersion, large unit cell crystallography • Subatomic (<0.85 Å) resolution • 6-20 keV • On-site, remote • Accepting general users

18-ID-D • **Biophysics (Bio)-CAT** • Life sciences • Fiber diffraction, microdiffraction, small-angle x-ray scattering, time-resolved x-ray scattering • 3.5-35 keV • On-site • Accepting general users

19-BM-D • **Structural Biology Center (SBC)-XSD** • Life sciences • Multi-wavelength anomalous dispersion, macromolecular crystallography, single-wavelength anomalous dispersion, serial crystallography • 6-13.5 keV • Remote, on-site, mail-in • Accepting general users

19-ID-D • SBC-XSD • Life sciences • Macromolecular crystallography, multi-wavelength anomalous dispersion, subatomic (<0.85 Å) resolution, large unit cell crystallography, single-wavelength anomalous dispersion • 6.5-19.5 keV • On-site, remote, mail-in • Accepting general users

20-BM-B • XSD • Materials science, environmental science, chemistry • X-ray absorption fine structure, microfluorescence (hard x-ray) • 2.7-32 keV, 2.7-35 keV • On-site • Accepting general users

20-ID-B,C • XSD • Materials science, environmental science, chemistry • X-ray absorption fine structure, x-ray Raman scattering, micro x-ray absorption fine structure, microfluorescence (hard x-ray), x-ray emission spectroscopy • 4.3-27 keV, 7-52 keV • On-site • Accepting general users

21-ID-D • **Life Sciences (LS)-CAT** • Life sciences • Macromolecular crystallography • 6.5-20 keV • On-site, remote, mail-in • Accepting general users

21-ID-F • LS-CAT • Life sciences • Macromolecular crystallography • 12.7 keV • Remote, on-site, mail-in • Accepting general users

21-ID-G • LS-CAT • Life sciences • Macromolecular crystallography • 12.7 keV • Remote, on-site, mail-in • Accepting general users

22-BM-D • **Southeast Regional (SER)-CAT** • Life sciences • Macromolecular crystallography, single-wavelength anomalous dispersion, multi-wavelength anomalous dispersion • 8-20 keV • On-site, remote • Accepting general users

22-ID-D • SER-CAT • Life sciences • Macromolecular crystallography, multi-wavelength anomalous dispersion, single-wavelength anomalous dispersion, microbeam • 6-20 keV • On-site, remote • Accepting general users

23-ID-B • **National Institute of General Medical Sciences and National Cancer Institute (GM/CA)-XSD** • Life sciences • Macromolecular crystallography, microbeam, large unit cell crystallography, subatomic (<0.85 Å) resolution, multi-wavelength anomalous dispersion, single-wavelength anomalous dispersion • 3.5-20 keV • On-site, remote • Accepting general users

23-ID-D • GM/CA-XSD • Life sciences • Macromolecular crystallography, microbeam, large unit cell crystallography, subatomic (<0.85 Å) resolution, multi-wavelength anomalous dispersion, single-wavelength anomalous dispersion, serial crystallography • 5-20 keV • On-site, remote • Accepting general users

24-ID-C • **Northeastern (NE)-CAT** • Life sciences • Macromolecular crystallography, microdiffraction, single-wavelength anomalous dispersion, single-crystal diffraction, microbeam, multi-wavelength anomalous dispersion, subatomic (<0.85 Å) resolution • 6.5-20 keV • On-site, remote • Accepting general users

24-ID-E • NE-CAT • Life sciences • Macromolecular crystallography, microbeam, microdiffraction, single-wavelength anomalous dispersion, single-crystal diffraction • 12.68 keV • On-site, remote • Accepting general users

26-ID-C • **Center for Nanoscale Materials (CNM)/XSD** • Physics, materials science • Nanodiffraction, nano-imaging, coherent x-ray scattering, synchrotron x-ray scanning tunneling microscopy • 6-12 keV • On-site • Accepting general users

27-ID-B • XSD • Physics • Resonant inelastic x-ray scattering • 5-14 keV, 5-30 keV • On-site • Accepting general users

29-ID-C,D • XSD • Physics, materials science • Resonant soft x-ray scattering, angle-resolved photoemission spectroscopy • 250-2200 eV, 2200-3000 eV • On-site • Accepting general users

30-ID-B,C • XSD • Physics, materials science • Inelastic x-ray scattering • 23.7-23.9 keV • On-site • Accepting general users

31-ID-D • **Lily Research Laboratories (LRL)-CAT** • Life sciences • Macromolecular crystallography, single-wavelength anomalous dispersion • 9-13.5 keV • Mail-in • Accepting general users

32-ID-B,C • XSD • Materials science, life sciences, geoscience • Phase contrast imaging, radiography, transmission x-ray microscopy, tomography • 7-40 keV • On-site • Accepting general users

33-BM-C • XSD • Materials science, physics, chemistry • Diffuse x-ray scattering, general diffraction, powder diffraction, x-ray reflectivity, grazing incidence diffraction, anomalous and resonant scattering (hard x-ray) • 5-35 keV • On-site • Accepting general users

33-ID-D,E • XSD • Materials science, physics, chemistry, environmental science • Anomalous and resonant scattering (hard x-ray), diffuse x-ray scattering, general diffraction, surface diffraction, surface diffraction (UHV), x-ray reflectivity • 4-40 keV, 6-25 keV • On-site • Accepting general users

34-ID-C • XSD • Materials science, physics • Coherent x-ray scattering • 5-15 keV • On-site • Accepting general users

34-ID-E • XSD • Materials science, physics, environmental science, geoscience • Microdiffraction, Laue crystallography, microbeam, microfluorescence (hard x-ray) • 7-30 keV • On-site • Accepting general users

35-ID-B,C,D,E • **Dynamic Compression Sector (DCS)** • Physics, materials science, geoscience • Time-resolved x-ray scattering, phase contrast imaging, radiography • 7-35 keV, 7-100 keV, 24-24 keV • On-site • Accepting general users

Other abbreviations: AES: APS Engineering Support Division; ASD: Accelerator Systems Division; XSD: X-ray Sciences Division

WELCOME

Stephen Streiffer

June 2020

This issue of our bi-annual highlights roundup includes a bit of time shifting.

The book features a second batch of articles looking back on the calendar year 2019 work of our incomparable users and staff, but included also are some science highlights and other content driven by the COVID-19 pandemic.

As I write this “Welcome,” Argonne and the APS are just leaving minimum safe operations status and planning for transitioning to limited operations. The former restricted research at our facility (and the other DOE light sources) to remote molecular x-ray crystallography and a few other coronavirus-related studies, with limited on-site staff and no on-site users. The latter is allowing us to somewhat broaden the scope of allowable experiments, while maintaining limits on beamline personnel and continuing to require remote and mail-in experimentation.

Of course, throughout this months-long new reality, we made the safety of on-site personnel our number one priority, with new controls in place to help protect against virus transmission.

Scattered throughout this book are photos and text spotlighting some of the APS technicians and engineers who kept our Upgrade moving forward and kept our facility running, and APS and non-APS beamline staff who supported remote research on the SARS-CoV-2 virus. These folks, and all the others doing similar work, are truly heroes. We cannot possibly say enough about their dedication to our mission and their expert work in keeping the APS up and running at this critical time.

The 17 laboratories that comprise the U.S. national laboratory complex, which is funded by the Department of Energy (which also funds the APS), have roots in the World War II era (most notably with the Manhattan Project, forerunner of Argonne) as a way of focusing U.S. scientific and technological resources on a dire threat to our nation and the world. Since then, the DOE national labs have been “a cornerstone of the United States’ innovation ecosystem, performing leading-edge research in the public interest.”

Now, history repeats, and the DOE national labs and user facilities like the APS have been called upon to once again pivot from a broad range of vitally important research topics to concentrate our resources on doing our part to meet another global threat.

All of us look forward to the end of this pandemic. And all of us at the APS and in our far-flung and exceptional user community also look forward to resumption of the kinds of science highlighted here, such as how to improve batteries, steel, cement, catalysts and solar cells; a possible treatment for Alzheimer’s disease; how strengthening cardiac muscle helps heart disease; aquifer remediation; and the many other studies by our users that you can sample in these pages.

There have been many bright spots for the APS and its users in 2019. Our staff and users continued to collect well-deserved honors, and our physicists and engineers made great contributions to advancing the development of innovative accelerators, insertion devices, detectors, x-ray beam diagnostics, and other technologies that are the foundations of our field.

Of course, we are proud of our excellent APS Upgrade Project, and the Project and APS Operations staff who are assembling what promises to be a groundbreaking addition to our nation’s research facility portfolio. (Speaking of groundbreaking: we expect to break ground in 2020 for the long-beamline building that is part of the Upgrade Project.)

We know that brighter days are ahead for all of us.

Stephen Streiffer

Argonne Associate Laboratory Director for Photon Sciences and Director, Advanced Photon Source

The APS Upgrade: Full Speed Ahead

Robert Hettel

June 2020

A project like upgrading the Advanced Photon Source (APS) is a massive endeavor. It requires years of planning and design work before anything can be built, and review after review by the U.S. Department of Energy (DOE) to make sure we are on track and have properly estimated our schedule and budget. This is all important and necessary work on the path toward a fully realized project.

2019 was the year that the execution phase of the APS Upgrade (APS-U) project – which will see the original APS storage ring replaced with a newly designed, multi-bend achromat lattice, with many more bending magnets and magnet-focusing cells that will increase the instrument's brightness up to 1,000 times – received the green light. In July 2019, the DOE granted the upgrade a Critical Decision 3 (CD-3) approval, officially beginning the start of the construction phase. Also included in the project are nine "feature beamlines" that will exploit the very high brightness and transverse coherence of the x-ray produced in the new ring, two of which will be housed in a new Long Beamline Building (LBB); many new permanent magnet and superconducting insertion devices; and enhancements to several existing x-ray beamlines.

CD-3 is a major milestone for the project, and I want to take a moment to thank everyone who got us to this point. I'm grateful to our DOE partners in the Basic Energy Sciences Scientific User Facilities Division for their expert guidance, to Argonne Director Paul Kearns and Laboratory management for their unflagging support, to APS Director Stephen Streiffer, APS-U Project Manager Jim Kerby, and Deputy APS-U Project Manager Elmie Peoples-Evans for their consistent leadership. And I thank the entire APS-U team and our partners in APS Operations, without whom this project would not be possible.

If there is a theme that describes our 2019 and beyond, it is this: full speed ahead.

Our current schedule has the APS suspending operations in June of 2022 for one year as we replace the current storage ring. We will see a flurry of activity between now and then, with work proceeding on the components for the storage ring, the new upgraded front ends, new insertion devices, new scientific instruments, and the nine new and 15 enhanced beamlines that, together with the LBB, will enable new types of research. The CD-3 approval gave the APS-U Project the authority to procure the necessary components to move forward. Here are just some of the achievements to date:

- Acceptance-tested more than 400 lattice magnets, out of the 1321 total needed for the upgrade project multi-bend achromat storage ring; the magnets (dipoles, quadrupoles, and sextupoles) are all being carefully measured upon arrival
- Received and tested dozens of magnet power supplies;
- Received first articles of the precision beam position (BPM) monitor processing units and successfully tested the first BPM vacuum chamber assembly
- Installed three shielded enclosures at beamline 28-ID and began installation on five shielded enclosures at beamline 25-ID
- Installed BPMs at Sector 25 after receiving them from our colleagues at Brookhaven National Laboratory
- Began construction of two of the nine new beamlines
- Conducted the first design review of the LBB
- Designs of the accelerator and beamlines are well advanced, and the final design of the new beamline instruments progressed with help from our partner labs

Our goal for the near term is to finalize all designs and execute the contracts necessary for the project. Once completed, the APS will be a global leader among the fourth-generation storage-ring x-ray light sources delivering not only world-class, intensely bright hard x-rays, but tightly focused ones as well.

The upgraded APS will allow our users to conduct small-beam scattering and spectroscopy, coherent scattering and imaging, and x-ray photon correlation spectroscopy at resolutions unattainable by today's x-ray light sources. It will allow researchers to see things at scale they've never seen before. This extreme level of detail will enable new discoveries in biofuels, energy storage, medicine, and other fields, and help us betterv understand everything from the structure of the Earth to the makeup of the human brain.

When it is completed, it will be thanks to the dedicated people who worked and are working tirelessly to bring this project to fruition. With all of us working together, the APS-U will be a brilliant jewel in the crown of the DOE science mission.

Robert Hettel, Project Director,
Advanced Photon Source Upgrade

Working Safely on the APS Upgrade during MinSafe Operations

Work was ongoing for the APS Upgrade Project during Argonne's minimum safe operations status in response to the COVID-19 pandemic between March and June, 2020, when Argonne on-site staff was severely limited. Even under those trying circumstances the dedication of APS people kept the APS Upgrade Project moving ahead. Here a few of those people.

Kris Mietsner (APS Engineering Support Division Survey and Alignment Group) at the APS-U Magnetic Measurement Laboratory in Bldg. 369, collecting data from an APS-U storage ring quadrupole magnet for analysis – this is called fiducializing the magnet. These data are used for aligning magnets to each other in a module assembly.

Spiro Skiadopoulos (APS Engineering Support Division Mechanical Engineering and Design Group) at the APS-U Magnetic Measurement Laboratory in Bldg. 369, analyzing the magnet data collected by Kris Mietsner.

Mike Johnson (APS Engineering Support Division Mechanical Operations and Maintenance Group) at the APS-U Magnetic Measurement Laboratory in Bldg. 369, verifying that the magnet polarity is correctly marked.

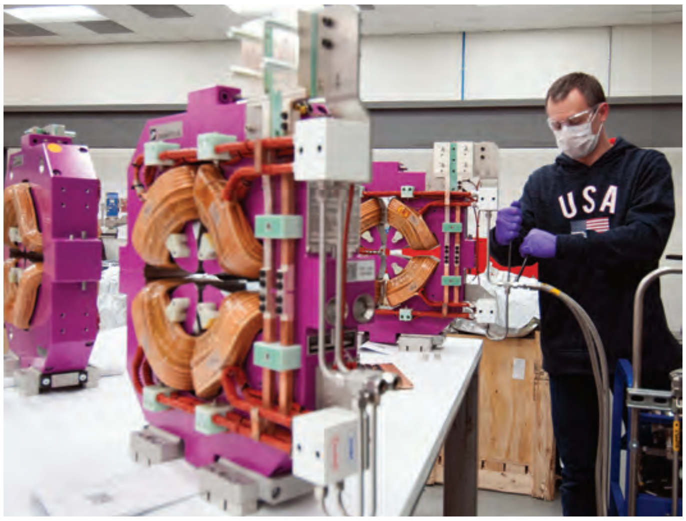

CJ Sarne (APS Engineering Support Division Mechanical Operations and Maintenance Group) at the APS-U Magnetic Measurement Laboratory in Bldg. 369, preparing to carry out a hydrostatic pressure test on quadrupole magnets for the APS Upgrade multi-bend achromat storage ring.

Technician Senior Bob Furst (APS Engineering Support Division Mechanical Operations and Maintenance Group) at the APS-U Magnetic Measurement Laboratory in Bldg. 369, testing the pole tips on sextupole magnets for the APS Upgrade multi-bend achromat storage ring.

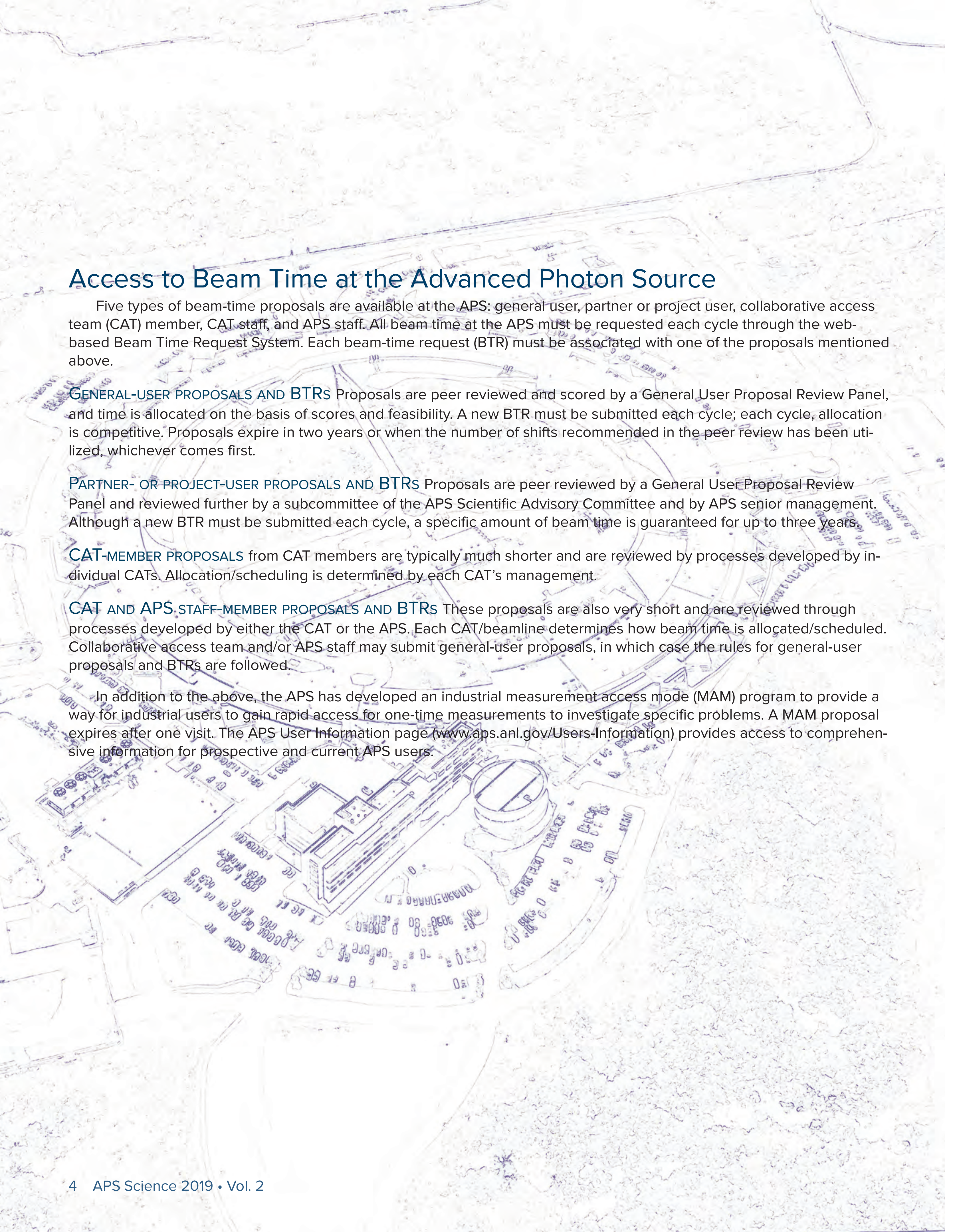

Access to Beam Time at the Advanced Photon Source

Five types of beam-time proposals are available at the APS: general user, partner or project user, collaborative access team (CAT) member, CAT staff, and APS staff. All beam time at the APS must be requested each cycle through the web-based Beam Time Request System. Each beam-time request (BTR) must be associated with one of the proposals mentioned above.

General-user proposals and BTRs Proposals are peer reviewed and scored by a General User Proposal Review Panel, and time is allocated on the basis of scores and feasibility. A new BTR must be submitted each cycle; each cycle, allocation is competitive. Proposals expire in two years or when the number of shifts recommended in the peer review has been utilized, whichever comes first.

Partner- or project-user proposals and BTRs Proposals are peer reviewed by a General User Proposal Review Panel and reviewed further by a subcommittee of the APS Scientific Advisory Committee and by APS senior management. Although a new BTR must be submitted each cycle, a specific amount of beam time is guaranteed for up to three years.

CAT-member proposals from CAT members are typically much shorter and are reviewed by processes developed by individual CATs. Allocation/scheduling is determined by each CAT's management.

CAT and APS staff-member proposals and BTRs These proposals are also very short and are reviewed through processes developed by either the CAT or the APS. Each CAT/beamline determines how beam time is allocated/scheduled. Collaborative access team and/or APS staff may submit general-user proposals, in which case the rules for general-user proposals and BTRs are followed.

In addition to the above, the APS has developed an industrial measurement access mode (MAM) program to provide a way for industrial users to gain rapid access for one-time measurements to investigate specific problems. A MAM proposal expires after one visit. The APS User Information page (www.aps.anl.gov/Users-Information) provides access to comprehensive information for prospective and current APS users.

Engineering Materials and Applications

How Bird Feathers Stick Together for Superior Flight Control

Among the variety of things that fly, from insects to airplanes, birds have the best flight control. This enhanced performance comes from birds' unique ability to morph their wings mid-air, which they achieve by changing the overlap of their feathers. Scientists have suggested that this so-called "variable feather overlap" occurs through underlying mechanisms that involve friction or fastening, but these processes have been poorly understood. Now, using microscale analysis of bird wings at the APS, a team of researchers has discovered new insights into the mechanisms that give morphing wings their flight advantage. They found that bird wings could passively redistribute overlapping feathers through elastic connective tissue and that feathers possess microstructures that slide and lock in a directional, probabilistic manner that keeps gaps from poking through. The team then built a biohybrid feathered robot and confirmed their observations under various turbulent conditions. These findings could help engineers design features for aircraft with improved flight control.

When birds flap their wings during flight, each movement is not just captivating, it also serves a valuable function for flight. By extending or flexing a wing, they're also moving elastic tissue, which controls the position of the connected flight feathers.

To understand how the parts of the wing work together, scientists at Stanford University analyzed how feathers were positioned in the wing of a rock pigeon. (All experimental procedures were conducted on bird cadavers and were approved by Stanford's Administrative Panel on Laboratory Animal Care.) They measured each feather angle with regard to the ulna bone and wrist angle in various poses, such as flexed, mid-tucked, and extended. The measurements revealed that feather angles had a linear rela-

Researchers used a biohybrid aerial robot to test their mechanistic observations about flight feathers. Photo Credit: Lentink Lab/Stanford University.

tionship to wrist angle, suggesting that the feathers are underactuated, which in robotics means that the system has more degrees of freedom than actuators, and is a typical feature of efficient systems. In this case, the feathers' underactuation results rom the connective tissues' elasticity, which passively redistributes overlapping feathers.

Next, the team investigated how neighboring pairs of feathers stick together to avoid gaps during wing extension. With help from researchers at the Smithsonian Institute and the California Council on Science and Technology, they visualized (Fig. 1) the microstructures that interlock the feathers using scanning electron microscopy (SEM) at the Smithsonian National Museum of Natural History and high-resolution computed-tomography (CT) x-ray imaging at the XSD 2-BM beamline at the APS.

The researchers found that feather microstructures, known as "lobate cilia," latch onto as many as hundreds of hooked structures, called "rami," in a probabilistic fashion. This property is also seen in bur fruit hooks, which led to the development of Velcro®. Additionally, the feather fastening is highly directional, as demonstrated by sticky gecko feet. This is the first time that both properties have been demonstrated by a single structure.

To test their findings about the feathers' elastic-enabled redistribution and directional fastening, the team built a biohybrid aerial robot equipped with underactuated pigeon flight feathers (previous page). They confirmed in outdoor and wind tunnel experiments, under low and high turbulence, that both features were crucial during flight: the directional fastening kept the feathers from separating and the elastic underactuation moved unlocked feather into place.

The researchers propose that the observed fastening mechanism likely appears across bird species based on three pieces of evidence. One, the lobate cilia structure is found in many species. Two, the team discovered fastening forces in more than a dozen bird species, including merlins and ospreys. However, this excludes silent flyers such as barn owls, and high-resolution CT scans of owl feathers confirmed that they lack the telltale lobate cilia and rami for fastening. And finally, by measuring the fastening forces, they found that the forces ended up being a similar fraction of body weight for a range of body sizes.

– Tien Nguyen

See: Laura Y. Matloff[1], Eric Chang[1], Teresa J. Feo[2,3], Lindsie Jeffries[1], Amanda K. Stowers[1], Cole Thomson[1], and David Lentink[1*], "How flight feathers stick together to form a continuous morphing wing," Science **367**, 293 (17 January 2020). DOI: 10.1126/science.aaz3358

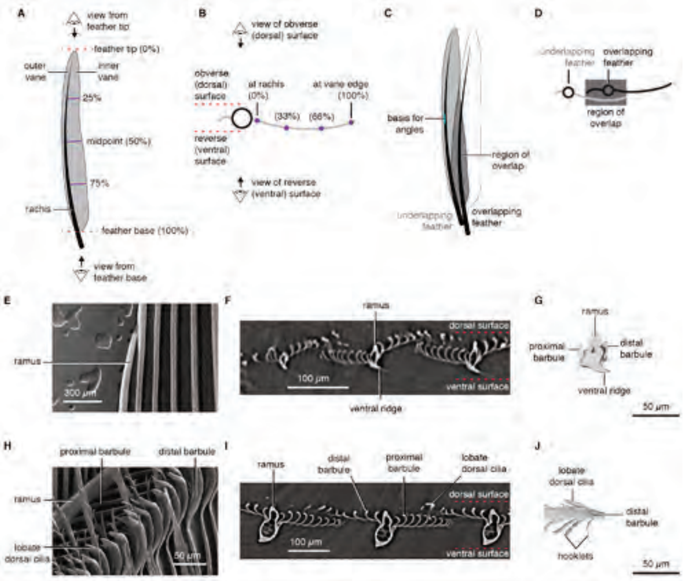

Fig. 1. (A) Diagram of flight feather, view of obverse (dorsal) surface; purple lines indicate example positions of images (i.e., SEM or CT) or measurements along length of feather. (B) Diagram of flight feather cross-section, view from feather base, purple points indicate example positions of images (i.e., SEM or CT) or measurements along the width of the feather vane. (C) Diagram of overlapping feather pair, view of obverse (dorsal) surface. Dark grey shading indicates region of overlap. Blue line at outer edge of rachis at midpoint of underlapping feather indicates basis for all angle measurements for a given feather pair. (D) Diagram of overlapping feather pair cross-section, view from feather base. Dark grey shading indicates region of overlap. (E) SEM of outer vane of overlapping feather, view of reverse (ventral) surface. Image reflected across vertical axis to maintain outer vane to left of page and tip of feather to top of page. (F) Beamline CT cross-section of outer vane of overlapping feather, view from feather base. (G) 3-D render from beamline CT dataset of outer vane ramus of overlapping feather. (H) SEM of inner vane of underlapping feather, view of obverse surface. (I) Beamline CT cross-section of inner vane of underlapping feather, view from feather base. Cross-section locally perpendicular to long axis of rami. (J) 3-D render from a beamline CT dataset of a distal barbule (partial) from inner vane of underlapping feather. Renders are viewed from the tip and have been reflected to match the SEM and beamline CT. From L.Y. Matloff et al., Science **367**, 293 (17 January 2020). © 2020 American Association for the Advancement of Science. All rights reserved.

Author affiliations: [1]Stanford University, [2]Smithsonian Institution, [3]California Council on Science and Technology
Correspondence: * dlentink@stanford.edu

This project was supported by Air Force Office of Scientific Research (AFOSR) Basic Research Initiative award number FA9550-16-1-0182 and AFOSR Defense Enterprise Science Initiative award number FA9550-18-1-0525, with special thanks to B. L. Lee, F. A. Leve, and J. L. Cambier leading the program. T.J.F. was supported by National Science Foundation (NSF) PRFB 1523857. E.C. and L.J. were supported by a NSF GRFP fellowship, A.K.S. by a NDSEG fellowship, and D.L. by a NSF CAREER award 1552419. This research used resources of the Advanced Photon Source, a U.S. Department of Energy (DOE) Office of Science User Facility operated for the DOE Office of Science by Argonne National Laboratory under Contract No. DE-AC02-06CH11357.

Resolving Some Mysteries of Cement Formation

Cement is a mineral-based material that binds together sand and rock to form concrete. Although the use of cement stretches back into antiquity, and in spite of decades of scientific inquiry, the exact process by which it transforms from a fresh paste into a solid largely remains a mystery. To shed light on this process, researchers utilized complementary imaging methods at the APS to continuously monitor changes in cement as it hardened over the first 15 h of hydration at nano- and micro-scale resolutions. Recording the changes to large numbers of particles over the first few hours of hydration allowed the researchers to draw important inferences about the mechanisms driving cement hydration. It is anticipated that the insights gained will aid in optimizing cement ingredients and processes to provide the most durable and cost-effective concrete for different applications.

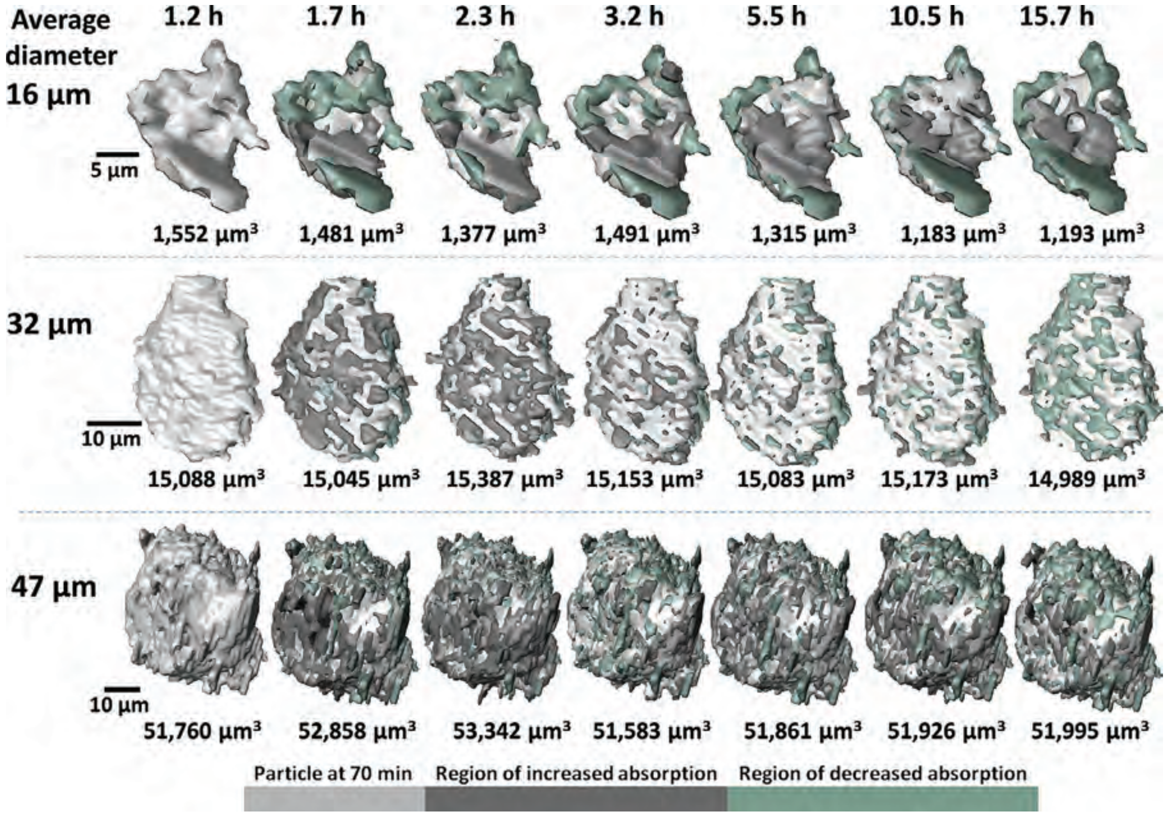

Fig. 1. Tomographic imaging showing the 3-D evolution of three cement particles over time. All length and volume measurements are in microns. Imaging begins during the induction phase (1.2 h), when heat output from the hydration process is lowest, and continues for nearly 15 more hours. Green colors are regions with lower x-ray absorption, indicative of minerals dissolved in solution, voids, and low-mass mineral compounds. Dark gray indicates solid, high-absorption materials. The imaging indicates that particle evolution depends strongly on size, with smaller particles tending to dissolve and larger precipitates grow through Ostwald ripening.

Portland cement is the world's most popular type of cement. It is produced by first mixing together limestone, which is mostly composed of calcium carbonate ($CaCO_{3)}$, along with minerals containing aluminum, iron, sulfur, and other elements. This mixture is then ground up and baked at high heat, forming small, dry lumps called “clinker.” The clinkers are subsequently milled into a powder, along with other ingredients to form finished Portland cement.

Adding water to cement initiates a cascade of complex exothermic chemical reactions collectively referred to as hydration. During hydration the cement begins as a slurry and increasingly hardens over time as different types of mineral compounds are formed.

Traditional studies have most often measured the large-scale physical and chemical properties of cement as it hardens. For instance, heat flow measurements show that hydration initially produces considerable heat for several minutes before falling to a minimum after an hour or so (the induction period), and then rapidly rising again (the acceleration period). Likewise, by examining cement samples extracted at various stages of hydration, chemists have identified the formation of many different types of minerals.

Scientists have also examined cement at the microscopic scale using techniques such as electron and x-ray microscopy. To do this, scientists stop the hydration process with alcohol or acetone to remove water prior to imaging.

Unfortunately, studying the bulk properties of cement during hydration cannot provide details about the microscopic mechanisms driving the process. Conventional microscopy methods have also proven to be inadequate. For one thing, applying a drying agent to halt hydration can alter the cement's microscopic structure and chemistry. Moreover, many x-ray techniques cannot fully penetrate the mineral sample, while particle movement has largely frustrated attempts at x-ray tomography (three-dimensional [3-D] imaging) due to the required hours-long exposure times. The inadequacies of previous investigations have left many fundamental questions unanswered, particularly about the induction and acceleration periods of hydration.

The key was the advanced imaging methods employed by the research team from Oklahoma State University and Princeton University, together with colleagues from the APS and the Argonne Center for Nanoscale Materials. The methods consisted of fast-computed tomography and nano-computed tomography, both carried out at XSD beamline 2-BM-A,B of the APS. The authors note that this was possible because of advances in x-ray beamline detector design and the high photon flux afforded by the APS. The two imaging techniques allowed 3-D imaging of particles at multiple length scales, from micron-sized particles down to nano-sized ones. These imaging techniques relied on the highly penetrating power of the APS x-ray beam, which required only seconds to obtain a 3-D tomographic data set. A new tomograph was produced every 10 min over approximately 15 h of sample hydration. After gathering the x-ray data, a region measuring around 1 mm across by 0.1 mm tall was selected for processing, allowing some 60,000 particles to be imaged.

Figure 1 shows the dramatic evolution of three particles, each representing a different size range. The 3-D images were captured near the end of the induction phase and continued throughout the acceleration phase.

The researchers in this study drew a number of broad conclusions from the accumulated 3-D images and measurements of particle composition. For instance, both micron-scale and nano-scale particles exhibit uneven growth and dissolution on their surfaces. However, size does matter: during the induction phase particles larger than 20 microns across accumulated minerals with a high x-ray absorption on their surfaces, while the surfaces of smaller particles mostly exhibited mineral dissolution. It is hoped that these and other conclusions drawn from the multi-scale imaging methods will improve control over the induction and acceleration phases of cement.   – Philip Koth

See: Masoud Moradian[1]*, Qinang Hu[1], Mohammed Aboustait[1], M. Tyler Ley[1], Jay C. Hanan[1], Xianghui Xiao[2], Volker Rose[2], Robert Winarski[2], and George W. Scherer[3], “Multi-scale observations of structure and chemical composition changes of portland cement systems during hydration,” Constr. Build Mater. **212**, 486 (2019). DOI: 10.1016/j.conbuildmat.2019.04.013

Author affiliations: [1]Oklahoma State University, [2]Argonne National Laboratory, [3]Princeton University
Correspondence: * Masoud.Moradian@okstate.edu

This work was sponsored by funding from the Federal Highway Administration (FHWA) Exploratory Advanced Research (EAR) program and funding from the United States National Science Foundation CMMI 1150404 CAREER Award. This research used resources of the Advanced Photon Source, a U.S. Department of Energy (DOE) Office of Science User Facility operated for the DOE Office of Science by Argonne National Laboratory under Contract No. DE-AC02-06CH11357.

Adding Stress Alters Material Aging

Metallic glasses are popular for a wide variety of uses, from cell phone cases to medical devices to sports equipment to electrical transformers. These alloys, which are glass-like because of their disordered atomic structure, are strong, elastic, resistant to corrosion, and can even have desirable magnetic or surface properties. Over time, however, that atomic structure can change, leading to degradation of their properties. Scientists had so far focused on aging as a function merely of time and temperature, but now researchers working at the APS have shown that mechanical stress plays a role, too. In fact, stress might even be applied to reverse the aging process.

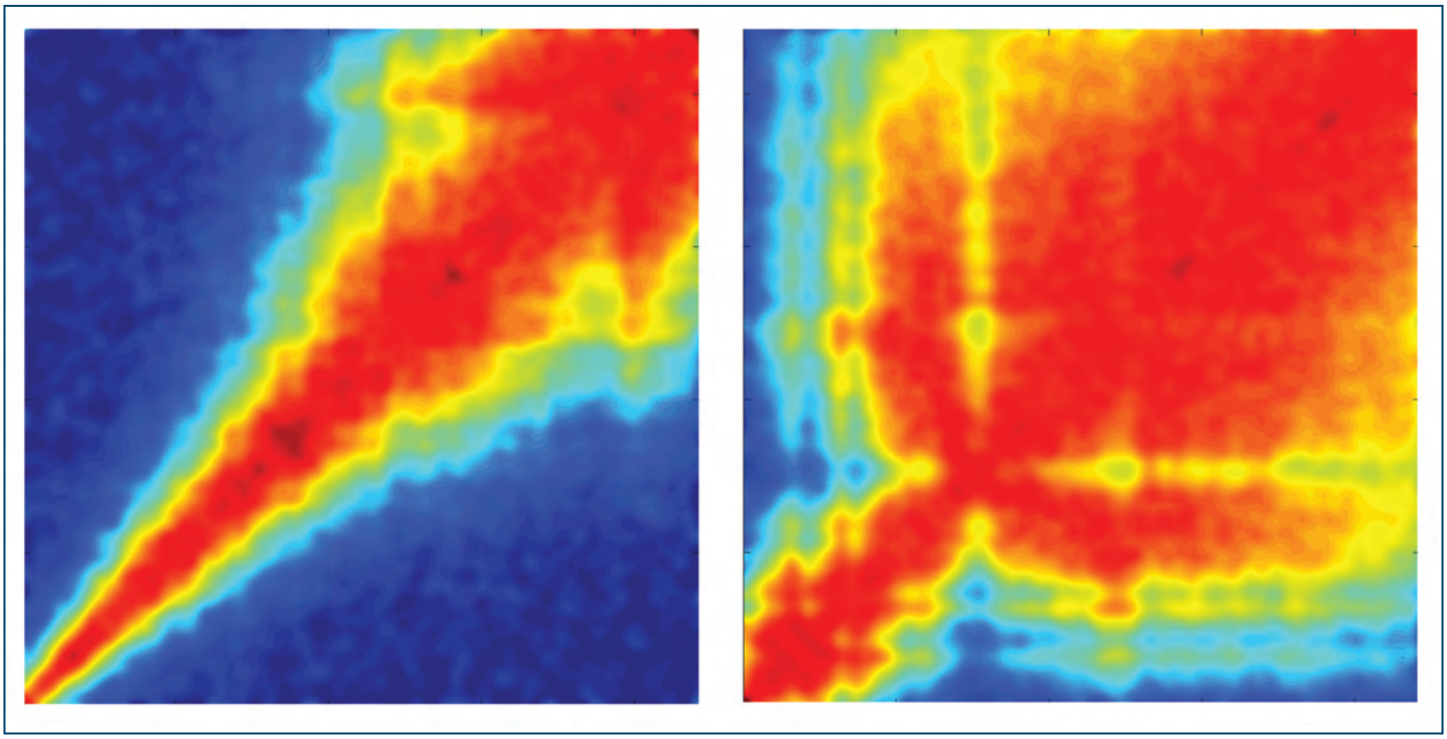

Fig. 1. Over time and at room temperature, an unstressed metallic glass relaxes in an expected way (left). This is called "aging." In contrast, adding a mechanical stress alters the dynamics dramatically (right), as revealed by x-ray photon correlation spectroscopy at the APS. Figures adapted from A. Das et al., Nat. Commun. **10**, 5006 (2019). © 2019 Springer Nature Limited

Unlike crystals, metallic glasses are amorphous. Over time, and increasingly with higher temperature, atoms in the structure may shift to a lower-energy state, moving to a different position and causing the material to relax (Fig. 1). A piece of metallic glass sitting on a shelf might shrink slightly, or become more brittle. Depending on time and temperature, the material may experience changes in strength, toughness, ductility, elasticity, hardness, and density. Scientists have referred to the time and temperature dependence of these changes as a universal aging process. It turns out, however, that stress breaks that universality by altering how atoms within the material rearrange themselves.

To study the process, the researchers from the University of Illinois at Urbana-Champaign, the Paul Scherrer Institute (Switzerland), and Argonne used metallic glass bars made of an alloy of zirconium, titanium, copper, nickel, and aluminum and performed x-ray photon correlation spectroscopy measurements on them at XSD beamline 8-ID-E at the APS (Fig. 2). The x-rays produce a speckle pattern based on the positions of atoms within the material. Researchers then applied a load to bend the bar, and repeated their measurements. They bent the bar to a higher load and measured it again. Finally they took a second piece from the same bar and bent it in the opposite sequence, and performed the measurements on that. In all, they recorded measurements every 10 sec over the course of many hours. Such a study is only possible with a synchrotron like the APS, which produces a coherent x-ray flux and allows both small-angle and wide-angle scattering experiments. The scattered x-rays are collected in a detector containing 1 million pixels. While the overall intensity of the image on the detector does not change, the intensity can vary between pixels over time. Because the scattering intensity is very sensitive to the position of the underlying atoms, changes in pixel intensity show how the atoms are moving, and studying the phenomenon over time shows how fast that movement takes place.

The unloaded sample showed the universal aging behavior that would be expected, and some of the results with loaded samples showed stress producing the same relaxation effects as temperature-driven aging. Other measurements, however, showed structural changes slowing or even reversing in response to stress. In general, the relaxation time of the material increased with the magnitude of applied stress.

Having shown that stress changes aging behavior, the researchers' next step will be to figure out which conditions produce which alterations. Currently, to reverse aging in a metallic glass, the only option is to melt it down and recast it, which can be expensive. The researchers hope to work out protocols for applications of stress — how much, for how long, whether it should be tensile or compressive stress — that might allow them to control the atomic structure enough to rejuvenate aging materials.

They would also like to design a new experiment to measure the changes that happen immediately after the application of the load. In this case, there was a lag between when they applied the stress to the metallic glass bars and when they subjected them to the x-rays, which could mean they missed many changes at the beginning of the process. The APS Upgrade 8-ID beamline will speed up such measurements by factors of 100-10,000, enabling faster studies with periodic cycling of stress.

– Neil Savage

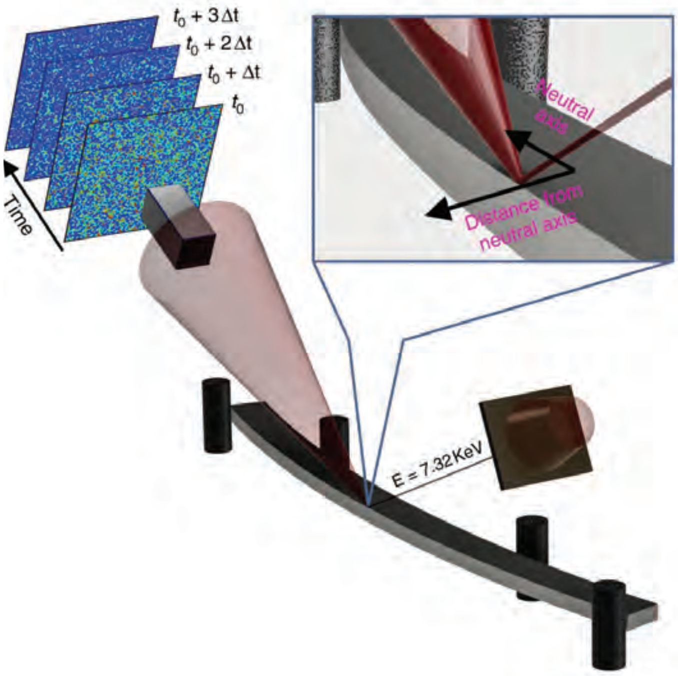

Fig. 2. *In situ* four-point bending test. A coherent x-ray beam from a synchrotron source is focused and slitted down to form a 10-µm x 10-µm probe on the sample surface. The x-ray beam position away from the neutral axis determines the sign of the applied stress. Photons from only 1° of scattered angular range are collected for correlation spectroscopy.

See: Amlan Das[1], Peter M. Derlet[2], Chaoyang Liu[1], Eric M. Dufresne[3], and Robert Maaß[1]*, "Stress breaks universal aging behavior in a metallic glass," Nat. Commun. **10**, 5006 (2019). DOI: 10.1038/s41467-019-12892-1

Author affiliations: [1]University of Illinois at Urbana-Champaign, [2]Paul Scherrer Institute, [3]Argonne National Laboratory
Correspondence: * rmaass@illinois.edu

This research was carried out in part at the Frederick Seitz Materials Research Laboratories Central Research Facilities, University of Illinois. R.M. gratefully acknowledges startup funds provided by the Department of Materials Science and Engineering at the University of Illinois at Urbana-Champaign. This research used resources of the Advanced Photon Source, a U.S. Department of Energy (DOE) Office of Science User Facility operated for the DOE Office of Science by Argonne National Laboratory under Contract No. DE-AC02-06CH11357.

Battling Parasitic Reactions for Better Batteries

Unwanted side reactions, commonly referred to as "parasitic reactions," are the bane of batteries. For example, one promising material that could make batteries more powerful, nickel (Ni)-rich lithium nickel manganese cobalt oxide, becomes unstable at higher voltages over multiple charging/discharging cycles due to parasitic reactions at the interface between electrode and electrolyte. To get a better handle on these parasitic reactions and the impact they have on battery durability, researchers studied a model system, chemically modified $LiNi_{0.6}Mn_{0.2}O_2$ (NMC 622), using the APS. Indeed, knocking down the parasitic reactions demonstrated myriad benefits to the battery life, suggesting that surface modification could be an effective approach to producing robust, long-lasting, and powerful battery materials.

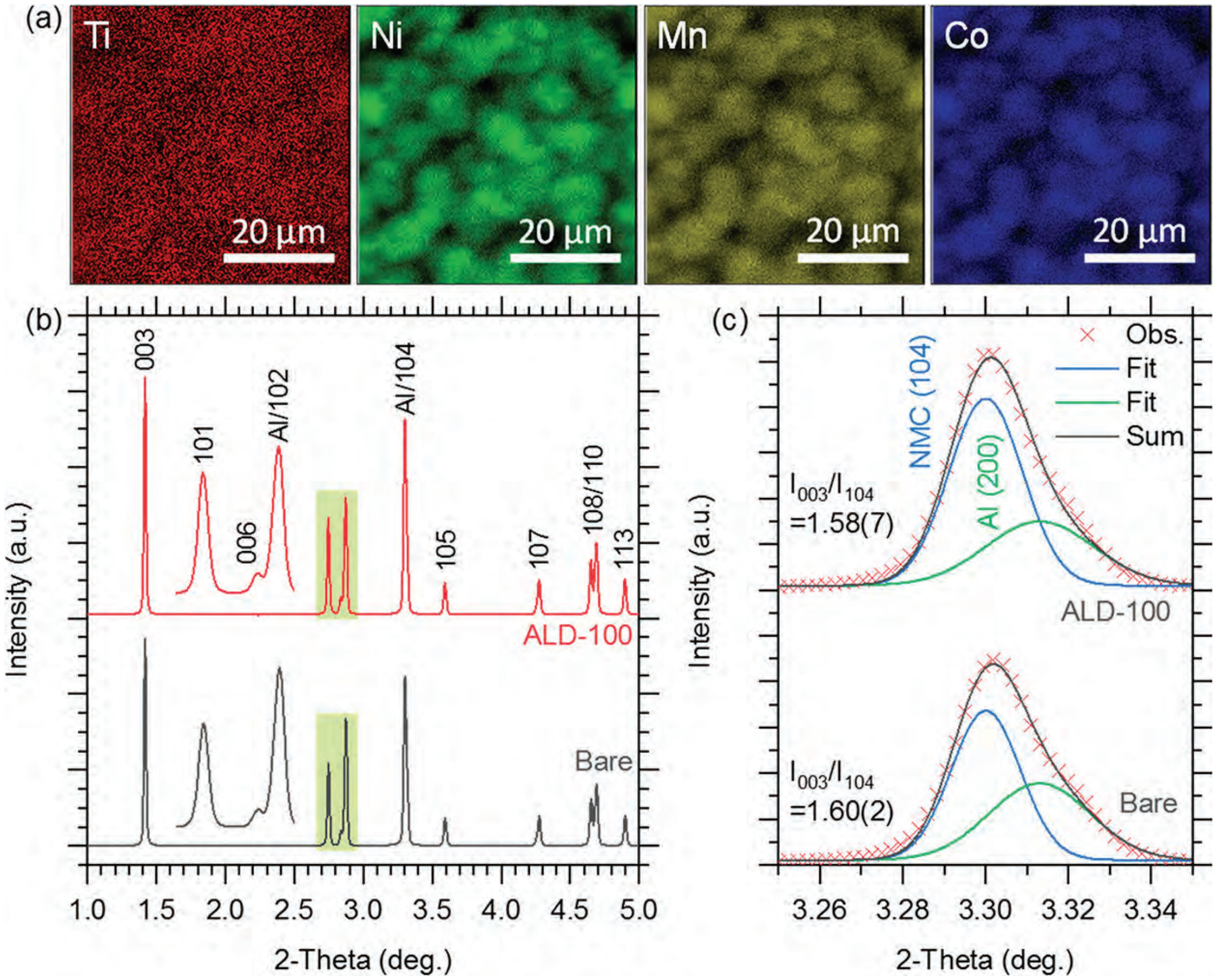

Ni-rich NMCs are high-capacity cathode materials for lithium-ion batteries, but they have poor cycling stability at potentials above 4.3 V relative to standard Li/Li$^+$ reference. The poor cycling stability has been pinned on parasitic reactions, which mostly consist of complicated chemical reactions involving electron transfer between the delithiated cathode material and the electrolyte. Based on earlier research, the research team from Argonne National Laboratory, the University of Arkansas, and Stanford University figured out that the parasitic reaction at a potential below 4.5 V is dominated by the chemical reaction between the delithiated (the incorporation of lithium into an electrode in a lithium-ion battery) cathode material and the electrolyte. Above 4.5 V, the dominant parasitic reaction is the direct electrochemical oxidation of solvent molecules. Regardless of the parasitic reactions details, the end result is that the cathode gets coated in oxidized solvent molecules – largely oxidized solvent molecules – that pose a detrimental impact on the life of the cathode material.

In this study, the team explored a strategy for protecting NMC-622 from parasitic reactions by covering it with TiO$_2$. This material is well known for its ability to protect cathodes. The researchers chemically modified NMC-622 with TiO$_2$ using the atomic layer deposition (ALD) technique. This method allowed them to create strong chemical bonds between the titanium atom and naturally existing surface hydroxyl sites on NMC-622 particles. The TiO$_2$ layer on the surface of NMC622 acts as a physical barrier to suppress the electron transfer reaction between the solvent molecules and the cathode materials, leading to a reduced level of proton-bearing species and a better electrochemical performance of the cathode material.

To get a handle on how titanium distributed on the NMC particles, the researchers turned to elemental mapping via synchrotron x-ray fluorescence (XRF) and high-energy x-ray diffraction (HEXRD) experiments carried out at beamlines XSD beamlines 2-ID-E and 11-ID-C, respectively, of the APS, as well as scanning electron microscopy at Argonne's Center for Nanoscale Materials. The XRF technique can show where particular elements map onto a surface. The data (Fig .1a) showed a uniform distribution of titanium on the electrode surface. Next, the researchers looked at the underlying structure of the NMC particles to see the impact of chemical modification using HEXRD. The HEXRD diffraction patterns (Fig. 1b) did not differ between modified and unmodified NMC particles, suggesting that ALD did not change the atomic structure of the material.

In addition, the research team deployed a prototype high-precision leakage current measurement system to quantitatively measure the rate of parasitic reactions occurring at the interface of the cathode materials at various working potentials. A negative correlation between the measured leakage current and the capacity retention of the cathode material was established. As expected, the surface modification with TiO2 leads to a reduction in oxidized solvent molecules that minimized impedance hike at the interface and that improved cycling stability of the cathode material. The authors report that this is a proof-of-principle step showing that it's possible to reduce parasitic reactions by surface modifications of the cathode and to design advanced batteries.

The upgraded APS will allow for focusing the beam down to submicrometer size enabling the structural analysis of buried interlayers like in battery materials using high-energy x-rays.   – Erika Gebel Berg

< Fig. 1. (a) XRF elemental mapping of the 20 ALD cycle-treated NMC electrodes for Ti, Ni, Mn, and Co. (b) HEXRD patterns of the 100 ALD cycle-treated and bare NMC electrodes under pristine condition. (c) Deconvolution of the overlapping diffraction peaks from both NMC and Al current collectors for the two samples.

See: Han Gao[1], Jiyu Cai[2], Gui-Liang Xu[1], Luxi Li[1], Yang Ren[1], Xiangbo Meng[2]*, Khalil Amine[1,3]**, and Zonghai Chen[1]***, "Surface Modification for Suppressing Interfacial Parasitic Reactions of a Nickel-Rich Lithium-Ion Cathode," Chem. Mater. **31**, 2723 (2019). DOI: 10.1021/acs.chemmater.8b04200

Author affiliations: [1]Argonne National Laboratory, [2]University of Arkansas, [3]Stanford University

Correspondence: * xbmeng@uark.edu, ** amine@anl.gov,
*** zonghai.chen@anl.gov

Research at Argonne was supported by the U.S. Department of Energy (DOE) Office of Energy Efficiency and Renewable Energy, Vehicle Technologies Office. Support from Tien Duong of the U.S. DOE's Office of Vehicle Technologies Program is gratefully acknowledged. H.G. also acknowledges the NSERC Canada Postdoctoral Fellowships Program. X.M. and J.C. acknowledge partial support from the Center for Advanced Surface Engineering, under National Science Foundation Grant OIA-1457888 and the Arkansas EPSCoR Program, ASSET III. X.M. and J.C. also appreciate the financial research support from the University of Arkansas. The authors acknowledge the use of the Advanced Photon Source (APS) and the Center for Nanoscale Materials (CNM), which are supported by the U.S. DOE Office of Science-Basic Energy Sciences, under Contract DE-AC02-06CH11357.

Boosting the Performance of Li-S Batteries

Lithium-sulfur (Li-S) batteries boast a theoretical energy density that is 10-fold greater than the energy offered by today's best lithium-ion batteries. Yet for a decade, researchers have struggled to make such powerful Li-S batteries a reality. One limiting factor for this type of battery is sulfur's poor electronic conductivity. Scientists have made some progress on this front by introducing conductive materials into the cathode such as carbon or selenium, which are more promising because of their electrochemical activity, but researchers still face a challenge known as the "shuttle effect." This effect comes from the formation of polysulfide and polyselenides compounds, which degrade the battery over time and lower its overall capacity. Now, researchers have developed a new Se-doped cathode material that minimizes the unwanted shuttle effect to achieve high capacities. Using synchrotron x-ray analysis at the APS, the team showed that the battery's improved performance owes to the formation of a robust solid-electrolyte interphase (SEI). These findings emphasize the importance of the SEI layers and the authors suggest that their work will spark more research focused on optimizing these layers.

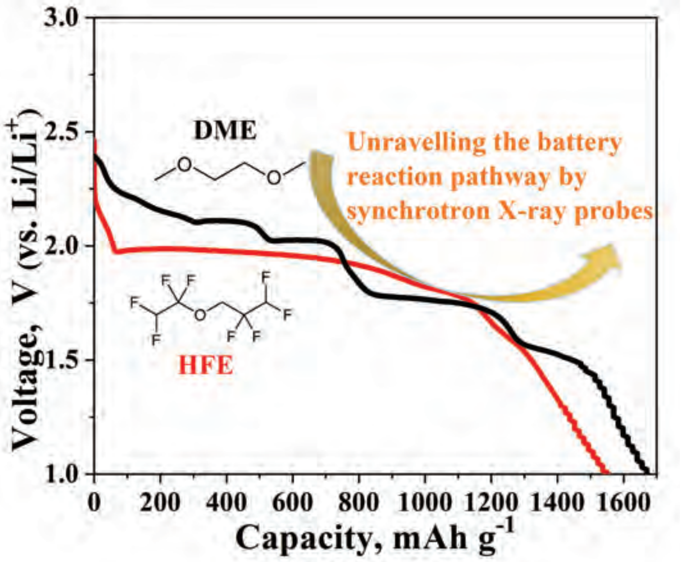

Fig. 1. Using x-ray synchrotron data, researchers found that an HFE-based electrolyte promotes a solid-solid mechanism, resulting in high-energy capacities for a Se-doped Li-S battery.

Despite Li-ion batteries' long reign in the electronics world, powering everything from smart phones to electric cars, these batteries provide a fraction of the theoretical energy offered by other cathode materials. Classic Li-ion batteries with a lithium cobalt oxide cathode can reach energy densities up to 250 W h/kg, whereas Li-S batteries have densities up to about 2600 W h/kg. Although sulfur is abundantly available, the element brings with it two inherent limitations as a battery material.

First, sulfur is a poor electronic conductor. To resolve this issue, researchers have added materials like carbon. While this improves the cathode's overall conductivity, carbon can't participate in electrochemical reactions, reducing both its effectiveness as a cathode material and the battery's overall capacity. As an alternative additive, scientists have introduced selenium, which is 25 times as conductive as sulfur and also electrochemically active, offering similar levels of energy capacity to sulfur. Selenium, however, suffers from the same, and second, major issue that sulfur does inside a battery: the shuttle effect.

Now, scientists at Argonne have developed a mixed cathode material called $S_{22.2}Se$/Ketjenblack that overcomes the shuttle effect to achieve excellent electrochemical performance, delivering a capacity of more than 1000 mAh/g within 50 cycles. To develop this high-performance material, the team undertook an investigation of its physical properties.

The researchers prepared a range of Se-S compounds, analyzing their structure via high-energy x-ray diffraction experiments carried out at XSD beamlines 11-ID-C and 11-ID-D of the APS, and *in operando* x-ray absorption near edge structure experiments on the Se K-edge at XSD beamline 20-BM-B of the APS. The team found that as they increased the selenium content, the theoretical capacity and electronic conductivity increased as well. Based on these findings, the researchers chose S_5Se_2 as a model material.

Then, they explored how S_5Se_2 performed when paired with conventional ether-based electrolytes. While conventional ether-based (DME) electrolytes resulted in severe shuttle effects, a hydrofluoroether-based (HFE) electrolyte showed minimal shuttle effects (Fig. 1). Based on x-ray diffraction data collected during the electrochemical reaction, the authors found that the HFE-based electrolyte promotes a solid-solid lithiation and delithiation mechanism (Fig. 2). This mechanism, confirmed by 7Li NMR and x-ray absorption near-edge spectroscopy experiments, bypasses the formation of soluble polysulfides and polyselenides for superior battery performance.

The team proposes that the advantageous solid-solid mechanism arises from the formation of an solid-electrolyte interface layer, observed via x-ray photoelectron spectroscopy. The layer protects the Se-S material from attack by electrolyte molecules to enable a solid-state reaction. The researchers suggest that S_5Se_2 molecules are encapsulated in the Ketjenblack carbon pores, which also helps keep them away from the electrolyte. Notably, the HFE-based electrolyte enabled the use of large porous carbon, which is crucial for high-loading batteries that could lead to increased volumetric energy for batteries.

– Tien Nguyen

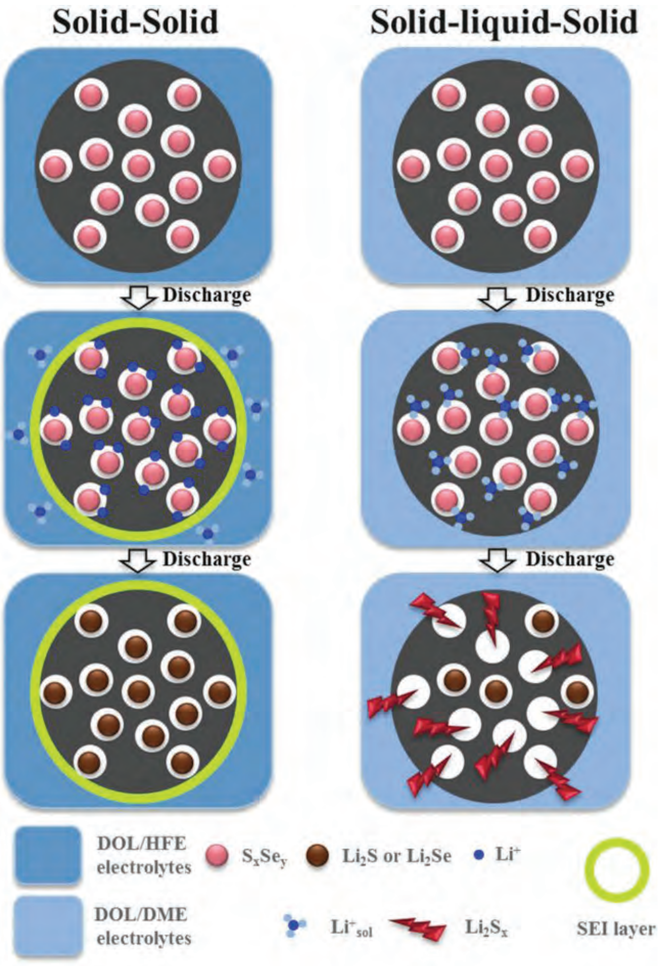

Fig. 2. Schematic illustration for different lithiation mechanism of Se-S cathodes in HFE-based and DME-based electrolytes.

See: Gui-Liang Xu[1], Hui Sun[2], Chao Luo[3], Luis Estevez[4], Minghao Zhuang[1], Han Gao[1], Rachid Amine[1], Hao Wang[1], Xiaoyi Zhang[1], Cheng-Jun Sun[1], Yuzi Liu, Yang Ren[1], Steve M. Heald[1], Chunsheng Wang[3], Zonghai Chen[1]*, and Khalil Amine[1]**, "Solid-State Lithium/Selenium–Sulfur Chemistry Enabled via a Robust Solid-Electrolyte Interphase," Adv. Energy Mater. **9**, 1802235 (2019).
DOI: 10.1002/aenm.201802235

Author affiliations: [1]Argonne National Laboratory, [2]China University of Petroleum-Beijing, [3]University of Maryland, [4]Pacific Northwest National Laboratory
Correspondence: * zonghai.chen@anl.gov, ** amine@anl.gov

Research at Argonne National Laboratory was funded by the U.S. Department of Energy (DOE), Vehicle Technologies Office. Use of the APS and the Center for Nanoscale Materials, both Office of Science user facilities, was supported by the U.S. DOE Office of Science-Basic Energy Sciences, under Contract No. DE-AC02-06CH11357. Support from Tien Duong of the U.S. DOE's Office of Vehicle Technologies Program is gratefully acknowledged. Sector 20 facilities at the Advanced Photon Source, and research at these facilities, were supported by DOE Basic Energy Sciences, the Canadian Light Source and its funding partners, and the APS.

Unraveling the Mechanisms Responsible for Hydrogen Embrittlement of Steel

Exposure to hydrogen gas (H_2) causes the embrittlement of steel, a phenomenon first observed nearly 150 years ago. Embrittlement means that the steel's ductility is reduced. Although this process has been extensively examined using a variety of analytical techniques, such as optical imaging and electron microscopy, the mechanisms, or combination of mechanisms, that are chiefly responsible for hydrogen-induced embrittlement remain unclear. One of the challenges encountered when investigating hydrogen embrittlement is that the sample being examined is usually removed from the hydrogen environment prior to analysis. This precludes real-time imaging of the hydrogen/steel dynamic. To address this limitation, researchers using the APS carried out the first application of high-energy x-ray diffraction (HEXD) to a steel sample during H_2 exposure. Analysis indicates that the hydrogen-induced embrittlement arose from a combination of two distinct mechanisms. Understanding the primary mechanisms responsible for steel embrittlement caused by H_2 exposure should help materials scientists develop strategies to ameliorate this problem, which has important ramifications for hydrogen storage and transport, as well as being a prerequisite for realizing a future hydrogen economy.

External forces acting on a steel object are translated into microscopic deformations and stresses within its polycrystalline structure. If the magnitude of these stresses is sufficiently large, microscopic fatigue cracks will form and propagate over time. Crucially, under the same external loading conditions, any fatigue cracks exposed to hydrogen will grow 10 to 100 times faster than those exposed to air. Microscopic fatigue cracks in steel are shown in Fig. 1. The crack in the upper panel formed in air, while the lower crack formed in H_2.

Numerous mechanisms have been proposed to explain the significantly higher fatigue crack growth observed in steels exposed to hydrogen. The two mechanisms tested in this study were hydrogen enhanced decohesion (HEDE) and hydrogen enhanced localized plasticity (HELP). The HEDE model explains increased crack growth as resulting from hydrogen promoting decohesion within the steel. Broadly speaking, decohesion refers to the loosening of atomic or molecular bonds. Sufficient decohesion allows a crack to propagate and can occur in two ways: Decohesion within individual

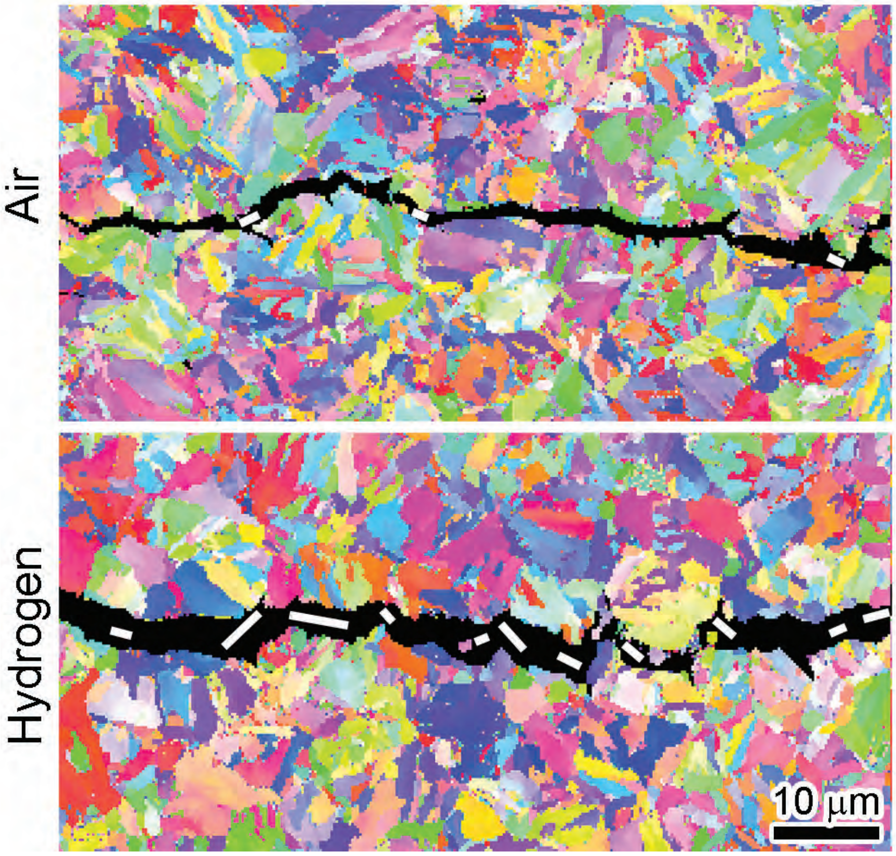

Fig. 1. Comparison of fatigue cracks in steel exposed to air (upper panel) and to hydrogen (lower panel). The larger crack appearing in the lower panel is indicative of the accelerated growth caused by H_2 exposure. Individual grains in the steel are identified by color. The small white bars highlight the locations where the crack formed between different grains, technically referred to as intergranular fracturing. Figures adapted from M. Connolly et al., Acta Mater. **180**, 272 (2019). Copyright ©2019 Elsevier B.V. or its licensors or contributors.

grains is referred to as transgranular decohesion (labeled T-HEDE), while decohesion between grains is called intergranular decohesion (IG-HEDE).

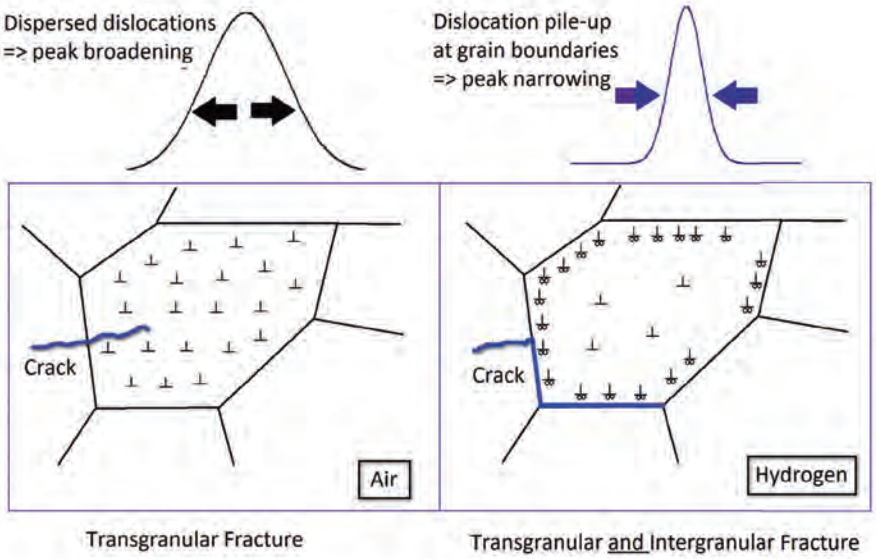

Fig. 2. Illustration of dislocation movement within steel grains as determined by x-ray diffraction. Narrowing or broadening of the diffraction peaks (top of figure) indicates dislocation distribution. Left side shows that under an air environment the dislocations are evenly spread over the entire grain. By contrast, in a hydrogen environment dislocations migrate to grain boundaries (right side) due to the HELP mechanism. Additionally, dislocation accumulation at grain boundaries leads to an increase in intergranular (between grain) fractures as predicted by the IG-HEDE mechanism, which is illustrated by the blue line segments along grain boundaries.

The HELP model invokes a different mechanism to explain hydrogen-enhanced crack growth. According to HELP, the presence of hydrogen facilitates the movement of dislocations within the grains (individual crystals) of the steel. A dislocation is a mobile line defect in a grain's crystalline structure whose movement causes plastic deformation. The presence of dislocations within individual grains can actually be helpful by alleviating stress buildup, thereby limiting fatigue crack nucleation and growth. However, the presence of hydrogen can cause redistribution of the dislocations within steel grains, causing a crucial buildup in strain that enhances crack propagation.

Over the years, materials scientists have cited different experimental results to promote either the HEDE or HELP models. However, recent studies favor a more balanced approach in which the HEDE and HELP mechanisms are seen as complimentary, with both playing a role in explaining hydrogen's deleterious effect on crack formation and growth.

To unravel which mechanisms play significant roles in hydrogen embrittlement, samples of the low-alloy steel AISI 4130 were subjected to several experimental tests, including high-energy x-ray diffraction (HEXD) at the XSD 1-ID-E x-ray beamline at the APS. In the HEXD protocol, 4130 steel samples were placed in either air or hydrogen environments. The samples were then cyclically stretched and relaxed to induce microscopic fatigue cracks.

Figure 2 illustrates some of the HEXD results. Broadening of the diffraction peaks occurred for the sample in air (left side of Fig. 2), indicating that dislocations were spread more-or-less evenly across the entire grain. In contrast, the narrower diffraction peaks recorded for the sample in hydrogen (right side of Fig. 2) indicate an accumulation of dislocations at the grain boundary. The accumulation of dislocations supports the HELP model of H_2-induced embrittlement. However, the fact that the fracture in the hydrogen environment (right side of Fig. 2) also appeared between the grain boundary, i.e., was intergranular, lends support to the intergranular decohesion, or IG-HEDE, model.

The experimental results indicate that both the HEDE and HELP mechanisms play important roles in the hydrogen embrittlement of steel. Moreover, the HEXD data should also prove useful in calibrating models of fatigue crack formation for use in future studies. – Philip Koth

See: Matthew Connolly[1]*, May Martin[1], Peter Bradley[1], Damian Lauria[1], Andrew Slifka[1], Robert Amaro[2], Christopher Looney[3], and Jun-Sang Park[4], “In situ high energy X-ray diffraction measurement of strain and dislocation density ahead of crack tips grown in hydrogen,” Acta Mater. **180,** 272 (2019).
DOI: 10.1016/j.actamat.2019.09.020

Author affiliations: [1]National Institute of Standards and Technology, [2]Southern Research, [3]Colorado School of Mines, [4]Argonne National Laboratory
Correspondence: * matthew.connolly@nist.gov

This work was supported by the U.S. Department of Transportation under grant DTPH5615X00015 and the U.S. Department of Energy (DOE) contract DE-NA-0003525. This research used resources of the Advanced Photon Source, a U.S. DOE Office of Science User Facility operated for the DOE Office of Science by Argonne National Laboratory under Contract No. DE-AC02-06CH11357.

Coupling Single Platinum Atoms to Form Clusters Improves Catalytic Activity

Environmental and sustainability issues demand that new motor vehicles produce lower emissions while increasing fuel economy. These goals require improvements to many vehicle systems, including the catalytic converter. Catalytic converters reduce noxious emissions, chiefly by converting carbon monoxide (CO), hydrocarbons, and nitrous oxides into carbon dioxide (CO_2), nitrogen, and water. In many converters, this task is achieved by mating platinum-group metals with cerium oxide (CeO_2)-based materials. An exciting development in recent years has been the appearance of single-atom catalysis, which greatly reduces the amount of expensive platinum (or similar metal) that is needed. In the single-atom approach, individual platinum atoms are dispersed throughout a matrix of CeO_2. A multi-institution collaboration of researchers demonstrated that enhancing the single-atom approach can lead to vastly greater catalytic activity. The innovative approach demonstrated in this study could lead to improved catalytic converters for the next generation of ultra-low-emission vehicles.

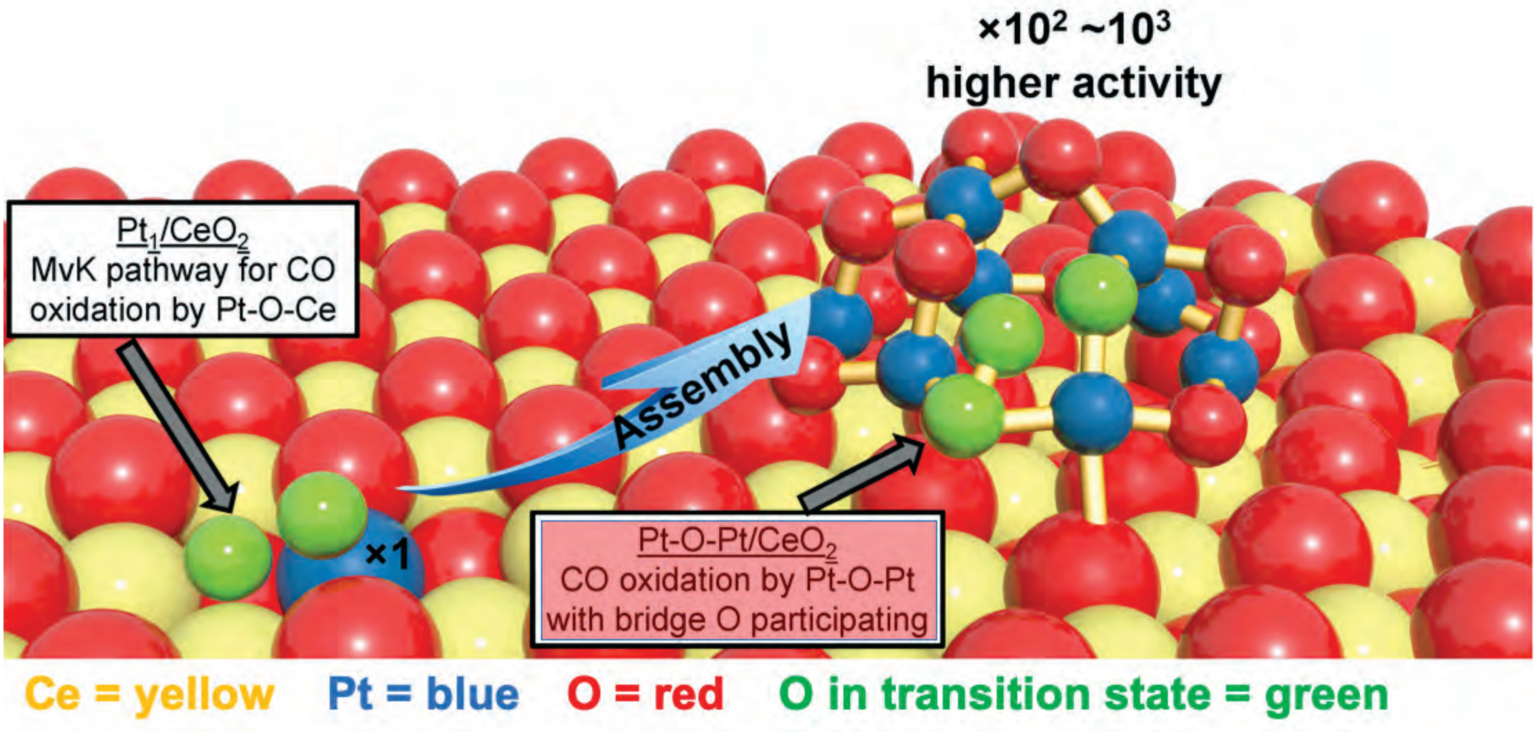

Fig. 1. Oxygen activation by a single platinum atom (left side) and a platinum cluster (right). The two catalytic sites are situated on a bed of cerium oxide (CeO_2), with cerium (Ce) atoms shown in yellow and oxygen (O) in red. Platinum (Pt) atoms are colored blue. Note how the lone Pt atom at left is embedded within the cerium oxide layer (denoted Pt/CeO_2). The single platinum atom actives oxygen atoms (little green spheres) from the cerium oxide layer to convert CO to CO_2. Researchers assembled platinum/oxygen clusters (labeled $Pt\text{-}O\text{-}Pt/CeO_2$) from their single-atom platinum cousins. The resulting $Pt\text{-}O\text{-}Pt/CeO_2$ cluster stands atop the cerium oxide layer and activates oxygen atoms much more effectively, as indicated by the more-numerous green spheres.

The first catalytic converters first appeared in cars in the mid-1970s. While many different materials have since been used, Pt and related metals, such as palladium and rhodium, remain among the most popular catalytic elements. One drawback of these metals is their limited supply and high cost. Traditionally, the platinum-group metals in catalytic converters exist in the form of nanoparticles. This inevitably causes a significant waste because most of the metal atoms are buried inside the nanoparticles and cannot participate in catalysis.

In the early 2000s, scientists serendipitously discovered how to disperse single platinum atoms throughout cerium oxide (commonly called ceria) and other materials. The resulting single-atom catalyst allows all the platinum present to participate, so much less of the precious metal is required. Even though the single-atom catalyst utilizes all the available platinum, the researchers in this study considered whether coupling the isolated and dispersed platinum atoms to form clusters would substantially multiply their overall effectiveness. This hypothesis was tested by preparing and testing both single-atom and clustered platinum systems.

A single-atom catalytic system was produced by dispersing platinum atoms throughout a ceria matrix. The resulting platinum single-atom system is denoted Pt/CeO_2. To produce the clustered system, single platinum atoms were used as seeds to generate a much more active Pt cluster through a facile activation treatment, wherein a mild hydrogen gas (H_2) reduction was followed by CO-plus-O_2 treatment. In the resulting Pt clusters (~1 nanometer in diameter without stacked layers), an oxygen atom is juxtaposed between a pair of platinum atoms (Pt-O-Pt). The platinum/oxygen/ceria unit is denoted $Pt\text{-}O\text{-}Pt/CeO_2$. The two types of catalytic units and their relative positions to the cerium oxide layer are illustrated in Fig. 1.

The number of platinum and oxygen atoms in a typical cluster was determined using sophisticated computer modeling and various imaging methods. One such method consisted of the x-ray absorption spectroscopy (XAS) measurements performed at XSD beamline 12-BM of the APS. The XAS measurements helped determine that the chemical formula Pt_8O_{14} best reflected the relative numbers of platinum and oxygen atoms in the clusters. In addition, aberration-corrected high-angle annular dark-field scanning transmission electron microscopy images of Pt species were obtained at the DOE's Advanced Microscopy Laboratory at Oak Ridge National Laboratory (ORNL).

In testing the relative effectiveness of the two systems, the researchers focused on CO oxidation, i.e., the conversion of carbon monoxide to carbon dioxide. For temperatures between 80° C and 150° C, the $Pt\text{-}O\text{-}Pt/CeO_2$ clusters exhibited up to 1000 times greater catalytic activity in oxidizing CO. Analysis further indicated that the oxygen participating in the CO-to-CO_2 conversion came from the Pt-O-Pt layer and not the underlying ceria. This is in stark contrast to conventional reaction pathways, where oxygen is contributed by CeO_2.

The vastly improved oxidation of CO at lower temperatures achieved by the platinum clusters has important ramifications for the low-temperature period following cold-engine start, during which current catalytic converters are not being adequately heated to purify the noxious exhaust emissions. Furthermore, the methods used in this research can readily be applied to other catalytic systems; for instance, the platinum clusters can be dispersed on substrates other than ceria. Also, the size of the clusters can be tuned to adapt their catalytic activity and selectivity to better fit different emission environments. – Philip Koth

See: Hui Wang[1], Jin-Xun Liu[2], Lawrence F. Allard[3], Sungsik Lee[4], Jilei Liu[5], Hang Li[1], Jianqiang Wang[1], Jun Wang[1], SeH. Oh[6], Wei Li[6], Maria Flytzani-Stephanopoulos[5], Meiqing Shen[1]*, Bryan R. Goldsmith[2]**, and Ming Yang[6]***, "Surpassing the single-atom catalytic activity limit through paired Pt-O-Pt ensemble built from isolated Pt1 atoms," Nat. Commun. **10**, 3808 (2019).
DOI: 038/s41467-019-11856-9

Author affiliations: [1]Tianjin University, [2]University of Michigan, [3]Oak Ridge National Laboratory, [4]Argonne National Laboratory, [5]Tufts University, [6]General Motors Global Research and Development

Correspondence: *mqshen@tju.edu.cn, **bgoldsm@umich.edu, ***ming.yang@gm.com

The work from Tianjin University was supported by the National Key R&D Program (2017YFC0211303), the Natural Science Foundation of China (Grant No. 21576207), and the academic collaboration with GM Global R&D. The computational work was supported by start-up funds provided by the University of Michigan. Microscopy work at ORNL was supported by a Strategic Partnership Project funded by GM Global R&D, and, in part, by the U.S. DOE Office of Energy Efficiency and Renewable Energy, Vehicle Technologies Office, Propulsion Materials Program. This research used resources of the APS, a DOE Office of Science User Facility operated for the DOE Office of Science by Argonne National Laboratory under Contract No. DE-AC02–06CH11357.

Crystals, Lasers, Glasses, and Bent Molecules: Adventures in Nonlinear Optics

Light is an indispensable scientific tool. For example, laser-based optical sensors can detect oxygen in the environment, proteins in biomedical samples, and process markers in industrial settings, among other applications. However, not all wavelengths of light can be generated by a single laser, which limits what chemicals can be detected with optical sensing. That's where nonlinear optical crystals can help. By shining multiple lasers with different wavelengths through such crystals, researchers can tune laser beams via frequency conversion and cover more of the optical spectra. This has been a successful approach for wavelengths from ultraviolet to near-infrared(IR), but the mid-IR region has lacked practical, nonlinear optical crystals. However, crystals may not be the only game in town. A multi-institution international research team is exploring a possible solution to the crystal problem: cutting-edge glasses containing mercuric iodide. The idea is that these glasses could behave like nonlinear optical crystals, offering an enticing approach to the generation of novel amorphous optical materials. But first, the researchers needed to figure out what these glasses look like at the atomic scale. For that, they went to the APS to collect high-energy x-ray diffraction data. By combining the diffraction data with other structural data and computer modeling, the team uncovered the secrets behind how a glass can act like a crystal.

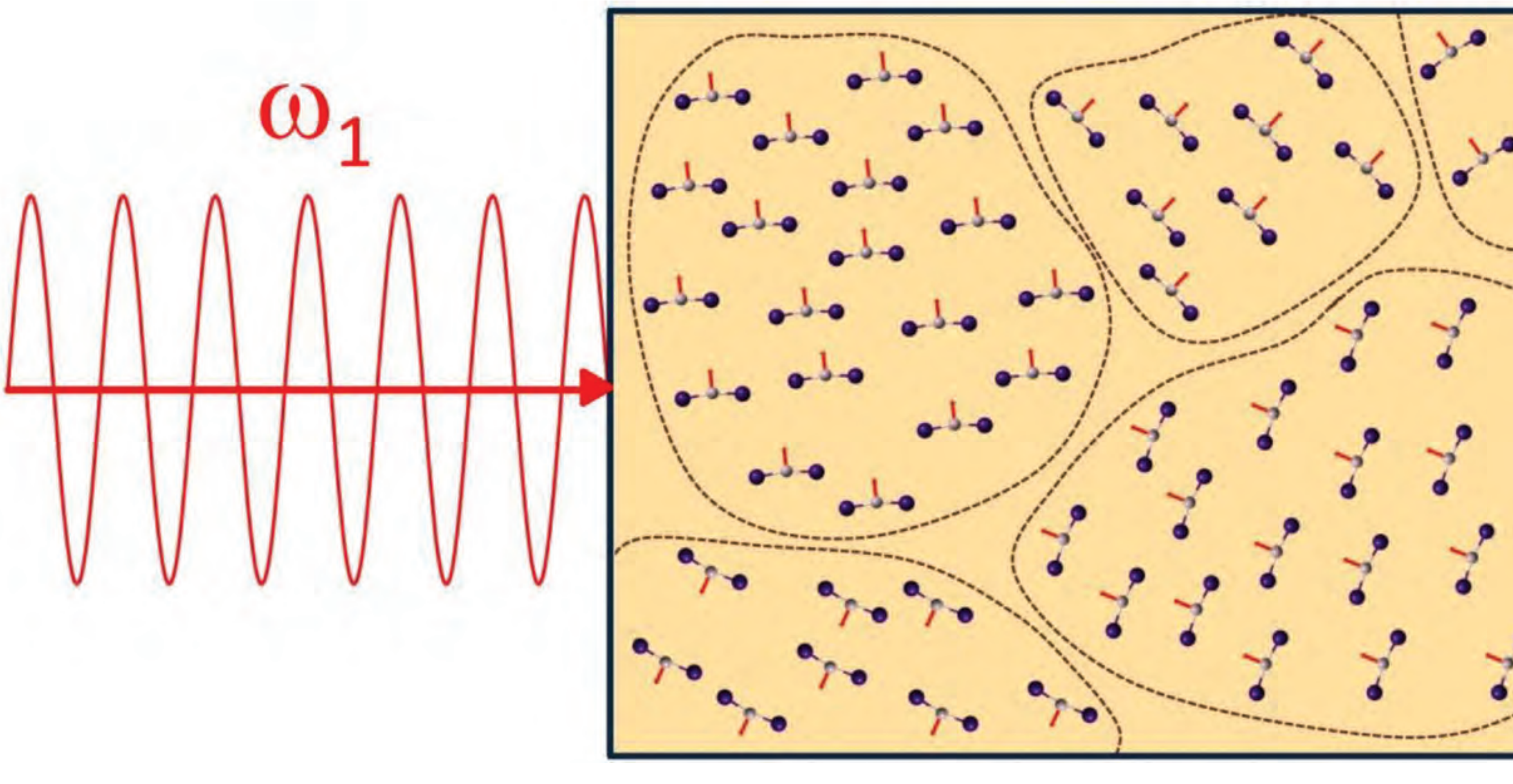

Nonlinear optical crystals are widely used in photonics applications, but can be challenging to synthesize. To sidestep the need for crystals, scientists have been pursuing glassy materials that can tune lasers. One challenge is that glassy materials with isotropic internal structures aren't able to perform the frequency conversion necessary to tune lasers. However, glasses with chiral asymmetric properties have nonlinear optical potential. This research team is investigating hybrid molecular/network glasses with non-centrosymmetric mercuric iodide (HgI_2).

To explore this material, the researchers probed the atomic structure of liquid mercury iodide as it transitions to a solid form at low temperatures, as well as its transition to molecular vapor at high temperatures. They employed several techniques to get at this molecular architecture, including high-energy x-ray diffraction at the XSD 6-ID-D beamline at the APS, and at the BL04B2 beamline at SPring-8 (Japan); time-of-flight neutron diffraction at the ISIS Neutron and Muon Source (Rutherford-Appleton Laboratory, UK); and Raman spectroscopy. Furthermore, they fed these data into a density functional theory-modeling program to come up with a working structural model for this glassy material in different states of matter.

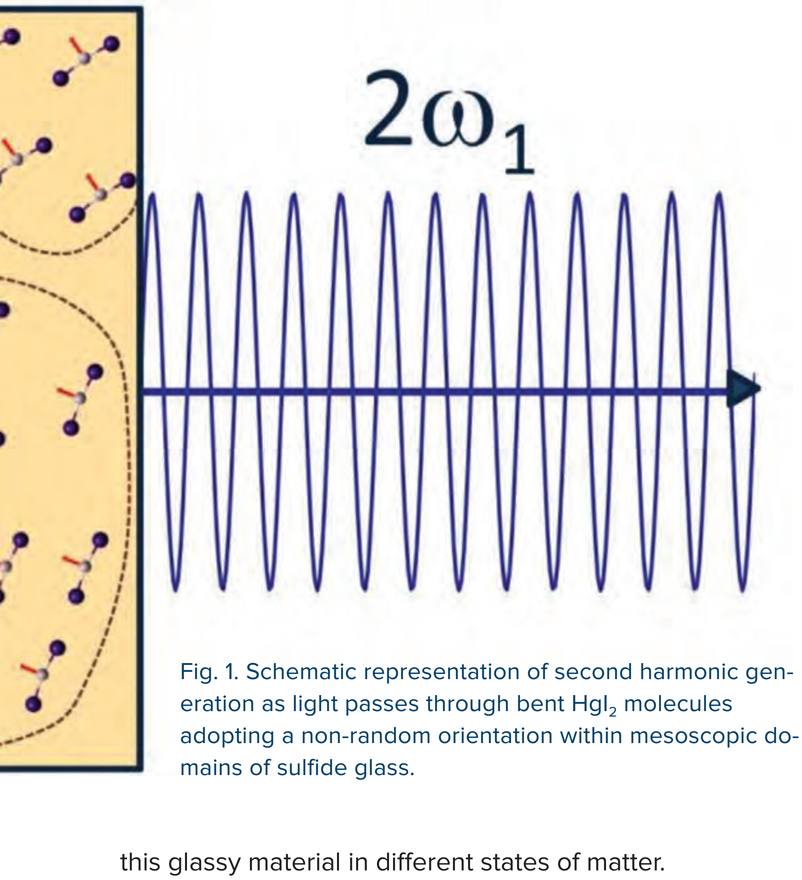

Fig. 1. Schematic representation of second harmonic generation as light passes through bent HgI_2 molecules adopting a non-random orientation within mesoscopic domains of sulfide glass.

At higher temperatures, above 400 K, HgI_2 exists as a linear triatomic molecule. However, the experimental data and structural modeling suggest that in a stable liquid and related glassy solid states, HgI_2 becomes bent, with a bond angle of around 156° degrees. That's important, because that bend creates asymmetry in the material, in turn generating intrinsic optical nonlinearity. To bolster these structural insights, the researchers checked the material's second harmonic generation (Fig. 1). This property is one of the main avenues for frequency conversion in nonlinear optical crystals. Indeed, the bent HgI_2-containing sulfide glass showed strong second-harmonic generation.

The team developed a hypothesis to help explain how the bent HgI_2 containing materials generated second harmonic generation in a sulfide glass. At one extreme, the bent HgI_2 molecules could be completely randomly oriented, conditions under which the second harmonic generation effect would be eliminated. At the other extreme, the molecules could arrange themselves nonrandomly in preferred orientations within mesoscopic domains, the result of which would be the observed second harmonic generation effects.

In future research, the team plans to perform small-angle neutron scattering and anomalous small-angle x-ray scattering on the glass. These data could provide verification for their hypothesis that nonrandom orientation within mesoscopic domains is responsible for the second harmonic generation effects.

A full understanding of this phenomena may help explain more generally the manifestation of nonlinear optical effects in isotropic media, as well provide a basis for the development of new materials with improved nonlinear optical properties. – Erika Gebel Berg

See: Mohammad Kassem[1], Maria Bokova[1], Andrey S. Tverjanovich[2], Daniele Fontanari[1], David Le Coq[3], Anton Sokolov[1], Pascal Masselin[1], Shinji Kohara[4], Takeshi Usuki[5], Alex C. Hannon[6], Chris J. Benmore[7], and Eugene Bychkov[1]*, “Bent HgI_2 Molecules in the Melt and Sulfide Glasses: Implications for Nonlinear Optics,” Chem. Mater. **31**, 4103 (2019).
DOI: 10.1021/acs.chemmater.9b00860

Author affiliations: [1]Université du Littoral Côte d’Opale, [2]St. Petersburg State University, [3]Institut des Sciences Chimiques de Rennes, [4]Research Center for Advanced Measurement and Characterization, [5]Yamagata University, [6]Rutherford Appleton Laboratory, [7]Argonne National Laboratory
Correspondence: * Eugene.Bychkov@univ-littoral.fr

This work was partly supported by Agence Nationale de la Recherche (ANR, France) under Grant No. ANR-15-ASTR-0016-01. The experiments at the SPring-8 were approved by the Japan Synchrotron Radiation Research Institute (proposal No. 2014B1197) and supported by the Centre for Advanced Science and Technology (Japan). Work at the Advanced Photon Source, Argonne National Laboratory, was supported in part by Basic Energy Sciences, Office of Science, U.S. Department of Energy, under Contract No. DE-AC02-06CH11357. A.T. is grateful to Saint-Petersburg State University grant No. 12.40.1342.2017.

Vanadium Nitride Supercapacitors Save the Day

Sometimes you just need lots of little bursts of power fast, and for that, there's not much that's better than a supercapacitor. These energy storage devices are found in cameras, electric vehicles, trains, airplanes, and many other advanced electronics, but the cost for the materials used in standard supercapacitors can be high, preventing wider use. Scientists are exploring transition metal nitrides as low-cost electrode materials for supercapacitors due to their high surface areas and high electronic conductivities. Vanadium nitrides have a particularly high capacitance, but little has been known about the charge storage mechanism, limiting the utilization of the material in supercapacitors. To close this knowledge gap, a research team characterized vanadium nitride electrodes *in situ* using the APS, among other experiments. Their findings revealed that the key to vanadium nitride's pseudocapacitance is the movement of anions into and out of the material's micropores (Fig. 1). This insight paves the way for a future of cost-effective energy storage systems with high-energy and high-power densities.

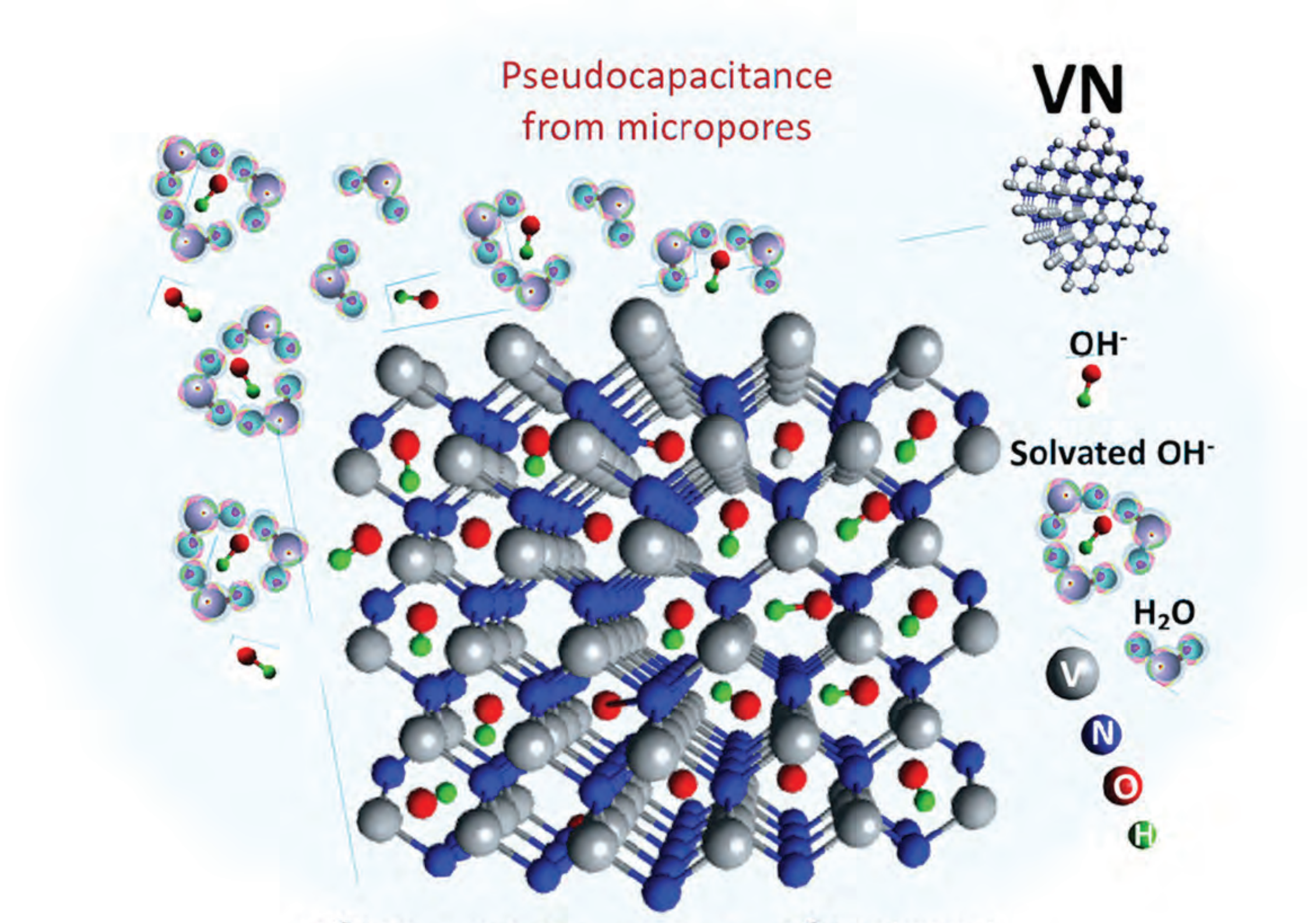

$$V^{3+}N + 2OH^- + e^- \leftrightarrow V^{2+}N(OH^-)_2$$

Fig. 1. Pseudocapacitive charge storage mechanism of vanadium nitride in aqueous alkaline electrolyte. Adsorption and desorption of hydroxide anion in and out of micropores lead to reduction and oxidation of the V metal during electrochemical charge discharge. From A. Djire et al., Nano Energy **60**, 72 (2019). ©2019 Published by Elsevier Ltd.

Supercapacitor electrode materials like vanadium nitride store charges via pseudocapacitive mechanisms. Pseudocapacitance is the electrochemical storage of energy and relies on the very fast oxidation or reduction of a chemical substance at the surface of an electrode. These reactions are called "faradaic redox reactions" and they are at the heart of a material's pseudocapacitance capabilities. The researchers from the University of Michigan and Oak Ridge National Laboratory knew that these faradaic redox reactions were happening on the vanadium nitride surfaces, but the details needed to be sorted out to maximize the potential of this material.

As a first step, the researchers synthesized the nanostructured vanadium nitride from a V_2O_5 precursor with a temperature-controlled reaction. They characterized the surface area and pore size distribution of the material, finding that the average crystallite size was about 21 nm. Pore-size analysis indicated the presence of micropores (those less than 2 nm across) as well as mesopores (2-50 nm). There was also a gap in pores in the 3-10-nm range, which had been previously reported. The surface area measurements suggested the material was highly porous, a fact that facilitates experiments probing the adsorption of electrolyte ions on the vanadium nitride material during chemical cycling.

Next, the team performed a series of studies aimed at unraveling the electrochemical mechanism. These experiments were performed *in situ* while the reaction was taking place, allowing the researchers to observe the redox cycling as it happened. To initiate the reaction, vanadium nitride electrodes were submerged in an alkaline electrolyte solution; previous research had shown that hydroxide ions were the active ion that triggers vanadium nitride's pseudocapacitance. The researchers collected *in situ* small-angle neutron scattering (SANS) at Oak Ridge National Laboratory (ORNL), using a General Purpose SANS instrument; and *in situ* x-ray absorption spectroscopy (XAS) data at the DND-CAT bending magnet beamline station 5-BM-D at the APS, along with other physical and electrochemical characteristics. Taken together, they found some surprising results.

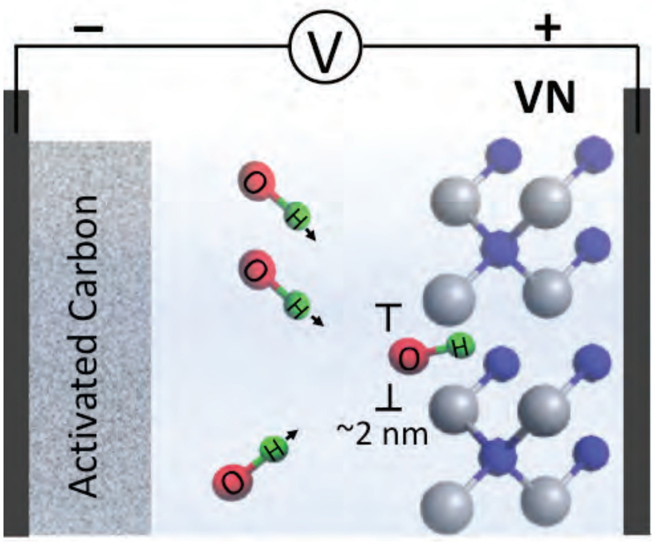

Fig. 2. Schematic of an asymmetric vanadium nitride supercapacitor.

Previously, scientists had assumed that vanadium nitride's pseudocapacitance was mostly tethered to the large pores that are more accessible to electrolyte ions and therefore can store more charge. But in reality, the SANS and XAS results revealed that the hydroxide anion was spending a lot of time in vanadium nitride's micropores, and that was the real source of pseudocapacitance (Fig. 2). As the anion entered a micropore, the vanadium metal became reduced. Then as the anion exited the micropore, the vanadium metal became oxidized. The electrochemical charging and discharging data suggested that pseudocapacitances above 1300 Fg^{-1} could be achieved in 1.2 V of aqueous alkaline electrolytes.

These findings bring the commercialization of supercapacitors based on inexpensive nitrides within reach, and vanadium nitrides may have energy storage applications beyond supercapacitors as well. Furthermore, the approach outlined in this study could be used generally to characterize energy storage devices. – Erika Gebel Berg

See: Abdoulaye Djire[1]*, Priyanka Pande[1], Aniruddha Deb[1], Jason B. Siegel[1], Olabode T. Ajenifujah[1], Lilin He[2], Alice E. Sleightholme[1], Paul G. Rasmussen[1], and Levi T. Thompson[1]**, "Unveiling the pseudocapacitive charge storage mechanisms of nanostructured vanadium nitrides using in-situ analyses," Nano Energy **60**, 72 (2019). DOI: 10.1016/j.nanoen.2019.03.003
Author affiliations: [1]University of Michigan, [2]Oak Ridge National Laboratory
Correspondence: * adjire@umich.edu, ** ltt@umich.edu

The authors acknowledge technical and financial support from the Automotive Research Center (ARC) in accordance with Cooperative Agreement W56HZV-14-2-0001, Army Tank Command and Army Research Office (grant number W911NF-11-1-0465), and Michigan Memorial Phoenix Project Seed grant. DND-CAT is supported by Northwestern University, The Dow Chemical Company, and DuPont de Nemours, Inc. ORNL's High Flux Isotope Reactor is sponsored by the Scientific User Facilities Division, Office of Science-Basic Energy Sciences, U.S. Department of Energy (DOE). This research used resources of the Advanced Photon Source, an Office of Science User Facility operated for the U.S. DOE Office of Science by Argonne National Laboratory under contract no. DE-AC02-06CH11357.

Illuminating the Path Toward High-Performance Organic Solar Cells

Solar energy is a robust source of green power that has the potential to transform society and improve global ecology. An international team of researchers used the APS to study next-generation organic solar cell devices with a goal of identifying their most important features to speed up development of solar energy production. These devices, which are referred to as "polymer solar cells," have as their photoactive layer a blend of organic semi-conductor materials capable of converting sunlight into usable energy. Polymer solar cells are uniquely comprised of organic materials and are presently not in widespread use because of their low efficiency. However, they harness enormous potential and have the capacity to become an inexpensive, lightweight, and scalable solar energy solution. To try and actualize the potential of polymer solar cells, the team of researchers synthesized a series of polymers that systematically differ in the size of their side chains. They then studied them with an array of functional and structural characterization techniques to discover which structural features most strongly impact performance, and developed computer modeling to interpret the results and point the way toward rational design of optimal organic materials for harvesting energy from the sun. These findings have exciting implications for commercial renewable energy and ecological sustainability.

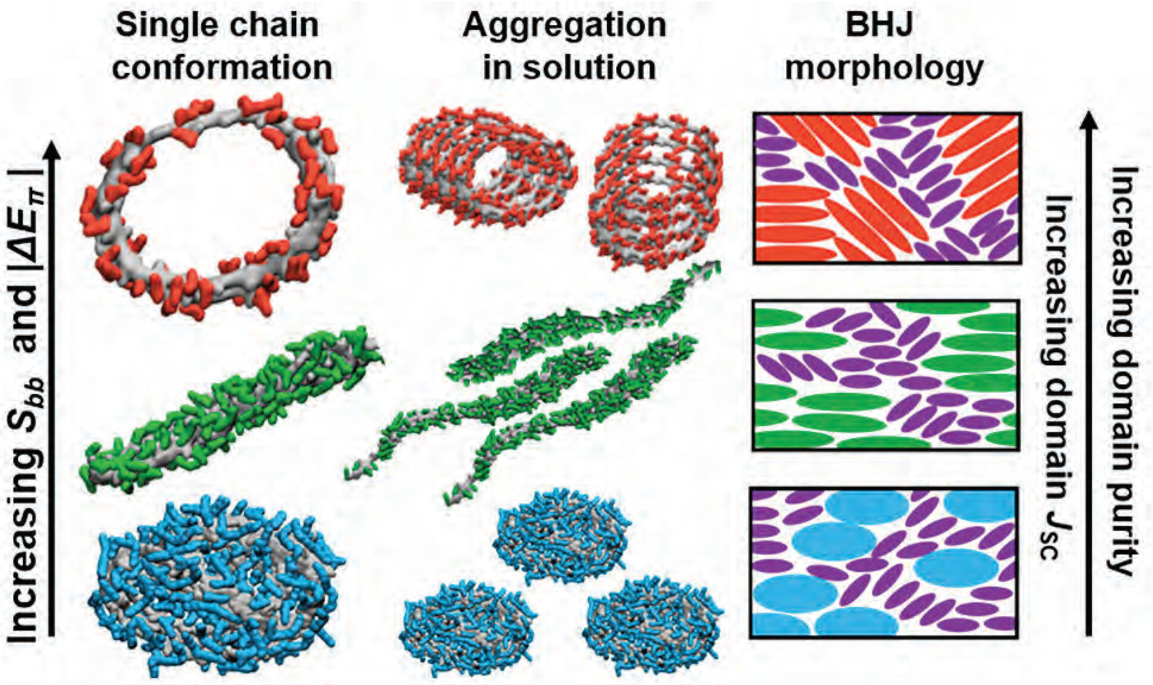

Fig. 1. Schematic of polymer conformations affecting aggregation in solution and the resulting film morphology. Left: Single polymer chain conformations highlighting the backbone surface area (gray) and that of the alkyl side chains from smallest to largest: (red: P-EH; green: P-BO; blue: P-HD). Center: Polymer nucleation at early stages of film formation. Right: The resulting solid-state BHJ morphologies with the non-fullerene acceptor domains shown in purple.

A material that has electrical conductivity intermediate between a conductor (material that permits a flow of electric charge) and an insulator (material that resists the flow of electric charge) is known as a semi-conductor. Solar cells have as their active layer semi-conducting material capable of converting sunlight (i.e., photons) into electric energy (i.e., a voltage difference). In organic solar cells, the photoactive layer consists of organic semiconductor material, that is, chemical compounds containing the element carbon. In fact, organic solar cells contain at least two types of organic material, an electron donor material and an electron acceptor material, which interact differently with incident light. Absorption of a photon causes an electron to be transferred from the donor to the acceptor material, leaving behind the absence of an electron, known as a hole, which acts like an electron, only with positive charge.

The two kinds of materials must be blended very finely so that the charge transfer between the materials can occur. Also, each individual material must form a continuous pathway for the charge carriers (the electrons in the acceptor material and the holes in the donor material) to reach the contacts of the solar cell, allowing the photocurrent to do work such as charging a battery; this configuration is known as the bulk heterojunction (BHJ). In polymer solar cells, the electron donor material consists of polymers, molecules formed from of a combination of repeating subunits giving rise to long chains of bonded atoms. The electron acceptor material is typically a small organic molecule, often a fullerene, an organic caged molecule. One example is based on C_{60}, or 60 carbon atoms bonded together, one at each corner of a soccer ball.

While polymer solar cell technology is not especially efficient vis a vis energy production, the ability to generate robust polymer solar cells would pave the way for inexpensive, scalable, and powerful solar energy. Progress in improving the performance of organic solar cells is difficult due to the dizzying array of parameters to consider. There is a very complex interplay between the molecules used, thin film fabrication processes and the structural details or morphology, of the donor/acceptor blend. Despite the best efforts of chemists synthesizing new molecules, engineers optimizing fabrication procedures and materials scientists characterizing the structure and performance of test devices, performance had stalled, lagging behind the efficiency of other technologies.

Recently, there has been a new surge in performance gains to over 17%, driven by new synthetic efforts, replacing the electron acceptor material with a new class of molecules, non-fullerene acceptors. Given the interconnected, interdisciplinary nature of the challenge, the researchers decided to re-evaluate the connection between structure and performance for a series of systematically tweaked electron donor polymers blended with a non-fullerene acceptor and see which characterization techniques were most predictive of the performance.

In this study, the researchers sought to determine if they could customize a polymer material to enhance its solar efficiency. For the subject of the study, they synthesized a series of electron donor materials based on a backbone of benzodithiophene–benzothiadiazole polymer, but with different size side chains on the repeating unit. Benzodithiophene is a central benzene carbon ring connected to two sulfur-containing carbon rings. In contrast, benzothiadiazole is a carbon ring connected to another ring containing nitrogen and sulfur. The authors blended each member of this polymer series with a unique compound known as ITIC-Th. ITIC-Th has the molecular formula of $C_{86}H_{74}N_4O_2S_8$ and is a type of compound referred to as a non-fullerene acceptor. Compared to fullerene acceptors, which are widely used in solar cells, non-fullerene acceptors have the ability to be freely tuned to have their optical and electrical properties modified. Historically, organic solar cell devices containing non-fullerene acceptors have not been as efficient as devices containing fullerene acceptors.

After combining their chosen polymer series with a non-fullerene acceptor, they then fabricated a series of solar cell devices and characterized both their solar power conversion efficiency, characterized their structure by different synchrotron-based x-ray scattering techniques, and modeled the blends with computer simulations. They found that the polymer containing the smallest alkyl substituent was able to achieve a power conversion efficiency of 11%. This was due to the presence of small, high-purity domains enabling large maximum photocurrent density (Jsc), as determined by resonant soft x-rayscattering (R-SoXS) measurements carried out at the Advanced Light Source, Lawrence Berkeley National Laboratory beamline 11.01.2, and interpreted with additional results measured by near-edge x-ray absorption fine structure (NEXAFS) performed at the Soft X-ray Beamline of the Australian Synchrotron. An alkyl substituent is an alkane group lacking a hydrogen atom, and alkane chemical compounds are carbon and hydrogen atoms fitted in a unique orientation. Polymer morphology (Fig. 1), notably texture, was assessed via grazing-incidence wide-angle x-ray scattering measurements performed at XSD beamline 8-ID-E of the APS.

The results showed that while the substituent size affected the relative amounts of molecules oriented with their carbon rings parallel or perpendicular to the substrate significantly, the sample texture was not strongly

"Illuminating" cont'd. on page 27

Ultrafast Snapshots of Laser-Metal Dynamics in Additive Manufacturing

As additive manufacturing (AM) technologies become ever more prevalent and important in various industries, efforts to better characterize and understand the complex phenomena of various AM techniques are accelerating to keep pace. Such efforts are essential to improve and expand the utility of AM methods. The major AM technique for fabricating metal parts is laser powder bed fusion (LPBF), which shares similarities with laser welding. At the heart of both are laser-metal interactions, which because of their optical opacity have only been indirectly studied, leaving important details of their underlying dynamics incompletely defined. Recently, however, synchrotron x-ray imaging techniques have been developed that allow *in situ* investigations under real-time processing conditions, offering vital new insights. Investigators used ultra-high-speed transmission x-ray imaging at the APS to study LPBF phenomena in two commonly-used AM alloys. Achieving the most complete understanding possible of the unseen intricacies of laser-based additive manufacturing processes will allow their continued improvement, resulting in increasingly reliable and versatile AM-fabricated metal components.

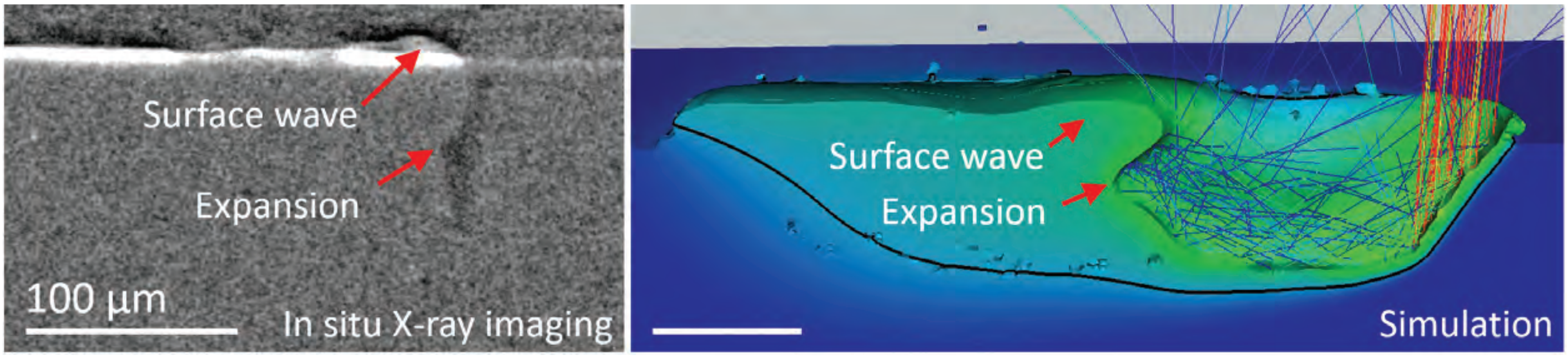

Fig. 1. *In situ* x-ray imaging and simulation of laser-material interaction during LPBF AM process. Observation of the laser-induced melt pool dynamics leads to an understanding of how surface morphology and pores are formed during LPBF.

Working at the DCS 35-ID x-ray beamline at the APS, researchers from Lawrence Livermore National Laboratory (LLNL) studied a range of laser heating mechanisms in alloys of aluminum (AL6061) and titanium (Ti-6Al-4V) at very fine temporal resolution from 0.3 to 30 µs. Such resolution at the nano- and microsecond level afforded detailed characterization of laser-metal interactions below the materials' surface, which is beyond the reach of other *in situ* methods. The experiments were complemented by multiphysics simulations.

Images of high-energy-density, 400-W laser irradiation scanning at a 500-kHz frame rate in Al6061 show the rapid formation of a keyhole vapor depression, which displays dynamic instabilities including the formation of ledges and humps of material. Some of these quickly change shape and vaporize within the melt void while others reattach or are absorbed into the vapor depression wall. Some form close to the metal surface, where waves create chevron patterns on the surface similar to those seen in laser welding. Simulations show that laser energy is reflected from the front of the vapor depression toward the rear wall, vaporizing and expanding material and strongly contributing to the observed instabilities. Similar phenomena are seen at all laser powers utilized and in the Ti-6Al-4V alloy, both under vacuum and in an argon environment.

Pore formation under steady-state laser scanning was also studied in both alloys. Experimental observations show similar findings in an argon environment, indicating that pores generally form near the base of the vapor depression, and are then trapped as the melt pool front so-

"Ultrafast" cont'd. on next page

"Ultrafast" cont'd. from previous page

lidifies. In the vacuum environment, however, pore entrainment also occurs closer to the surface and pores are driven deeper into the metal by Maragoni convection. The experimental observations and multi-physics simulations confirm that pores can be difficult to prevent or remove and that further post-processing can drive them deeper into the metal.

When laser power is shut off, the vapor depression collapses in less than 5 µs and a solidification front occurs that can trap pores near the base of the depression. Cracks can also form when solidification fronts from the back and front of the depression converge. Experiments in Ti-6Al-4V under an argon environment in the end-of-track region also show that pores and bubbles can become trapped as the laser shuts off, the metal suddenly cools, and the vapor depression collapses. These oscillate in shape and size due to acoustic cavitation until the metal solidifies. The investigators note that such end of track effects could be minimized or avoided by optimizing processing conditions, perhaps by varying laser output or scanning speed in ways that would better control laser power density in the melt pool.

Even with the detailed picture of the range of laser-metal heating phenomena and defect formation offered by the ultrafast x-ray imaging techniques used in these experiments, the research team states that further such experiments will be needed to fully characterize the complex dynamics in play, in conjunction with multi-physics simulations. – Mark Wolverton

See: Aiden A. Martin[1*], Nicholas P. Calta[1], Joshua A. Hammons[1], Saad A. Khairallah[1], Michael H. Nielsen[1], Richard M. Shuttlesworth[1], Nicholas Sinclair[2], Manyalibo J. Matthews[1], Jason R. Jeffries[1], Trevor M. Willey[1], and Jonathan R.I. Lee[1**], "Ultrafast dynamics of laser-metal interactions in additive manufacturing alloys captured by in situ X-ray imaging," Mater. Today Adv. **1**, 100002 (2019). DOI: 10.1016/j.mtadv.2019.01.001

Author affiliations: [1]Lawrence Livermore National Laboratory, [2]Washington State University
Correspondence: * martin248@llnl.gov, ** lee204@llnl.gov

This work was performed under the auspices of the U.S. Department of Energy (DOE) by Lawrence Livermore National Laboratory under Contract No. DE-AC52e07NA27344. Projects 17-ERD-042 (experimental) and 18-SI-003 (simulation) were funded by the LDRD Program at LLNL. The Dynamic Compression Sector is operated by Washington State University under the U.S. DOE/National Nuclear Security Administration award no. DE-NA0003957. The authors gratefully acknowledge the support (x-ray imaging at DCS) of P. Rigg, D. Rickerson, J. Klug, and N. Weir (DCS). This research used resources of the Advanced Photon Source, a U.S. DOE Office of Science User Facility operated for the DOE Office of Science by Argonne National Laboratory under contract no. DE-AC02-06CH11357.

"Illuminating" cont'd. from page 25

correlated with device performance. A deep investigation into the molecular dynamics of polymers revealed that different molecular substituents give rise to unique polymer conformations. The authors devised an energetic parameter ($\Delta E\pi$) related to the surface area of the polymer backbone accessible to solvent (Sbb) to explain the observed morphological trends and suggest novel strategies for how to further optimize organic solar cells, a step toward rational design of optimally performing electron donor/acceptor blends. For the full potential of solar energy to be globally realized, the devices that convert sunlight into electricity must be affordable, easily scalable, and efficient. These novel data produced in this study suggest a route toward further optimization of polymer solar cells.

– Alicia Surrao & Joseph Strzalka

See: Gang Wang[1], Steven M. Swick[1], Micaela Matta[1], Subhrangsu Mukherjee[2], Joseph W. Strzalka[3], Jenna Leigh Logsdon[1], Simone Fabiano[4], Wei Huang[1], Thomas J. Aldrich[1], Tony Yang[1], Amod Timalsina[1], Natalia Powers-Riggs[1], Joaquin M. Alzolav[1], Ryan M. Young[1], Dean M. DeLongchamp[2###], Michael R. Wasielewski[1##], Kevin L. Kohlstedt[1#], George C. Schatz[1***], Ferdinand S. Melkonyan[1**], Antonio Facchetti[1,5**] and Tobin J. Marks[1*], "Photovoltaic Blend Microstructure for High Efficiency Post-Fullerene Solar Cells. To Tilt or Not To Tilt?," J. Am. Chem. Soc. **141**, 13410 (2019). DOI: 10.1021/jacs.9b03770

Author affiliations: [1]Northwestern University, [2]National Institute of Standards and Technology, [3]Argonne National Laboratory, [4]LinkŠping University, [5]Flexterra Corporation
Correspondence: *t-marks@northwestern.edu,
**a-facchetti@northwestern.edu, **fmelkonyan@northwestern.edu,
***g-schatz@northwestern.edu, #kkohlstedt@northwestern.edu,
##m-wasielewski@northwestern.edu,
###dean.delongchamp@nist.gov

Photovoltaic device fabrications and evaluations, spectroscopy, and MD simulations were supported by the Center for Light Energy Activated Redox Processes (LEAP) and Energy Frontier Research Center funded by the U.S. Department of Energy (DOE) Office of Science-Basic Energy Sciences, under Award DE-SC0001059 (G.W., M.M., J.L.L., W.H., T.J.A., N.P.-R., J.A., R.M.Y., M.R.W., K.L.K., G.C.S., T.J.M.). Synthesis, SCLC device fabrications and evaluations, and R-SoXS were supported by Award 70NANB14H012 from U.S. Department of Commerce, National Institute of Standards and Technology, as part of the Center for Hierarchical Materials Design (CHiMaD) (G.W., S.M.S., S.M., D.M.D., F.S.M., T.J.M.). The Advanced Light Source is supported by the Director, Office of Science-Basic Energy Sciences, of the U.S. DOE under Contract DE-AC02-05CH11231. The Australian Synchrotron is part of ANSTO. This work made use of the EPIC, Keck-II, and/or SPID facilities of Northwestern University's NUANCE Center, which received support from the Soft and Hybrid Nanotechnology Experimental (SHyNE) Resource (NSF NNCI-1542205); the MRSEC program (NSF DMR-1121262) at the Materials Research Center; the International Institute for Nanotechnology (IIN), the Keck Foundation, and the State of Illinois. S.M.S. and T.J.A. thank the NSF for a Predoctoral Fellowship. S.F. thanks VINNOVA (2015-04859) and the Swedish Research Council (2016-03979) for financial support. This research used resources of the Advanced Photon Source, a U.S. DOE Office of Science User Facility operated for the DOE Office of Science by Argonne National Laboratory under Contract No. DE-AC02-06CH11357.

A Comparison of Shockwave Dynamics in Foams

Stochastic foams have a random topology that causes the material to compress in response to high-speed shock waves, with some heterogeneity to the shock-wave front due to the scale of the cells in the structure. Foams created by additive manufacturing (AM) have a hierarchical assembly; the structure of the material is controlled at a variety of scales, from atomic/molecular to micron. The ordered topology results in a fundamentally different response to shockwave loading, and especially stress localization, even at the same initial density. Using x-ray phase-contrast imaging (XPCI) experiments at the APS and simulations at Los Alamos National Laboratory, the mechanics of stochastic vs. AM foam deformation were understood on the micron-length scale, which will lead to design principles for cellular solids tailored to high-rate loading applications.

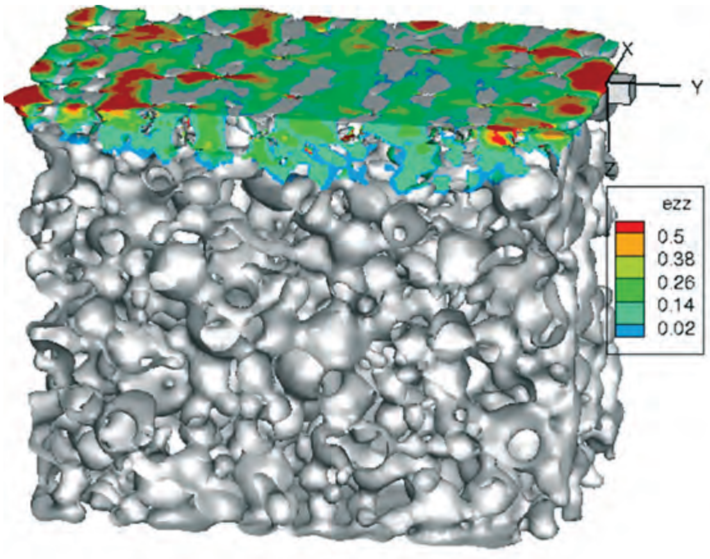

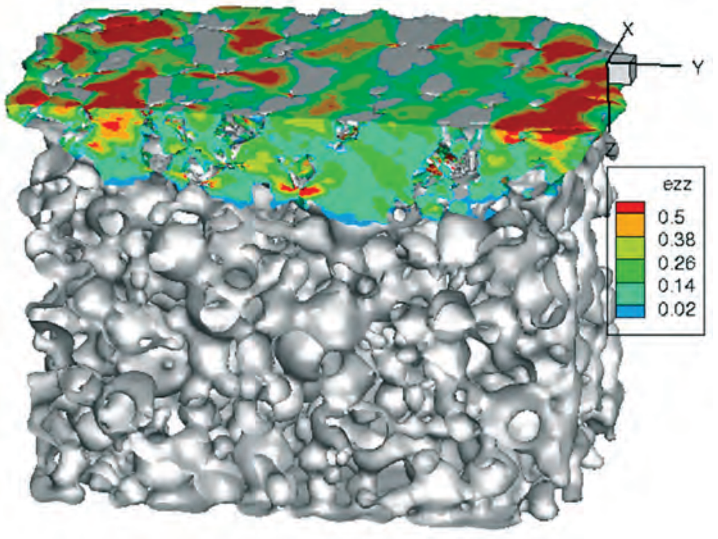

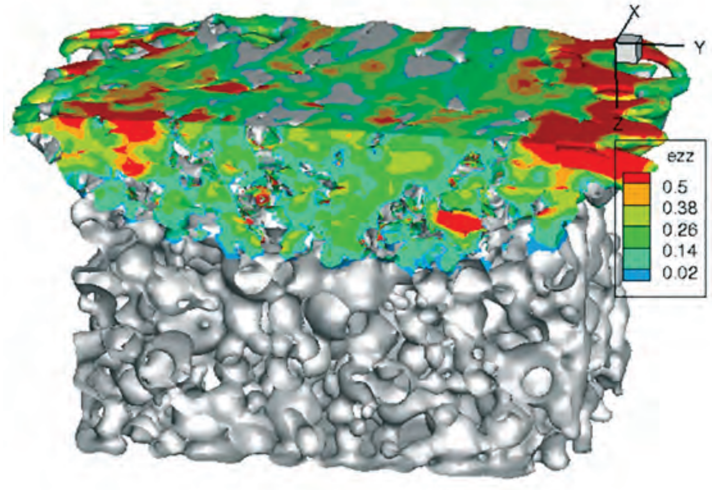

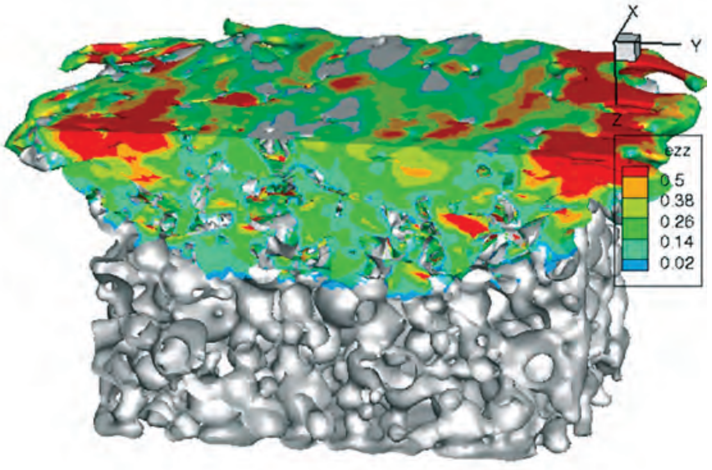

Cellular solids – an assembly of packed cells with solid edges or faces, such as cork or sponge – have unique and useful mechanical, electrical and thermal properties. One type, polymeric foams, have desirable mechanical properties for a variety of applications; they are lightweight, can be tailored for a range of compressive strength, and often recover their dimensions after compression. Polymeric foams have many applications, from thermal insulation to support components to vibration dampening to shockwave mitigation, and they are important to industries including automotive, aerospace, electronics, and defense.

The individual cells in polymeric foams have variable sizes, wall thicknesses, and arrangements. In a typical stochastic, open-cell foam, energy is absorbed unevenly through the foam architecture. While manufacturers can control many features of polymeric foams, such as overall porosity, void dimensions, and relative density, often the microstructure cannot be tailored and thus, mesoscale deformation cannot be controlled. So, the deformation of polymer foams under conditions of high strain rate loading – conditions that are common in aerospace, automotive and military applications – cannot be improved.

The recent development of AM has brought major advances to porous foams. Using hierarchical assembly, AM foams have similar densities to open-cell stochastic foams, but microstructures that are assembled by the additive manufacturing process. By designing microstructures, makers of AM foams have unprecedented control of deformation mechanics and structural instabilities. Examples include ultra-lightweight lattice structures with high strength-to-density, and energy dissipation and recoverability to mechanical loading.

In recent work at the DCS 35-ID beanline at the APS, researchers from Los Alamos National Laboratory examined the response of both stochastic and AM foams to high-speed shock waves using *in situ*, time-resolved XPCI to measure the wave dynamics through the structure. The experiments – performed using the IMPULSE gun platform installed in the DCS B-hutch – were compared with finite element modeling of imported microstructures obtained by x-ray computed tomography. Although both foam types had similar initial densities, the spatial arrangement of the ligaments were different, with one being stochastic, and the other being periodic and lattice-like in structure.

In the stochastic foams, the spatial distribution of stress during shock experiments was highly localized and randomly variable, resulting in a bulk compaction of the pore structure (Fig. 1). By contrast, the behavior of AM foams during shock experiments showed localization of compression and stress caused by the periodic structure; similarly, reflective of their initial starting microstructure.

Shockwave dynamics are dramatically different in polymeric and AM foams of similar density, due to stress localization within the microstructure of the material on the timescale of the shockwave compression. This arises from coupling of the wave to the filaments and layer symmetry within the AM structures. In the future, additive manufacturing will produce foams that are tailored to better control their response to shock and compaction, and thereby improve their functionality. – Dana Desonie

< Fig. 1. Pressure distribution in shocked stochastic foam. Red indicates regions of high localized strain. From B. Branch et al., Polymer **160**, 325 (2019). © 2018 Published by Elsevier Ltd.

See: Brittany Branch, Axinte Ionita, Brian M. Patterson, Andrew Schmalzer, Bradford Clements, Alexander Mueller, and Dana M. Dattelbaum*, "A comparison of shockwave dynamics in stochastic and periodic porous polymer architectures," Polymer **160**, 325 (2019). DOI: 10.1016/j.polymer.2018.10.074

Author affiliation: Los Alamos National Laboratory
Correspondence: * danadat@lanl.gov

The authors would like to acknowledge support from the Laboratory Directed Research and Development program at Los Alamos National Laboratory (project# 20160103DR) and the U.S. Department of Energy (DOE)/National Nuclear Security Administration Campaign 2. We would like to thank Brian Jensen, Chuck Owens, and Joe Rivera for firing of the IMPULSE gun platform at the Dynamic Compression Sector. Paulo Rigg, Nick Sinclair, and the DCS staff are acknowledged for supporting the hutch operations during these experiments. A.J. Iverson, C.A. Carlson, and M. Teel from National Security Technologies (NSTech) are acknowledged for their technical support in operating the x-ray PCI detector system. Los Alamos National Laboratory is operated by Los Alamos National Security, LLC, for the U.S. DOE under Contract No. DE-AC52-06NA25396. The Dynamic Compression Sector is operated by Washington State University under the U.S. DOE/National Nuclear Security Administration award no. DE-NA0003957. This research used resources of the Advanced Photon Source, a U.S. DOE Office of Science User Facility operated for the DOE Office of Science by Argonne National Laboratory under Contract No. DE-AC02-06CH11357.

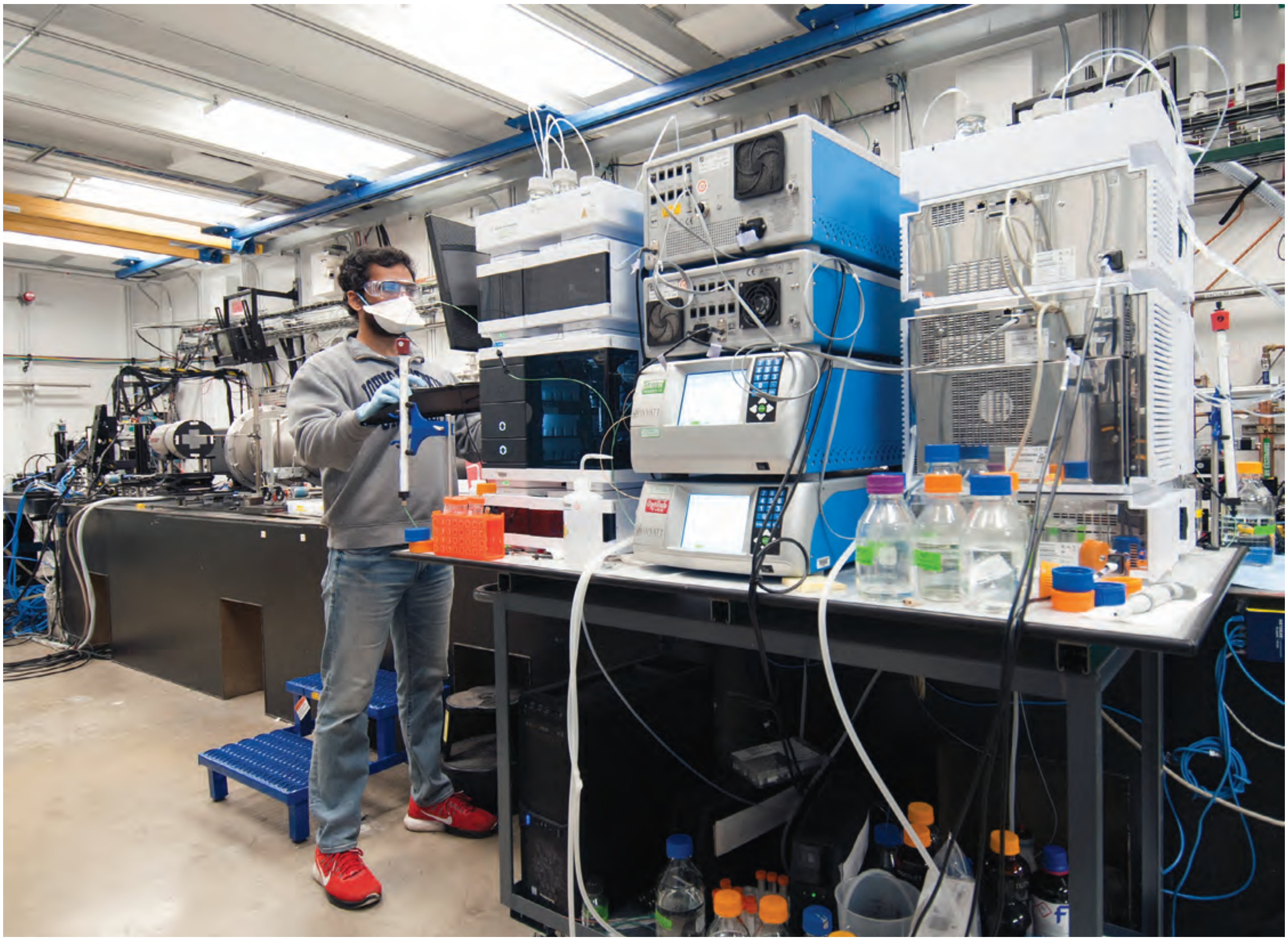

SAXS Studies of RNA Elements from the SARS-CoV-2 Virus at the Bio-CAT Beamline 18-ID

Small-angle solution x-ray scattering and biochemical characterization studies at the Bio-CAT beamline 18-ID at the APS were used to study the structure of portions of RNA from the SARS-CoV-2 virus. This RNA contains the genetic instructions the virus uses to replicate itself. These experiments are designed to see how these structures change when they interact with selected small molecules that are potential drug candidates. This work is a collaboration between Blanton Tolbert (Department of Chemistry, Case Western Reserve University), Amanda Hargrove (Duke Unversity) , Srinivas Chakravarthy (Illinois Institute of Technology, pictured above) and a nuclear magnetic resonance consortium coordinated by Harald Schwalbe at the Goethe University (Germany).

Electronic and Magnetic Materials

Room-Temperature Superconductivity Moves One Step Closer

Ever since superconductivity was discovered in 1911, scientists have dreamed of achieving the zero-resistivity state at room temperature, a dream that has moved progressively closer to realization over the years, particularly with hydrogen-rich compounds, which become superconductive at very high critical temperatures (T_c) when under pressure. Recently the highest of all reported T_c values was achieved at the APS. The researchers in this study showed that at megabar pressures, phases of lanthanum superhydride (LaH_{10}) become superconductive above 260 K, which is nearly room temperature (~9°F) (Fig. 1).

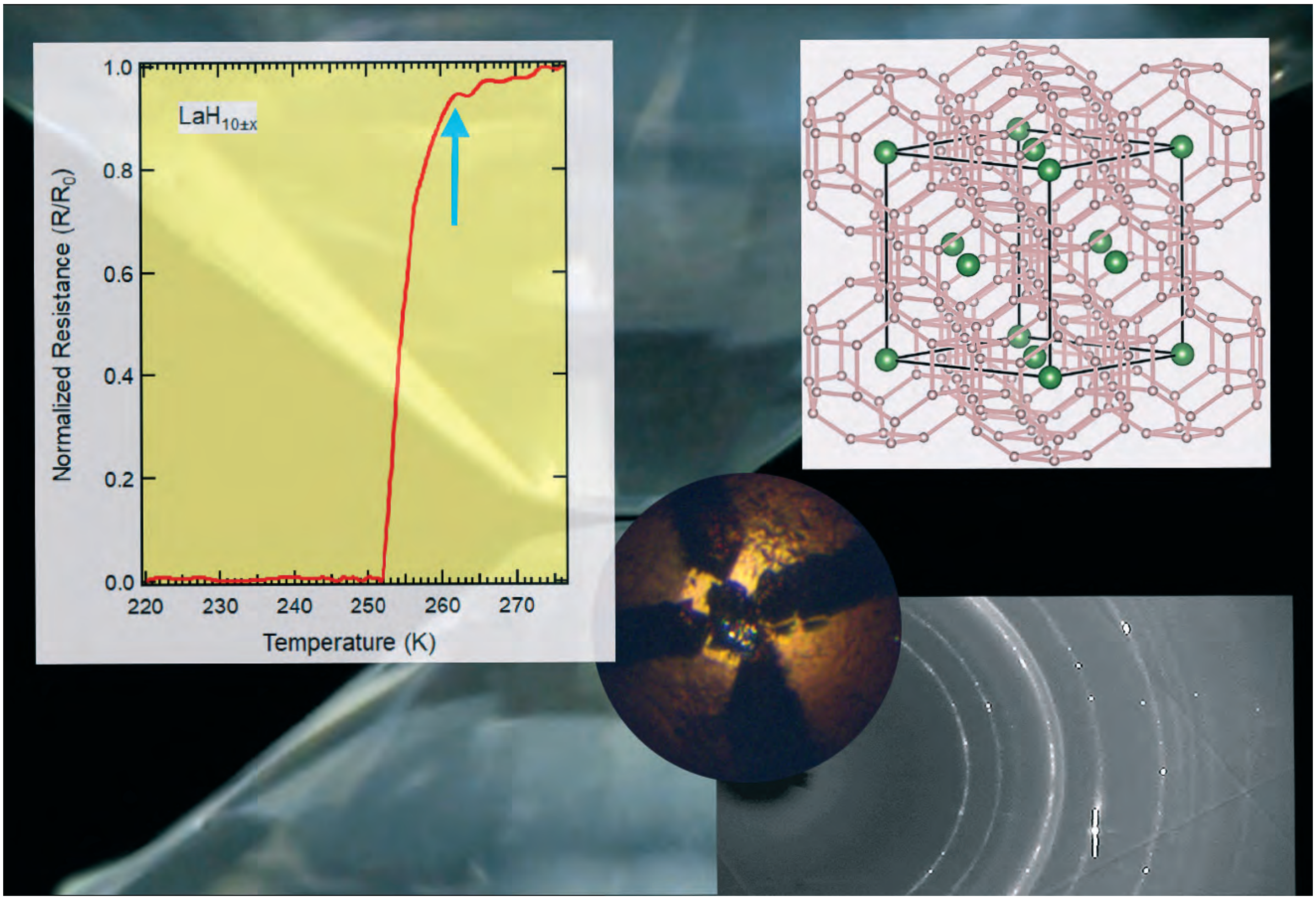

Fig. 1. Top left: LaH10 shows a drop in resistivity starting at around 265 K at 180 GPa in one of the samples synthesized (shown with four platinum leads in center image). The structure of LaH10 (top right) was confirmed with *in situ* x-ray diffraction (lower right). The data were obtained at HPCAT-XSD beamline 16-ID-B at the APS.

As is usual for such accomplishments, more was involved than meets the eye. It turns out that simply heating La and H_2 loaded into pressurized diamond-anvil cells (DACs) does not guarantee good electrical contact between the synthesized materials and the electrodes needed for resistivity measurements. So, the 5-µm-thick La samples were placed on platinum (Pt) electrodes and packed with ammonia borane (NH_3BH_3, AB). The AB yielded hydrogen and insulating cubic boron nitride, which served both as a solid pressure medium and as a support holding the hydride samples firmly against the electrical contacts.

A versatile diode-pumped ytterbium fiber laser heating system was developed for the *in situ* synthesis and structural characterization of the LaH_{10} samples at high pressure. For the electrical conductivity measurements, the researchers from George Washington University, the Carnegie Institution of Washington, and Argonne National Laboratory used a multistep process with DACs having diamond pistons that were coated with four 1-µm-thick Pt electrodes that were pressure-bonded to 25-µm-thick Pt electrodes. Pulsed laser heating above 175 GPa and to temperatures of 1000 2500 K resulted in the formation of $LaH_{10\pm x}$, where x was between +2 and −1.

All the samples for which AC resistance data (the resistance of the conductor) were taken were also characterized structurally by x-ray diffraction at the HPCAT-XSD 16-ID-B beamline at the APS. The low-temperature x-ray diffraction measurements ensured that any resistance drops seen were not due to temperature-induced structural transitions. Indeed, the x-ray diffraction patterns gave no indication of structural changes over the range of temperatures explored.

Multiple measurements revealed that the resistivity of LaH10±x decreased around 275 K, then dropped abruptly by more than three orders of magnitude, and remained constant thereafter from 253 to 150 K. Upon warming, the resistance increased steeply at 245 K, indicating the change was reversible but shifted at lower temperature. Since pressure was not measured as a function of temperature during thermal cycling, the pressure at which the resistance change occurred was not directly determined but was estimated to be 180 GPa to 200 GPa.

The researchers also carefully monitored possible changes in transition temperature with applied current in the small and mixed-phase samples. They observed a 10-K decrease in transition temperature upon increasing the current from 0.1 mA to 1 mA; the transition temperature also appeared to decrease at higher currents. Distinct *I-V* characteristics were observed above and below the transition temperature. The measurements suggest that $LaH_{10\pm x}$ could tolerate very large critical current densities well into the superconducting phase.

Whereas diamagnetic measurements are needed to confirm the present results, the magnitudes of the resistance drops repeatedly observed in the experiments were comparable to those observed in previous high-pressure studies in which the transitions were subsequently found to be correctly identified as signatures of superconductivity using magnetic susceptibility measurements. Also, because the transition temperature seen was close to that predicted for superconductive LaH10 at comparable pressures by Bardeen-Cooper-Schrieffer-type calculations, the researchers felt justified in interpreting the drop in resistance as signifying the onset of superconductivity. The researchers have begun applying diamagnetic methods to the small and complex superhydride samples produced in this experiment with the goal of corroborating its findings.

– Vic Comello

See: Maddury Somayazulu[1*††], Muhtar Ahart[1**], Ajay K. Mishra[2‡], Zachary M. Geballe[2], Maria Baldini[2§], Yue Meng[3], Viktor V. Struzhkin[2], and Russell J. Hemley[1**], “Evidence for Superconductivity above 260 K in Lanthanum Superhydride at Megabar Pressures,” Phys. Rev. Lett. **122**, 027001 (2019).
DOI: 10.1103/PhysRevLett.122.027001

Author affiliations: [1]George Washington University, [2]Carnegie Institution of Washington, [3]Argonne National Laboratory
[‡]Present address: Bhabha Atomic Research Center, [§]Present address: Fermilab, [††]Present address: Argonne National Laboratory, [‡]Present address: University of Illinois at Chicago
Correspondence: * zulu@anl.gov, ** rhemley@uic.edu

This research was supported by EFree, an Energy Frontier Research Center funded by the U.S. Department of Energy (DOE) Office of Science-Basic Energy Sciences (BES), under Award No. DE-SC0001057. The instrumentation and facilities used were supported by U.S. DOE-BES (DE-FG02-99ER45775, VVS), the U.S. DOE-National Nuclear Security Administration (DE-NA-0002006, CDAC; and DE-NA0001974, HPCAT-XSD), and the National Science Foundation (DMR-1809783). This research used resources of the Advanced Photon Source, an Office of Science User Facility operated for the U.S. DOE Office of Science by Argonne National Laboratory under contract no. DE-AC02-06CH11357, and the Canadian Light Source and its funding partners.

Controlling Magnetism in Superlattices via Structural Distortions

Superlattices (SLs) are engineered materials that often exhibit technologically promising features, for instance unique electronic properties. A SL is typically composed of alternating layers of two or more crystalline compounds. Many types of SLs have been constructed, and new types are continuously being developed. In this study, researchers investigated the magnetic properties of a superlattice consisting of single or double layers of the iridate compound $SrIrO_3$ separated by a single layer of strontium-titanate ($SrTiO_3$). X-ray experiments performed by a multi-national team of researchers at three different beamlines of the APS probed the magnetic and crystalline properties of the two superlattices. A notable achievement was the first-ever use of resonant inelastic x-ray scattering (RIXS) to characterize the magnetic interactions between the $SrTiO_3$ and $SrIrO_3$ layers. Particularly striking was the magnetic behavior of the two-layer $SrIrO_3$ superlattice, which was much stronger and oriented differently than expected. The researchers further determined that the net magnetic moment and magnetic orientation of this superlattice can be readily tuned via simple parameters, for instance by modifying the superlattice's underlying substrate. The magnetic tunability described in this study should prove applicable to numerous other superlattice systems, which may ultimately be adapted for improved electronic devices.

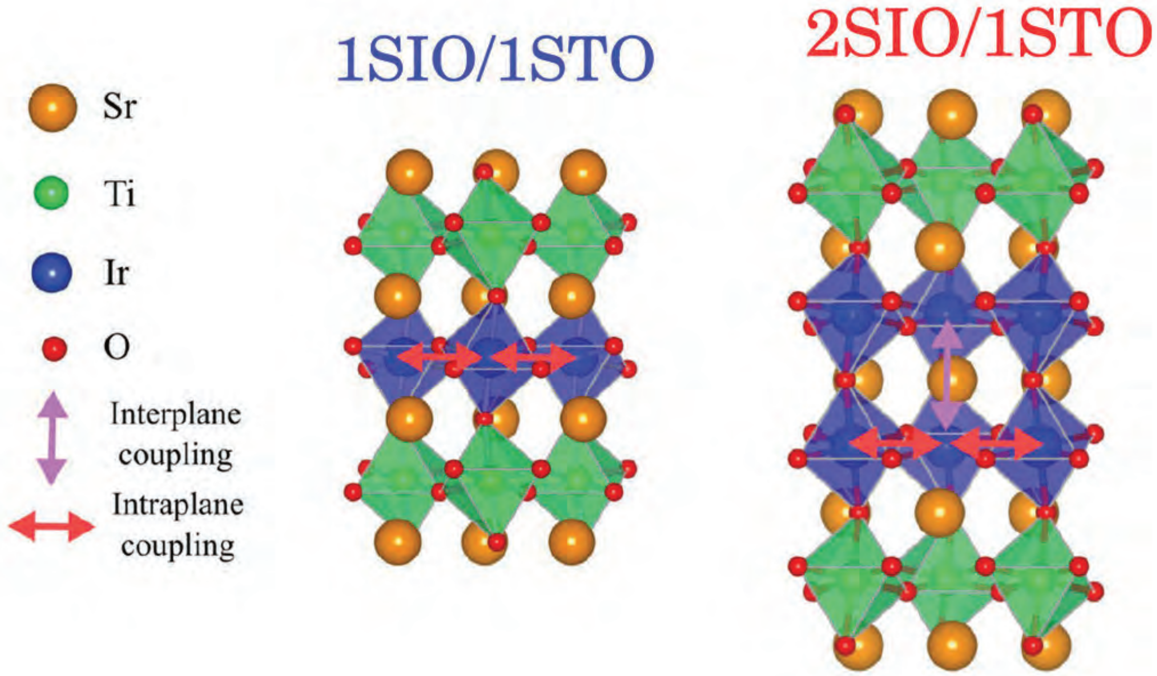

Both $SrTiO_3$ and $SrIrO_3$ are members of the perovskite family of compounds. Perovskites are composed of octahedra, as shown in Fig. 1. The octahedra associated with each $SrTiO_3$ layer appear green and encapsulate a single titanium atom, while $SrIrO_3$ octahedra are colored blue with one iridium atom inside. Note that the octahedra in each layer are tilted relative to the octahedra of adjacent layers. The unusual structure of perovskites cause these compounds to exhibit many unusual electric and magnetic properties, such as interactions between the spin and motion of certain electrons in the compound, referred to as spin-orbit coupling (SOC), which can significantly alter the internal magnetic fields of the superlattice.

The superlattice composed of alternating $SrIrO_3$ and $SrTiO_3$ layers is denoted 1SIO/1STO (middle of Fig. 1) while the superlattice with two layers of $SrIrO_3$ separated by single layers of $SrTiO_3$ is denoted 2SIO/1STO (right side of Fig. 1). The researchers wished to precisely evaluate the magnetic behavior within both superlattices. An excellent technique for this task is RIXS, which uses x-rays to probe certain electrons in the superlattice. In particular, the x-rays were tuned to excite electrons in the iridium atoms at the L_3 subshell, providing insight into each superlattice's magnetism.

Although RIXS is ideal for revealing superlattice magnetic behavior, applying the technique was problematic. This is because the high-energy x-rays tend to penetrate deeply into a sample, hence mostly pass right through the thin-film superlattice. The researchers overcame this obstacle in two ways. First, the superlattices were thickened by depositing many additional layers. And second, the RIXS measurements were performed at an extremely shallow angle of 1° from the sample surface. Both these adaptations provided the x-rays with sufficient path length within the sample to interact strongly with the superlattice.

The RIXS measurements were performed at XSD beamline 27-ID-B of the APS. Two additional x-ray techniques were also employed, namely resonant elastic x-ray scattering at XSD beamline 6-ID-B and (non-resonant) x-ray diffraction at XSD beamline 33-BM-C. Taken together, these x-ray measurements provided insight into the overall magnetic and structural properties of the two distinct superlattices.

< Fig. 1. A side-by-side illustration of the two superlattices examined in this study. The color scheme used to identify individual atoms and directional interactions appears on the left. The superlattice consisting of alternating $SrIrO_3$ and $SrTiO_3$ layers is denoted 1SIO/1STO, as illustrated in the middle panel. The right-hand side shows the superlattice with two layers of $SrIrO_3$ separated by single layers of $SrTiO_3$, denoted 2SIO/1STO.

The RIXS measurements revealed ferromagnetism in both superlattice types within the planes formed by their iridium octahedra, as illustrated in Fig. 1 (red arrows). While the in-plane magnetism is present in both superlattices, only 2SIO/1STO exhibited an out-of-plane magnetism (pink arrow in Fig. 1, right-hand superlattice). The strongly directional magnetic interactions between superlattice planes is an unusual characteristic that the researchers anticipate will be searched for in related types of iridium crystals.

Theoretical modeling indicated that the observed out-of-plane magnetism in the 2SIO/1STO superlattice is highly dependent upon the tilt between the octahedra of adjacent layers. Even slight shifts in this tilt can produce significant changes in the magnetic states and other quantum behavior of the superlattice. The researchers suggest that the octahedral tilt can be manipulated via substrate modification, thereby controlling the superlattice's quantum behavior. This manipulation could also be realized by substituting calcium for strontium atoms. The innovative RIXS measurements performed in this study, as well as the manipulation of quantum behavior through physical or chemical changes, should be applicable to many other superlattice systems. – Philip Koth

See: D. Meyers[1*], Yue Cao[1], G. Fabbris[1], Neil J. Robinson[1], Lin Hao[3], C. Frederick[3], N. Traynor[3], J. Yang[3], Jiaqi Lin[4,5], M. H. Upton[2], D. Casa[2], Jong-Woo Kim[2], T. Gog[2], E. Karapetrova[2], Yongseong Choi[2], D. Haskel[2], P. J. Ryan[2,6], Lukas Horak[7], X. Liu[4,8], Jian Liu[3**], and M. P. M. Dean[1***], "Magnetism in iridate heterostructures leveraged by structural distortions," Sci. Rep. **9**, 4263 (2019). DOI: 10.1038/s41598-019-39422-9

Author affiliations: [1]Brookhaven National Laboratory, [2]Argonne National Laboratory, [3]University of Tennessee, Knoxville, [4]Chinese Academy of Sciences, [5]University of Chinese Academy of Sciences, [6]Dublin City University, [7]Charles University, [8]Collaborative Innovation Center of Quantum Matter
Correspondence: * dmeyers@bnl.gov, ** jianliu@utk.edu,
*** mdean@bnl.gov

This material is based upon work supported by the U.S. Department of Energy (DOE) Office of Science-Basic Energy Sciences, Early Career Award Program, under Award No. 1047478. Work at Brookhaven National Laboratory was supported by the U.S. DOE Office of Science-Basic Energy Sciences, under Contract No. DE-SC0012704. J.L. acknowledges the support by the Science Alliance Joint Directed Research & Development Program and the Transdisciplinary Academy Program at the University of Tennessee. J.L. also acknowledges support by the Department of Defense-Defense Advanced Research Projects Agency under Grant No. HR0011-16-1-0005. A portion of the fabrication and characterization was conducted at the Center for Nanophase Materials Sciences, which is a DOE Office of Science User Facility. X. Liu acknowledges support by MOST (Grant No. 2015CB921302) and CAS (Grant No. XDB07020200). This research used resources of the Advanced Photon Source, a U.S. DOE Office of Science User Facility operated for the DOE Office of Science by Argonne National Laboratory under Contract No. DE-AC02-06CH11357.

Oxygen Vacancies in Complex Oxides Enable Analog Switching Behavior

Complex oxygen-bearing compounds form the basis of many advanced electronic technologies. For instance, complex copper oxides are among the leading candidates for practical high-temperature superconductors. Complex oxides may also form the basis of next-generation semiconductors and catalysts. Often, the properties of these varied oxides can be significantly altered by changing the number of oxygen vacancies within them. As the name implies, an oxygen vacancy occurs when an oxygen atom is missing from an oxide's ordered structure. In this study, researchers using the APS investigated the rare-earth oxides $NdNiO_3$ and $SmNiO_3$ by varying the number of oxygen vacancies in each and then measuring the impact on its electronic behavior. A dramatic increase in electrical resistance was observed as the number of oxygen vacancies grew. Together, the experimental results and prototype device employed highlight the potential of the two oxides for advanced electronics, including as analog electronic devices for neuromorphic computing (computing mimicking the human brain) and artificial intelligence (AI).

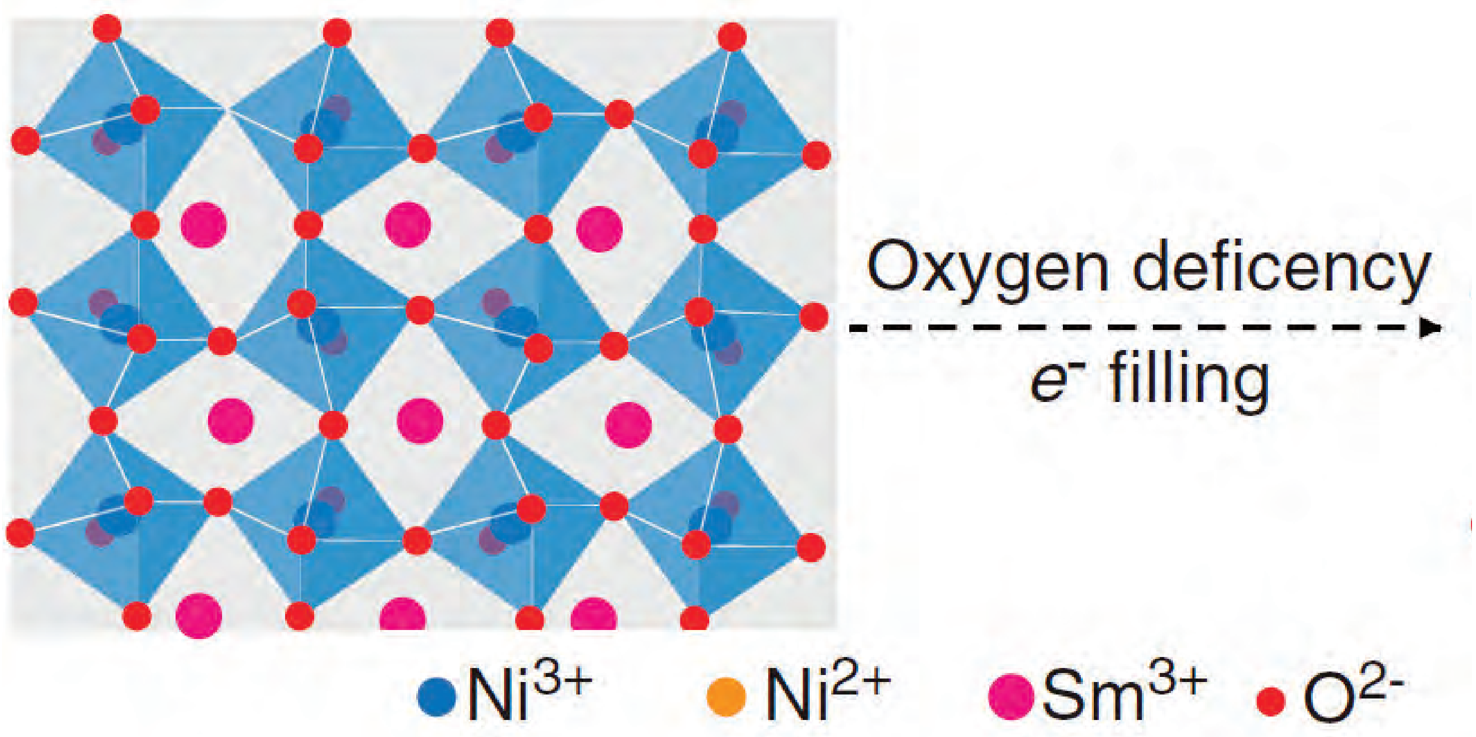

Fig. 1. Left side shows the crystalline structure of the rare-earth oxide $SmNiO_3$, composed of layers of octahedral units. Six oxygen atoms (small red spheres) occupy each octahedral vertex, surrounding a single nickel atom (dark blue). Samarium atoms (pink spheres) lie outside and between the octahedra. The ionization states of each atom are also indicated (for instance, Ni^{3+}). The outer electrons in the crystal form an electron cloud (gray background) that conducts electricity. Right side of figure depicts removal of oxygen atoms (O_2). Every oxygen vacancy frees up two electrons (e— e—) that disrupt the electron cloud and increase electrical resistance.

The research team constructed a prototype programmable resistor from $NdNiO_3$ to systematically investigate the effect in question. The rare-earth oxides were probed using x-ray photoelectron spectroscopy (XPS), performed at XSD beamline 29-ID at the APS; and x-ray absorption spectroscopy (XAS) performed at beamline 10ID-2 (REIXS) of the Canadian Light Source.

Both $NdNiO_3$ and $SmNiO_3$ are considered rare-earth oxides because they contain the rare-earth elements neodymium (Nd) and samarium (Sm), respectively. They are also referred to as nickelates since they both contain nickel (Ni). Significantly, the two oxides have a perovskite structure, which is often associated with peculiar electronic properties. Perovskites are composed of layers of octahedral unit cells. An octahedron can be regarded as two pyramids sharing a common base, with one pyramid pointing up and the other down. Each octahedral cell has eight faces and six vertices, with one oxygen atom occupying each vertex. The left side of Fig. 1 depicts adjacent octahedral layers in $SmNiO_3$. Note that a single nickel atom resides at the center of each octahedron.

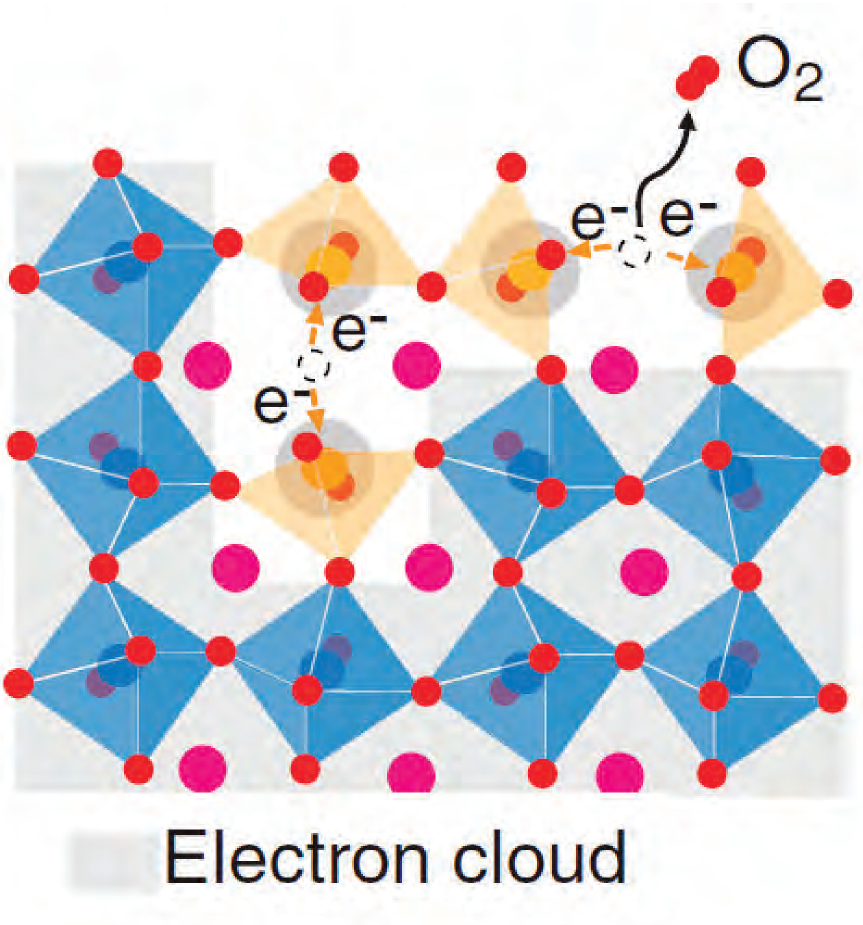

Numerous samples of the two oxides were prepared in the form of thin films. Additional processing was used to vary the proportion of oxygen vacancies in the thin-film oxides. The right side of Fig. 1 illustrates the removal of oxygen to form oxygen vacancies in the perovskite structure. The x-ray photoelectron spectroscopy measurements performed at the APS were used to quantify the exact level of oxygen vacancies within individual films.

Each oxygen vacancy in the thin-film oxides freed up two electrons. Normally the availability of extra electrons lowers a material's resistance to an electrical current. But in this case, the opposite effect occurred. Due to the structure of the Nd and Sm oxides, the liberated electrons were localized, unable to conduct electricity. This meant that resistance to electric flow in the thin-film oxides increased as the number of oxygen vacancies increased. Amazingly, the thin film with the highest number of vacancies had an electrical resistance ten million times greater than the film with the fewest vacancies.

The researchers exploited the relationship between oxygen vacancies and resistance to create a unique proof-of-concept electronic device. The device was based on the Nd oxide examined in this study. Applying a positive electric bias (voltage) compelled some of its oxygen vacancies to move away from the device's positive electrode. Applying a negative bias reversed the effect, causing the vacancies to move in the opposite direction. The rearrangement of oxygen vacancies was repeated over a number of cycles.

Redistributing the oxygen vacancies in the Nd oxide altered the device's electrical resistance. Moreover, this change in resistance was highly non-linear, with a small change in vacancy distribution producing a large change in resistance. The researchers demonstrated that their prototype device behaves as an analog switch, a type of electronic device in which its electrical resistance can be programmed. This programming is non-volatile, meaning that the resistance profile is retained even if electric power to the device is removed. Such tunable resistors are currently being investigated for use in a variety of applications, including as replacements for traditional computer memory, and as hardware components for brain-inspired computing.

The presence of oxygen vacancies was also shown to

“Oxygen” cont’d. on page 39

Rise Up: Diffusion of the Substrate into Growth Layers in Multicomponent Layered Films

Perovskite heteroepitaxial thin films composed of layers of two or more different types of perovskite minerals have attracted significant attention due to the possibility of attaining electronic properties greater than the sum of the parts. For example, although $LaTiO_3$ and $SrTiO_3$ (STO) are both insulators, heteroepitaxial films composed of these two materials demonstrate both metallic and superconducting behaviors. This film, and others based on STO as a substrate, are possible because of a milestone discovery in 1994 that allows researchers to chemically remove SrO at the substrate surface, leaving behind an atomically smooth, TiO_2-terminated surface. This surface is ideal for the layered growth of perovskite (i.e., ABO_3, in which A and B are two different cations) materials since it allows continuation of the AO-BO_2 stacking sequence with digital synthesis techniques such as oxide molecular beam epitaxy (MBE). Being able to precisely control the surface has been key to discovering an array of unusual phenomena in ultra-thin complex oxide films. Research by users of the APS challenges commonly held assumptions regarding the assembly of heteroepitaxial films on TiO_2-terminated STO and provides a new model for engineering the interactions between components in the complex oxides that make up these films.

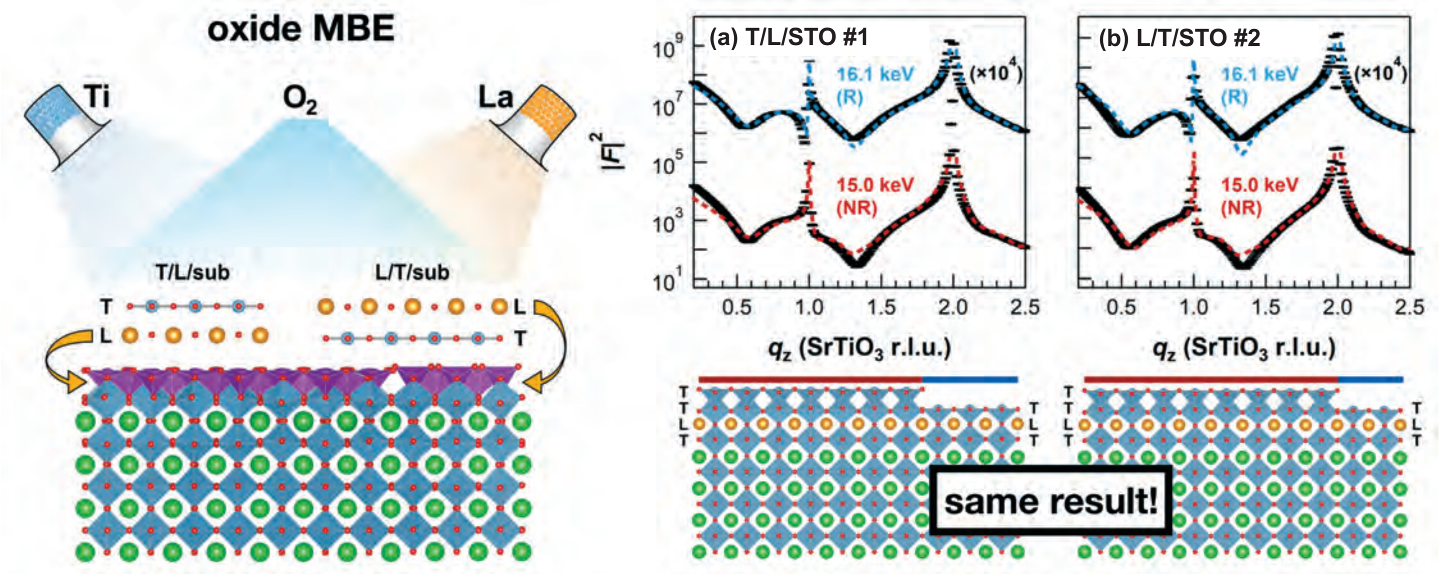

Fig. 1. Left: Schematic of $LaTiO_3$ growth by oxide MBE following either the TiO_2/LaO (T/L) or LaO/TiO_2 (L/T) growth sequence at 700° C in a background of 1×10^{-7} Torr O_2. Right: Fitted specular reflectivity curves (top) for the final structures after the T/L/STO #1 and L/T/STO #2 depositions modeled as mixtures of the TTLT and TLT surface structures (bottom). Fit results are presented as dashed lines for the T/L/STO #1 (a) and L/T/STO #2 (b) final structures.

While the surface consists of TiO_2, the actual picture is more complex: the removal of SrO leads to the formation of a TiO_2 double layer composed of a bulk-like TiO_2 plane topped by a TiO_2 adlayer; the adlayer itself is comprised of corner and edge-sharing TiO_5 octahedral units. This surface has been thought to mainly act as a crystalline template for the layers built on top of it, dictating the initial roughness of the film and the degree of strain with subse-

"Diffusion" cont'd. on next page

“Diffusion” cont’d. from previous page

quent layers. However, research by scientists at Argonne National Laboratory and Northwestern University using the using a custom-built oxide MBE chamber at XSD 33-ID-E beamline at the APS to perform *in situ* surface x-ray diffraction (SXRD) during growth by oxide MBE (Fig. 1, left) suggests that may not be the substrate’s only role. Their results indicate that for the heteroepitaxial growth of $LaTiO_3$ on STO, the TiO_2 adlayer acts as an active participant in the film’s growth process, continually diffusing to the surface throughout deposition. These findings reveal the critical role of excess TiO_2 on the initial stages of heteroepitaxial growth on this fundamental oxide substrate.

The researchers prepared STO substrates by chemically etching and then annealing these materials, resulting in a double layer of TiO_2 at the (001) surface. SXRD suggests that the TiO_2 adlayer covers about 80% of this surface and is composed of a mixture of two different types of reconstructions – areas where the atoms at the surface form a different crystal structure than in the underlying bulk — in a 3:1 ratio.

They then deposited a layer of $LaTiO_3$ on top of STO using molecular beam epitaxy. Because $LaTiO_3$ is itself comprised of LaO and TiO_2 planes, the researchers deposited individual monolayers of LaO and TiO_2 sequentially. Two distinct growth sequences were explored: on one STO substrate, LaO was grown first (T/L). On another substrate, TiO_2 was grown first (L/T).

The results of the *in situ* SXRD experiment showed that regardless of the growth sequence, the final structures were nearly identical, resulting in a dominant TTLT sequence (Fig. 1, right). When the team compared these findings with the initial SXRD results for the bare STO surface, they found similar coverage for the TiO_2 adlayers as the TTLT layers in the new heteroepitaxial film, suggesting that the TiO_2 adlayer had diffused to the surface.

The researchers found further evidence for this phenomenon using time-resolved measurements during deposition to observe the dynamic layer rearrangement that takes place at the surface. These findings again revealed that the TTLT sequence gradually forms for both T/L and L/T after the final layer is deposited.

The authors note that these results mirror those of another study in which heteroepitaxial $LaTiO_3$/STO films were assembled using pulsed laser deposition, a surprising finding since these assembly methods are so different. This suggests a universal tendency for the TiO_2 adlayer on bare STO to diffuse toward the growth surface during thin-film deposition.   – Christen Brownlee

See: Seyoung Cook[1,2], Kendra Letchworth-Weaver[1‡], I-Cheng Tung[1], Tassie K. Andersen[1,2], Hawoong Hong[1], Laurence D. Marks[2], Dillon D. Fong[1*], “How heteroepitaxy occurs on strontium titanate,” Sci. Adv. **5**, eaav0764 (2019).
DOI: 10.1126/sciadv.aav0764

Author affiliations: [1]Argonne National Laboratory, [2]Northwestern University ‡Present address: James Madison University
Correspondence: * fong@anl.gov

The work by S.C., T.K.A., and D.D.F. was supported by the U.S. Department of Energy (DOE) Office of Science-Basic Energy Sciences (BES), Materials Science and Engineering Division. The work by L.D.M. was supported by the DOE, Office of Science-BES, under award no. DE-FG02-01ER45945. The use of the Advanced Photon Source and Center for Nanoscale Materials, Office of Science User Facilities, was supported by the U.S. DOE Office of Science-BES, under contract no. DE-AC02-06CH11357.

“Oxygen” cont’d. from page 37

affect other physical properties of the Nd and Sm oxides. For instance, the presence of oxygen vacancies in the Sm oxide was shown to increase the transmittance of visible and infrared light by up to 300%. – Philip Koth

See: Michele Kotiuga[1*], Zhen Zhang[2], Jiarui Li[3], Fanny Rodolakis[4], Hua Zhou[4], Ronny Sutarto[5], Feizhou He[5], Qi Wang[2], Yifei Sun[2], Ying Wang[6], Neda Alsadat Aghamiri[7], Steven Bennett Hancock[7], Leonid P. Rokhinson[6], David P. Landau[7], Yohannes Abate[7], John W. Freeland[4], Riccardo Comin[3], Shriram Ramanathan[2], and Karin M. Rabe[1], “Carrier localization in perovskite nickelates from oxygen vacancies,” Proc. Natl. Acad. Sci. U.S.A. **116**(44,) 21992 (October 29, 2019).
DOI: 10.1073/pnas.1910490116

Author affiliations: [1]Rutgers University, [2]Purdue University, [3]Massachusetts Institute of Technology, [4]Argonne National Laboratory, [5]Canadian Light Source, [6]Purdue University, [7]University of Georgia
Correspondence: * mkotiuga@physics.rutgers.edu

M.K. and K.M.R. acknowledge support from Office of Naval Research Grant N00014-17-1-2770 and computational support from Department of Defense High Performance Computing Modernization Program. S.R., Q.W., and Z.Z. acknowledge Air Force Office of Scientific Research Grant FA9550-16-1-0159, National Science Foundation (NSF) Grant 1609898, and Army Research Office Grant W911NF-16-1-0042. F.R. acknowledges additional support from NSF Grant DMR-0703406. J.L. and R.C. acknowledge support from NSF Grant 1751739. Part of the research described in this paper was performed at the Canadian Light Source, which is supported by the Canada Foundation for Innovation, Natural Sciences and Engineering Research Council of Canada, the University of Saskatchewan, the Government of Saskatchewan, Western Economic Diversification Canada, the National Research Council Canada, and the Canadian Institutes of Health Research. Y.W. and L.P.R. acknowledge the support from U.S. Department of Energy (DOE) Award DE-SC0008630 (Y.W.) and NSF Grant DMR-1610139 (L.P.R.). N.A.A. acknowledges support from NSF Grant 1553251. S.B.H. and Y.A. acknowledge support from Air Force Office of Scientific Research Grant FA9559-16-1-0172. This research used resources of the Advanced Photon Source, a U.S. DOE Office of Science User Facility operated for the DOE Office of Science by Argonne National Laboratory under Contract DE-AC02-06CH11357.

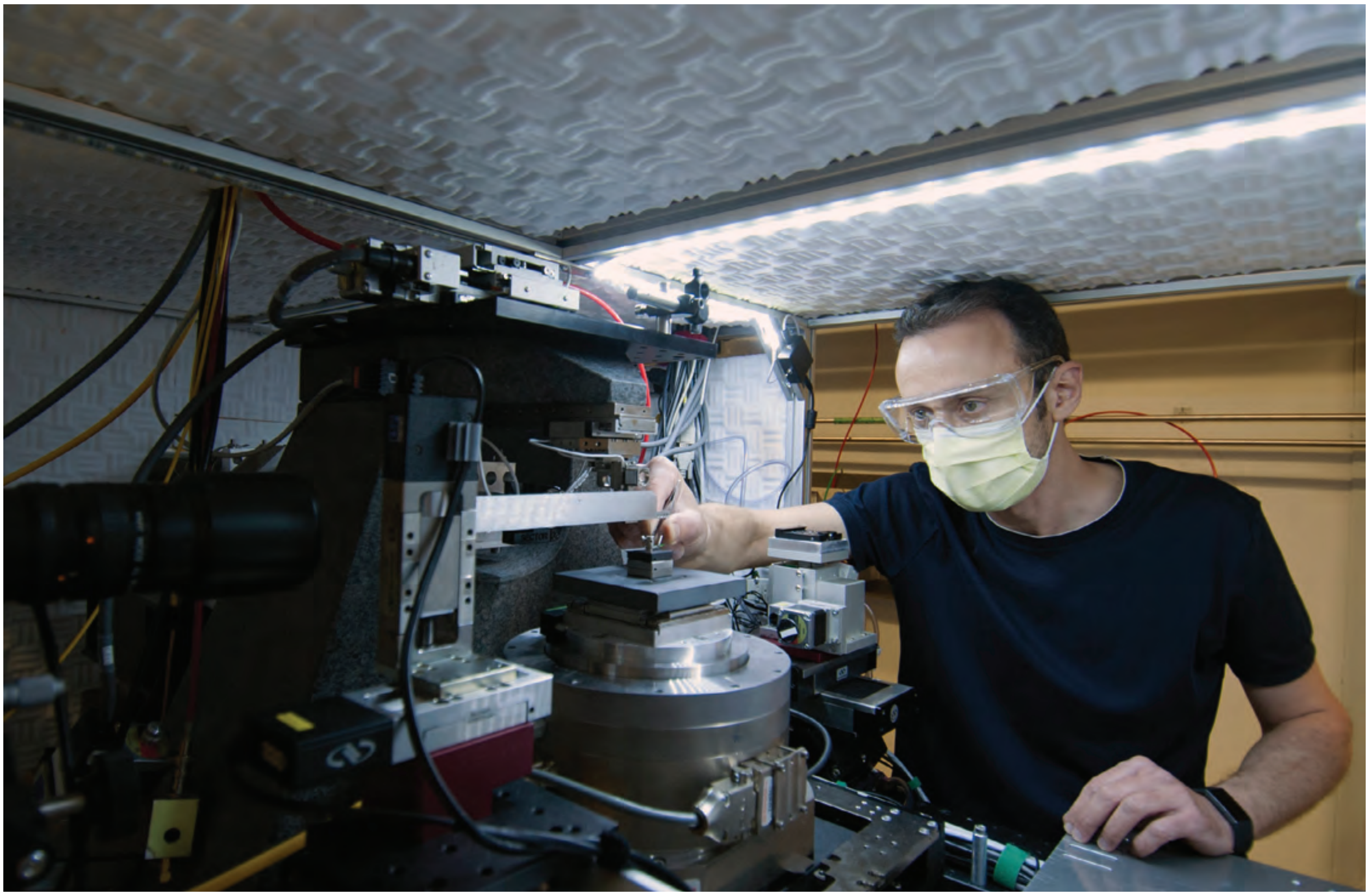

Nanotomography Studies of Potential N95 Mask Materials at XSD Beamline 32-ID-C

X-ray Science Division physicist Vincent De Andrade prepares an experiment performed with the transmission x-ray microscope at the XSD 32-ID beamline at the APS. The experiment is part of Argonne's COVID-19 activities devoted to developing filter materials for N95-grade medical masks to protect first-line medical personnel from contaminated air. Nanotomography is used to characterize in three dimensions new fiber-based materials fabricated using electrospinning technology. This technique can generate much finer polymer fibers, smaller pore sizes, and higher filtration efficiency than the state-of-the-art filter media. Highly thermal and chemical resistive polymers were introduced into the filter medium to improve its sterilization response and realize reusability.

Soft Materials and Liquids

Splitting Water in a Neutral Way

Hydrogen is a vital resource not only for various industrial purposes but also as an energy vector, such as in hydrogen fuel cells. In fuel cells, hydrogen is combined with oxygen to create electricity and water, but the process can also be reversed in an electrolyzer, which uses electricity to produce hydrogen in what's known as water splitting or water dissociation. However, the most effective catalysts for these hydrogen evolution reaction (HER) techniques, such as platinum, are most effective in acidic environments. A team of experimenters used the APS to study an electrolyzer design they developed that is highly effective in neutral conditions. These design principles offer a major new direction for the development of large-scale seawater splitting and the production of hydrogen for efficient biofuels and energy systems.

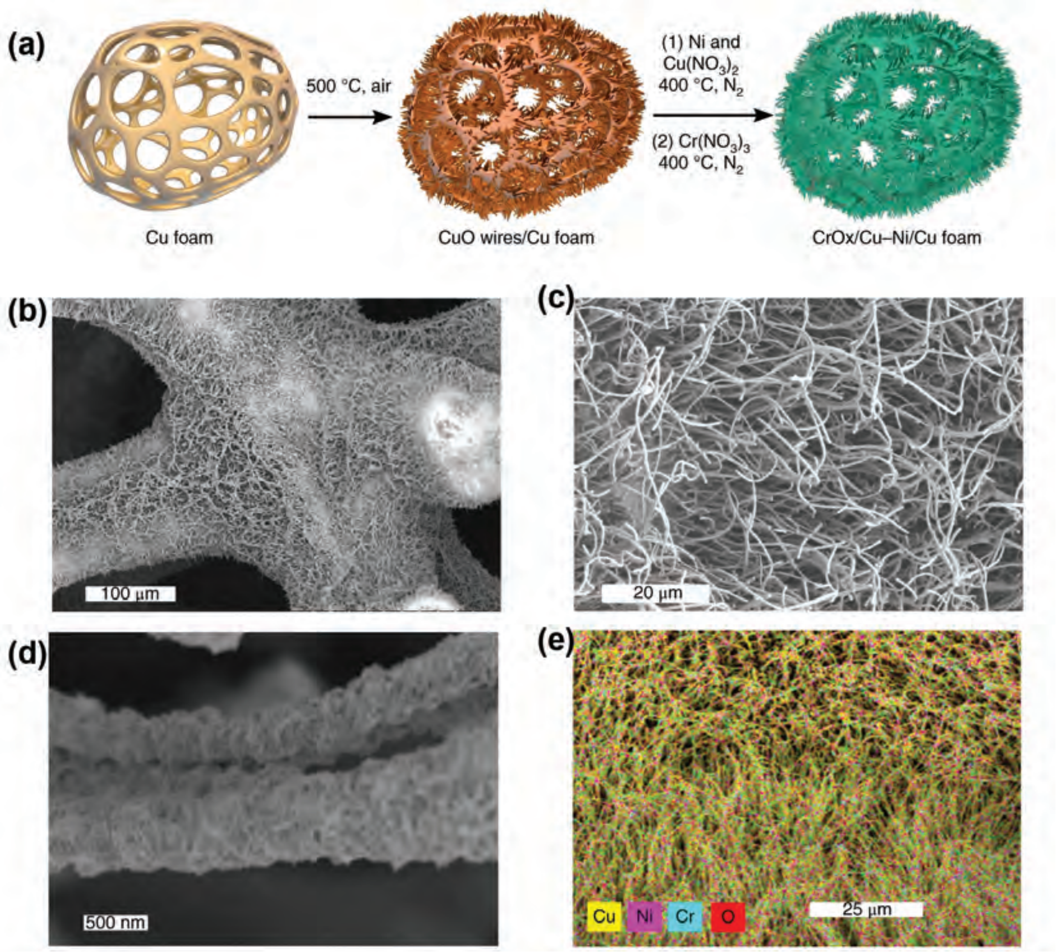

Fig. 1. (a) Schematic illustration of the preparation pathway for 3D CrO$_x$/Cu–Ni from Cu foam as a substrate followed by the growth of CuO nanowires and coating of the CrO$_x$/Cu–Ni active phase. (b–e), SEM images at different magnifications (b–d) and elemental EDX mapping (e) for CrO$_x$/Cu–Ni deposited on the 3D Cu nanowire structure. From C.-T. Dinh et al., “Multi-site electrocatalysts for hydrogen evolution in neutral media by destabilization of water molecules,” Nat. Ener. **4**, 107 (February 2019). ©2020 Springer Nature Limited.

A method of achieving HER in neutral pH conditions would make large-scale hydrogen production easier and more efficient, allowing the use of seawater without prior desalination and catalysts based on cheap and readily available transition metals. Neutral HER also facilitates the production of biofuels through processes involving microorganisms that are impossible in acidic media. The two chief strategies for developing neutral HER electrocatalysts involve either adjusting the catalyst surface texture or incorporating additional compounds within the catalyst to improve water dissociation.

The present work combines both approaches, anisotropically doping the surface using a metal with strong hydrogen binding energy and a metal oxide with strong hydroxide (OH) binding energy. With two types of surface sites that each interact with different atoms, water dissociation can be accelerated. The catalyst structures were studied using scanning electron microscopy and various x-ray techniques, including x-ray absorption spectroscopy (XAS) at the XSD 9-BM-B,C beamline of the APS; and ambient-pressure x-ray photoelectron spectroscopy studies at Advanced Light Source beamline 9.3.2 at Lawrence Berkeley National Laboratory (LBNL).

The investigators from the University of Toronto and LBNL tested catalysts using copper (Cu) for hydrogen (H) binding and a variety of metal oxide clusters for OH, measuring the HER activity. They found that a CrO_x/Cu system promoted the best HER performance. To improve catalytic activity even further, they doped the Cu surface with Ni to take advantage of its strong hydrogen binding energy, then tested the deposition of the different components in various combinations. This demonstrated that the order of CrO_x and Cu-Ni deposition greatly affects the catalytic performance, with the CrOx/Cu-Ni system substantially more effective than the Cu-Ni/CrO_x catalyst (Fig. 1).

While experiments confirmed that CrO_x is not a particularly HER-active agent, it strongly modulates the oxidation of copper-nickel (Cu-Ni), particularly the Ni structure. On the Cu-Ni/CrO_x samples, it induces water dissociation, an effect, which can be maximized through an even dispersal on the Cu-Ni active layer.

The team used density functional theory (DFT) modeling to more closely investigate the catalytic activity of the CrO_x/Cu-Ni system on four surfaces with various doping configurations. They found that an Ni-doped surface greatly improves the stability of dissociated water. The minimum energy barrier for water dissociation is seen with the hybrid catalyst. Water dissociation is shown by the DFT calculations to be the major factor for H_2 generation in the Cu-based catalysts, and can be improved with specific configurations of the Cu, Ni, and CrO_x components.

The investigators then used the information obtained in these experiments to attempt the fabrication of the most optimal chromium-copper-nickel catalyst, depositing Ni and CrO_x on a scaffolding composed of CuO nanowires. Tests of the system's electrochemical performance displayed highly stable and impressive results, with a 48-mV overpotential at a current density of 10 mA cm^{-2} in a buffer electrolyte of pH 7. This represents markedly superior performance compared to other known HER catalysts, and arises not merely from higher surface area but from the intrinsic structure that greatly reduces the energy barrier for water dissociation.

The work demonstrates that it is both possible and practical to create high-performance hydrogen evolution reaction catalysts that not only perform in neutral conditions but can do so without using rare and expensive elements. – Mark Wolverton

See: Cao-Thang Dinh[1], Ankit Jain[1], F. Pelayo García de Arquer[1], Phil De Luna[1], Jun Li[1], Ning Wang[1], Xueli Zheng[1], Jun Cai[2], Benjamin Z. Gregory[2], Oleksandr Voznyy[1], Bo Zhang[1], Min Liu[1], David Sinton[1], Ethan J. Crumlin[2], and Edward H. Sargent[1]*, "Multi-site electrocatalysts for hydrogen evolution in neutral media by destabilization of water molecules," Nat. Ener. **4**, 107 (February 2019). DOI: 0.1038/s41560-018-0296-8

Author affiliations: [1]University of Toronto, [2]Lawrence Berkeley National Laboratory

Correspondence: * ted.sargent@utoronto.ca

This work was supported by the Ontario Research Fund: Research Excellence Program, the Natural Sciences and Engineering Research Council (NSERC) of Canada, and the Connaught Global Challenge program of the University of Toronto. F.P.G.d.A. acknowledges financial support from the Connaught Fund. P.D.L acknowledges financial support from NSERC in the form of the Canada Graduate Scholarship – Doctoral (CGS-D) award. This research used resources of the Advanced Light Source, which is a DOE Office of Science User Facility under contract no. DE-AC02-05CH11231. This research also used resources of the Advanced Photon Source, an Office of Science User Facility operated for the U.S. DOE Office of Science by Argonne National Laboratory under contract no. DE-AC02-06CH11357, and the Canadian Light Source and its funding partners.

For Better Pickering Emulsions, Keep the Sound Down

Homogenized milk, skin cream, and mayonnaise are just a few examples of Pickering emulsions, mixtures of oil and water stabilized with solid particles. Pickering emulsions are just as common in cosmetics, agrochemicals, and drug delivery systems as they are in food preparations, and for the same reasons: instead of using a surfactant (like a soap) to keep oil and water mixed, they use a particle such as a protein or metal oxide that can have additional functionality beyond simply keeping the emulsion together. Despite how common Pickering emulsions are, the mechanics of how they form are not well understood. Multiple repulsive forces involving electrical charge or particles shape work to prevent emulsification. Mechanical forces such as shaking or ultrasound waves have to be applied to overcome the repulsions. Researchers used the APS to understand how sound waves overcome the energy barriers to Pickering emulsification. Their findings should lead to more efficient manufacturing of drug, food, and chemical emulsions, was well as medical applications, in the future.

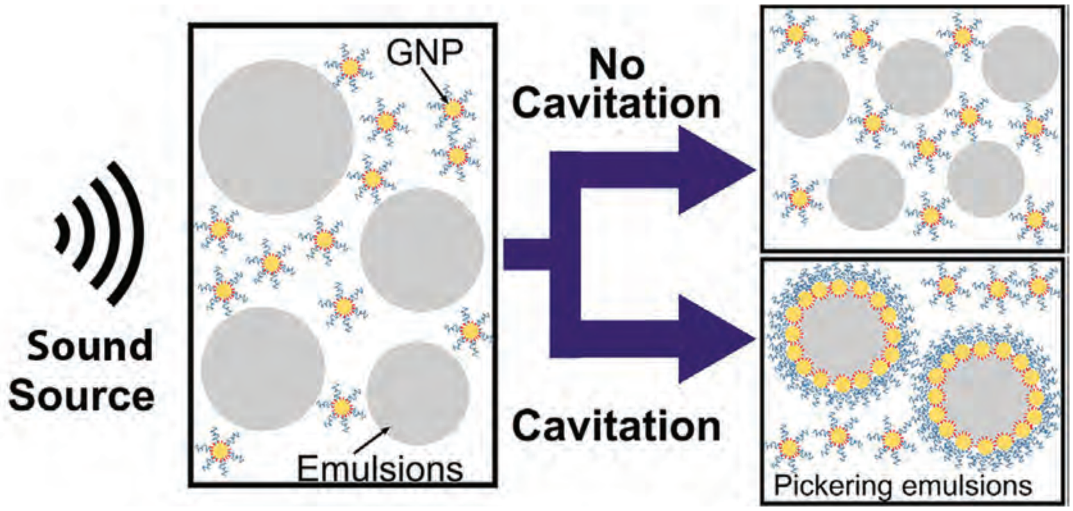

Fig. 1. A source of sound waves sonicates a mixture of oil (grey spheres) and gold nanoparticles (GNP) in water. If the sound source is powerful enough to produce sonication (waves of bubbles in low pressure areas), then the oil droplets break apart and become coated by gold nanoparticles to create a Pickering emulsion (bottom right). If the sound source is not powerful enough, the mixture does not emulsify (top).

Pickering emulsions using perfluorinated oils have recently gained a following in the medical community as potential imaging agents. Using a combination of ultrasound and laser pulses, these emulsions can simultaneously provide contrast and break up blood clots, making them potentially useful for doctors treating victims of stroke and embolism. Researchers from the University of Washington teamed up with colleagues at Argonne to investigate exactly how sonication — that is, exposing the ingredients to powerful sound waves — creates Pickering emulsions of these valuable medical compounds. They found suggestive evidence that cavitation, meaning the creation of bubbles, may be the key.

The researchers chose gold nanoparticles as the solid particles that would stabilize the Pickering emulsion. Onto the gold nanoparticles they added polyethylene glycol molecules with a hydrophilic ("water-loving") end, and then added hydrophobic ("oil-loving") molecules to the other side of the nanoparticles. Then they gently mixed the nanoparticles with water and perfluorinated oils, and waited.

But no matter how long they waited, the mixture did not emulsify. The water and perfluorinated oil stayed in separate layers. It did not spontaneously form a Pickering emulsion, showing that the mere presence of stabilizing particles was insufficient to make the emulsion happen. The researchers also tried mixing with a magnetic stirrer, which caused some shear in the liquid, but this did not lead to emulsification either.

But when they tried sonicating the mixture, everything came together. Rapidly moving sound waves of high enough acoustic pressure create cavitation (bubbles) in the low-pressure areas, as the quick drop in pressure causes some of the liquid to evaporate. When these bubbles subsequently collapse, they create tiny little shock waves.

When the researchers sent sound waves above 7.2 MPa through the mixture, it quickly formed a Pickering emulsion of droplets of oil in water and the droplets were stabilized by the gold nanoparticles. However, the mixture did not emulsify when sonicated at sound pressures below 6.4 MPa, which is too low to create cavitation (Fig. 1.) This indicated that bubbles are essential to the Pickering emulsion process.

To better understand exactly what was changing structurally within the mixture as it became a Pickering emulsion, the team used the XSD 9-ID-C beamline at the APS. They employed the ultra small-angle x-ray scattering (USAXS) technique, which uniquely provides the ability to quantitatively measure structural changes while applying sound waves. The APS had the capacity to design a custom acoustic environment in which the sound pressure, sound pulse frequency, and pulse duration could all be precisely controlled.

The USAXS data showed that sonication at sound pressures too low to create cavitation was actually bad for the Pickering emulsion, destabilizing the oil and causing it to evaporate without reforming droplets. The emulsion lost oil that way.

From analyzing the USAXS data, the researchers now have two specific hypotheses as to how Pickering emulsification occurs. The first assumes that cavitation happens in the water, and then momentum from the shock waves of collapsing bubbles breaks up the oil and encourages the gold nanoparticles to adsorb onto the oil droplets. The second hypothesis assumes, instead, that cavitation happens in the oil. Oil bubbles expand very quickly and then collapse. The high velocity and displacements that occur during the rapid expansion and collapse could entrap the gold nanoparticles and induce them to adsorb onto the surface of the oil droplet.

The researchers hope to use the time-resolved small-angle x-ray scattering technique to tease out these different scenarios in the next stage of their research. But based on the results they already have, they suggest that manufacturers of medical Pickering emulsions should seek to use a lower-frequency sonication method to minimize oil evaporation and loss, or consider using a pre-emulsification treatment to create smaller oil droplets to start with before beginning the Pickering emulsification process. — Kim Krieger

See: Yi-Ting Lee[1], David S. Li[1], Jan Ilavsky[2], Ivan Kuzmenko[2], Geng-Shi Jeng[1], Matthew O'Donnell[1], and Lilo D. Pozzo[1*], "Ultrasound-based formation of nano-Pickering emulsions investigated via in-situ SAXS," J. Colloid Interf. Sci. **536** 281, (2019). DOI: 10.1016/j.jcis.2018.10.047

Author affiliations: [1]University of Washington, [2]Argonne National Laboratory
Correspondence: * dpozzo@uw.edu

Acknowledgment is made to the Donors of the American Chemical Society Petroleum Research Fund for support of this research. The research performed was also supported by the National Institutes of Health under grant R01HL125339. We also acknowledge Yuyin Xi for his help collecting scattering data at Argonne National Laboratory. This research used resources of the Advanced Photon Source, a U.S. Department of Energy (DOE) Office of Science User Facility operated for the DOE Office of Science by Argonne National Laboratory under Contract No. DE-AC02-06CH11357.

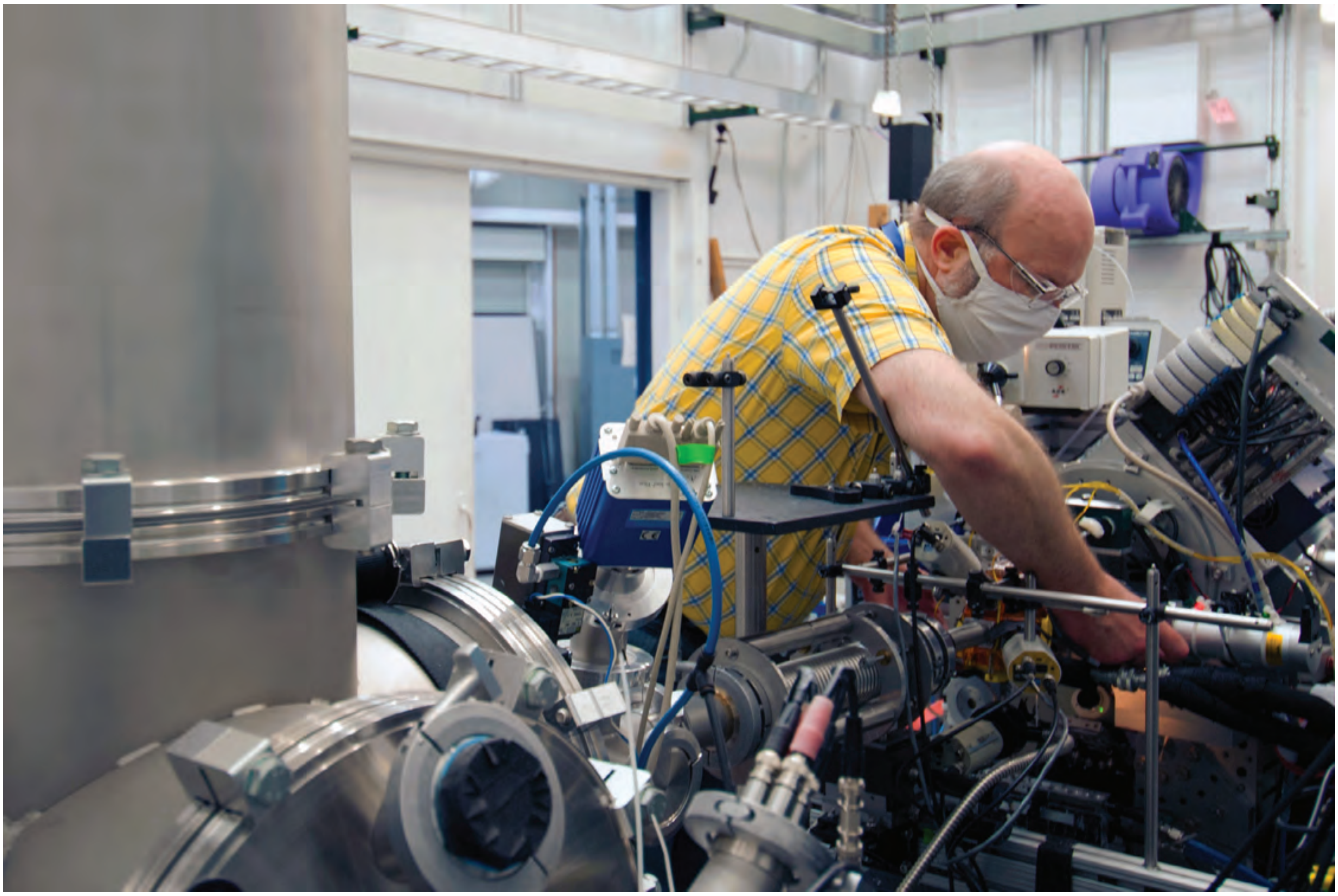

Novel Coronavirus Research at DND-CAT Beamline 5-ID-D

Steven Weigand (DND-CAT research scientist) is shown collecting data for a COVID-19 project from the Stupp Laboratory at Northwestern University while wearing a face mask as required by Illinois' COVID-19 prevention controls. The measurements were solution scattering experiments carried out at the DND-CAT x-ray beamline 5-ID-D station at the APS. Weigand used the DND-CAT in-vacuum flow cell and small-angle scattering/mid-angle scattering/wide-angle scattering set of detectors. The Northwestern group, headed by Samuel I. Stupp, submitted an online, COVID-19 related beam-time proposal/request titled "Peptide amphiphiles as a supramolecular system delivering COVID-19 inhibitor."

Chemical Science

The Good and the Bad of Defects in Catalysts

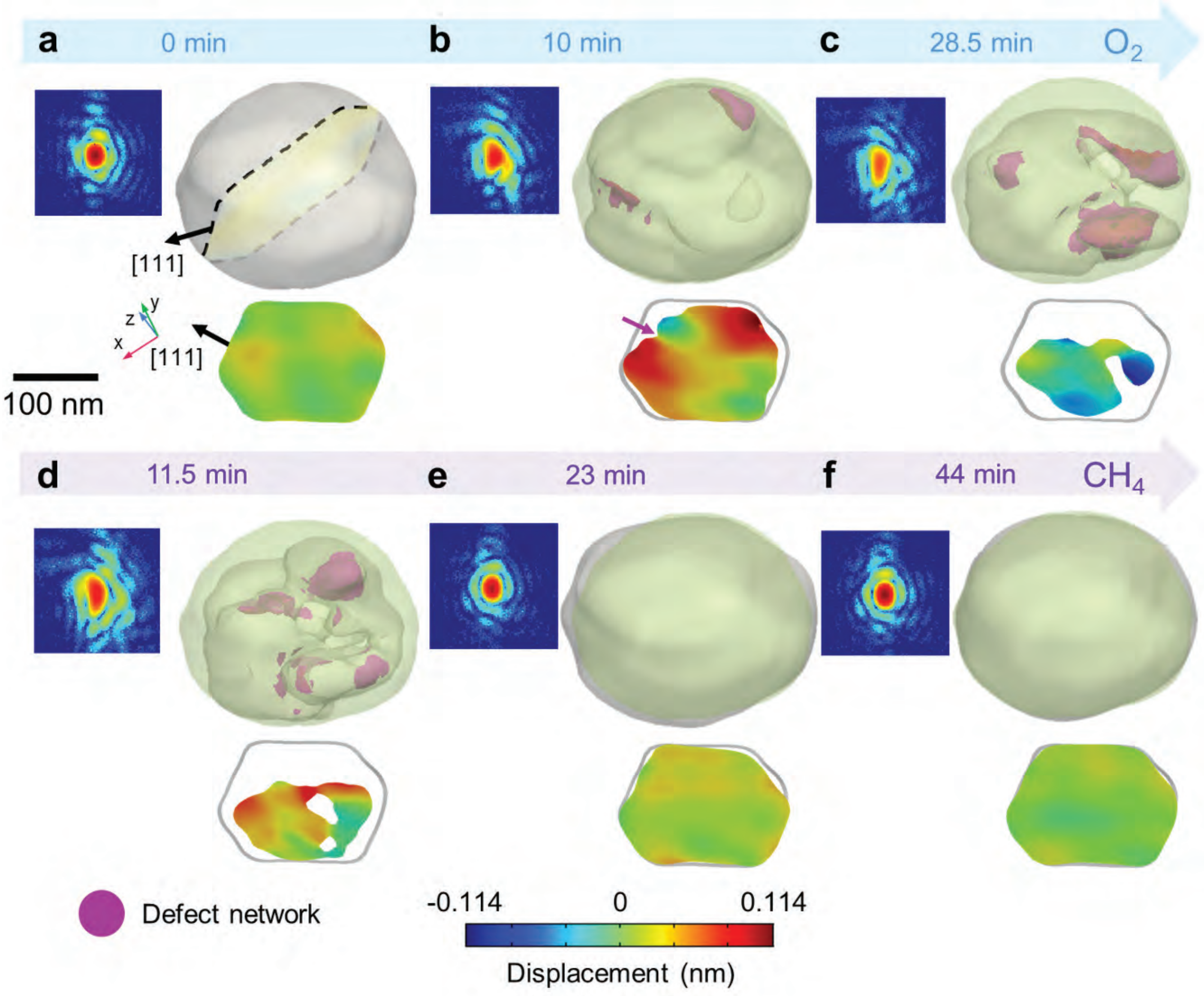

Fig. 1. X-ray diffraction patterns and reconstructed three-dimensional images of a platinum nanoparticle show how defects evolve as oxygen (top row) or methane (bottom) is added. Figure adapted from D. Kim et al., Nano Lett. **19**, 5044 (2019). © 2019 American Chemical Society

Defects can play an important role in determining the electronic properties of materials, such as those used as catalysts. In some cases, defects in a catalyst can enhance the efficiency, for instance by causing more of the material they're reacting with to adhere to the defect. At the same time, they can ultimately cause the catalyst to fail by putting stress on the structure over many cycles. Most studies of defects in catalysts have been done on the surface of the material, and because of that have only been able to give an overview of the effects. A group of researchers using the APS looked at the process in nanoparticles, allowing them to focus on exactly what is happening at the defect site and pointing the way toward improving how well the catalysis works.

Common catalysts such as platinum, widely used to treat the exhaust streams from automobiles, often have defects such as layers of atoms in their crystalline structure that are out of alignment with other layers in the stack. The materials reacting with the reactants, such as methane gas, tend to form oxides preferentially at the site of such defects, which improves the catalytic activity.

In methane oxidation reactions with a platinum nanoparticle as a catalyst, for example, defects have been shown to play an important role in adsorbing oxygen atoms at specific sites. Locations on the nanocrystal where many molecules of oxygen collect are more active catalytic sites because the oxygen is so reactive. In addition, the defects can cause strain on the crystal, which makes it easier for the reactants to adhere to the catalyst. Unfortunately, however, the strain can also cause the catalyst to degrade.

To observe exactly what is happening at defect sites, the researchers from Sogang University (South Korea) and Argonne performed Bragg x-ray coherent diffraction imaging at XSD beamline 34-ID-C at the APS, which allowed them to see the atomic deformation of the nanoparticle (nanoparticles are usually 500-100000 times "thinner" than a human hair). They first took readings under a flow of hydrogen and nitrogen, which cleaned the surface of the nanoparticle. They then flowed a mixture of oxygen and nitrogen and observed the oxygen being adsorbed on the surface. After that, they used a flow of methane and nitrogen so they could see what happened during the catalytic reaction (Fig. 1).

Adding the oxygen caused a distortion in the coherent x-ray pattern that revealed the molecules sticking to the nanoparticle and causing strain. Adding the methane below the temperature needed for a catalytic reaction did not cause a change in the pattern, but when methane was introduced at higher temperatures above the activation temperature, the strain increased and the pattern became more distorted, suggesting that it was the reaction causing the changes. About 10 min after all the oxygen was used up by the reaction, the image returned to its original state. Even though the nanocrystal recovered its shape, it may be that repeated structural changes over many cycles eventually leads to degradation of the catalyst.

The results showed that the areas with initial strain caused by the presence of defects acted as seeds for further dislocations under the pressure of the catalytic process. While platinum is a good example of catalysts for studying the impact of such defects in general, the researchers would also like to perform similar experiments on other catalysts to make sure their results apply more widely. They hope that by understanding the dynamics of defects, engineers will be able to design better catalysts. By controlling the concentration of defects in the nanoparticles, they could strike a balance between higher catalytic efficiency and longer lifetimes for the materials.

– Neil Savage

See: Dongjin Kim[1], Myungwoo Chung[1], Sungwon Kim[1], Kyuseok Yun[1], Wonsuk Cha[2], Ross Harder[2], and Hyunjung Kim[1*], "Defect Dynamics at a Single Pt Nanoparticle during Catalytic Oxidation," Nano Lett. **19**, 5044 (2019).
DOI: 10.1021/acs.nanolett.9b01332
Author affiliations: [1]Sogang University, [2]Argonne National Laboratory
Correspondence: * hkim@sogang.ac.kr

This research was supported by the National Research Foundation of Korea (Grants NRF-2014R1A2A1A10052454, 2015R1A5A1009962, and 2017K1A3A7A09016379). This research used resources of the Advanced Photon Source, a U.S. Department of Energy (DOE) Office of Science User Facility operated for the DOE Office of Science by Argonne National Laboratory under Contract No. DE-AC02-06CH11357.

Resolving Redox Inequivalence within Isovalent Clusters

In biological and non-biological systems, metal clusters facilitate electron transport and mediate multi-electron processes. Due to the polynuclear nature of metal clusters, changes in the oxidation state during such processes may be disproportionately localized at some metal sites or equally distributed across the cluster. While researchers can assign the overall oxidation state of an isolated cluster, it is difficult to allot a redox load per metal site, redox being a process in which one substance or molecule is reduced and another oxidized; oxidation and reduction considered together as complimentary processes. Using multiple-wavelength anomalous diffraction (MAD) at the APS, a team of researchers studied trinuclear iron clusters to determine the redox load distribution by the free refinement of atomic scattering factors. MAD is a site-specific analytical technique that resolves differences in relative redox states within molecular species. A better understanding of MAD data will allow researchers to decipher redox in more complicated biological systems, such as metalloenzymes, to better interpret MAD data on more complicated systems, including model complexes relevant to industrial and enzymatic catalysis.

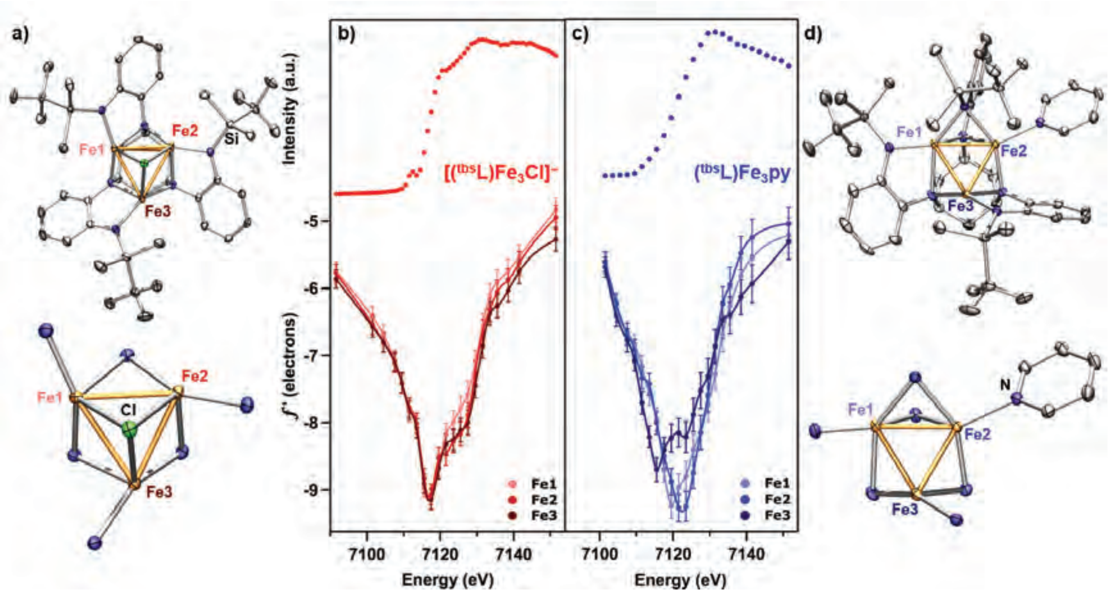

Fig. 1. a) Crystal structure of $[NBu_4][(^{tbs}L)Fe_3Cl]$ with counterion omitted for clarity, b) fluorescence edge scan (top) and f′ curves (bottom) for the three iron sites of $[NBu_4][(^{tbs}L)Fe_3Cl]$, c) fluorescence edge scan (top) and f' curves (bottom) for the three iron sites of (tbsL)Fe_3py, and d) crystal structure of (tbsL)Fe_3py."

Much like the oxidation state of a single metal in a mononuclear complex can be probed by x-ray absorption near-edge spectroscopy (XANES), site-specific oxidation states of polynuclear metal clusters can be examined using MAD. However, analysis of MAD data is complicated because atomic scattering within metal clusters can be impacted by 1) metal atom primary coordination sphere, 2) metal-metal bonding, and 3) redox delocalization in formally mixed-valent species. Deconvoluting these effects requires a careful series of experiments.

For this work, the researchers from Harvard University, The University of Chicago, and SLAC National Accelerator Laboratory probed redox states of metals in a series of trinuclear iron complexes using MAD at the ChemMatCARS 15-ID-B,C,D x-ray beamline at the APS. The MAD data were collected in up to 21 energy data points around the Fe K-edge (the energy required to eject a 1s electron). This strategy significantly improved the resolution of the resulting cattering factor (f′) curves compared to previous small molecule MAD studies. The data reveal differences based on local symmetry, electronic delocalization, and metal-metal bonding in the metal complexes (Fig. 1).

While Mössbauer spectra from multiple sites in a multinuclear complex are difficult to assign to specific local sites, MAD is a crystallographic technique so it is straightforward to assign each MAD trace to its corresponding metal site. The researchers refined the Fe scattering factors for each partial dataset to determine the value of the real f′ at each of the measured energies. The researchers then plotted real f′ versus energy for each iron atom in each complex. In previous, low-resolution MAD studies, the minimum of the f′ plot was taken as a direct indication of the relative oxidation states, as it should loosely correspond to a XANES edge.

In this study, a comparison of the f′ traces of homovalent iron sites in different local geometries showed that differences in local coordination geometry can dramatically impact the shape of the curve. Additionally, the high-resolution f′ curves were significantly broadened compared to the sharp profile of theoretical f′ curves. This roadening, which results from the covalency of bonding between the metal sites and the coordinating ligand, and also between the two metal sites, prevents oxidation-state assignment based on the minimum of the f′ trace. Thus, relative oxidation levels within the clusters were determined by comparing the entire envelope of the atomic scattering factor data. In particular, the location of the right-hand rising edge was most indicative of oxidation state, with more oxidized sites shifting to higher energies as expected.

This work exposes the effects of aggregate oxidation level, deviations in primary coordination sphere, and metal-metal bonding levels on the capability of MAD to decipher site-specific redox levels. While differences in local coordination geometry dramatically impact the appearance of site-specific f′ curves, when control compounds are structurally very similar to the compounds of interest, MAD reveals the relative oxidation states of each metal site in a polynuclear cluster. Differences in oxidation levels undergo systematic shifts of scattering factor envelopes to increasingly higher energies. – Dana Desonie

See: Amymarie K. Bartholomew[1‡], Justin J. Teesdale[1], Raúl Hernández Sánchez[1‡‡], Brian J. Malbrecht[1], Cristin E. Juda[1], Gabriel Ménard[1‡‡‡], Wei Bu[2], Diana A. Iovan[1‡‡‡‡], Alexandre A. Mikhailine[1], Shao-Liang Zheng[1], Ritimukta Sarangi[3], SuYin Grass Wang[2], Yu-Sheng Chen[2], and Theodore A. Betley[1*], “Exposing the inadequacy of redox formalisms by resolving redox inequivalence within isovalent clusters,” Proc. Natl. Acad. Sci. U.S.A. **116**, 15836 (August 6, 2019). DOI: 10.1073/pnas.1907699116

Author affiliations: [1]Harvard University, [2]The University of Chicago, [3]SLAC National Accelerator Laboratory Present address: ‡Columbia University, ‡‡University of Pittsburg, ‡‡‡University of California, Santa Barbara, ‡‡‡‡ University of California, Berkeley

Correspondence: * betley@chemistry.harvard.edu

This work was supported by grants from the National Institutes of Health (GM 098395), the U.S. Department of Energy (DOE) (DE-SC0008313, DE -SC0019144), and Harvard University. R.H.S. gratefully acknowledges Consejo Nacional de Ciencia y Tecnología and Fundaciŏn México for a doctoral fellowship. C.E.J. acknowledges support from a National Science Foundation (NSF) predoctoral fellowship. A.A.M. acknowledges support from the Natural Sciences and Engineering Research Council of Canada Postdoctoral Fellowship. T.A.B. gratefully acknowledges support from the Dreyfus Foundation (Teacher-Scholar Award). ChemMatCARS is supported by the NSF under Grant NSF/CHE-1834750. Portions of this research were carried out at the Stanford Synchrotron Radiation Lightsource, a Directorate of SLAC National Accelerator Laboratory and an Office of Science User Facility operated for the U.S. DOE Office of Science by Stanford University. The Stanford Synchrotron Radiation Lightsource Structural Molecular Biology Program is supported by the DOE Office of Biological and Environmental Research, and by the National Institutes of Health, National Institute of General Medical Sciences (including P41GM103393). This research used resources of the Advanced Photon Source, a U.S. DOE Office of Science User Facility operated for the DOE Office of Science by Argonne National Laboratory under Contract DE-AC02- 06CH11357.

Dialing-Up Diamagnetism to Search for a New Material

Chemistry's magic is in its mixtures, the novel combinations of elements that make unexpected properties possible. Even simple, two-element compounds can surprise us. The classic example is sodium chloride, which combines element Na (which by itself is an explosive metal) with Cl (which, in the form of Cl2, is a poisonous gas) to create table salt. But many more esoteric compounds are yet to be explored. A team of chemists in search of novel two-dimensional compounds used the APS to look at a custom-made nickel bismuth compound and see how its bizarre structure might facilitate superconductivity or other new-to-science properties.

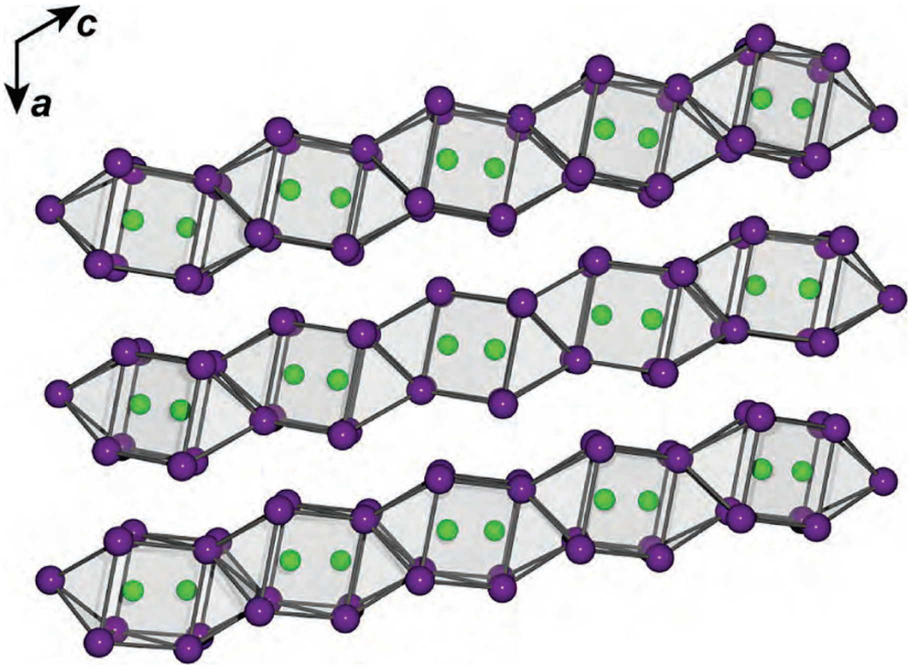

Fig. 1 Structure of $NiBi_2$ emphasizing the layered nature of the material. Violet and green spheres represent Bi and Ni, respectively.

Nickel and bismuth are both metals known since ancient times. But combining them—nickel is a transition metal, and bismuth a heavy Group-7 element often confused with lead—has rarely been done. It could be very worthwhile, because both nickel and bismuth have unusual magnetic properties. Nickel is one of the four elements that are magnetic near room temperature; bismuth, on the other hand, is the strongest natural diamagnetic material known. Diamagnetic materials have a strange ability to produce the opposite of the magnetic field going through them. In simpler terms, metals like iron are attracted to magnets; metals like bismuth repel them.

Diamagnetism is not dramatic on the everyday scale of pens and apples and cars and other objects we can touch. But down on the scale of atoms and molecules, it can be significant. Diamagnetism is caused by the combined magnetic fields generated by electrons. Electrons generate magnetic fields in two ways: by orbiting their atoms, and by spinning on their axes at the same time. All those spinning electrons create tiny magnetic fields that add together in different ways, depending on the arrangement of atoms and electrons in space. It is hard to understand intuitively, because it depends on quantum mechanics. But in bismuth, the net result is that whenever the material is exposed to an external magnetic field, its internal magnetic fields generate an opposing field that repels the external one.

Superconductivity and other exotic properties also depend on quantum mechanics. Combining a strongly diamagnetic material with a strongly magnetic material (which behaves in a very different way, creating its own strong and usually permanent magnetic field) might generate a material with very unusual behavior.

A team of researchers from Northwestern University, The University of Chicago, and the DOE's Argonne and Lawrence Livermore national laboratories were intrigued by nickel bismuth compounds. They were already familiar with NiBi (nickel bismuthide) and $NiBi_3$ (nickel tribismuthide). $NiBi_3$ forms itself into chains of Ni-Bi polyhedral that arrange in hexagonal patterns and it is a superconductor at low temperatures. They wondered what $NiBi_2$ (nickel dibismuthide) would be like.

The challenge to making $NiBi_2$ was that it wouldn't form at regular atmospheric pressure. So the team used a diamond anvil cell (DAC), originally developed by geophysicists to study conditions deep within planets, to create the material. By combining bismuth and nickel in the right proportions and then heating and squeezing the mixture at about 14 GPa, a pressure close to what one would expect to find in the interior of Mercury, they made $NiBi_2$ (Fig. 1).

Once the researchers had made $NiBi_2$, they needed a very high-intensity, high-flux x-ray source to look at its structure. The HPCAT-XSD beamline 16-ID-B at the APS is specialized for just these sorts of applications. The team used the DAC in combination with the x-ray diffraction technique to reveal the atomic structure of the $NiBi_2$. The data they obtained showed that $NiBi_2$ forms into columns similar to those of $NiBi_3$, but the columns are squashed together. To scale up the new intermetallic compound, they performed high-pressure reactions using the 1000-ton multi-anvil press at the GSECARS 13-ID-D beamline, also at the APS.

The researchers also confirmed that the material is indeed a superconductor at very cold temperatures close to that of liquid helium. Now, they are working on flaking it into single, two-dimensional sheets. They suspect that when $NiBi_2$ electrons are confined to a single plane, and the bonds between the atoms are forced to localize in two dimensions, more intriguing properties may emerge.

— Kim Krieger

See: Samantha M. Clarke[1,2], Kelly M. Powderly[1‡], James P. S. Walsh[1], Tony Yu[3], Yanbin Wang[3], Yue Meng[4], Steven D. Jacobsen[1], and Danna E. Freedman[1*], "Controlling Dimensionality in the Ni–Bi System with Pressure," Chem. Mater. **31**, 955 (2019). DOI: 10.1021/acs.chemmater.8b04412

Author affiliations: [1]Northwestern University, [2]Lawrence Livermore National Laboratory, [3]The University of Chicago, [4]Argonne National Laboratory ‡Present address: Princeton University
Correspondence: *dannafreedman@northwestern.edu

The collaborative project between D.E.F. and S.D.J. is supported by Northwestern University (NU) through the Innovative Initiatives Incubator (I3). This experimental work is supported by the Air Force Office of Scientific Research (FA9550-17-1-0247). GSECARS is supported by the National Science Foundation (NSF) (EAR-1634415) and the U.S. Department of Energy (DOE) (DE-FG02-94ER14466). S.M.C. acknowledges support from the National Science Foundation (NSF) Graduate Research Fellowship Program (GRFP) (DGE-1324585) and P.E.O. Scholar Award. Part of this work was performed under the auspices of the U.S. DOE by Lawrence Livermore National Security, LLC, under Contract DE-AC52-07NA27344. K.M.P. acknowledges support for the NSF GRFP (DGE-1656466) and the NU MRSEC URI (DMR-1121262). S.D.J. acknowledges support from NSF (DMR-1508577) and the Capital/DOE Alliance Center (CDAC) for providing beam time at HPCAT-XSD. HPCAT-XSD operations are supported by the U.S. DOE National Nuclear Security Administration under Award No. DE-NA0001974, with partial instrumentation funding by the NSF. Y.M. acknowledges the support of DOE-Basic Energy Sciences Materials Sciences and Engineering Division under Award No. DE-FG02-99ER45775. This research used resources of the Advanced Photon Source, a U.S. DOE Office of Science User Facility operated for the DOE Office of Science by Argonne National Laboratory under Contract No. DE-AC02-06CH11357.

Making the Most of Methane

The world is awash in methane, a potent greenhouse gas that is the main component of natural gas. The expansion of hydraulic fracturing, or fracking, has greatly increased the U.S. natural gas supply, and fueled ambitions to upgrade methane into more valuable chemicals, such as through oxidation to methanol. Methanol is a chief feedstock for chemicals, including those used to make plastics, and can fuel vehicles or power fuel cells. However, the simple and inexpensive selective oxidation of methane remains a holy grail of catalysis. Current conversion methods rely on high temperatures and pressures, and are only economically feasible at large scale. But natural gas is produced in many locations at lower volumes, so alternative strategies to turn methane into methanol under milder conditions at smaller scale are needed. One promising approach involves copper-exchanged zeolites that catalyze methane oxidation using only water and oxygen at low temperatures, but the reaction mechanism has been elusive. To unravel the catalytic mechanism, researchers probed the copper-exchanged zeolite's active site using data collected at the APS. Their insights may lead to the development of improved zeolite catalysts, and a robust methane economy.

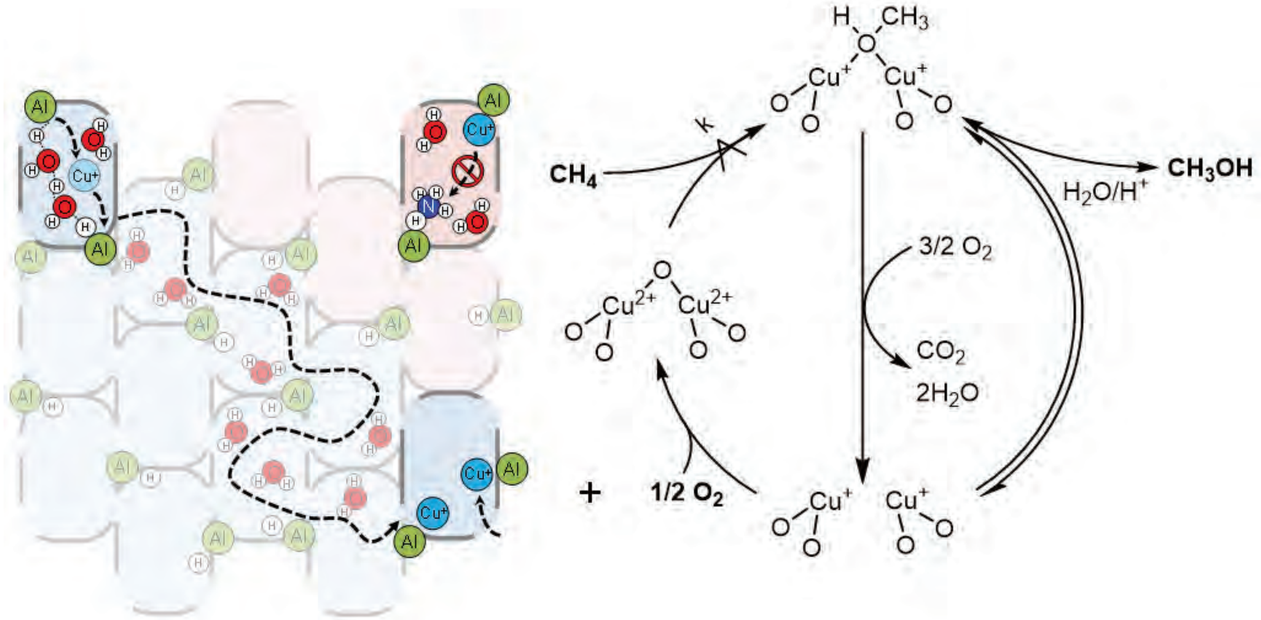

Fig. 1. Left: Depiction of high aluminum content and low copper loading zeolites enabling hydrated Cu ions to diffuse and generate a $[Cu\text{-}O\text{-}Cu]^{2+}$ during methane partial oxidation. Right: Hypothesized reaction mechanism for the conversion of methane to methanol.

Metalloenzymes with copper or iron centers effectively convert methane to methanol, but these biological molecules denature easily and are unstable at the high temperatures common in industrial settings. However, proteins aren't the only scaffolds that can harbor the catalytic metal active sites that oxidize methane. A common catalytic scaffold in industrial settings are zeolites, minerals composed mainly of aluminum and silicon that contain many tiny pores. Zeolites occur naturally, but large amounts are manmade and have numerous industrial applications. A zeolite's regular microporous structure allows the substance to act as a “molecular sieve,” selectively sorting molecules based primarily on size.

In recent work, researchers showed for the first time that they could oxidize methane to methanol in a continuous gas phase process using synthetic zeolites that housed copper ions inside their pores. These copper-exchanged zeolites required only methane, oxygen, and water to catalyze the reaction to methanol at 473 K. While the selectivity for methanol was good (>70% with undesirable carbon dioxide as the only byproduct), the researchers were only able to convert 0.001% of the methane to methanol, on par with step-wise processes over the same materials, leaving a lot of room for improvement.

To move toward optimizing the copper-exchanged zeolites for methane oxidation, the researchers in this study, from the Massachusetts Institute of Technology and ExxonMobil Research and Engineering, realized they needed more information, as the catalytic mechanism and active site were largely unknown. They delved into a series of experiments to unravel the kinetics and identify the active site for methane conversion in the copper-exchanged zeolites.

As a first step, the researchers synthesized a series of copper-exchanged zeolites containing varying amounts of copper and aluminum. They then measured the kinetics of the partial oxidation reaction for the different zeolites, and found that those catalysts with moderate copper loadings and high aluminum content offered the best route to well-dispersed active sites.

As a next step, the researchers headed to the APS to probe the active site with x-ray absorption near edge structure (XANES) spectroscopy and extended x-ray absorption fine structure (EXAFS) spectroscopy of the copper-exchanged zeolites during the partial oxidation reaction itself. These studies were carried out at the MR-CAT 10-BM-A,B bending magnet beamline, and the XSD 9-BM-B,C bending magnet beamline.

The XANES data indicated the oxidation state of Cu cycled between Cu(I) and Cu(II) as methane's C-H bond is activated, which is the reaction's rate-limiting step. This, taken together with the EXAFS data, revealed that the active site s likely a $[\text{Cu-O-Cu}]^{2+}$ motif. The formation of copper dimers is enhanced in zeolites with high aluminum content and low copper loadings (Fig. 1), offering researchers a pathway to the development of better methane to methanol catalysts. — Erika Gebel Berg

See: Kimberly T. Dinh[1], Mark M. Sullivan[1], Karthik Narsimhan[1], Pedro Serna[2], Randall J. Meyer[2], Mircea Dincặ[1], and Yuriy Román-Leshkov[1]*, "Continuous Partial Oxidation of Methane to Methanol Catalyzed by Diffusion-Paired Copper Dimers in Copper-Exchanged Zeolites," J. Am. Chem. Soc. **141**, 11641 (2019).

DOI: 10.1021/jacs.9b04906

Author affiliations: [1]Massachusetts Institute of Technology, [2]ExxonMobil Research and Engineering
Correspondence: * yroman@mit.edu

The authors gratefully acknowledge the financial support of ExxonMobil. K.D. acknowledges the partial support from the National Science Foundation Graduate Research Fellowship under Grant No. 1122374. MR-CAT operations are supported by the U.S. Department of Energy and the MR-CAT member institutions. This work made use of the MRSEC Shared Experimental Facilities at MIT, supported by the National Science Foundation under Award No. DMR-14-19807. This research used resources of the Advanced Photon Source, a U.S. DOE Office of Science User Facility operated for the DOE Office of Science by Argonne National Laboratory under Contract No. DE-AC02-06CH11357.

Zeolites from Z to Z

Zeolites are natural volcanic minerals with a number of unique characteristics. Zeolites were formed when volcanic ash was deposited in ancient alkaline lakes. The interaction of the volcanic ash with the salts in the lake water altered the ash into various zeolite materials.

In 1756, the Swedish mineralogist Axel Fredrick Cronstedt discovered that stilbite, a natural mineral, visibly lost water when heated, and he named the class of materials zeolites from the classical Greek words meaning "boiling stones." Zeolites were considered an obscure group of minerals with unique properties for almost 200 years, and Cronstedt was remembered primarily for discovering the element nickel.

Zeolites have an unusual crystalline structure and a unique ability to change ions. A very large number of small channels, called microporosity, present in its structure have typical diameters of 0.5 to 0.7 nm, only slightly larger than the diameter of a water molecule. Beside this there are a number of larger pores, the so-called mesoporosity. Positive ions are present in the channels, which can be exchanged for other ions. This substitution of ions enables zeolites to selectively adsorb certain harmful or unwanted elements from soil, water, and air. Zeolites also have strong affinity for certain harmful heavy metals such as lead, chromium, nickel, and zinc.

Considering all of these properties and abilities, zeolites' commercial and environmental possibilities seem to be limitless. One example is the application of zeolites in landfills and at industrial sites, which can help prevent the release of a number of harmful or unwanted elements into the environment.

Helix Formation Caught in Real Time

Adaptable biomaterials, whether natural or synthetic, respond to changes in environments such as temperature or pH (a measure of hydrogen ion concentration, acidity, or alkalinity) by altering their molecular conformation so that they function in a different way. An example might be a biomaterial designed to deliver a drug in response to a specified signal. By using time-resolved x-ray scattering at the APS to study structural changes on time scales from nanoseconds to microseconds, researchers have elucidated how a commonly used peptide switches from a loosely coiled structure to a tightly-wound helical form as pH falls. Understanding the mechanism and dynamics of such transformations can improve the design of other adaptive molecules.

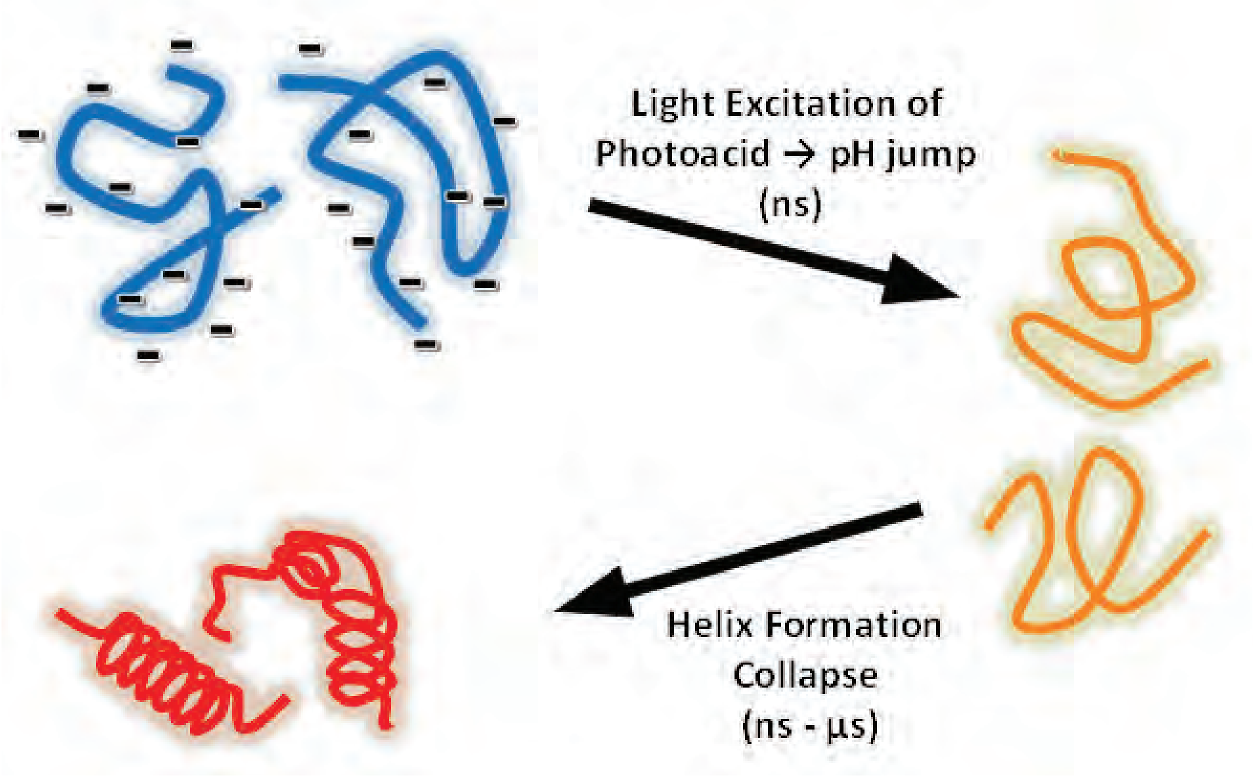

Fig. 1. In an acidic solution, –COO⁻ anions of glutamic acid side-chains repel each other, leading to an unfolded conformation (blue). Light excitation of a photoacid releases protons to turn the anions into neutral –COOH side-chains, causing the peptide chains to fold into intermediate conformations (orange) and eventually collapse into helical conformations (red).

In a low-pH solution, poly-L-glutamic acid (PGA) has the form of an alpha helix. As the solution becomes less acidic, at a pH of about 5, the helices unwind and the peptide turns into an extended coil. Scientists have used PGA to build adaptive biomaterials, including drug delivery systems and membranes with apertures that open and close. Earlier studies using infrared, optical, and ultraviolet spectroscopic techniques have shown that PGA's structure changes because in a more neutral environment, carboxyl side groups (–COOH) on the glutamic acid molecules that form the helices are deprotonated (that is, removal of hydrogen), becoming –COO⁻ anions. Those ions repel each other, pushing the components of the helices apart. Even when fully protonated, however, only some 30% to 50% of the glutamic acid residues in PGA adopt a helical form, with more loosely coiled structures in between.

Optical spectroscopy data are limited in the length scales they probe and do not provide direct structural information in terms of conformations. To gain better insight into how an effect that starts with interactions between adjacent peptide units develops into a wholesale transformation along the full length of the peptide chain, researchers from Northwestern University, the University of Chicago and Argonne employed time-resolved x-ray solution scattering (TRXSS) to follow those structural changes in real time, and on a wider range of length scales.

First, they performed x-ray scattering measurements at the DND-CAT 5-ID-D beamline at the APS to determine the static structure of PGA peptides of various lengths, from 20 to 200 glutamic acid residues, in aqueous solutions at various pH values. These studies added some detail to what was previously known. The degree of deprotonation at a given pH depends somewhat on the overall length of the peptide, and the distance between the repulsive $-COO^-$ side chains is greater for longer polymers. Also of note was the finding that although the degree of protonation changes continuously with pH, the structural transformation happens abruptly when about 40% of the glutamic acid residues are protonated.

Working at the BioCARS beamline 14-ID-B, also at the APS, the team performed TRXSS studies by sending a 200mer PGA solution through a flow cell. To the solution, which started at a pH of 6, they added *o*-nitrobenzaldehyde, a photoacid (a photoacid releases protons after being illuminated by light). Laser pulses with a wavelength of 300 nm triggered the photoacid to release protons, decreasing the pH of the solution by about half a pH unit. By sending x-ray pulses through the solution at chosen intervals after the laser pulses, ranging from 250 nsec up to 100 µsec, the researchers were able to track the structural transformation of the peptide as it happened. The scattering data revealed that PGA's structure began to change in the very shortest intervals after the pH decrease, but that full transformation to the more tightly wound helix form took as much as 10 µsec.

Detailed analysis of the TRXSS results found a good fit using a two-component model. When protonation occurs on the abrupt pH decrease, ionized side chains become neutral carboxyl groups, and the loss of repulsion causes extended stretches of PGA to transform into a less coherent intermediate structure (Fig. 1). But it takes longer for the glutamic acid residues to move closer together and form tightly wound alpha-helices. TRXSS studies of PGA with less than 200 residues showed the same process, except that it occurred somewhat faster.

The new study shows that time-resolved x-ray diagnostics are an effective complement to investigations using optical wavelengths, allowing the exploration of small- and intermediate-scale molecular structures on a range of timescales. These precise insights into molecular transformation will be of great value, the researchers say, in the rational design of new adaptive biomaterials.

– David Lindley

See: Dolev Rimmerman[1], Denis Leshchev[1], Darren J. Hsu[1], Jiyun Hong[1], Baxter Abraham[2], Robert Henning[3], Irina Kosheleva[3], and Lin X. Chen[1,4]*, "Revealing Fast Structural Dynamics in pH-Responsive Peptides with Time-Resolved X-ray Scattering," J. Phys. Chem. B **123**, 2016 (2019). DOI: 10.1021/acs.jpcb.9b00072

Author affiliations: [1]Northwestern University, [2]University of Delaware, [3]The University of Chicago, [4]Argonne National Laboratory
Correspondence: * l-chen@northwestern.edu, lchen@anl.gov

This work was supported by the National Institutes of Health, under Contract no. R01-GM115761. B.A. acknowledges support from the U.S. Department of Energy (DOE) Office of Science Graduate Student Research program, administered by the Oak Ridge Institute for Science and Education, managed by ORAU under contract number DE-SC0014664, as well as from the U.S. DOE Office of Science-Basic Energy Sciences, under award number DE-SC0016288. Use of BioCARS was supported by the National Institute of General Medical Sciences of the National Institutes of Health under grant number P41GM118217. Time-resolved setup at Sector 14 was funded in part through a collaboration with Philip Anfinrud (NIH/NIDDK). We would also like to acknowledge Guy Macha (BioCARS) for his assistance in designing the sample holder. DND-CAT is supported by Northwestern University, The Dow Chemical Company, and DuPont de Nemours, Inc. Data were collected using an instrument funded by the National Science Foundation under Award number 0960140. This research used resources of the Advanced Photon Source, a U.S. DOE Office of Science User Facility operated for the DOE Office of Science by Argonne National Laboratory under Contract no. DE-AC02-06CH11357.

Readying a SARS-CoV-2 Sample at GM/CA-XSD Beamline 23-ID

Steve Corcoran of GM/CA-XSD prepares an inert sample of SARS-CoV-2 for remote-control data collection to determine the structure of the protein at the GM/CA 23-ID beamline of the APS. In the photo, Corcoran, an Engineering Specialist, has just retrieved the inert sample from a dewar, where it was transported frozen at -320º F.

Life Science

Probing a Paradox in Pharmaceutical Formulation

Pharmaceuticals aren't much use if they can't get into the body in sufficient levels to perform their function. Some modern crystalline formulations have this problem, displaying relatively poor solubility, and thus decreased bioavailability. One strategy to overcome this difficulty is the use of amorphous solid dispersions (ASD), which combine an amorphous form of an active drug with a polymeric excipient at the molecular level, making it easier to deliver necessary medications at their proper therapeutic levels. But more isn't always better. As the drug loading (DL) of ASDs is increased, a phenomenon called amorphous-amorphous phase separation (AAPS) can set in, reducing or even halting active drug release. To better understand this problem, researchers studied the process of AAPS in a model ASD system through direct *in situ* visualization using x-ray fluorescence (XRF) imaging at the APS. Their results open the way to some promising opportunities for the development and design of a new and improved ASD system.

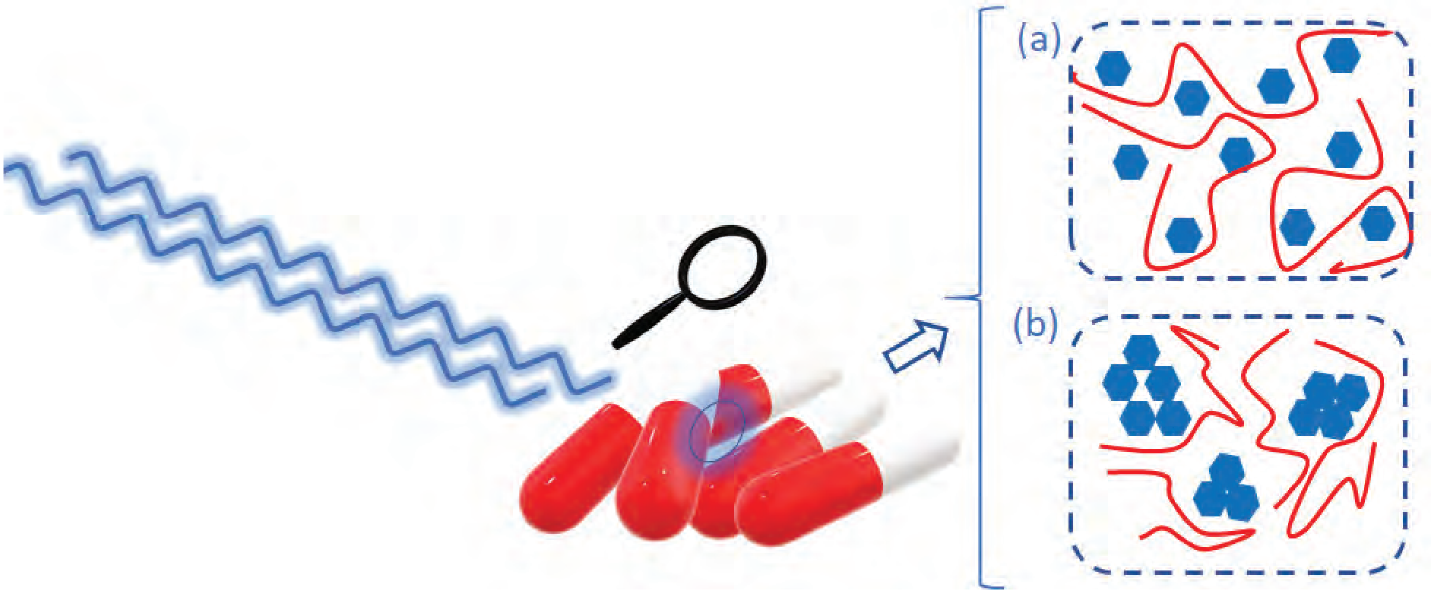

Fig. 1. The kinetics of phase separation of Ritonavir-PVPVA amorphous solid dispersion is readily accessible by synchrotron x-ray fluorescence imaging technique: (a) at a low drug loading, drug and polymer molecules are uniformly mixed (b) at high drug loadings, the phase separation is observed.

Because the antiretroviral medication Ritonavir (RTV), commonly used to treat HIV/AIDS and hepatitis C, is poorly water-soluble, it is generally administered in an ASD formulation trade-named NORVIR®. For this study, the investigators from AbbVie, Inc., chose an ASD system combining RTV and a PVPVA (polyvinylpyrrolidine vinyl acetate) polymer, using thin films with DLs of 20, 25, 30, and 50 wt%, sealed in a humidity chamber at 100% relative humidity. Working with a colleague from Argonne, the team excited the ASD samples with x-rays and the fluorescence signals were collected at the XSD 2-ID-E beamline of the APS, (Fig. 1). The APS was selected for this study because its high photon flux permits good visualization of fast dynamic phenomena such as AAPS.

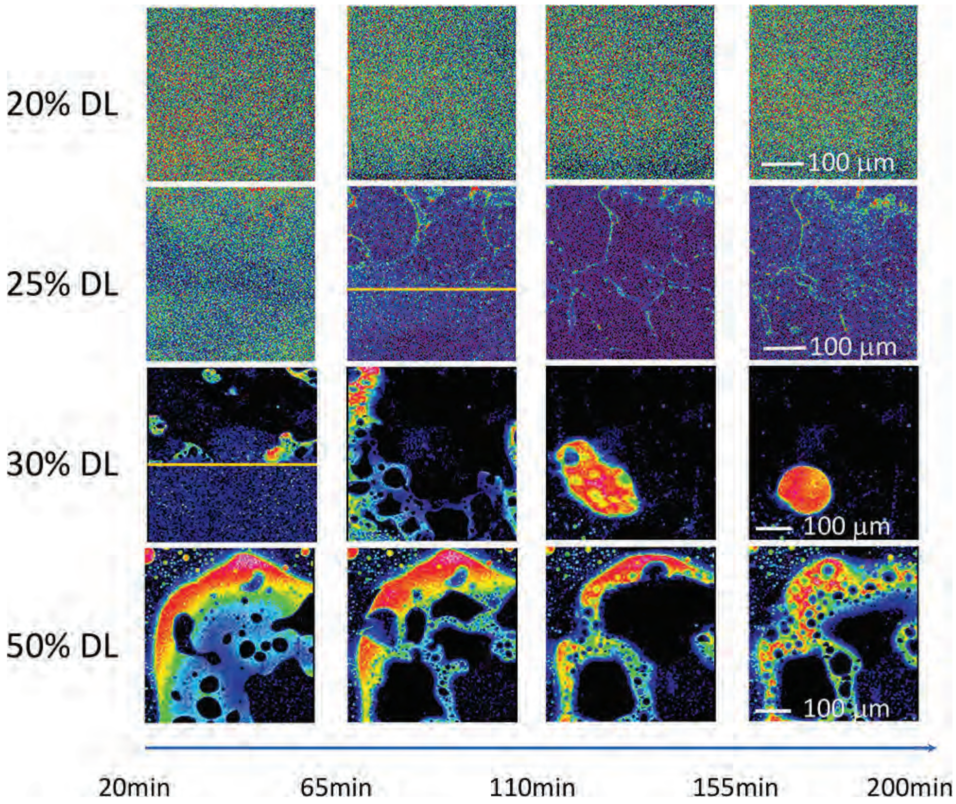

Fig. 2. Repeated fine scans of ASD films at 20%, 25%, 30%, and 50% DL in 100% relative humidity; the onsets of AAPS are marked with orange lines for 25% and 30% DL. All images with the same DL are displayed with the same color scale. The images are top views of the films. From C. Shi et al., Mol. Pharmaceut. **16**, 4751 (2019). Copyright © 2019 American Chemical Society

Each sample was first studied with a coarse scan of the entire film, after which a specific area was chosen for a finer-resolution scan. The intrinsic fluorescence signals from the RTV sulfur atoms were readily distinguishable from the sulfur-free PVPVA without any additional labeling (Fig. 2).

After approximately 10 min, AAPS was already seen occurring within the 50% DL films, at about 52 min in the 30% DL, and at 79 min in the 25% DL samples. The AAPS process evolves somewhat differently at the various DLs, with a less distinct separation between the RTV and PVPVA at 25% DL and only through part of the film thickness; whereas at 30% DL, clear separation is seen throughout the entire thickness of the film. Both the 20% DL and 25% DL sample films display 100% drug release, although this is somewhat delayed in the 25% DL film. The investigators hypothesize that because the AAPS is occurring only at the surface in the 25% DL film, drug release is still unaffected deeper inside the ASD. At 30% DL, however, the AAPS phenomenon penetrates deeper, reducing drug release to only about 50% at similar time scales. Later *ex situ* measurements of the behavior of the 20% DL sample showed that AAPS finally occurred about a week after exposure to 100% relative humidity conditions.

The results demonstrate strongly that higher levels of drug loading in ASDs actually impede rather than increase the efficiency of drug delivery, and thus its bioavailability, because of the onset of amorphous-amorphous phase separation affecting dissolution at those levels. While phase separation is too slow at DLs below about 20% to affect drug release in a meaningful way, it occurs much faster at higher DLs, changing the surface of a tablet to a layer of amorphous drug that prevents any further dissolution.

ASD formulations will remain an indispensable method for the effective delivery of new and essential drugs, making it important to find ways to increase their efficiency and effectiveness. By performing direct XRF visualization and thus a better understanding of the mechanics of the amorphous-amorphous phase separation in an ASD system, this *in situ* study opens up some promising opportunities for the development and design of new ASD systems. The upcoming APS Upgrade, which will provide orders of magnitude higher focus flux, will further enable the study of fast phase separation at higher drug loadings or the use of ASD thin films with reduced thickness. – Mark Wolverton

See: Chenyang Shi[1]*, Luxi Li[2]**, Geoff G. Z. Zhang[1], and Thomas B. Borchardt[1], "Direct Visualization of Drug–Polymer Phase Separation in Ritonavir–Copovidone Amorphous Solid Dispersions Using *in situ* Synchrotron X-ray Fluorescence Imaging of Thin Films," Mol. Pharmaceut. **16**, 4751 (2019).
DOI: 10.1021/acs.molpharmaceut.9b00651

Author affiliations: [1]AbbVie, Inc., [2]Argonne National Laboratory
Correspondence: * chenyang.shi@abbvie.com, ** luxili@anl.gov

C.S., T.B.B., and G.G.Z.Z. thank various individuals from Drug Product Development, Research and Development, at AbbVie, Inc., for their helpful insights and discussions. The authors wish to thank Dr. Zhonghou Cai (XSD) for the design of the humidity chamber for *in situ* XRF experiments and Mr. Evan Maxey (XSD) for the contribution to Scheme 1. This research used resources of the Advanced Photon Source, a U.S. Department of Energy (DOE) Office of Science User Facility operated for the DOE Office of Science by Argonne National Laboratory under Contract No. DE-AC02-06CH11357.

Cool Temperatures during Hibernation May Freeze Muscle Contraction to Save Energy

Striated muscle contraction is a highly regulated process that involves an orchestrated series of events within the muscle's contractile units, which are also known as sarcomeres. In a recent study, which involved collecting x-ray diffraction data at the APS, researchers studied the effect of low temperature on mammalian skeletal muscle contraction. They found that cooler temperatures reduce force generation by trapping filaments in the muscle sarcomeres in a refractory state that cannot undergo contraction and utilize adenosine triphosphate (ATP). This mechanism provides important insight into how hibernating animals may conserve energy while still allowing vital functions in the body to continue.

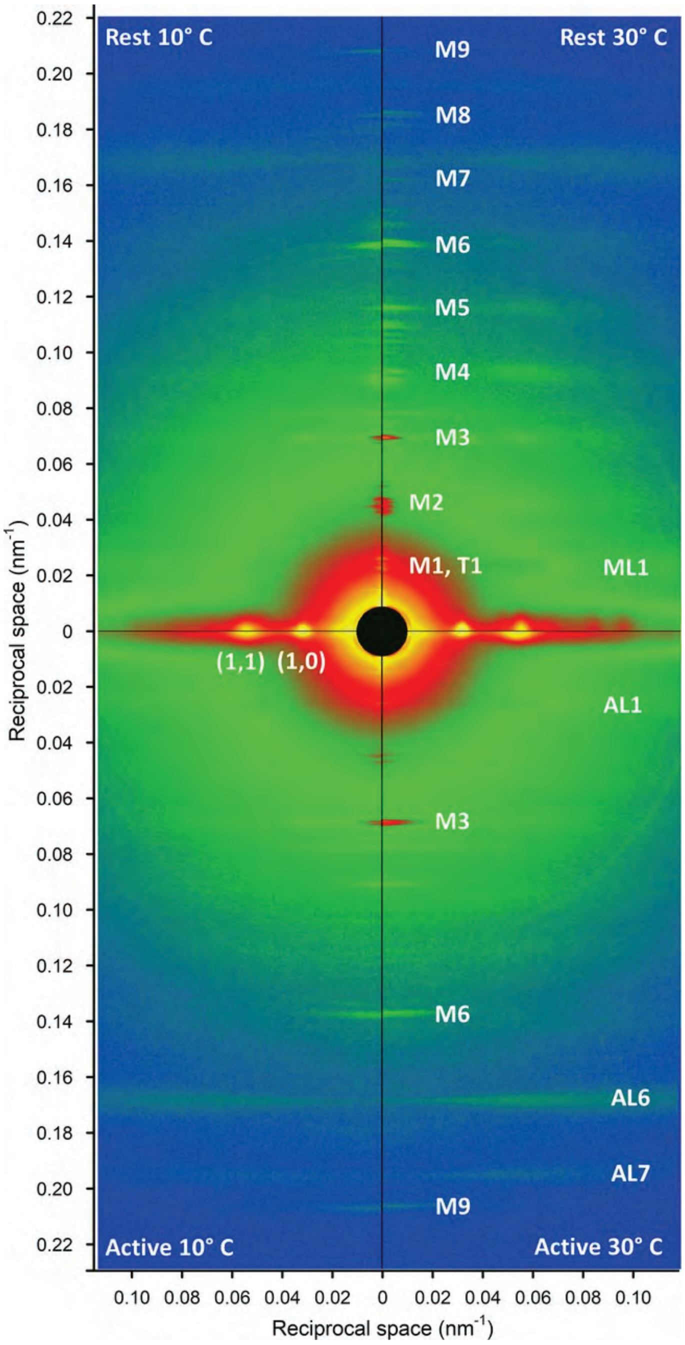

Muscle tissue's repeating functional units, the sarcomeres, impart a striated or striped appearance to the tissue when examined under a microscope. Sarcomeres contain thin (containing the protein actin) and thick (containing the protein myosin) filaments that power contraction of skeletal muscle and cardiac muscle, both of which are striated.

Contraction of striated muscle is triggered when calcium enters the muscle fibers. This leads to structural changes in proteins known as troponin and tropomyosin that reside in the thin filament. Ultimately, this allows actin and myosin to interact with each other in a way that allows hydrolysis of ATP, the source of energy for muscle contraction.

However, recent studies have shown that structural changes in the thick filament play an important regulatory role in contraction. Researchers have discovered that when striated muscle is in its relaxed state, myosin is trapped in helical tracks on the surface of the thick filament, thus preventing its interaction with actin and hydrolysis of ATP. Additional studies have also found that myosin protein in relaxed muscle is sensitive to temperature changes.

A multi-national, multi-institution group of researchers recently set out to investigate the structural changes that take place in the thick filament of mammalian skeletal muscle in response to temperature changes. They vertically mounted sections of mouse skeletal muscle on the x-ray path of the Bio-CAT 18-ID-D x-ray beamline at the APS. Then, they collected x-ray diffraction patterns (Fig. 1) from the muscle at different temperatures ranging from near-physiological at 35° C to 10° C.

Their results showed that lowering the temperature below the physiological level converts the thick filament from its ordered OFF state to a disordered one in which myosin is trapped in a refractory state that cannot bind actin or utilize ATP. Also, this effect is temperature-dependent. Progressive reductions in temperature lead to more myosins being disrupted on the surface of the thick filament. Indeed, only half as many thick filaments were left in the ordered OFF state at 10° C as were present at 35° C.

The drop from physiological temperature to 10° C also produced a 3-fold reduction in the amount of force generated by the mouse muscle. This refractory state of the thick filament may help explain the decreased power output of mammalian muscle at cooler temperatures, and this could have important implications for hibernating animals. When animals enter hibernation, their body temperature drops to near ambient level, and their energy-costly metabolic activities also decrease. Based on the results of this study, which show that ATP hydrolysis and energy output also drop substantially in resting muscle under cooler temperatures, the researchers suggest that this mechanism may contribute to helping animals conserve energy during hibernation. Because muscles comprise approximately 40% of mammalian body mass, having a regulatory mechanism like this at low temperatures can further reduce ATP consumption during hibernation, while still maintaining the body's vital functions. – Nicola Parry

< Fig. 1. Low-angle x-ray diffraction patterns from mouse extensor digitorum longus muscle. The left and the right quadrants are collected at 10° C and 30° C respectively, both at rest (upper quadrants) and at the plateau of the isometric tetanus (lower quadrants). The vertical (meridional) axis is parallel to the muscle axis. Each quadrant is obtained with 2 × 20-ms exposure windows with 3.5-m camera length. On the meridional axis are indicated the myosin-based (M) and troponin-based (T) reflections. On the horizontal (equatorial) axis are indicated the strong 1,0 and 1,1 reflections arising from the filament lattice. The myosin (ML) and actin (AL) layer lines that extend in the radial direction are due to the helical arrangement of the two proteins in the thick and thin filaments. From M. Caremani et al., "Low temperature traps myosin motors of mammalian muscle in a refractory state that prevents activation," J. Gen. Physiol. **151**(11), 1272 (2019). © 2019 Caremani et al.

See: Marco Caremani[1], Elisabetta Brunello[1‡], Marco Linari[1,2], Luca Fusi[3], Thomas C. Irving[4], David Gore[4], Gabriella Piazzesi[1], Malcolm Irving[3], Vincenzo Lombardi[1*], and Massimo Reconditi[1,2], "Low temperature traps myosin motors of mammalian muscle in a refractory state that prevents activation," J. Gen. Physiol. **151**(11), 1272 (2019). DOI: 10.1085/jgp.201912424

Author affiliations: [1]University of Florence, [2]Consorzio Nazionale Interuniversitario per le Scienze Fisiche della Materia, [3]King's College London, [4]Illinois Institute of Technology ‡Present address: King's College London
Correspondence: * vincenzo.lombardi@unifi.it

This project was supported by Fondo per gli Investimenti della Ricerca di Base (Futuro in Ricerca project RBFR08JAMZ; Italy), Consorzio Nazionale Interuniversitario per le Scienze Fisiche della Materia (Progetto d'Innesco della Ricerca Esplorativa 2007; Italy), and Ente Cassa di Risparmio di Firenze (2012.0611; Italy); Medical Research Council (MR/M026655/1; U.K.); and the National Institute of General Medical Sciences of the National Institutes of Health grant P41 GM103622 to Bio-CAT. This research used resources of the Advanced Photon Source, an Office of Science User Facility operated for the U.S. Department of Energy (DOE) Office of Science by Argonne National Laboratory under contract no. DE-AC02-06CH11357, and the Canadian Light Source and its funding partners.

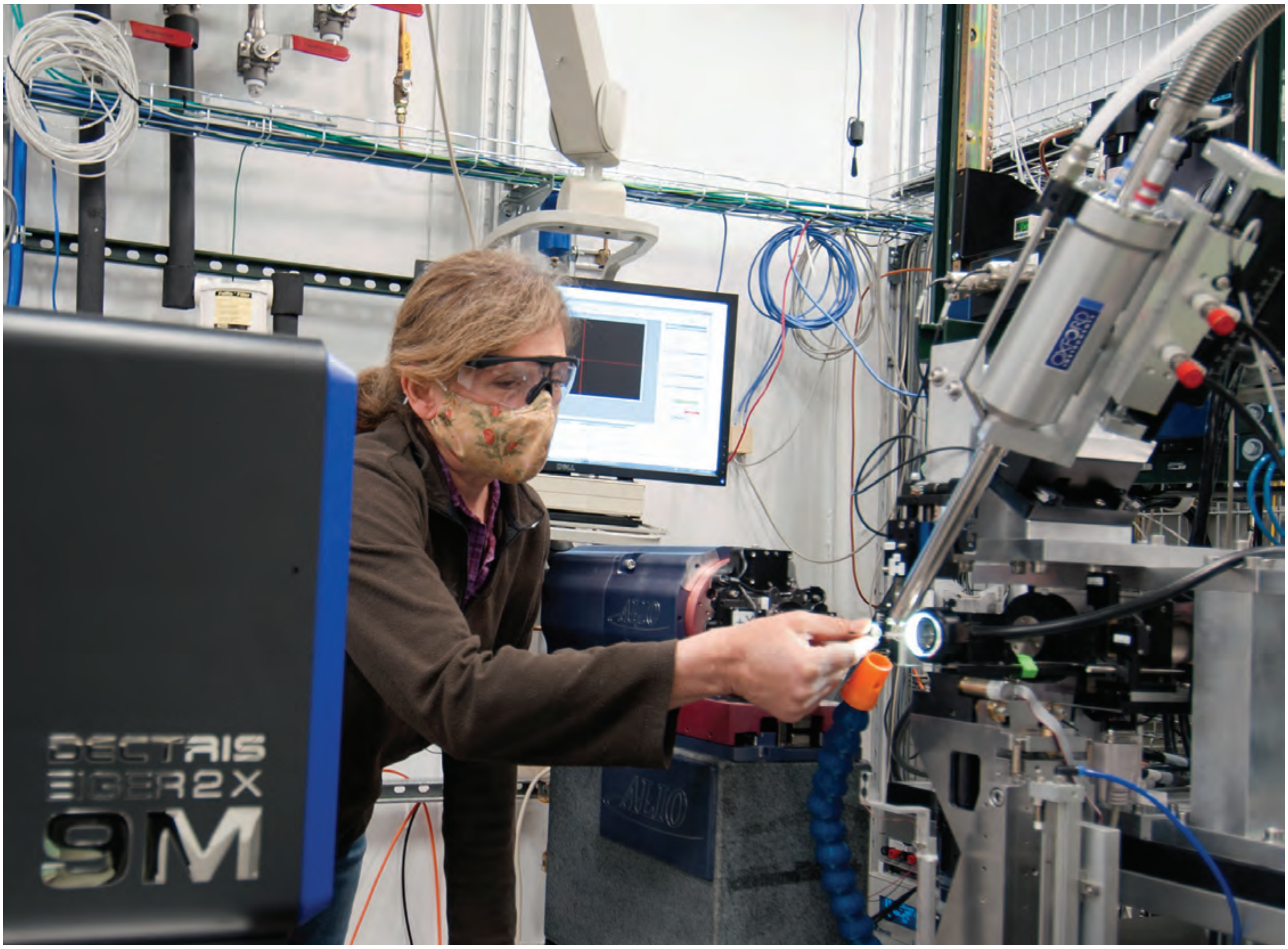

Collecting SARS-CoV-2 Structures at the IMCA-CAT Beamline 17-ID

Anne Mulichak, scientist at IMCA-CAT aligns the beamline prior to collecting data on a COVID-19 project for an IMCA member pharmaceutical company. The x-ray diffraction data measured at APS beamline 17-ID are used to determine the atomic structure of protein-ligand complexes and are a critical component of pharmaceutical drug design programs. IMCA-CAT specializes in providing high-quality, high-throughput data while maintaining the security of proprietary research.

Structural Biology

3-D Structure of SARS-CoV-2 Explains High Infectivity vs. Other Coronaviruses

As we all know too well, a novel severe acute respiratory syndrome-like coronavirus (SARS-CoV-2) emerged and rapidly spread among humans. A key to tackling this pandemic is to learn how the virus attaches to receptors on human cells. This mechanism would likely explain the levels of SARS-CoV-2 infectivity, how it jumped to humans from an animal host, and host range. SARS-CoV-2 and its close coronavirus relative, SARS-CoV, recognize the same receptor in humans called angiotensin-converting enzyme 2 (hACE-2). Researchers using the APS have determined the crystal structure of the receptor-binding domain (RBD) of the spike protein of SARS-CoV-2 — engineered to facilitate crystallization — in complex with ACE2. In comparison with the SARS-CoV RBD, an ACE2-binding site in SARS-CoV-2 RBD has a more compact, stable conformation. These structural features of SARS-CoV-2 RBD increase the likelihood of the coronavirus binding to hACE-2. Additionally, the researchers show that RaTG13, a bat coronavirus that is closely related to SARS-CoV-2, also uses hACE-2 as its receptor. The differences among SARS-CoV-2, SARS-CoV and RaTG13 in hACE-2 recognition shed light on the potential animal-to-human transmission of SARS-CoV-2. This study provides guidance for intervention strategies that target receptor recognition by SARS-CoV-2.

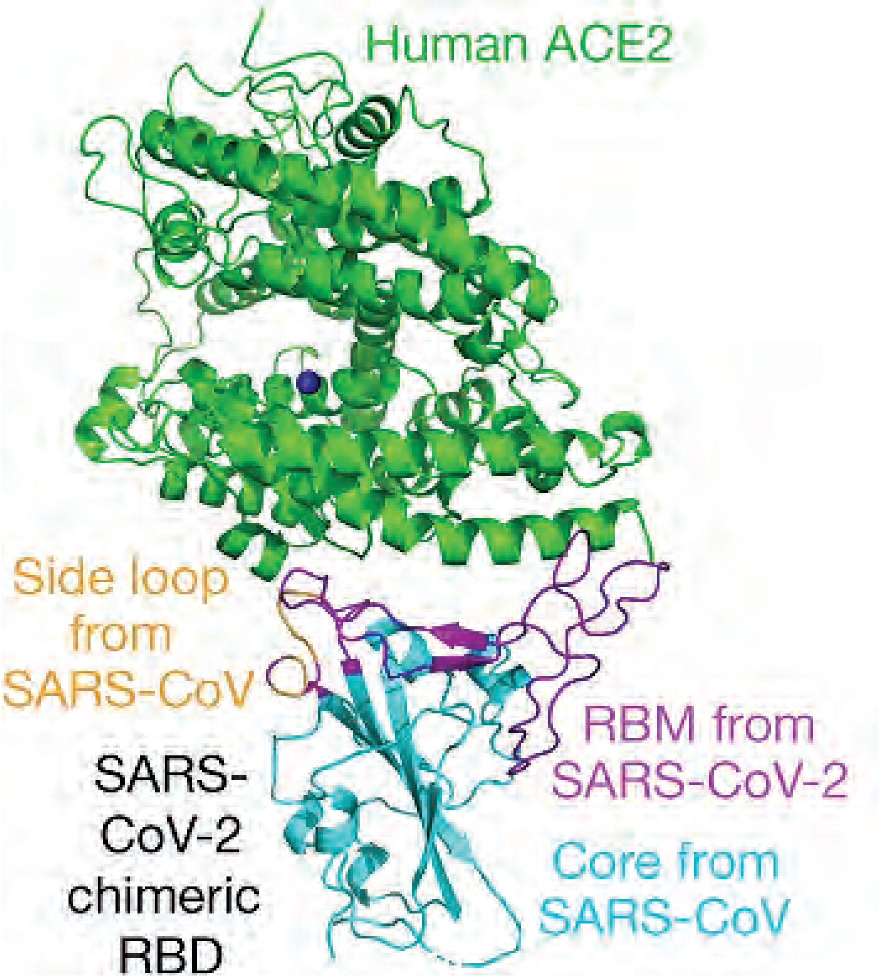

Fig. 1. Crystal structure of the engineered SARS-CoV-2 RBD in complex with hACE-2. hACE-2 is shown in green. The RBD core is shown in cyan. The receptor binding motif (RBM), which mediates contacts with hACE-2 is shown in magenta. A zinc ion in hACE-2 is shown in blue. From J. Shang et al., Nature **581**, 221 (14 May 2020). © 2020 Springer Nature Limited

The recent emergence of SARS-CoV-2 in China has caused hundreds of thousands of deaths and overwhelmed health care systems around the globe. Following other notable recent coronavirus outbreaks, including SARS-CoV in 2002 and MERS-CoV in 2012, SARS-CoV-2 is the seventh coronavirus known to cause human disease.

Coronaviruses are a group of large, enveloped viruses with single-stranded RNA genomes. All coronaviruses share a similar means of infection: When the virus encounters a human cell, spike-shaped proteins on its surface attach to cell receptors called hACE-2, if the cell possesses them, allowing the virus to gain entry to the cell and begin replicating.

In some important ways, SARS-CoV-2 behaves very differently from other coronaviruses, including its close relative SARS-CoV, which was responsible for approximately 8000 infections and 775 deaths. While both SARS-CoV and SARS-CoV-2 replicate in the lungs, SARS-CoV-2 also efficiently infects the throat and the nose. However, because levels of hACE-2 are thought to be lower in the throat and nose, there has been a question about whether SARS-CoV-2 does a better job of clinging onto hACE-2.

To answer this question, researchers from the University of Minnesota used x-ray crystallography data obtained at the NE-CAT beamline 24-ID-E at the APS to create the first atomic-scale three-dimensional (3-D) map of the receptor binding domain (RBD) on the spike protein of a SARS-CoV-2 in complex with hACE-2 [1]. To facilitate crystallization, the researchers designed a chimeric RBD that uses the core from the SARS-CoV RBD as the crystallization scaffold and the RBM from SARS-CoV-2 as the functionally relevant unit. They then compared the crystal structure with those of other coronaviruses, primarily SARS-CoV. (No live viruses are studied at the APS.)

The 3-D structure of SARS-CoV-2 (Fig. 1) shows that the club-like spike proteins it uses to establish infections are more compact and have the potential to latch onto the hACE-2 receptor about four times more strongly than the spike proteins on SARS-CoV. In addition, several residue changes in the SARS-CoV-2 RBD stabilize two virus-binding hotspots at the RBD–hACE-2 interface. This results in the SARS-CoV-2 RBD having a tighter and more stable binding affinity for the human cells.

In theory, this finding would suggest that SARS-CoV-2 should infect humans more easily than SARS-CoV, which it does. Yet, a more recent publication from the researchers used a biochemical technique called a protein pull-down assay to show that although SARS-CoV-2 RBD has a higher hACE2-binding affinity than SARS-CoV RBD, the hACE2 binding affinity of the entire SARS-CoV-2 spike is comparable to or lower than that of SARS-CoV spike. The researchers hypothesize that the reason for this is likely due to the SARS-CoV-2 RBD being less accessible than that of SARS-CoV.

Binding affinity, however, is not the sole determinant of infectivity success. The researchers' new paper also demonstrates that SARS-CoV-2 does a better job of evading the human immune system. It's likely this aspect of the virus that ultimately determines its ability to infect more humans than SARS-CoV.

The researchers went on to compare the structure of SARS-CoV-2 with related strains found in bats and pangolins. They found that both animal strains could bind to the same hACE-2 receptor. This evidence supports previous work suggesting the human coronavirus came from bats either directly, or via pangolins acting as an intermediate host. To infect humans, however, the bat or pangolin coronavirus would have needed to undergo mutations to better attach to the human receptor.

The knowledge gained through the biochemical assays and the creation of 3-D crystal structures of SARS-CoV-2 not only provides a better understanding of the mechanisms involved in the infectivity of the virus, but also sheds light on its animal origin and offers guidance on vaccine and antiviral drug designs. – Chris Palmer

See:

[1] Jian Shang, Gang Ye, Ke Shi, Yushun Wan, Chuming Luo, Hideki Aihara, Qibin Geng, Ashley Auerbach, and Fang Li, "Structural basis of receptor recognition by SARS-CoV-2," Nature **581**, 221 (14 May 2020). DOI: 10.1038/s41586-020-2179-y

Author affiliation: University of Minnesota
Correspondence: * lifang@umn.edu

This work was supported by National Institutes of Health (NIH) grants R01AI089728 and R01AI110700 (to F.L.) and R35GM118047 (to H.A.). We thank staff at the Northeastern Collaborative Access Team for assistance in data collection. The Northeastern Collaborative Access Team beamlines are funded by the National Institute of General Medical Sciences from the National Institutes of Health (P30 GM124165). The Eiger 16M detector on the 24-ID-E beamline is funded by a NIH-ORIP HEI grant (S10OD021527). This research used resources of the Advanced Photon Source, a U.S. Department of Energy (DOE) Office of Science User Facility operated for the DOE Office of Science by Argonne National Laboratory under Contract No. DE-AC02-06CH11357.

[2] Jian Shang, Yushun Wan, Chuming Luo, Gang Ye, Qibin Geng, Ashley Auerbach, and Fang Li*, "Cell entry mechanisms of SARS-CoV-2," Proc. Natl. Acad. Sci. U.S.A. **117**(21), 11727 (May 26, 2020). DOI: 10.1073/pnas.2003138117

Author affiliation: University of Minnesota
Correspondence: * lifang@umn.edu

This work was supported by National Institutes of Health Grants R01AI089728 and R01AI110700 (to F.L.).

Clues to COVID-19 Coronavirus's Vulnerability

An antibody recovered from a survivor of the severe acute respiratory syndrome (SARS) epidemic in the early 2000s has revealed a potential vulnerability of the new coronavirus at the root of COVID-19, according to a study from scientists at Scripps Research. The study, based upon research carried out at the APS, was the first to map a human antibody's interaction with the new coronavirus at near-atomic-scale resolution. Although the antibody was produced in response to an infection of SARS, which is caused by the SARS-CoV virus, it cross-reacts with the new coronavirus, SARS-CoV-2.

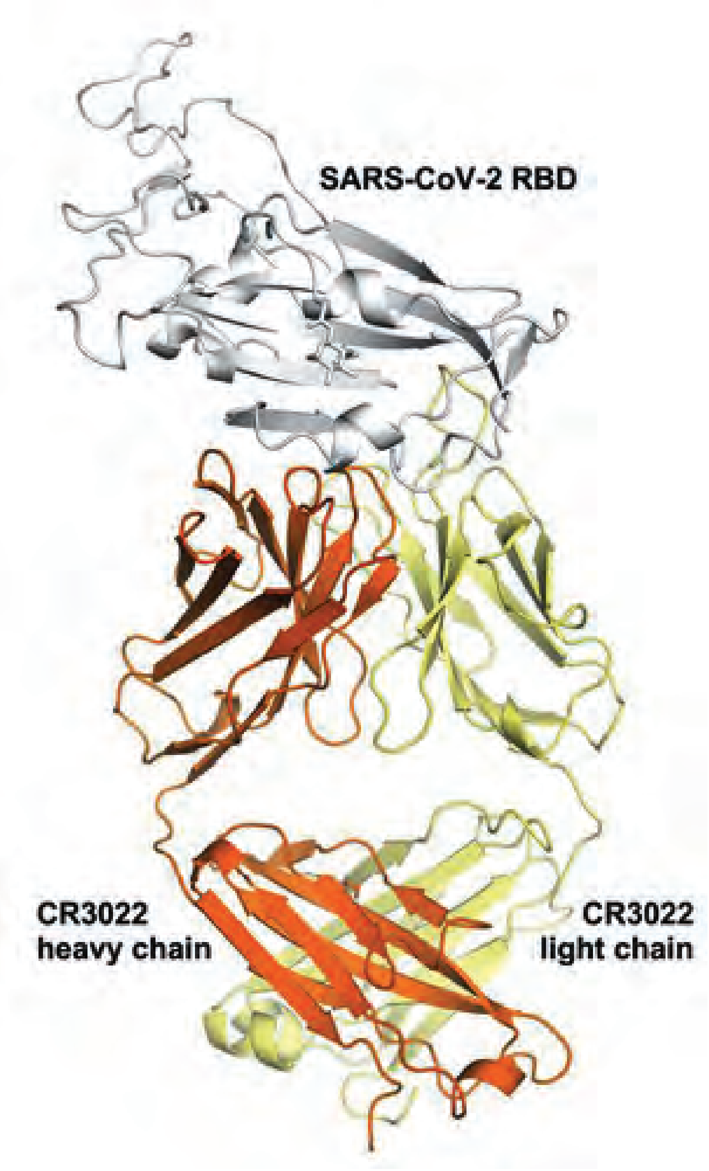

Fig. 1. Crystal structure of CR3022 in complex with SARS-CoV-2 RBD obtained at the General Medical Sciences and National Cancer Institute structural biology facility at the APS. From M. Yuan et al., Science **368**, 630 (8 May 2020). © 2020 American Association for the Advancement of Science. All rights Reserved.

The structural mapping revealed a nearly identical site on both coronaviruses to which the antibody binds, suggesting a functionally important and vulnerable site for this family of coronaviruses. “The knowledge of conserved sites like this can aid in structure-based design of vaccines and therapeutics against SARS-CoV-2, and these would also protect against other coronaviruses—including those that may emerge in the future,” said the study’s senior author Ian Wilson, Hansen Professor of Structural Biology and Chair of the Department of Integrative Structural and Computational Biology at Scripps Research.

SARS-CoV, which causes SARS, originated in horseshoe bats, but jumped to humans in South China in 2002, eventually infecting more than 8,000 people and killing almost 800 before it was quelled by lockdowns, quarantines and other measures. SARS-CoV-2, a closely related coronavirus that causes COVID-19, first emerged in the Chinese city of Wuhan in late 2019. Much more infectious than its viral cousin, it has led to a pandemic, causing far more cases of illness and fatalities than SARS. The development of a vaccine or even an effective treatment could significantly ameliorate the crisis.

“Our ultimate goal here is to obtain structural information on antibodies and their binding sites, and use that to guide SARS-CoV-2 vaccine design, just as our lab has done with influenza and HIV,” said the study’s co-first author Nicholas Wu, a postdoctoral research associate in the Wilson lab.

The new study centers on an anti-SARS-CoV antibody called CR3022 that was originally isolated in 2006 by the pharmaceutical company Crucell Holland B.V. in the Netherlands. A report from Chinese scientists earlier in 2020 indicated that CR3022 cross-reacts against SARS-CoV-2. Wilson’s team used their structural mapping expertise to determine how the antibody binds to SARS-CoV-2. The mapping was made possible by diffraction data from the CR3022 antibody in complex with the SARS-CoV-2 RBD (Fig. 1) collected at the GM/CA-XSD beamline 23-ID-D at the APS.

A key finding is that the antibody’s binding site is highly similar between the two coronaviruses—differing by just four protein building blocks called amino-acids. That high degree of similarity implies that the site has an important function that would be lost if it mutated significantly.

Yet, the site’s function remains mysterious. The Scripps Research analysis found that the antibody binding site is relatively remote from the part of the virus that grabs hold of cell-surface protein receptors in preparation for penetrating cells in our lungs. That suggests that, at least for SARS-CoV, CR3022 neutralizes the virus’s ability to infect cells in some indirect way. Adding to the mystery is the finding that the antibody binding site on these viruses is not normally accessible to antibodies.

“We found that this region is usually hidden inside the virus, and only exposed when that part of the virus changes its structure, as it would in natural infection,” says co-first author Meng Yuan, also a research associate in the Wilson lab.

Despite the slightness of difference between the two coronaviruses, the antibody binds much less tightly to SARS-CoV-2 than it does to the SARS virus, and cannot neutralize SARS-CoV-2 in lab dish tests as it does SARS-CoV. Still, the findings suggest that the binding site for this antibody on SARS-CoV-2 is a site of vulnerability, and that antibodies binding it more tightly would plausibly succeed in neutralizing the virus. Such neutralizing antibodies, if developed into therapies, could be used to treat COVID-19 patients and to provide temporary protection from the virus to uninfected individuals, for example healthcare workers.

The fact that this binding site is highly conserved between SARS-CoV and SARS-CoV-2 also hints that there may be antibodies, still to be discovered, that can effectively neutralize both viruses—and perhaps in the same way, can neutralize future emergent coronaviruses before they can cause pandemics.

See: Meng Yuan[1], Nicholas C. Wu[1], Xueyong Zhu[1], Chang-Chun D. Lee[1], Ray T. Y. So[2], Huibin Lv[2], Chris K. P. Mok[2]*, Ian A. Wilson[1]**, “A highly conserved cryptic epitope in the receptor binding domains of SARS-CoV-2 and SARS-CoV,” Science 368, 630 (8 May 2020). DOI: 10.1126/science.abb7269

Author affiliations: [1]The Scripps Research Institute, [2]The University of Hong Kong
Correspondence: * ch02mkp@hku.hk, ** wilson@scripps.edu

This work was supported by National Institutes of Health grant K99 AI139445 (N.C.W.); a Calmette and Yersin scholarship from the Pasteur International Network Association (H.L.); Bill and Melinda Gates Foundation grant OPP1170236 (I.A.W.); Guangzhou Medical University High-level University Innovation Team Training Program (Guangzhou Medical University released [2017] no. 159) (C.K.P.M.); and National Natural Science Foundation of China (NSFC)/Research Grants Council (RGC) Joint Research Scheme (N_HKU737/18) (C.K.P.M.). GM/CA-XSD has been funded by federal funds from the National Cancer Institute (ACB-12002) and the National Institute of General Medical Sciences (AGM-12006). This research used resources of the Advanced Photon Source, a U.S. Department of Energy (DOE) Office of Science User Facility operated for the DOE Office of Science by Argonne National Laboratory under contract no. DE-AC02-06CH11357.

This article is based upon a Scripps Research Institute news story published on April 3, 2020 (https://bit.ly/2Vh2b5I) It subsequently was featured as an APS/User News item (https://bit.ly/2Za6GjF). @ 2020 The Scripps Research Institute. All Rights Reserved)

A Coronavirus Protein Reveals a Drug Target

A potential drug target has been identified in a newly mapped protein of SARS-CoV-2, the virus that causes coronavirus disease 2019 (COVID-19). The structure was solved by a team including researchers from the University of Chicago, Argonne, the Northwestern University Feinberg School of Medicine, and the University of California, Riverside School of Medicine.

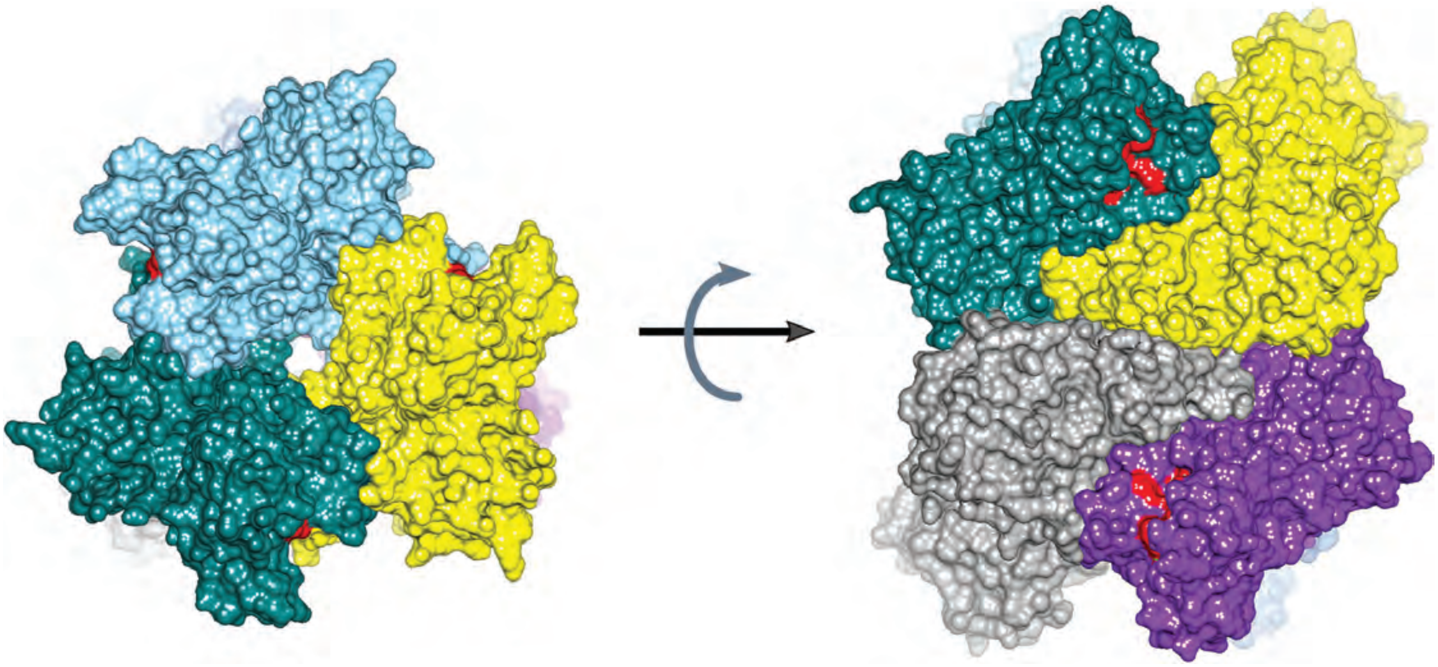

Fig. 1. Structure of SARS-CoV-2 NSP15 hexamer in surface representation with each subunit shown in different color. The active site residues are colored red. From Y. Kim et al., Prot. Sci. **1** (2020). Copyright © 1999-2020 John Wiley & Sons, Inc. All rights reserved

The protein Nsp15 from Severe Acute Respiratory Syndrome Coronavirus 2 (SARS-CoV-2) is 89% identical to the protein from the 2003 outbreak of SARS-CoV. Studies published in 2010 on SARS-CoV revealed that inhibition of Nsp15 can slow viral replication. This suggests drugs designed to target Nsp15 could be developed as effective drugs against COVID-19.

The structure of Nsp15 (Fig . 1), determined at the SBC-XSD beamline 19-ID, was released to the scientific community on March 4 in the RSCB Protein Data Bank (www.rcsb.org.) This new structure was solved by the group of Andrzej Joachimiak, Distinguished Fellow of Argonne, professor at The University of Chicago , and director of SBC-XSD at the APS in conjunction with the Center for Structural Genomics of Infectious Diseases.

Karla Satchell, principal investigator for the Center for Structural Genomics of Infectious Diseases and professor of microbiology-immunology at Northwestern, leads the team of scientists investigating the structure of the SARS-CoV-2 virus to understand how to stop it from replicating.

The initial genome analysis and design of constructs for protein synthesis were performed by the bioinformatics group of Adam Godzik, a professor of biomedical sciences in the University of California, Riverside. "The newly mapped protein, called Nsp15, is conserved among coronaviruses and is essential in their life cycle and virulence. Initially, Nsp15 was thought to directly participate in viral replication, but more recently, it was proposed to help the virus replicate possibly by interfering with the host's immune response," said Joachimiak.

Mapping a 3-D protein structure of the virus allows scientists to work on how to interfere in the pathogen's replication in human cells. Satchell said, "The NSP15 protein has been investigated in SARS as a novel target for new drug development, but that never went very far because the [2003] SARS epidemic went away, and all new drug development ended. Some inhibitors were identified but never developed into drugs. The inhibitors that were developed for SARS now could be tested against {the similar SARS-CoV-2 NSP15] protein." Rapid upsurge and proliferation of SARS-CoV-2 raised questions about how this virus became so much more transmissible as compared to the SARS and Middle East respiratory syndrome coronaviruses. The scientists map the proteins of these two viruses to address this issue.

"While the SARS-CoV-2 is very similar to the SARS virus that caused epidemics in 2003, new [SARS-CoV-2] structures shed light on the small, but potentially important differences between the two viruses that contribute to the different patterns in the spread and severity of the diseases they cause," Godzik said.

Satchell, Joachimiak, and Godzik — along with the entire center team — will map the structure of some of the 28 proteins in the SARS-CoV-2 virus in order to see where drugs can throw a chemical monkey wrench into its machinery.

The first step is to clone and express the genes of the virus proteins and grow them as protein crystals in miniature ice cube-like trays.

Viewing these proteins down to the arrangement of their atoms requires an intense x-ray beam. Thus, once the crystals are grown, the center scientists image them using the APS' extremely bright light source in a process called x-ray crystallography.

See: Youngchang Kim[1,2], Robert Jedrzejczak[1,2], Natalia I. Maltseva[1,2], Mateusz Wilamowski[1], Michael Endres[2], Adam Godzik[3], Karolina Michalska[1,2], and Andrzej Joachimiak[1,2]*, "Crystal structure of Nsp15 endoribonuclease NendoU from SARS-CoV-2," Prot. Sci. **1** (2020). DOI: 10.1002/pro.3873
Author affiliations: [1]The University of Chicago, [2]Argonne National Laboratory, [3]University of California Riverside
Correspondence: * andrzejj@anl.gov

Funding for this project was provided in part by federal funds from the National Institute of Allergy and Infectious Diseases, National Institutes of Health, Department of Health and Human Services, under Contract HHSN272201700060C. SBC-XSD is operated by UChicago Argonne, LLC, for the U.S. Department of Energy (DOE) Office of Biological and Environmental Research under contract DE-AC02-06CH11357. This research used resources of the Advanced Photon Source, a U.S. DOE Office of Science User Facility operated for the DOE Office of Science by Argonne National Laboratory under Contract No. DE-AC02-06CH11357.

This article is based upon a Northwestern University press release by Marla Paul published on March 9, 2020. The original press release can be read at https://bit.ly/38dOwS5. It subsequently was featured as an APS science highlight: https://bit.ly/3hD6KB8 (© 2020 Northwestern University)

Revealing a MERS-CoV Vulnerability

Middle East respiratory syndrome coronavirus (MERS-CoV) is one of five β-coronaviruses in the family *Coronaviridae* found to infect humans. In 2012, it emerged as a highly fatal cause of severe acute respiratory infection. Although no anti-MERS-CoV therapy is available yet, potently neutralizing antibodies targeting the receptor-binding domain (RBD) on the MERS-CoV spike glycoprotein have been characterized, but much less is known about antibodies targeting non-RBD epitopes. Researchers have now derived the molecular structure and functional characterization of G2, a neutralizing antibody targeting the N-terminal domain (S1-NTD) of the S1 subunit of the MERS-CoV spike glycoprotein. Crystal structures of G2 alone and in complex with the MERS-CoV S1-NTD obtained at the APS, along with biochemical, biophysical, and cell-based assays reveal a site of vulnerability on the MERS-CoV spike glycoprotein and point to a neutralization mechanism whereby G2 inhibits the attachment of DPP4 to the spike protein. These results increase the understanding of the viral attachment mechanism and may facilitate the development of S1-NTD-based vaccines against MERS-CoV.

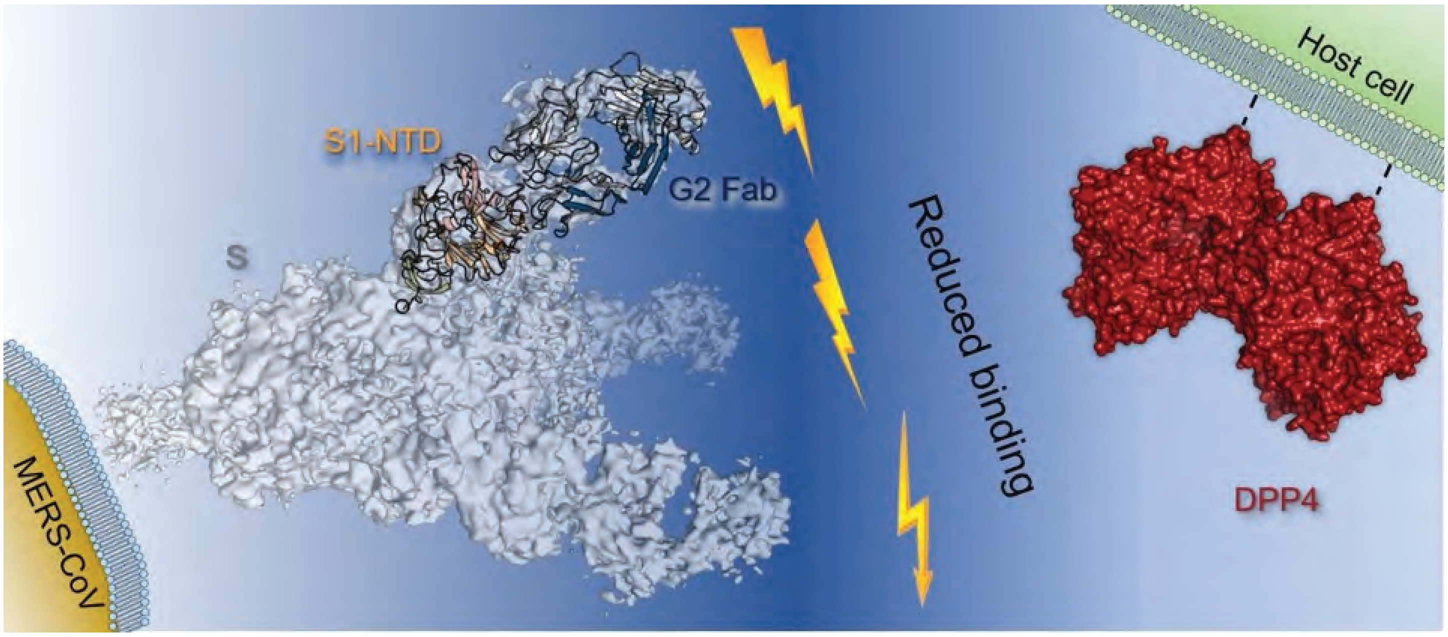

Fig. 1. Binding of the antibody G2 (black ribbon structure) to the N-terminal domain (S1-NTD) of the S1 subunit (pink ribbon structure) of the spike glycoprotein (grey) protruding form MERS-CoV (gold) prevents the attachment of S1 to the dipeptidyl peptidase-4 (DPP4) receptor (red) on the host cell (green).

MERS-CoV was first identified in Saudi Arabia in June 2012. Infection by this pathogen causes an acute respiratory disease designated as MERS, with symptoms that are very similar to those of SARS. Globally, MERS-CoV infections have been confirmed in dozens of countries causing more than 800 deaths over the years, with most cases coming from the Middle East.

MERS-CoV likely originated from bats, with camels functioning as a secondary or intermediate host. However, many infected patients without bat or camel exposure demonstrate that large-scale human-to-human transmissions can occur through close contacts. Due to its potential for mutating toward efficient human-to-human transmission and causing a pandemic, MERS-CoV was listed as a Category C Priority Pathogen by the U.S. National Institute of Allergy and Infectious Diseases. The high case fatality rate, vaguely defined epidemiology, and absence of prophylactic or therapeutic measures against this novel virus raise the persistent concern about a possible pandemic and create an urgent need for an effective vaccine.

Past efforts to develop coronavirus vaccines have used whole-inactivated virus, live-attenuated virus, recombinant protein subunit or genetic approaches. The primary target for neutralizing antibodies is the Spike (S) glycoprotein, cleaved into two subunits: S1, which is distal to the virus membrane and S2, which contains both a transmembrane domain and two heptad-repeat sequences typical of class I fusion glycoproteins. The S1 subunit has been the focus of most immunization strategies against MERS-CoV, as it contains the receptor-binding domain (RBD) that mediates virus attachment to its receptor, dipeptidyl peptidase-4 (DPP4), on the membrane of host cells.

Several neutralizing antibodies targeting MERS-CoV S1-NTD have been reported, including human antibody CDC2-A2, murine antibodies G2 and 5F9, and macaque antibodies FIB-H1 and JC57-13. Of these antibodies, G2 is the most potent, with broad neutralization potential against an array of MERS-CoV strains. Additionally, G2 and other NTD-specific MERS-CoV antibodies have been shown to confer protection against lethal challenge in animal models. However, the lack of structural information for G2 has hindered the definition of its epitope and determination of its mechanism of action.

To better understand G2, researchers at the University of Texas at Austin, the Vaccine Research Center at the National Institute of Allergy and Infectious Diseases, the Scripps Research Institute, and Vanderbilt University School of Medicine, derived the crystal structures of G2 Fab alone and bound to the MERS-CoV S1-NTD. Diffraction data were collected at the SBC-XSD beamline 19-ID at the APS. The crystal structures define a site of vulnerability comprising two loops, each of which contain a residue mutated in G2-escape variants. Cell-surface binding studies and in vitro competition experiments demonstrate that G2 strongly disrupts the attachment of the MERS-CoV spike glycoprotein to its host receptor, dipeptidyl peptidase-4 (DPP4), with the inhibition requiring the native trimeric spike protein conformation (Fig. 1).

This study advances the understanding of antibody-mediated neutralization of coronaviruses and may inspire structure-based vaccine design to thwart MERS-CoV.

– Chris Palmer

See: Nianshuang Wang[1], Osnat Rosen[2‡], Lingshu Wang[2], Hannah L. Turner[3], Laura J. Stevens[4], Kizzmekia S. Corbett[2], Charles A. Bowman[3], Jesper Pallesen[3], Wei Shi[2], Yi Zhang[2], Kwanyee Leung[2], Robert N. Kirchdoerfer[3], Michelle M. Becker[4], Mark R. Denison[4], James D. Chappell[4], Andrew B. Ward[3], Barney S. Graham[2], and Jason S. McLellan[1*], "Structural Definition of a Neutralization-Sensitive Epitope on the MERS-CoV S1-NTD," Cell Rep. **28**, 3395 (September 24, 2019).
DOI: 10.1016/j.celrep.2019.08.052

Author affiliations: [1]The University of Texas at Austin, [2]National Institute of Allergy and Infectious Diseases, [3]Scripps Research Institute, [4]Vanderbilt University School of Medicine, ‡Present address: Israel Institute for Biological Research
Correspondence: * jmclellan@austin.utexas.edu

This work was supported by National Institutes of Health (NIH) grant R01AI127521 (to J.S.M. and A.B.W.), NIH contract HHSN261200800001E agreement 16x142 (to M.R.D. and J.D.C.), and intramural funding from National Institute of Allergy and Infectious Diseases for work at the VRC (B.S.G.). SBC-XSD is operated by UChicago Argonne, LLC, for the U.S. Department of Energy (DOE) Office of Biological and Environmental Research under contract DE-AC02-06CH11357. This research used resources of the Advanced Photon Source, an Office of Science User Facility operated for the U.S. DOE Office of Science by Argonne National Laboratory under contract no. DE-AC02-06CH11357.

Moving Toward a Universal Vaccine for Influenza

Everyone knows you should get your vaccination against influenza virus each year, but why is that? For many other diseases, we get a single vaccination that lasts our whole life, but we have to get a new flu shot each year. The problem with flu lies in its ability to change from year to year. Flu vaccines are generally focused on triggering an immune response to the influenza surface protein hemagglutinin (HA). Upon vaccination, the body generates antibodies that recognize HA and neutralize the virus, stopping potential infections. However, due to the influenza virus' propensity to mutate HA rapidly, this protein changes over time and can escape detection by the antibodies generated in last year's immune response. This means we have to be re-vaccinated each year to recognize the new version. HA has been the focus of influenza vaccination for many years, but researchers are also interested in targeting another influenza virus surface protein that changes more slowly than HA – a receptor-destroying enzyme called neuraminidase (NA). Now, new work from an international team of investigators carrying out studies at the APS has identified antibodies against the NA protein in a patient with influenza that could lead to the development of a longer-lasting NA-focused universal influenza vaccine that could potentially recognize a broad array of current and future strains of the virus.

The work began with isolation of anti-influenza antibodies from a patient who had been sick with the flu. The team identified three different antibodies that recognized the NA protein and had broad binding to different strains of influenza, including some to which the patient had never been exposed, and strains from both the A and B influenza groups that cause seasonal epidemics.

The next step was to characterize the three candidates antibodies. They found that all the antibodies inhibited the enzymatic activity of NA in two different assays, one of which suggested that the antibodies all bound to the active site of NA. Further, although antibodies against NA do not usually work in viral neutralization assays, testing showed that these three antibodies blocked viral replication and egress from cells. The antibodies also displayed broad activity in assays that measured how they activate the immune system, even in strains where the antibody had weak binding to NA.

In order to follow-up on the suggestion that these NA antibodies might bind to the active site of the enzyme directly, the team solved the structures of the NA-binding domain for each antibody bound to NA using x-ray diffraction data collected at the GM/CA-XSD structural biology facility on the 23-ID-B beamline of the APS (Fig. 1), and at the Stanford Synchrotron Radiation Light Source (SSRL) beamline 12-2. Structural data confirmed that each antibody binds to NA in a one-to-one manner and fully blocks the active site of NA. This structural data will be used by the team to design a universal influenza vaccine that generates a response that both neutralizes NA and has the broad specificity of these antibodies.

However, their data also suggest that these antibodies might have therapeutic value on their own. To test this idea, the researchers administered the antibodies to mice either before or after they had been exposed to various strains of influenza. The antibodies successfully blocked infection when given before exposure and were effective for treating an existing infection at 48 h and 72 h after exposure. One of the antibodies was effective against every influenza strain tested.

Taken together, these data suggest that NA is a very good target for influenza treatments and a universal vaccine and this study has provided the groundwork needed to make that promise a reality. – Sandy Field

See: Daniel Stadlbauer[1,2], Xueyong Zhu[3], Meagan McMahon[1], Jackson S. Turner[4], Teddy J. Wohlbold[1,5,6], Aaron J. Schmitz[4], Shirin Strohmeier[1], Wenli Yu[3], Raffael Nachbagauer[1], Philip A. Mudd[4], Ian A. Wilson[3]*, Ali H. Ellebedy[4]**, and Florian Krammer[1]***, "Broadly protective human antibodies that target the active site of influenza virus neuraminidase," Science **366**, 499 (25 October 2019).
DOI: 10.1126/science.aay0678

Author affiliations: [1]Icahn School of Medicine at Mount Sinai, [2]University of Natural Resources and Life Sciences, [3]The Scripps Research Institute, [4]Washington University School of Medicine, [5]Columbia Irving Medical Center, [6]NewYork-Presbyterian Morgan Stanley Children's Hospital
Correspondence: *wilson@scripps.edu,
**ellebedy@wustl.edu,
***florian.krammer@mssm.edu

The Krammer laboratory was supported by National Institute of Allergy and Infectious Diseases (NIAID) Centers of Excellence for Influenza Research and Surveillance (CEIRS) contract HHSN272201400008C and NIAID grant R01 AI117287; the Ellebedy laboratory was supported by NIAID R21 AI139813, U01 AI141990, and NIAID CEIRS contract HHSN272201400006C; and the Wilson laboratory was supported in part by National Institutes of Health (NIH) NIH R56 AI117675 (to I.A.W.). GM/CA-XSD has been funded in whole or in part with Federal funds from the National Cancer Institute (ACB-12002) and the National Institute of General Medical Sciences (AGM-12006). The Eiger 16M detector at GM/CA-XSD was funded by NIH grant S10 OD012289. Use of the SSRL, SLAC National Accelerator Laboratory, is supported by the U.S. Department of Energy (DOE) Office of Science-Basic Energy Sciences under contract DE-AC02-76SF00515. The SSRL Structural Molecular Biology Program is supported by the DOE Office of Biological and Environmental Research and by the National Institute of General Medical Sciences (including P41 GM103393). This research used resources of the Advanced Photon Source, a U.S. DOE Office of Science User Facility operated for the DOE Office of Science by Argonne National Laboratory under Contract No. DE-AC02-06CH11357.

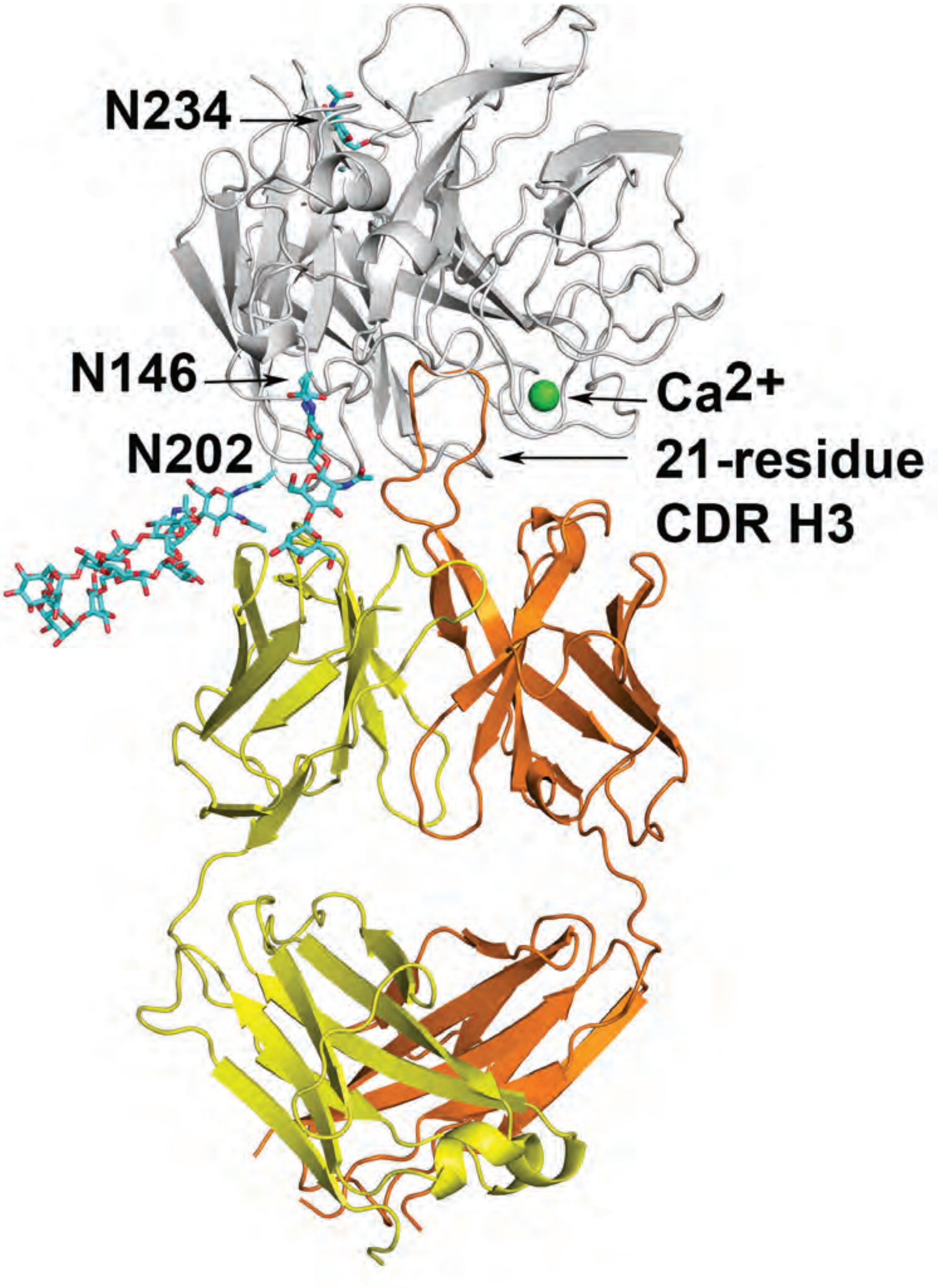

Fig. 1. Crystal structure of 1G04 with Hunan N9 NA at 3.45-Å resolution, determined at the GM/CA-XSD 23-ID-B beamline at the APS. From D. Stadlbauer et al., Science **366**, 499 (25 October 2019). © 2019 American Association for the Advancement of Science. All rights reserved.

Building a Platform for Better Structure-based Drug Design for Alzheimer's Disease

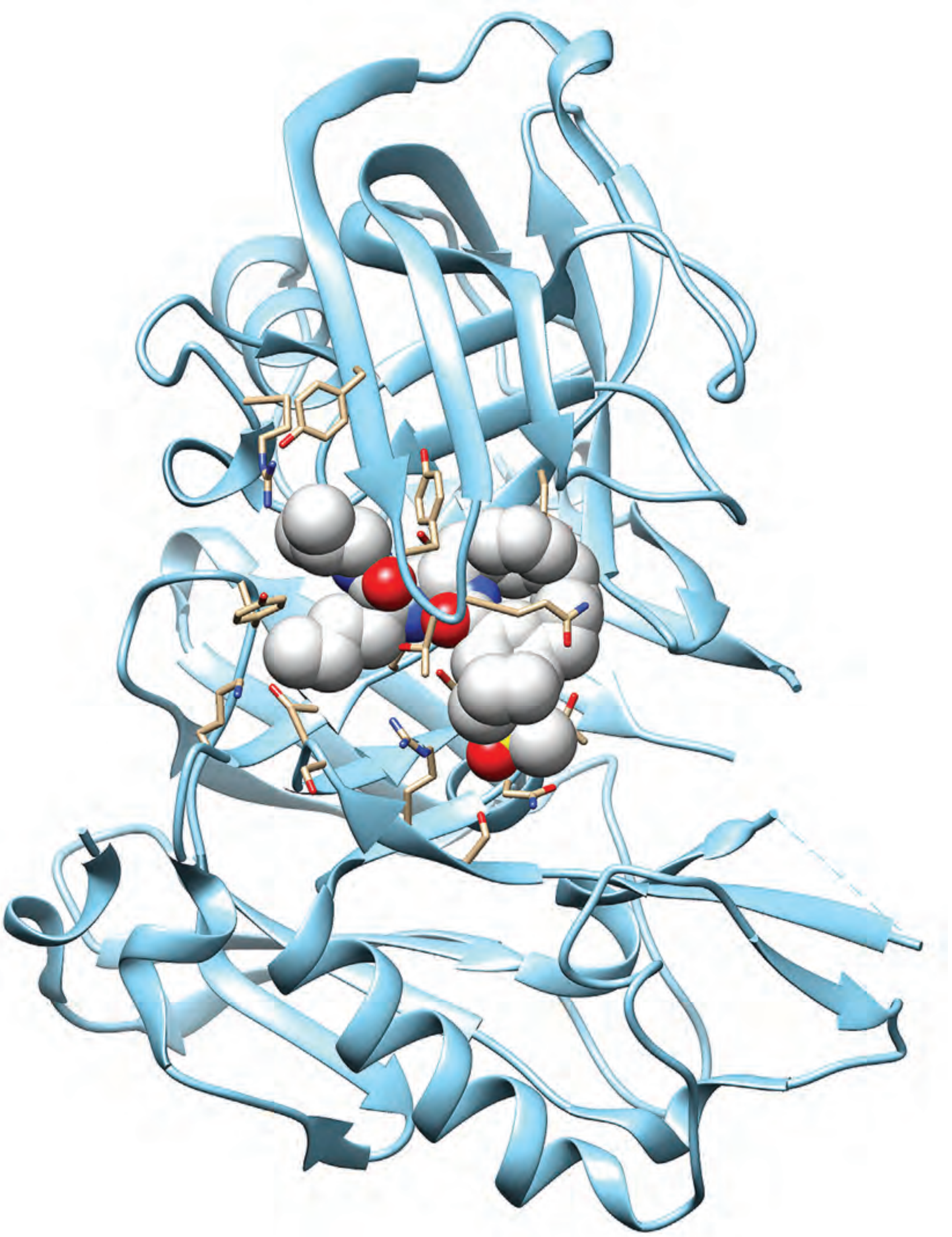

Fig. 1. X-ray structure (6NW3) of BACE1 bound to a potent macrocyclic inhibitor, determined at LRL-CAT. The BACE1 monomer is depicted as a ribbon diagram colored as sky blue and the bound inhibitor 1 is depicted as a space filling model (carbon atoms are white, nitrogen atoms are blue, oxygens are red, and sulfur is yellow). The BACE1 amino acid side chains that interact with the inhibitor are shown as stick models and are colored tan.

Alzheimer's disease (AD) is the primary cause of dementia and is estimated to affect more than 40 million people around the world. Unfortunately, currently available therapies treat the symptoms but not the underlying causes of the disease. Alzheimer's disease is caused by the formation of insoluble amyloid plaques and neurofibrillary tangles that disrupt the function of brain cells. Although considerable research effort has been focused on trying to find a way to block or reverse the formation of these plaques and tangles, this has not been successful. Recently, work carried out at the APS has provided a new platform from which to launch structure-based drug design projects aimed at reducing amyloid plaque formation. The work provides important steps toward development of a disease-modifying treatment for this intractable disease.

The "amyloid hypothesis" of AD is based on the idea that the accumulation of amyloid-β (Aβ) peptides in the brains of AD patients is an important driver of AD pathology and that their removal or the prevention of their formation could treat the disease. Amyloid-β peptides are created through the action of a number of enzymes, principally one called β-site amyloid precursor protein cleaving enzyme (BACE1). Researchers have identified inhibitors of this enzyme that could potentially be used as AD treatments. Unfortunately, the BACE1 inhibitors that have so far been tested in the clinic have either not led to cognitive improvement in patients or have been associated with significant adverse effects. These side effects may, in part, be due to the fact that the drugs tested in the clinic also potently inhibit the closely related homolog enzyme BACE2. For these reasons, a structure-based drug design approach is needed to characterize inhibitors and optimize them for BACE1 and clinical use. However, BACE1 has proved to be challenging to produce in a high enough quantity for enzymatic characterization and the crystallization studies needed for structure-based optimization of candidate inhibitors. Therefore, new approaches to drug design are needed.

In order to address the challenge of coming up with a new approach to BACE1 inhibitor design, the research team from Purdue University sought to develop a protein purification procedure that would be appropriate for large-scale, structure-based drug optimization studies. They started by working to generate more BACE1 protein through expression of larger quantities in bacteria. Expression was complicated by partitioning of the protein as partially-folded or unfolded aggregates in inclusion bodies inside the bacterial cells. Therefore, the first step was to develop a simple way to remove the protein from the inclusion bodies and get it to refold. They did this by rapidly denaturing the protein in highly concentrated urea and then diluting the urea over the course of four days to allow the protein to refold. Further purification on two chromatographic columns yielded a large amount of active BACE1 that crystallized well and was appropriate for kinetic assays.

The next step was to optimize kinetic assays to enable the team to characterize potential inhibitors. Careful analysis of the kinetics of BACE1 allowed the researchers to develop kinetic assays that provided reproducible results with three known inhibitors of BACE1. This was followed by crystallization of BACE1 with each inhibitor to identify the basis for differences they had observed in their assay and the determination of important diffraction data regarding structural features that are important for BACE1 inhibition and selectivity (Fig. 1). These studies were carried out at the LRL-CAT 31-ID-D beamline at the APS.

The team will scale up the protein purification, kinetic analysis, and structure-based drug design processes developed here to provide a platform for large-scale drug optimization studies. The team hopes that their attention to simplifying and optimizing each step of the process will be the key to identifying new AD therapies that reduce amyloid-β formation and restore cognitive function in people afflicted by this debilitating disease. – Sandy Field

See: Yu-Chen Yen, Annalissa M. Kammeyer‡, Katherine C. Jensen, Jagannadharao Tirlangi, Arun K. Ghosh, and Andrew D. Mesecar*, "Development of an Efficient Enzyme Production and Structure-Based Discovery Platform for BACE1 Inhibitors," Biochemistry **58**, 4424 (2019). DOI: 10.1021/acs.biochem.9b00714

Author affiliation: Purdue University ‡Present address: Marian University College of Osteopathic Medicine
Correspondence: * amesecar@purdue.edu

We would like to thank the LRL-CAT beamline staff for their help in acquiring x-ray data. Use of the Lilly Research Laboratories Collaborative Access Team beamline at the APS was provided by Eli Lilly and Company, which operates the facility. This research used resources of the Advanced Photon Source, a U.S. Department of Energy (DOE) Office of Science user facility operated for the DOE Office of Science by Argonne National Laboratory under Contract No. DE-AC02-06CH11357.

Recruiting a Cellular Trash Collector to Take Out Cancer

Sometimes, it's best to just let the body use its own tricks to get rid of disease. For years, scientists have been attempting to develop drugs that target signal transducer and activator of transcription 3 (STAT3), a protein that runs amuck in cancer and other diseases. But STAT3 had proven resilient against these strategies. Now, a research team is testing a new tactic against the nefarious protein. They developed a small molecule, named SD-36, that could both bind STAT3 and also recruit the machinery that breaks down the body's cellular trash. To aid in their efforts, the team collaborated with the Center of Structural Biology of the University of Michigan to solve a structure of SD-36 in complex with STAT3 with data collected at the APS. Their study suggests protein degradation may be an effective anti-cancer strategy.vaccines against MERS-CoV.

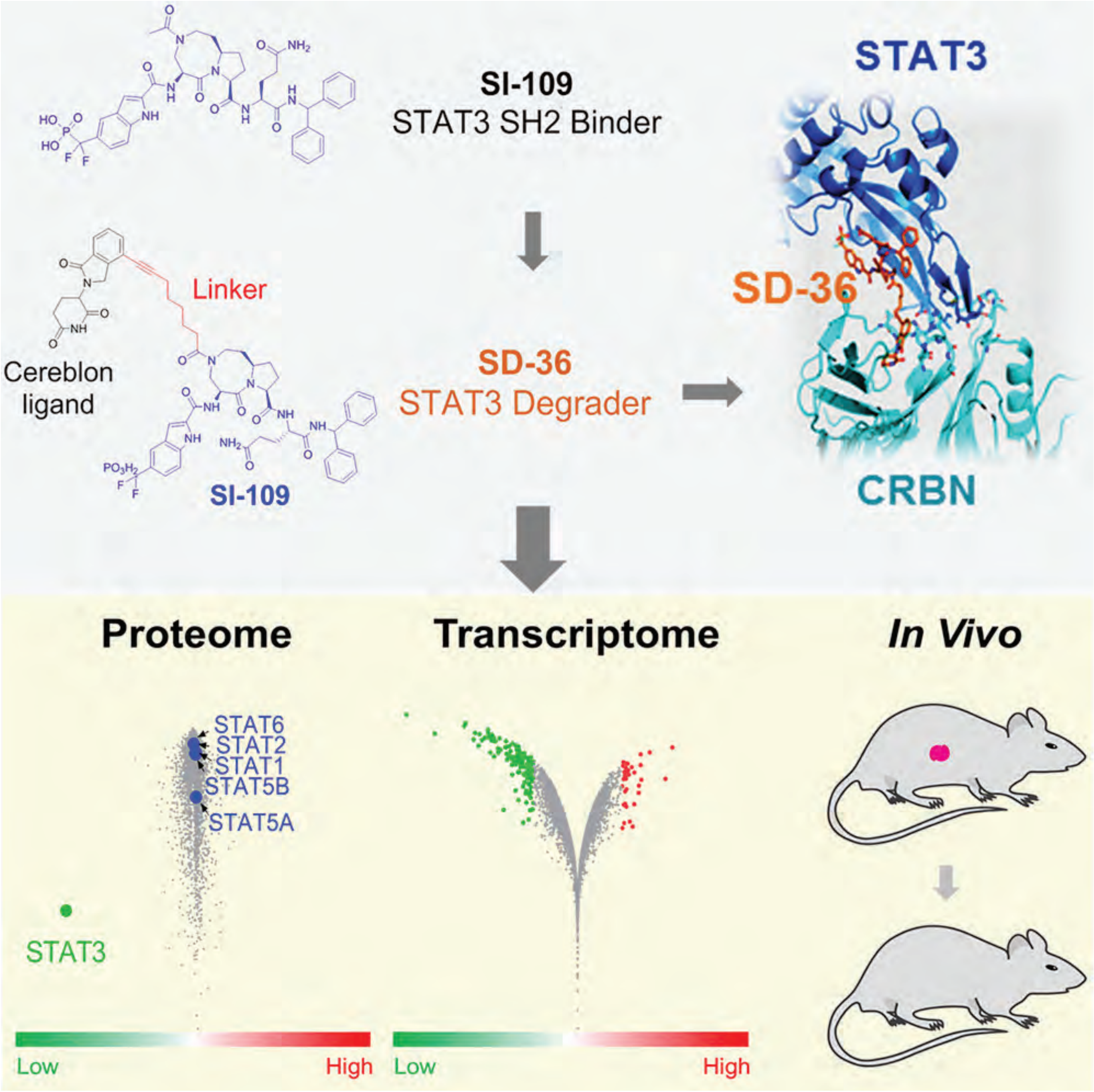

While STAT3 is absolutely essential during embryogenesis, the protein can be trouble for adults. STAT3 is a transcription factor that goes into overdrive in various human cancers, promoting the expression of a set of genes that makes cancer cells more robust, promotes cancer's spread, and helps the cancer resist treatment. As such, and because data suggests that STAT3 is not essential for the health of adults, scientists have been trying to develop new therapies that hobble the transcription factor. Many of these therapies are small molecules that bind STAT3 in its SH2 domain, blocking STAT3 dimerization; the dimer is the transcription factor's “active” form. Scientists have successfully created compounds that bind STAT3 and prevent dimerization, but none seem to be a promising treatment. For starters, they aren't specific, and tend to impact other members of the STAT family. Another issue is that, while the molecules block dimerization, it now seems that the monomer maintains some capacity to function. That's what prompted the team to look at other options; enter an emerging drug development technology called proteolysis targeting chimera (PROTAC).

The technology behind PROTAC was initially described in 2001, and several drug-discovery laboratories are attempting to apply the method to the development of novel therapies. The key to PROTAC is the creation of a small molecule with two business ends connected by a linker; one of the ends specifically binds to the molecule being targeted for degradation. The other end recruits an enzyme called an E3 ubiquitin ligase. This protein tags the cell's trash with strings of the protein ubiquitin, which targets the unwanted molecule for degradation by the proteasome, the cellular garbage disposal. The team first developed a small molecule, SI-109, that binds strongly to STAT3, and then tethered SI-109 to a ligand for an E3 ligase and creating a new drug candidate, SD-36, that was hoped to lead to the specific degradation of STAT3 (Fig. 1).

To test SD-36, the researchers embarked on a series of experiments to tease out the molecule's anti-cancer potential, including solving a structure of SD-36 in complex with STAT3 with data collected at the LS-CAT 21-ID-D x-ray beamline at the APS. First, they tested SD-36 in human cells, and found that the molecule could successfully trigger the degradation of the STAT3 protein. In another cell line, one that expresses all seven members of the STAT protein family, the team was able to establish that SD-36 specifically degrades STAT3, leaving the other STAT proteins alone. The researchers also tested whether SD-36 could not only degrade STAT3, but also turn off the protein's transcriptional activities. Indeed, when they looked at the expression of the cancer-spurring genes under STAT3's control, the researchers found that SD-36 specifically diminished STAT3's transcriptional targets.

< Fig. 1. The authors developed SD-36, a proteolysis targeting chimera (PROTAC) that selectively degrades STAT3 and inhibits the growth of leukemia and lymphoma cell lines. SD-36 is well tolerated in immune-competent mice and induces durable tumor regression in vivo in xenograft models. From L. Bai et al., Cancer Cell **36**, 498 (November 11, 2019). © 2019 Elsevier Inc.

And what about cancer itself? For starters, SD-36 inhibited growth in leukemia and lymphoma cells. Next, the researchers found that SD-36 degrades STAT3 in mouse xenograft tumors, and, most important, the small molecule completely and persistently abolished tumors in living mice. The mice tolerated the molecule well, though this research is only the first step toward a cancer treatment. However, it is clear that the PROTAC technology offers a promising approach for targeting undruggable molecules, like STAT3, that have resisted traditional drug development strategies. Future research will be needed to determine whether SD-36 will make it in the clinic, but scientists are excited about the potential to put cancer in the trash bin. – Erika Gebel Berg

See: Longchuan Bai, Haibin Zhou, Renqi Xu, Yujun Zhao, Krishnapriya Chinnaswamy, Donna McEachern, Jianyong Chen, Chao-Yie Yang, Zhaomin Liu, Mi Wang, Liu Liu, Hui Jiang, Bo Wen, Praveen Kumar, Jennifer L. Meagher, Duxin Sun, Jeanne A. Stuckey, and Shaomeng Wang*, “A Potent and Selective Small-Molecule Degrader of STAT3 Achieves Complete Tumor Regression *In Vivo*,” Cancer Cell **36**, 498 (November 11, 2019). DOI: 10.1016/j.ccell.2019.10.002

Author affiliation: University of Michigan
Correspondence: *shaomeng@umich.edu

The authors are grateful for the financial support from Oncopia Therapeutics, Inc. (to S.W.), and for the Rogel Cancer Center Core grant (P30 CA046592) from the National Cancer Institute, National Institutes of Health. Use of LS-CAT was supported by the Michigan Economic Development Corporation and the Michigan Technology Tri-Corridor (grant 085P1000817). This research used resources of the Advanced Photon Source, a U.S. Department of Energy (DOE) Office of Science User Facility operated for the DOE Office of Science by Argonne National Laboratory under contract no. DE-AC02-06CH11357.

A Common Lipid Could Be the Key to Tackling Drug Resistance in Skin Cancer

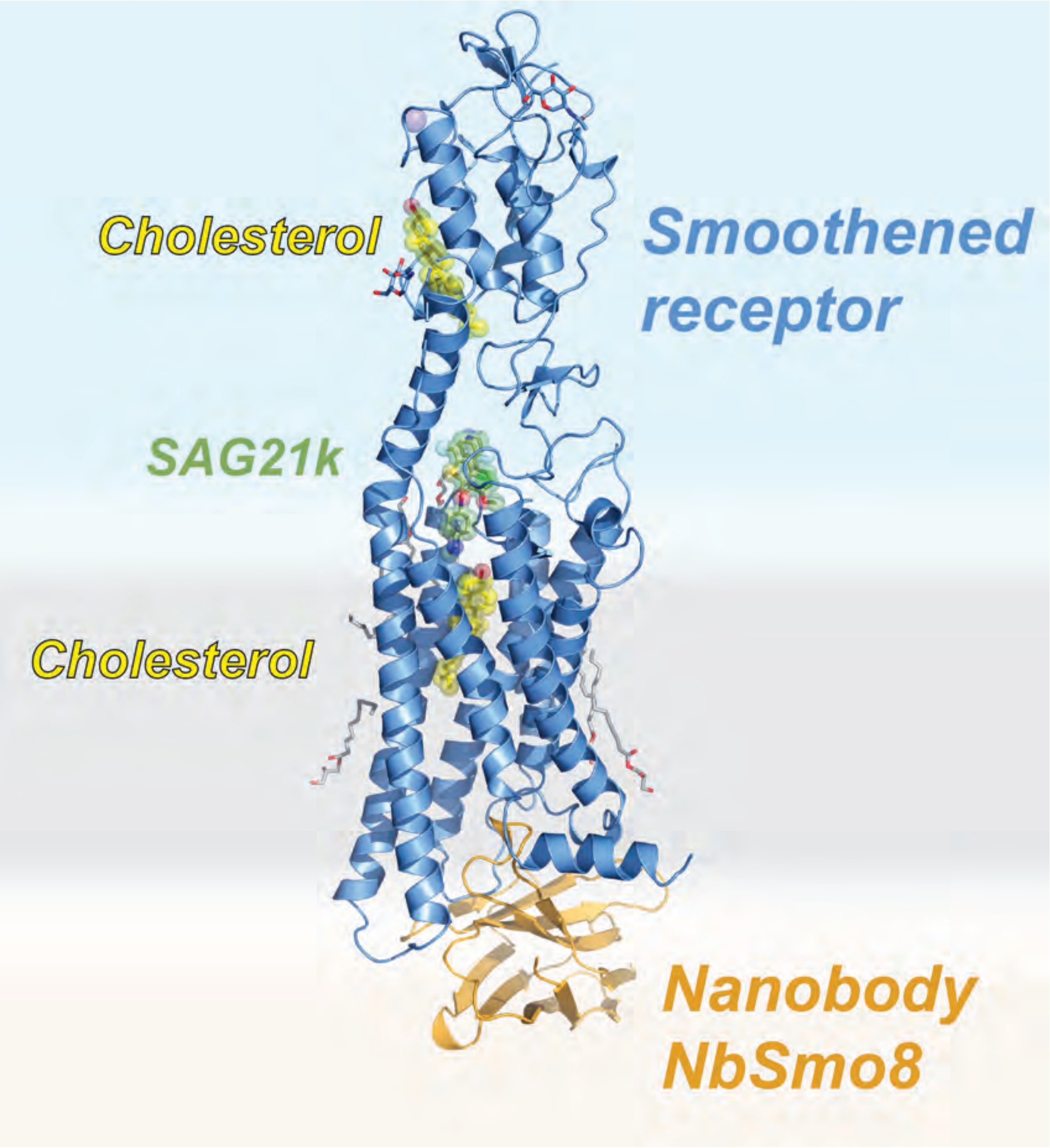

Fig. 1. The three-dimensional structure of active Smoothened (blue) bound to a synthetic nanobody from a yeast-display library (brown) needed to aid crystallization. Also bound to Smoothened are two cholesterol molecules (yellow) and SAG21k, synthetic agonist (green).

Despite significant advances in the understanding and treatment of basal cell carcinoma skin cancer, its treatment has remained plagued by the development of drug resistance that commonly arises during treatment with Smoothened inhibitor therapy. Smoothened is a key protein in the Hedgehog signalling pathway that, when inappropriately activated, drives progression of basal cell carcinoma. In a recent study, which involved collecting x-ray diffraction data at the APS, researchers aimed to improve understanding of how Smoothened becomes activated to a state that, in turn, activates Hedgehog signalling. Interestingly, they found that an extremely common lipid holds the key to the Smoothened lock. The results of this study will be critical to the design of Smoothened inhibitors that may overcome the resistance mechanisms that have so far hindered the success of these targeted cancer therapies.

The amazing body plans of animals rely on important signals that tell cells where to go and what to become. The Hedgehog signalling pathway is one mechanism that is foundationally critical for the normal development of almost all animals. At the heart of this pathway is a protein called Smoothened, and its activity is required for appropriate Hedgehog signalling. In addition to playing significant roles in areas such as embryonic development and postnatal tissue regeneration, this pathway is also involved in tumor formation. Defective Hedgehog signalling is implicated in the development of several cancers, most prominently basal cell carcinoma—a malignant skin tumor and the most common form of skin cancer (as well as the most common type of all cancers) in people. Indeed, defects in Smoothened are known to underpin the faulty signalling that leads to the formation of these tumors. As a result, Smoothened has now become a clinically useful target in the development of drugs to help treat cancers like basal cell carcinoma. However, in the clinic, successful cancer therapies are often challenged by the development of tumor drug resistance.

With this in mind, a group of scientists set out to understand the fundamental mechanism of how Smoothened turns on by conducting a study that aimed to improve understanding of Hedgehog signalling and to serve as a foundation for the development of better inhibitors.

According to the researchers, catching the "on" state of proteins that reside on the cellular membrane is often challenging. This is because these proteins are flexible and dynamic, making it difficult to freeze them in a single conformation for study purposes. To combat this problem, the researchers first developed an antibody fragment known as nanobody Smoothened 8 (NbSmo8) that freezes Smoothened in its active conformation. Next, they determined an x-ray crystal structure of Smoothened in the "on" state (Fig. 1), using data collected at the GM/CA-XSD 23-ID-B and 23-ID-D beamlines at the APS.

The researchers found two cholesterols in the crystal structure, and were particularly surprised to find that one was buried deep within Smoothened (Fig. 1). By comparing the new structure to previously determined structures of Smoothened in its "off" state, they discovered that the buried cholesterol is required to turn Smoothened to its "on" state.

This discovery provides a critical missing link that enables us to understand how the Hedgehog signal crosses the cellular membrane. It also provides a rationale to explain why resistance develops when Smoothened inhibitors are used to treat basal cell carcinomas in the clinic.

These findings will guide studies that use this new information to try designing Smoothened inhibitors that may overcome such resistance. – Nicola Parry

See: Ishan Deshpande[1], Jiahao Liang[1], Danielle Hedeen[2], Kelsey J. Roberts[3], Yunxiao Zhang[3], Betty Ha[3,4], Naomi R. Latorraca[3,4], Bryan Faust[1], Ron O. Dror[3,4], Philip A. Beachy[3,5], Benjamin R. Myers[3,2]*, and Aashish Manglik[1]**, "Smoothened stimulation by membrane sterols drives Hedgehog pathway activity," Nature **571**, 284 (11 July 2019). DOI: 10.1038/s41586-019-1355-4

Author affiliations: [1]University of California, San Francisco, [2]University of Utah School of Medicine, [3]Stanford University School of Medicine, [4]Stanford University
Correspondence: * Benjamin.Myers@hci.utah.edu,
** Aashish.Manglik@ucsf.edu

This work was supported by National Institutes of Health (NIH) grants DP5OD023048 (A.M.), R01GM127359 (R.O.D.) and R01GM102498 (P.A.B.). I.D. acknowledges support from the Swiss National Science Foundation. A.M. acknowledges support from the Pew Charitable Trusts. B.R.M. acknowledges support from the American Cancer Society. N.R.L. and K.J.R. were supported by National Science Foundation Graduate Research Fellowships and K.J.R. by a Gerhard Casper Stanford Graduate Fellowship. We thank the staff at the GM/CA-XSD beamlines at the APS, which have been funded in whole or in part with federal funds from the National Cancer Institute (ACB-12002) and the National Institute of General Medical Sciences (AGM-12006). The Eiger 16M detector at GM/CA-XSD was funded by NIH grant S10 OD012289.. This research used resources of the Advanced Photon Source, a U.S. Department of Energy (DOE) Office of Science User Facility operated for the DOE Office of Science by Argonne National Laboratory under Contract No. DE-AC02-06CH11357.

Changing the VISTA Could Lead the Way to New Cancer Therapies

VISTA (V-type immunoglobulin domain-containing suppressor of T-cell activation) is a negative immune checkpoint regulator protein that mediates immune system function and its loss can result in the development of unwanted immune responses. But VISTA may also be a valuable target in regulating the immune response in diseases such as cancer. In a recent study, which involved collecting x-ray diffraction data at the APS, researchers aimed to improve understanding of how VISTA functions as a checkpoint inhibitor. In particular, they found that it binds to a receptor known as P-selectin glycoprotein ligand-1 (PSGL-1), and that acidic conditions selectively allow the two molecules to interact and suppress immune activation in the tumor bed. This discovery bridges a key knowledge gap that will help serve as a foundation for designing novel cancer immunotherapeutic strategies that target VISTA.

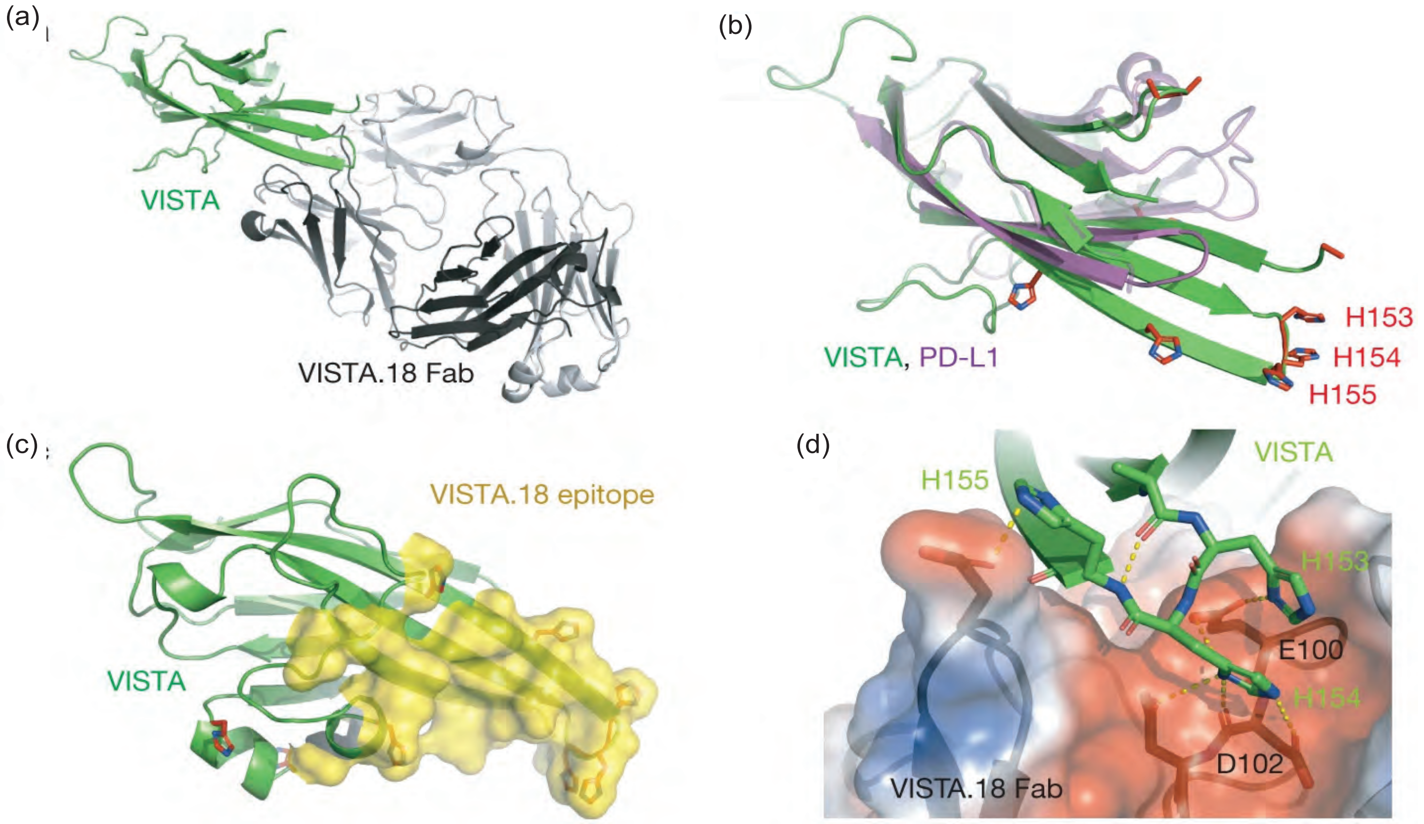

Immune responses must be tightly regulated to allow the body to efficiently clear invading pathogens or cancer cells, while still recognizing its own antigens as a non-threat. The immune checkpoint signalling pathway helps to regulate T cell immune responses that allow the body to mount an effective immune response and to prevent the onset of autoimmunity. Various proteins can interact with these checkpoint signaling pathways to control this balance. These checkpoint proteins can be positive regulators (activating T cells so they can function) or negative regulators (inhibiting T cells and shutting them off).

Immunotherapy is increasingly used to treat cancer in recent decades. And checkpoint inhibitor therapy has emerged as an effective option for various types of advanced cancers. In particular, PD-1 (programmed cell death-1) and CTLA-4 (cytotoxic T lymphocyte antigen-4) have become part of the standard therapy for treating a variety of cancers, including metastatic melanoma, non-small-cell lung carcinoma, and liver cancer.

VISTA is a novel immune checkpoint inhibitor protein that plays an important role in immune suppression associated with cancer. This means that strategies to block the actions of VISTA could be used to enhance the body's anti-cancer response. Research has shown that VISTA inhibits T cell responses in vitro and in animal studies. And it has also been recognized as a potential mediator of resistance to anti-PD-1 and anti-CTLA-4 immunotherapies in patients.

However, opportunities to use VISTA therapeutically have been limited by a lack of understanding of its mechanism of action in immune responses.

With this in mind, a group of researchers recently set out to better understand this. Collecting x-ray diffraction data (Fig. 1) at the IMCA-CAT beamline 17-ID at the APS, they conducted a study that aimed to improve understanding of exactly how it functions in the checkpoint signaling pathway. The researchers discovered that VISTA binds to a receptor molecule known as PSGL-1 which has been identified as a negative regulator of T cell responses in a variety of disease contexts, including cancer.

They found that VISTA binds to PSGL-1 under acidic conditions, similar to what is encountered in tumor microenvironments in which the pH can be as low as 5.85. VISTA-transfected cells more potently inhibited T cells in acidic conditions, and VISTA bound to leukocytes when the pH was lower than 6.5, but not in physiologic conditions of pH 7.4. The binding of VISTA to PSGL-1 was also shown to be mediated by histidine residues on the extracellular domain of VISTA.

To examine VISTA-mediated suppression within tumor microenvironments, the researchers treated mice with acidic pH-selective and non-pH-selective VISTA-blocking antibodies. In particular, they found that acidic pH-selective antibodies accumulated preferentially within tumors. The researchers also used an MC38 mouse tumor model to examine the role of VISTA in anti-tumor immune responses. They found that animals treated with a combination of anti-VISTA and anti-PD-1 therapy had significantly less tumor growth than animals treated with just anti-PD-1 therapy had.

These findings will contribute to the investigation and discovery of novel cancer immunotherapies that target VISTA. – Nicola Parry

< Fig. 1. (a) The structure of the human VISTA IgV domain (green) in complex with the VISTA.18 Fab (heavy chain, dark grey; light chain, light grey). (b) Superimposition of the VISTA (green) and PD-L1 (purple) IgV domains. VISTA histidine residues are depicted in stick representation. Histidine residues occupying the loop between the central β-sheets of VISTA (H153, H154 and H155) are labelled. H100, H101 and H104 are in disordered regions and are not depicted. (c) The molecular surface of the VISTA.18 epitope (yellow). (d) An enlarged view of the interface between VISTA (green, with epitope residues depicted in stick representation) and VISTA.18 (depicted as an electrostatic surface). From R.J. Johnson et al., Nature **574**, 565 (24 October 2019). © 2019 Springer Nature Limited

See: Robert J. Johnston[1*], Linhui Julie Su[1], Jason Pinckney[1], David Critton[1], Eric Boyer[1], Arathi Krishnakumar[1], Martin Corbett[1], Andrew L. Rankin[2], Rose Dibella[1], Lynne Campbell[1], Gaelle H. Martin[3], Hadia Lemar[1], Thomas Cayton[1], Richard Y.-C. Huang[1], Xiaodi Deng[1], Akbar Nayeem[1], Haibin Chen[1], Burce Ergel[1], Joseph M. Rizzo[1], Aaron P. Yamniuk[1], Sanjib Dutta[3], Justine Ngo[1], Andrea Olga Shorts[1], Radha Ramakrishnan[1], Alexander Kozhich[1], Jim Holloway[1], Hua Fang[1], Ying-Kai Wang[1], Zheng Yang[1], Kader Thiam[3], Ginger Rakestraw[1], Arvind Rajpal[1], Paul Sheppard[1], Michael , Keith S. Bahjat[1], and Alan J. Korman[1‡], "VISTA is an acidic pH-selective ligand for PSGL-1," Nature **574**, 565 (24 October 2019). DOI: 0.1038/s41586-019-1674-5.

Author affiliations: [1]Bristol-Myers Squibb, [2]Five Prime Therapeutics, [3]genOway ‡Present address: Vir Biotechnology
Correspondence: * robert.johnston@bms.com

Use of the IMCA-CAT beamline 17-ID at the Advanced Photon Source was supported by the companies of the Industrial Macromolecular Crystallography Association through a contract with Hauptman-Woodward Medical Research Institute. This research used resources of the Advanced Photon Source, a U.S. DOE Office of Science User Facility operated for the DOE Office of Science by Argonne National Laboratory under Contract No. DE-AC02-06CH11357.

Breaching the Blood-Brain Barrier

The blood-brain barrier is a physiological "wall" that protects the brain from invading pathogens. It is very effective, so brain infections due to blood-borne pathogens are rare. However, the barrier also effectively blocks medications from reaching the brain and this has created a challenge for people working on diseases that affect the neuronal cells of the brain, such as Alzheimer's disease and related neurodegenerative disorders. Researchers are often frustrated to find that a drug they have discovered or designed to treat a specific neurological disease cannot get into the brain where it is needed. This was the case for research from a group of scientists who carried out research that was conducted, in part, at the APS. The team reported their successful effort to chemically modify a potentially effective drug to improve its access to the brain. As a result, the drug will move on to be tested in first-in-class phase 1 human clinical trials and offers promise for treatment of Alzheimer's and other related neurological diseases.

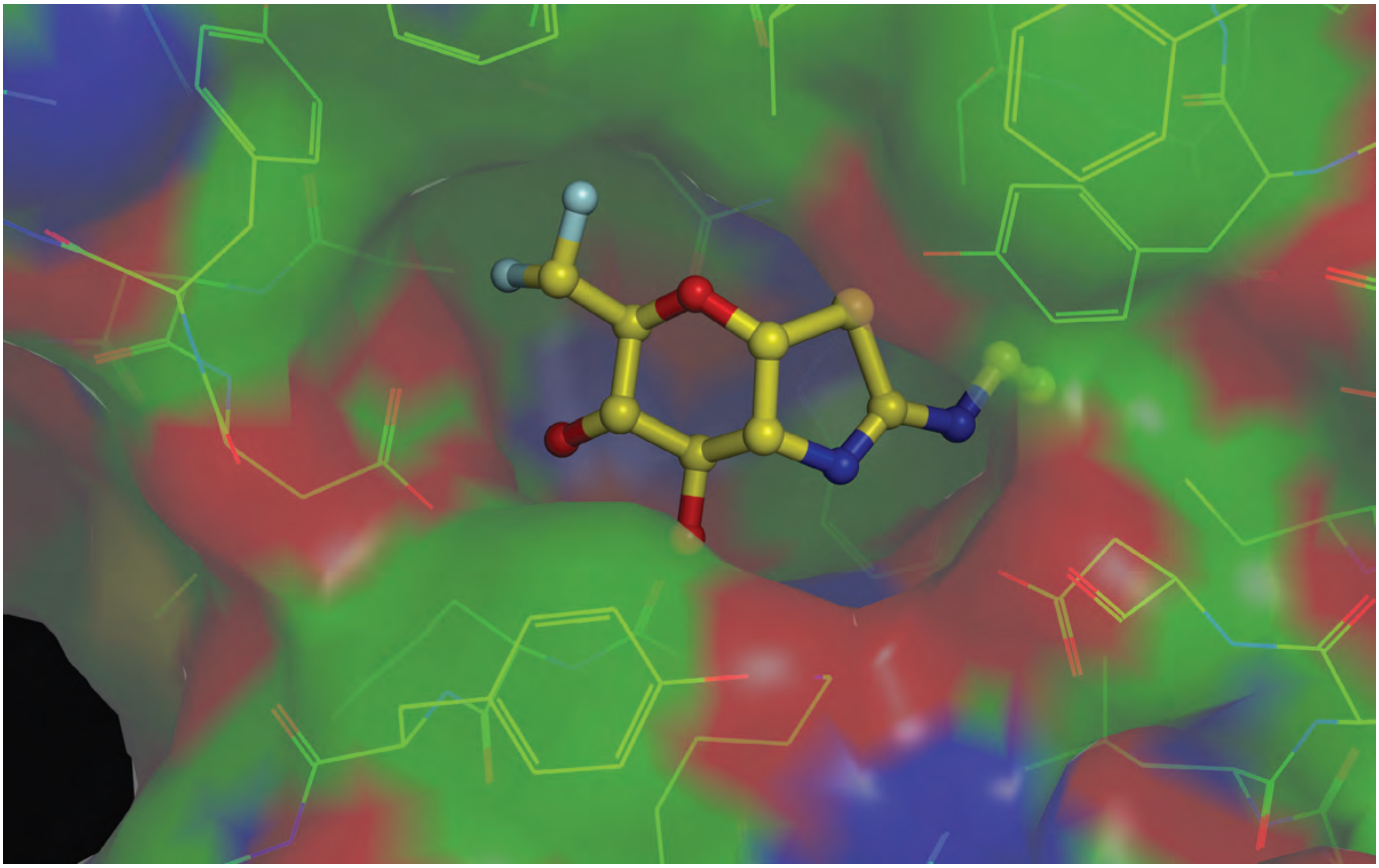

Fig. 1. MK-8719 bound to the active site of the O-GlcNAcase (OGA) enzyme.

Alzheimer’s disease is part of a family of neurodegenerative diseases that are referred to as “tau pathologies” due to the observation that the brains of afflicted patients are infiltrated with filamentous tangles composed of the tau protein. These are considered to be an important target for therapy because the extent of the tangles has been correlated with the progression of the disease. Previous research has shown that the tangles develop when a modification called phosphorylation is added, at a high level, to tau, causing tau molecules to self-assemble into filaments that then form the tangles. However, this phosphorylation competes for binding sites on tau with another modification, the carbohydrate O-GlcNAc. In fact, higher levels of O-GlcNAc on tau result in less aggregation and fewer tangles, making this a potential avenue for reversing the effects of Alzheimer’s.

O-GlcNAc is removed from tau by an enzyme called O-GlcNAcase (OGA) and inhibition of OGA is predicted to lead to increased O-GlcNAc on tau and thus, reduction of tangles. In fact, an excellent inhibitor of OGA – thiamet-G – has already been discovered. However, initial studies showed that it does not have good access to the brain; and this is where the story of this research project begins.

The team from Merck & Co., Inc., Alectos Therapeutics, Inc., and Pharmaron Beijing Co., Ltd., sought to improve thiamet-G to design an OGA inhibitory compound with the properties of a good potential treatment for Alzheimer’s. These properties include excellent inhibition of OGA, good blood-brain access, low inhibition of off-target enzymes involved in other diseases or general metabolism, and demonstrable increase in O-GlcNAc on tau proteins. Thiamet-G already has many of these properties; the main purpose of the effort was to improve blood-brain access while retaining the other desirable properties. To do this, the researchers undertook a systematic round of modifications of the thiamet-G molecule and tested each new compound in assays for each of the desired properties, modifying their approach based on the outcomes of each new round of trials. After designing, synthesizing, and testing 46 compounds, they chose a smaller group that underwent further bioavailability and pharmacodynamic testing. Finally, the team decided that number 42 was the best candidate and, after number 42 passed additional pharmacokinetic and safety tests in animals and humans, they renamed their potential new drug MK-8719.

MK-8719 retains the excellent OGA inhibition and high selectivity of thiamet-G but, importantly, also has high levels of brain exposure. MK-8719 requires a 10-fold lower dose than thiamet-G to get the same brain exposure. The final test before moving on to phase 1 clinical trials was to solve the structure of OGA in complex with MK-8719 to better understand the basis for its interactions with OGA and its differences from thiamet-G (Fig. 1). This feat of macromolecular x-ray crystallography was achieved at the IMCA-CAT 17-ID x-ray beamline at the APS. The structure confirmed the team’s hypothesis that MK-8719 retains the selectivity and inhibitory activity of thiamet-G and that the modifications they made do not significantly change important interactions with the enzyme. Next step, clinical trials! – Sandy Field

See: Harold G. Selnick[1], J. Fred Hess[1], Cuyue Tang[1], Kun Liu[1], Joel B. Schachter[1], Jeanine E. Ballard[1], Jacob Marcus[1], Daniel J. Klein[1], Xiaohai Wang[1], Michelle Pearson[1], Mary J. Savage[1], Ramesh Kaul[2], Tong-Shuang Li[2], David J. Vocadlo[2], Yuanxi Zhou[2], Yongbao Zhu[2], Changwei Mu[3], Yaode Wang[3], Zhongyong Wei[3], Chang Bai[3], Joseph L. Duffy[1], and Ernest J. McEachern[2]*, “Discovery of MK-8719, a Potent O-GlcNAcase Inhibitor as a Potential Treatment for Tauopathies,” J. Med. Chem. **62**, 10062 (2019). DOI: 10.1021/acs.jmedchem.9b01090

Author affiliations: [1]Merck & Co., Inc., [2]Alectos Therapeutics Inc., [3]Pharmaron Beijing Co., Ltd.
Correspondence: * emceachern@alectos.com

This work was funded entirely by Alectos Therapeutics, Inc., and Merck & Co., Inc. This research used resources of the Advanced Photon Source, a U.S. Department of Energy (DOE) Office of Science User Facility operated for the DOE Office of Science by Argonne National Laboratory under Contract No. DE-AC02-06CH11357.

About Alzheimer’s Disease

Alzheimer’s disease is currently ranked as the sixth leading cause of death in the United States, but recent estimates indicate that the disorder may rank third, just behind heart disease and cancer, as a cause of death for older people.

Alzheimer’s disease is named after Dr. Alois Alzheimer. In 1906, Dr. Alzheimer noticed changes in the brain tissue of a woman who had died of an unusual mental illness. Her symptoms included memory loss, language problems, and unpredictable behavior. After she died, he examined her brain and found many abnormal clumps (now called amyloid plaques) and tangled bundles of fibers (now called neurofibrillary, or tau, tangles).

These plaques and tangles in the brain are still considered some of the main features of Alzheimer’s disease.

Another feature is the loss of connections between nerve cells (neurons) in the brain. Neurons transmit messages between different parts of the brain, and from the brain to muscles and organs in the body. *Source: National Institutes of Health*

Uncovering a Transport Protein's Mechanism

All cells need nutrients to thrive and survive. For nutrients to make it into the cell, an array of transport proteins are necessary to move various molecules across the protective cell membrane. One such class of proteins are natural resistance-associated macrophage proteins, or "Nramps," which ferry transition metals, along with protons, into and out of cells. Nramps perform this crucial task for a range of organisms; human cells use the proteins to absorb Fe^{2+} while bacteria use them to take in Mn^{2+} needed to mount an infection. However, the mechanism by which proteins transfer these metal ions isn't well understood. Using the APS, researchers have revealed key shapes that the bacterial transport protein *Deinococcus radiodurans* (Dra)Nramp adopts during the transport process. By designing and producing mutated versions of the protein to obtain crystals, the researchers captured the protein in four distinct states. Their structural analysis suggests a new mechanism for this type of transport protein in which metal ions and protons travel along separate pathways during part of the process. The team's findings will improve scientists' understanding of how cells regulate metal ion concentrations, which is critical for maintaining healthy cells, and could help researchers understand other transport proteins' mechanisms as well.

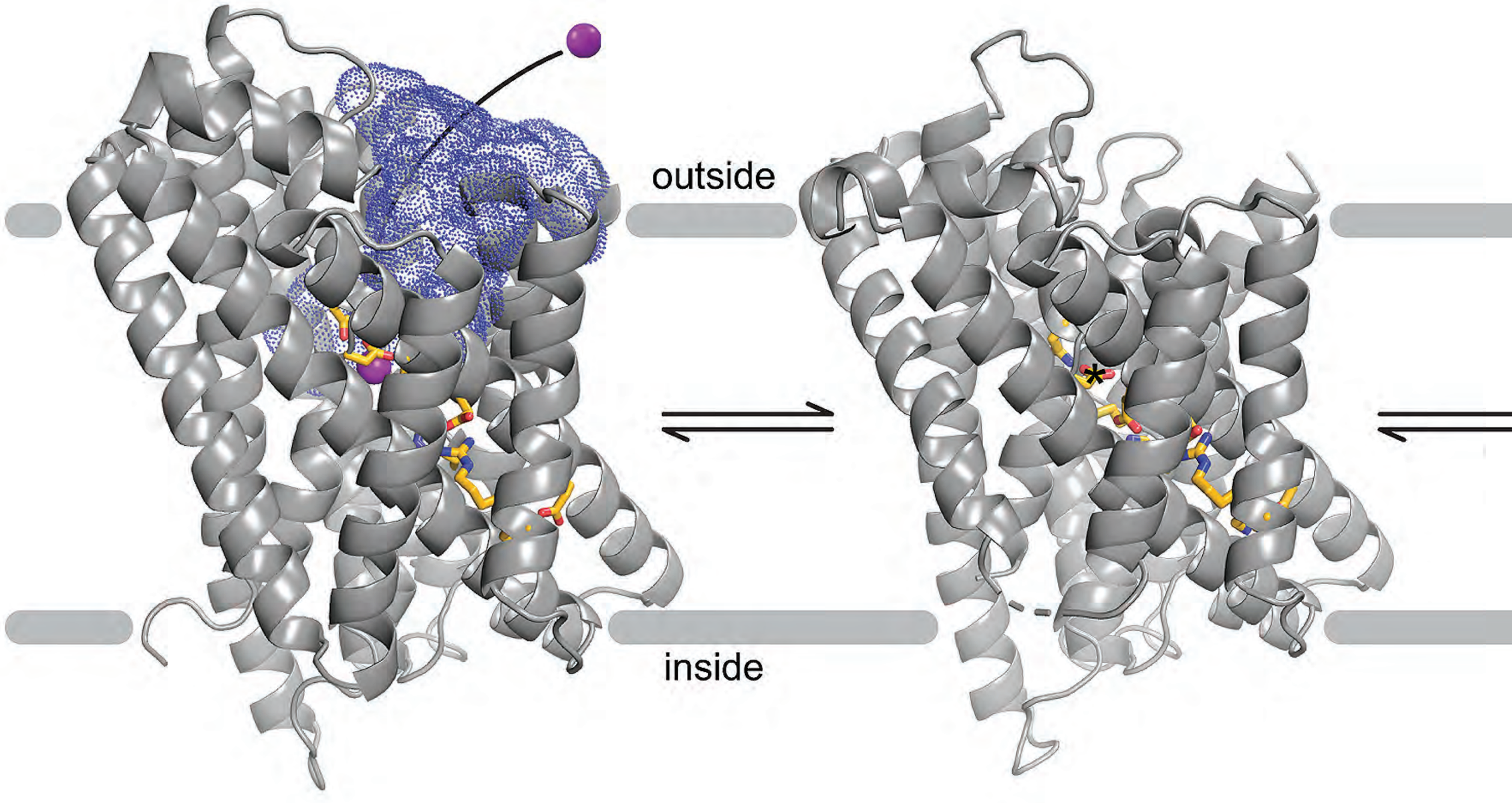

Fig. 1. Using x-ray crystallography, researchers capture the structure of a metal ion transporter protein in key stages of the transport process.

Embedded inside the cell membrane, Nramps are made of 11 or 12 transmembrane segments. These complex proteins bind rare, divalent transition metals and provide them passage into the cell. Scientists have suggested that this metal transport is coupled with proton transport, yet the exact details of this mechanistic relationship has eluded them.

To investigate Nramps' transport mechanism, researchers at Harvard University selected a model Nramp system from a bacterium called *Deinococcus radiodurans*. The team synthesized a series of DraNramp mutants and evaluated their ability to transport metals or protons. In *in vitro* experiments, they found that while metal transport required the proteins to rearrange themselves, proton transport could occur with minimal adjustment from the proteins. This suggests that metal and proton transport may take place through separate pathways.

Through x-ray diffraction experiments at the NE-CAT 24-ID-C beamline at the APS, the researchers determined the structure of protein crystals, capturing the protein in four key states throughout the metal transport process.

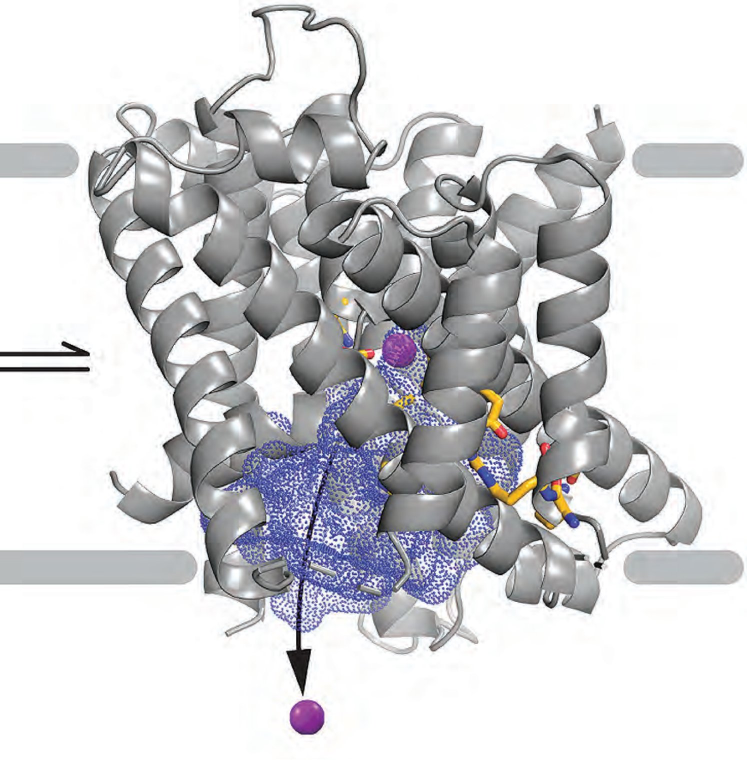

Focusing on the proton transport pathway, the researchers calculated the pKa values for specific residues on the protein in their structures. Based on these calculations and previous reports, they propose the aspartate residue in the metal-binding site as the most likely residue to become protonated and thus initiate the proton transfer.

Based on their structural data, the team propose a model for the conformation changes DraNramp cycles through to perform the metal transport (Fig. 1). In their model, the protein starts in an "outward-open" state. Then upon binding a metal ion, several transmembrane segments undergo a major rearrangement as the protein adopts an "inward-occluded" state. Another set of segments shifts to then lead the protein to an "inward-open" state which opens an inner vestibule that allows the metal ion to be released into the cell's cytoplasm.

As for the proton transport, the team suggests that while protons enter via the same transport mechanism, they exit through a separate route that's enabled by a salt-bridge network. This separate exit strategy is a unique mechanistic feature that hasn't been observed in other similar transport proteins. To close the loop, the protein cycles back through the inward-occluded state and assumes its original conformation. The precise order of proton and metal transport has yet to be determined.

Given that the mechanisms of only a few transport proteins have been explored at the structural level, the authors findings offer valuable new insights that could prove useful in understanding a wide range of transport proteins. – Tien Nguyen

See: Aaron T. Bozzi, Christina M. Zimanyi, John M. Nicoludis, Brandon K. Lee, Casey H. Zhang, and Rachelle Gaudet*, "Structures in multiple conformations reveal distinct transition metal and proton pathways in an Nramp transporter," eLife **8**, e41124 (2019). DOI: 10.7554/eLife.41124

Author affiliation: Harvard University
Correspondence: * gaudet@mcb.harvard.edu

This work was funded in part by National Institutes of Health (NIH) grant 1R01GM120996 (to R.G.) and a Jane Coffin Childs Postdoctoral Fellowship (to C.M.Z.). We thank the NE-CAT beamline staff at the APS for help with data collection. NE-CAT is funded by NIH (P41 GM103403 and S10 RR029205). This research used resources of the Advanced Photon Source, an Office of Science User Facility operated for the U.S. DOE Office of Science by Argonne National Laboratory under contract no. DE-AC02-06CH11357.

Structure of G-protein Chaperone and Nucleotide Exchange Factor Points to Function

Resistance to inhibitors of cholinesterase 8A (Ric8A) is an essential regulator of G protein α-subunits (Gα), acting as a guanine nucleotide exchange factor and a chaperone. Researchers recently derived two crystal structures of Ric8A, one in its apo form and the other in complex with a C-terminal fragment of Gα. These structures reveal two principal domains of Ric8A: an armadillo-repeat domain core and a flexible C-terminal tail. Additionally, they show that the Gα C-terminus binds to a highly conserved portion of the concave surface of the Ric8A armadillo-domain, with selectivity determined by specific residues of the Gα sequence. Small-angle x-ray scattering (SAXS) carried out at the APS revealed conformational changes in the Ric8A C-terminal tail, which are critical for the protein stability and function. A model of the Ric8A/Gα complex derived from mass spectrometry and molecular dynamics simulations suggests that the Ric8A C-terminal tail helps organize the GTP-binding site of Gα. This study lays the groundwork for understanding Ric8A function at the molecular level.

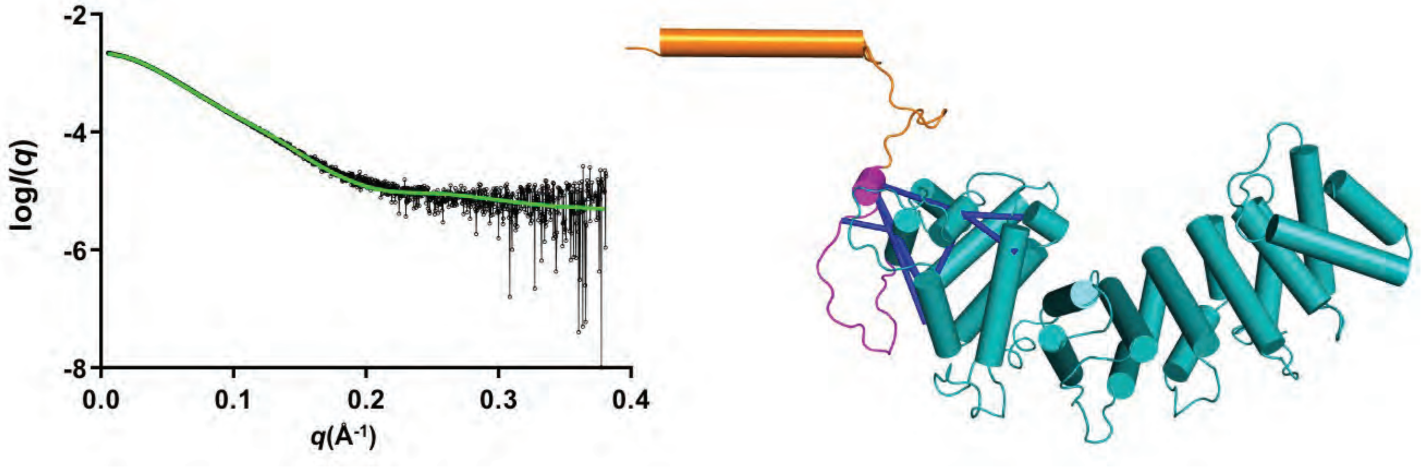

Fig. 1. (Left) Experimental SAXS profile (black curve) of Ric8A. Theoretical scattering profile the Ric8A model is shown in green. (Right) Model of Ric8A based on SAXS data. Essential functional segments of the Ric8A C-terminal tail are shown in magenta and orange.

Heterotrimeric G proteins, composed of Gα, Gβ, and Gγ subunits, relay the vast majority of intracellular signaling mediated by G protein-coupled receptors (GPCRs). GPCRs respond to a wide variety of extracellular stimuli, including light, ions, hormones, neurotransmitters, and natural chemicals. In turn GPCRs couple primarily to G proteins to facilitate the exchange of GDP for GTP on the Gα subunit, leading to downstream signaling through binding to effectors such as adenylyl cyclase, phospholipase C, and ion channels.

Because heterotrimeric G proteins undergo extensive conformational changes during highly tuned receptor coupling and dissociation, there has evolved robust quality control mechanisms for their structural and functional integrity. Previous studies have shown that multiple chaperones are necessary for proper folding, assembly, and localization of heterotrimeric G proteins.
Chaperonin-containing tailless complex polypeptide-1 (CCT) and dopamine receptor-interacting protein 78 (DRiP78) have been proposed to facilitate the folding of Gβ and Gγ subunits, respectively, while the chaperone phosducin-like protein-1 (PhLP-1) is subsequently involved in the formation of the Gβγ obligate heterodimer.

What about Gα subunits? Resistance to inhibitors of cholinesterase-8 (Ric-8) was initially discovered as a gene that positively influenced G protein signaling pathways in the worm *Caenorhabditis elegans*. Ric-8 proteins, which are evolutionarily conserved from fungi to humans, are now known to fold nascent Gα subunits prior to G protein heterotrimer formation. The initial *in vitro* work identified Ric-8 as a non-receptor guanine exchange factor (GEF) for Gα proteins, but more recent studies revealed that Ric-8 proteins are molecular chaperones for nascent Gα subunits, thereby explaining the positive influence of their activities on G protein signaling. Besides facilitating Gα subunit folding, the observed Ric-8 GEF activity for Gα subunits has raised the possibility that these chaperones may also be involved in alternative modes of Gα subunit activation or re-amplification of GPCR signaling.

Whereas the genomes of invertebrates encode a single ancestral Ric-8 isoform that is capable of interacting with Gα subunits of all types, their vertebrate counterparts encode two isoforms, each of which regulates a particular subset of Gα subunits: Ric-8A ($G\alpha_{i/t}$, $G\alpha_q$, and $G\alpha_{12/13}$) and Ric-8B ($G\alpha_s$). The interaction of Ric-8 with GDP-bound Gα stimulates release of GDP, leading to the formation of a stable intermediate complex of Ric-8 and nucleotide-free Gα. Once Gα binds GTP it dissociates from Ric-8, and thus the nucleotide-exchange cycle on Gα is completed.

However, the lack of structural information on full-length Ric-8-Gα complexes has hindered understanding of the chaperone activity and the mechanism of Gα release from Ric-8, which presumably takes place upon successful Gα folding. To gain mechanistic insights into the function of Ric-8 and its interaction with Gα, researchers at the University of Iowa Carver College of Medicine used small-angle x-ray scattering studies performed at the Bio-CAT beamline 18-ID-D at the APS to demonstrate critical conformational changes in the C-terminal tail of Ric8A that are important for the stability of the protein overall, and key for its GEF function (Fig. 1).

They also employed beamline 4.2.2 at the DOE's Advanced Light Source to solve the crystal structures of both apo Ric-8A and Ric-8A in complex with the C-terminal fragment of transducin-α ($G\alpha_t$) attached to a maltose-binding protein (MBP) tag. These structures revealed that Ric-8A has two major modules: the core armadillo/HEAT-repeat domain, and a flexible C-terminal tail. In addition, they show that the concave surface of the Ric-8A armadillo domain encompasses a conserved binding site for the C-terminus of Gα.

Modeling of the Ric-8A/Gα complex and flexible C-terminal tail of Ric-8A provides a foundation for understanding the molecular mechanisms that underlie the stability, GEF function, and chaperone function of Ric-8A.

– Chris Palmer

See: Dhiraj Srivastava, Lokesh Gakhar, and Nikolai O. Artemyev*, "Structural underpinnings of Ric8A function as a G-protein α-subunit chaperone and guanine-nucleotide exchange factor," Nat. Commun. **10**, 3084 (2019). DOI: 10.1038/s41467-019-11088-x

Author affiliation: University of Iowa Carver College of Medicine
Correspondence: * nikolai-artemyev@uiowa.edu

This work was supported by the National Institutes of Health grant RO1 EY-12682 to N.O. A. We thank Jay Nix (Molecular Biology Consortium 4.2.2 beamline at the Advanced Light Source) for aid in remote data collection, and Srinivas Chakravarty (Bio-CAT) for help in SAXS data collection. The work at Bio-CAT was supported by grant 9 P41 GM103622 from the National Institute of General Medical Sciences (NIGMS) of the National Institutes of Health. Use of the Pilatus 3 1M detector was provided by grant 1S10OD018090–01 from NIGMS. This research used resources of the Advanced Light Source, a U.S. Department of Energy (DOE) Office of Science user facility under Contract DEAC02–05CH11231, and resources of the Advanced Photon Source, a U.S. DOE Office of Science User Facility operated for the DOE Office of Science by Argonne National Laboratory under Contract No. DE-AC02–06CH11357.

Is it Better to Salvage or Make it From Scratch?

"Salvage" is a word that conjures images of junkyards where enterprising people find new gold in the old glory of worn out automobiles and appliances. In the world of biochemistry, the connotations are a bit different. Salvage may involve the development of energy-saving shortcuts or complex commensal relationships where one of two organisms benefits and the other derives neither benefit nor harm. But the idea is the same; how can we save time and energy by salvaging cast-offs? In biochemistry, as in automobiles, the answers are varied and reflect the specific needs and lifestyles of different organisms. Recently, work from an international team of researchers, including studies at the APS, has highlighted some of this variation by demonstrating how bacteria salvage precursors that allow the synthesis of the modified base of tRNA, queuosine (Q), that enhances the efficiency of protein synthesis. The work reveals the different ways that organisms make and salvage Q and its precursors to build pathways that match their lifestyles. It may also provide insights into how this unique micronutrient plays a role in bacterial pathogenesis and other cellular processes that impact health such as stress responses, cell proliferation, and cell signaling.

The Q pathway has been known for some time, but its physiological importance is not well understood. Organisms from bacteria to humans use Q to modify tRNAs involved in protein synthesis to enhance the speed and accuracy of the process. However, making this modification comes at some cost in terms of biosynthetic enzymes, cofactors, and energy, and some organisms, including humans, do not make Q but salvage Q precursors instead. For example, humans use a pathway common to eukaryotes to get the immediate precursor to Q (queuine, or q) from dietary sources and from commensal bacteria that live in our gut. The precursor q is now recognized as an important nutrient and is so beneficial that it has recently been called a "longevity" vitamin. Although many bacteria can make Q themselves, it is now becoming clear that this is not true for all bacterial species. This work highlights the fact that some bacteria, including many pathogens, have developed pathways to salvage Q precursors and are thus part of the competition for these precious raw materials (Fig. 1).

This work was based on earlier analyses of the genomes of over 10,000 types of bacteria that showed that some bacteria don't have all of the genes to make Q themselves. The team investigated the Q pathways for two pathogenic bacteria, *Chlamydia trachomatis* and *Clostridiodes difficile*, that lack the suite of enzymes for Q biosynthesis normally found in bacteria but do have genes that suggest they might salvage Q precursors from the environment. For *C. trachomatis*, gene analysis showed that this intracellular bacterial pathogen makes an enzyme that is similar to the one that uses the q precursor to make Q-modified tRNA in eukaryotes. Structural modeling showed that q could be docked in the enzyme, supporting its specificity for q and suggesting that *C. trachomatis* must salvage this precursor. This makes sense as *C. trachomatis* lives inside the cells of other organisms where q is probably available in the environment. To complete this unique Q pathway, the team identified the gene responsible for salvaging q and demonstrated that the two genes together were able to reconstitute the Q modification pathway in a model system.

In *C. difficile*, an important gastrointestinal pathogen, the researchers found a gene that incorporates the usual bacterial Q precursor for tRNA modification (preQ1) but lacks many of the enzymes for making the precursors in the biosynthetic pathway, suggesting some of these must be salvaged. *C. difficile* solves the precursor problem by making an enzyme that converts salvaged Q to q, and then another novel enzyme with previously unreported activity that converts q to preQ1. The team solved the crystal structure of this interesting new enzyme based on diffraction data collected at the LRL-CAT beamline 31-ID-D at the

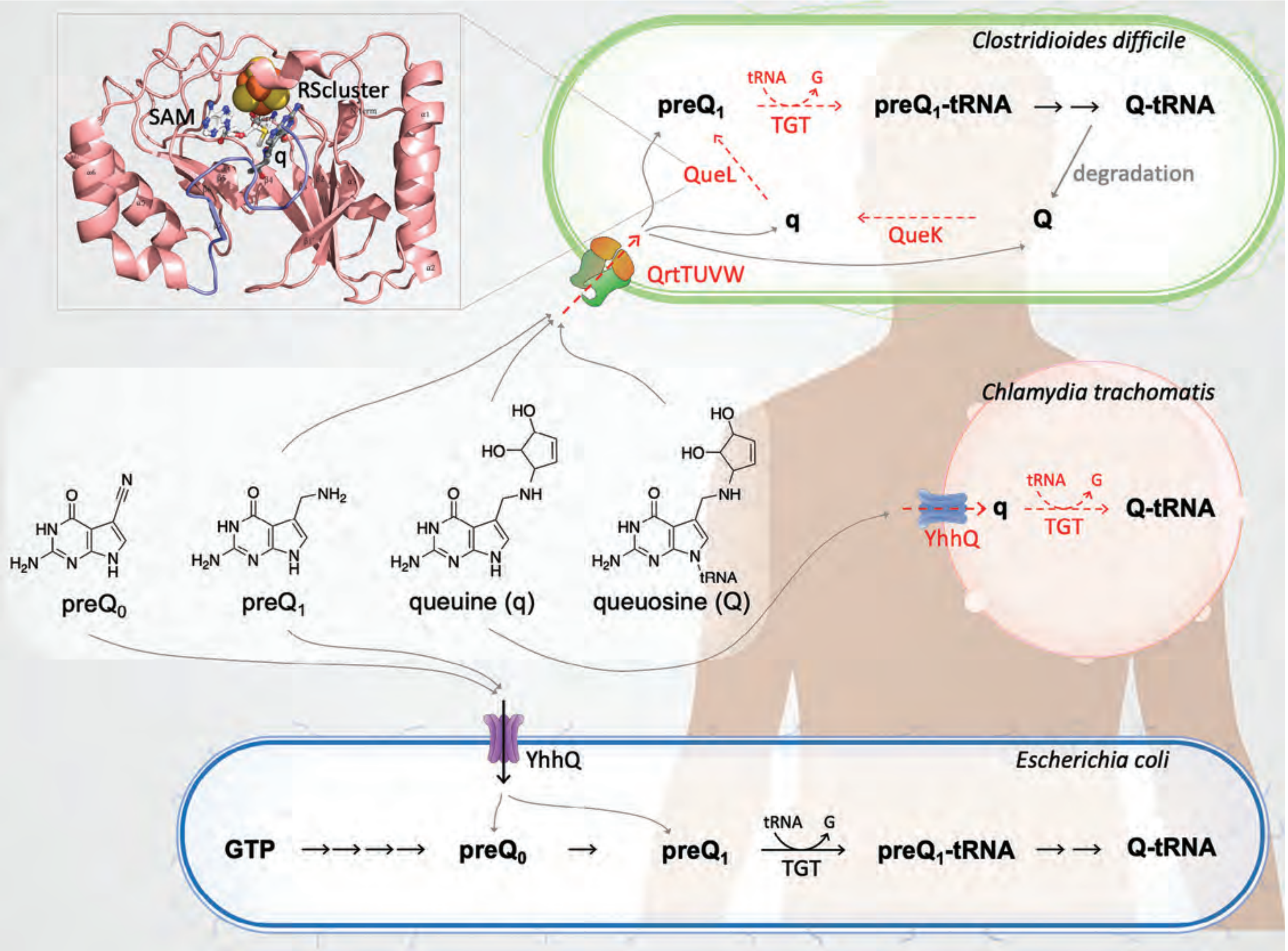

Fig. 1. Unique pathways for Q salvage and biosynthesis in *C. difficile*, *C. trachomatis*, and *E. coli* demonstrate the variety of approaches used by bacteria to make the precursors needed for the Q modification of tRNA that enhances the efficiency of protein synthesis. This work identified a new enzyme activity (ribbon structure shown in inset) that converts salvaged materials to required precursors.

APS and showed that it is a member of a known family but has unique properties.

Together, these studies show the incredible ability of biological systems to come up with creative new solutions that make the best use of the natural resources at hand.

– Sandy Field

See: Yifeng Yuan[1], Rémi Zallot[2], Tyler L. Grove[3], Daniel J. Payan[2], Isabelle Martin-Verstraete[4], Sara Šepić[1], Seetharamsingh Balamkundu[5], Ramesh Neelakandan[5], Vinod K. Gadi[5], Chuan-Fa Liu[5], Manal A. Swairjo[6], Peter C. Dedon[5,7], Steven C. Almo[3], John A. Gerlt[2], and Valérie de Crécy-Lagard[1,8]*, “Discovery of novel bacterial queuine salvage enzymes and pathways in human pathogens,” Proc. Natl. Acad. Sci. U.S.A. **116**(38), 9126 (September 17, 2019). DOI: 10.1073/pnas.1909604116

Author affiliations: [1]University of Florida, [2]University of Illinois at Urbana–Champaign, [3]Albert Einstein College of Medicine, [4]Institut Pasteur et Université de Paris, [5]Singapore-MIT Alliance for Research and Technology, [6]San Diego State University, [7]Massachusetts Institute of Technology, [8]University of Florida Genetics Institute

Correspondence: * vcrecy@ufl.edu

This work was funded by the National Institutes of Health (R01 GM70641 to V.d.C.-L.; P01 GM118303 to J.A.G. and S.C.A.; U54-GM093342 to J.A.G. and S.C.A.; R21-AI133329 to T.L.G. and S.C.A.; U54-GM094662 to S.C.A.; GM110588 to M.A.S.), the Price Family Foundation (S.C.A.), and the California Metabolic Research Foundation (M.A.S.). We acknowledge the Albert Einstein Anaerobic Structural and Functional Genomics Resource (http://www.nysgxrc.org/psi3/anaerobic.html). Use of the Lilly Research Laboratories Collaborative Access Team beamline at the APS was provided by Eli Lilly Company, which operates the facility. This research used resources of the Advanced Photon Source, a U.S. Department of Energy (DOE) Office of Science User Facility operated for the DOE Office of Science by Argonne National Laboratory under Contract No. DE-AC02-06CH11357.

How Bacteria Deploy a Novel Toxin to Inhibit the Growth of Rivals

Bacteria have evolved sophisticated methods for attacking and outcompeting neighboring cells. One such mechanism involves type VI secretion systems, which inject neighbors with toxins that can inhibit their growth or kill them. Many of these toxins exploit weaknesses in their neighbors' cell envelopes, but the full range of growth inhibitory mechanisms remains unknown. Researchers identified a novel type VI secretion effector, Tas1, in the pathogen *Pseudomonas aeruginosa* and, using the APS, determined the crystal structure to 2.2-Å resolution. They found that it shows a striking similarity to enzymes that synthesize (p)ppGpp, a group of widely conserved signaling molecules in bacteria that modulate cell growth rate, particularly in response to nutritional limitations. However, Tas1 is not involved in the synthesis of (p)ppGpp. Rather, Tas1 uses energy-carrying adenosine triphosphate (ATP) molecules to overproduce the signaling molecule (p)ppApp, a process that rapidly reduces ATP levels in host cells. In turn, (p)ppApp actively blocks production of ATP. The result of this two-pronged attack is the disruption of several essential pathways in the target cell, ultimately resulting in cell death within minutes. The discovery of Tas1 has potential implications for developing alternatives to antibiotics, which is a global priority in the fight against drug-resistant bacteria.

To ensure their own survival, bacteria must monopolize valuable resources. One way they do this is by inhibiting the growth of competitors. Using needle-like molecular machines, called "type VI secretion systems," bacteria inject antibacterial toxins directly into nearby cells. These toxins often destroy essential cellular structures, such as the cell wall, the cell membrane, or the genome itself.

During the investigation of a highly virulent strain of *P. aeruginosa*, researchers identified a region of the bacterium's genome that encodes the protein type VI secretion effector (p)ppApp synthetase, or Tas1, that allowed *P. aeruginosa* to outcompete other bacteria. Surprisingly, the amino acid sequence of Tas1 did not resemble any other type VI secretion system proteins.

After deriving the crystal structure of Tas1 (Fig. 1) using the SBC-XSD beamline 19-ID of the APS, it was clear that the toxin is structurally similar to a class of enzymes that synthesizes the molecules guanosine tetraphosphate (ppGpp) and guanosine pentaphosphate (pppGpp), collectively referred to as (p)ppGpp. Bacteria typically produce these so-called "alarmone" signaling molecules during times of stress or nutrient limitation. They inhibit various growth mechanisms, preventing excessive proliferation and allowing bacteria to survive in low-nutrient conditions. However, rather than synthesizing (p)ppGpp, Tas1 pyrophosphorylates adenosine nucleotides to produce adenosine tetraphosphate (ppApp) and adenosine pentaphosphate (pppApp) molecules—collectively referred to as (p)ppApp—at the scorching rate of nearly 180,000 molecules per minute. This process depends on ATP, meaning the rapid accumulation of (p)ppApp depletes the cell of its stores of ATP. In addition, (p)ppApp actually prevents the production of ATP by inhibiting the first enzyme in an ATP-synthesis pathway, a purine biosynthetic enzyme called PurF. So, the end result of Tas1 injection is widespread dysregulation of essential metabolic pathways, leading to rapid target cell death.

Additional structural analysis of the PurF-(p)ppApp binding interface, resulting from the 2.5-Å-resolution crystal structure obtained at the NE-CAT beamline 24-ID-C at the APS, suggested that (p)ppApp is likely to bind to many other (p)ppGpp binding proteins, further enhancing the toxicity of this molecule.

Tas1 is the first example of an alarmone-producing enzyme being transported between bacteria. So, not only does this study offer a broader understanding of how alarmone regulatory pathways rewire bacterial physiology, it represents a novel form of type VI secretion signaling mol-

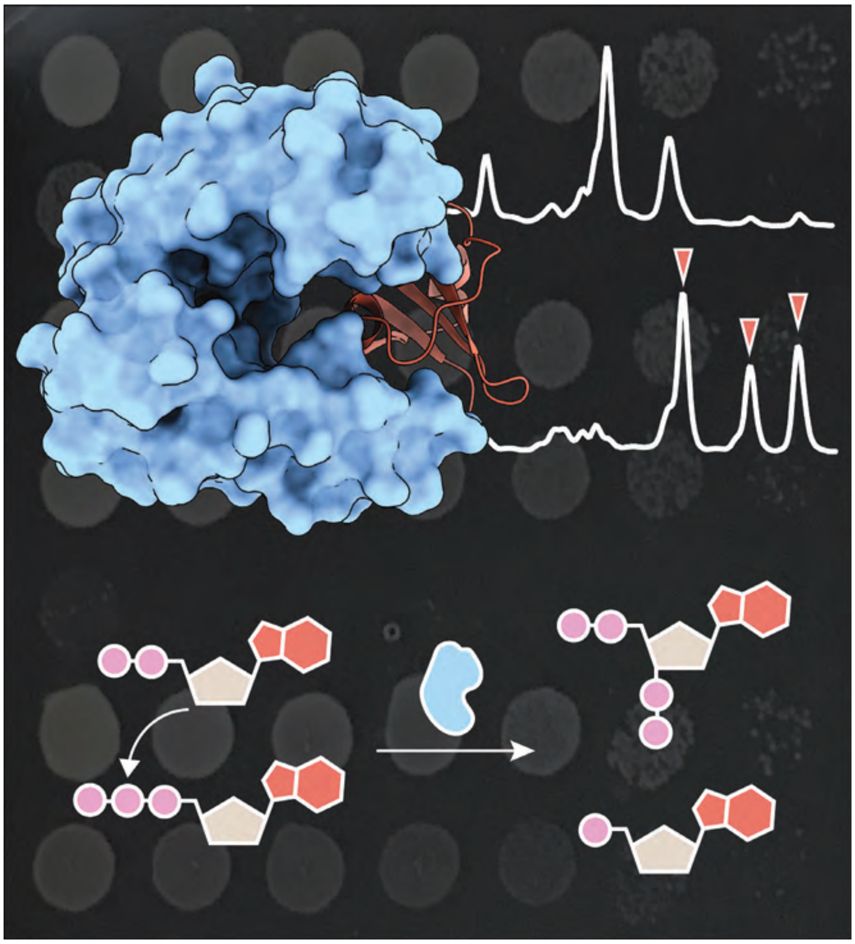

ecules that may be exploited as a means to fight bacterial infections that are otherwise resistant to existing antimicrobials. – Chris Palmer

See: Shehryar Ahmad[1], Boyuan Wang[2], Matthew D. Walker[1], Hiu-Ki R. Tran[1], Peter J. Stogios[3,4], Alexei Savchenko[3,4,5], Robert A. Grant[2], Andrew G. McArthur[1], Michael T. Laub[2]*, and John C. Whitney[1]**, "An interbacterial toxin inhibits target cell growth by synthesizing (p)ppApp," Nature **575**, 674 (28 November 2019). DOI: 10.1038/s41586-019-1735-9

Author affiliations: [1]McMaster University, [2]Massachusetts Institute of Technology, [3]University of Toronto, [4]Center for Structural Genomics of Infectious Diseases, [5]University of Calgary
Correspondence: * laub@mit.edu, ** jwhitney@mcmaster.ca

S.A. and B.W. were supported by an Ontario Graduate Scholarship and a fellowship from the Jane Coffin Childs Memorial Fund, respectively. A.G.M. holds a Cisco Research Chair in Bioinformatics and M.T.L is an Investigator of the Howard Hughes Medical Institute. SBC-XSD is funded by the U.S. Department of Energy (DOE) Office of Biological and Environmental Research. NE-CAT is funded by the National Institute of General Medical Sciences from the National Institutes of Health (P30 GM124165). This work was supported by grants from the Canadian Foundation for Innovation (34531 to A.G.M.), NIH (R01-GM082899 to M.T.L.) and CIHR (PJT-156129 to J.C.W.), and by seed funding from the David Braley Centre for Antibiotic Discovery (to J.C.W.). This research used resources of the Advanced Photon Source, a U.S. DOE Office of Science User Facility operated for the DOE Office of Science by Argonne National Laboratory under Contract No. DE-AC02-06CH11357.

Fig. 1. Crystal structure of the complex between Tas1 (top left, blue), and its cognate immunity protein Tis1 (top left, orange). Tas1 rapidly synthesizes (p)ppApp once injected into a target bacterial cell. The production of these nucleotides was tracked using anion-exchange chromatography (top right), where *E. coli* expressing the toxin for 30 minutes (bottom trace) showed a high abundance of the (p)ppApp nucleotides (red arrows indicating, from left to right pApp, ppApp and pppApp). Top trace indicates the nucleotide pool just before induction of expression. The synthesis of these nucleotides depletes their substrates ADP and ATP, causing an irreversible change to the cellular metabolome and subsequent cell death. The cartoon at the bottom depicts ppApp catalysis by Tas1 (blue enzyme, above straight arrow). The 3′-hydroxyl group of ADP (top left) attacks the pyrophosphate in an ATP molecule (bottom left), resulting in ppApp (top right) and AMP (bottom right) formation. Pink circles; phosphate groups, brown pentagon; ribose, red hexagon and pentagon; adenine base.

Could Crystallized Structures of Fungal-Repair Proteins Accelerate Antifungal Drug Discoveries?

DNA is the genetic code used to generate RNA by a process known as transcription. After RNA is transcribed from DNA, it can be utilized to create proteins via the translation process. Although some types of RNA can independently carry out important functions, proteins represent functional products and can be conceptualized as the primary molecular workers in any biological system. These fundamental processes form the basis of biological life and their disruption can give rise to significant dysfunction and disease. Carrying out research at the APS, a group published two high-impact studies of a unique fungal RNA protein. This protein, referred to as tRNA ligase, is an essential enzyme that repairs broken RNA molecules by connecting them back together. In the first study, the group characterized the crystallized structures of a particular domain of this ligase. They discovered that the restorative function of this enzyme requires a unique mechanism involving two metals. In the latter study, they unveiled the crystallized structure of two of the three domains of tRNA ligase. This enabled them to further characterize this protein and also to identify how these two domains are connected to each other. Since tRNA ligase enzymes are commonly found in human fungal pathogens, these findings have important implications for antifungal clinical therapies.

The term RNA is an abbreviation for ribonucleic acid, which is composed of polymers from the following four different repeating subunits: adenine, cytosine, guanine, and uracil. Polymeric chains of RNA play multiple functions in biology. Certain types of RNA, dubbed messenger RNA (mRNA), are translated into protein macromolecules. These proteins go on to carry out important, diverse functions. Other types of RNA serve regulatory functions, such as microRNAs and long non-coding RNAs. These RNA types can regulate the expression of genes and therefore affect how much protein is ultimately generated. Other versions of RNA, like transfer RNA (tRNA), are involved in the synthesis of proteins. Specifically, tRNA binds to mRNA at the ribosome and then transfers amino acid subunits to a growing molecular chain that ultimately becomes a protein.

Relevant to RNA, ligase enzymes connect two different strands of molecules. Thus, the fungal tRNA ligase Trl1 is responsible for repairing breaks in both tRNA and mRNA in fungus. It does this by ligating, or connecting, two different strands of disconnected RNA. Trl1 comprises three autonomous catalytic modules which perform three separate reactions: an N-terminal ligase, a central polynucleotide kinase, and a C-terminal cyclic phosphodiesterase domain. While Trl1 ligases are chemically similar among human fungal pathogens, no homolog exists in humans, making them a clinically relevant and unique drug target. Therefore, a greater understanding of this enzyme could allow for the development of novel, effective antifungal therapies which would not cross-react with human proteins.

The two papers by this research team provided substantial insights into the structure of tRNA ligase (Fig. 1). In the first publication [1], the authors generated novel crystal structures of the N-terminal ligase domain of this Tr1 from *Chaetomium thermophilum* to capture a catalytic intermediate in the ligation reaction. In this intermediate step, they discovered a substrate-enzyme complex where two manganese metals are required to stabilize the transition state of the RNA-repair reaction. Chemical analogs which disrupt the transition state in an enzyme reaction are a common therapeutic target making this structure a boon for structure-based drug design of anti-fungals.

In the second publication [2], the authors expand upon this work by generating additional crystal structures from the pathogenic fungus *Candida albicans*. Unlike the

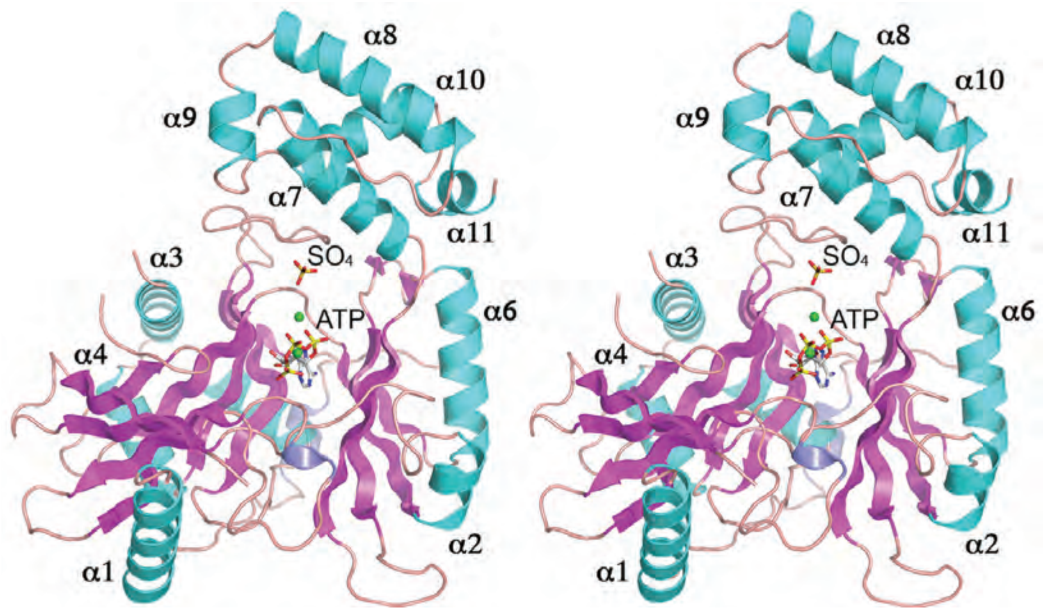

Fig. 1. Ribbon model of the Trl1-LIG structure with magenta β strands, cyan α helices, and blue 3_{10} helices, as determined at NE-CAT at the APS. The ATP in the active site and a nearby sulfate anion are shown as stick models. Mn^{2+} ions are shown as green spheres.

first study, which formed a crystal structure of the N-terminal ligase domain, this latter work focused on the central polynucleotide kinase and C-terminal cyclic phosphodiesterase domains. With this first atomic structure of a RNA phosphodiesterase domain, they were able to identify multiple active site motifs. An active site in an enzyme is where another molecule, termed a substrate, can bind and affect the function of that protein. These are therefore important regulatory sites that are paramount for drug discovery. Further study of these structures also revealed unique conformational changes that occur in the kinase domain upon binding of substrate at the substrate-binding pocket which makes this pocket an excellent drug-target candidate.

Both of these seminal studies were done at the NE-CAT 24-ID-C and 24-ID-E x-ray beamlines at the APS. For the first paper, x-ray diffraction data were collected from individual crystals. In the second manuscript, single crystals were again analyzed to yield x-ray diffraction data at this same beamline. These x-ray diffraction experiments were imperative for uncovering precise atomic details in the crystallized protein domains of the tRNA ligase Trl1.

In addition to broadening our scientific understanding of protein structures and providing evolutionary insights into protein formation in fungal organisms, the structural insights gleaned from these two studies have important implications for drug discovery. Now that detailed crystal structures have been created, follow up work has the capacity to identify unique anti-fungal drugs. The development of such drugs could help minimize the severity of fungal infections and improve patient outcomes.

– Alicia Surrao

See:

[1] Ankan Banerjee[1], Yehuda Goldgur[1], Beate Schwer[2], and Stewart Shuman[1],* “Atomic structures of the RNA end-healing 5′-OH kinase and 2′,3′-cyclic phosphodiesterase domains of fungal tRNA ligase: conformational switches in the kinase upon binding of the GTP phosphate donor,” Nucleic Acids Res. **47**(22), 11826 (2019). DOI: 10.1093/nar/gkz1049

Author affiliations: [1]Sloan-Kettering Institute, [2]Weill Cornell Medical College

Correspondence: * s-shuman@ski.mskcc.org

Funding was provided by the National Institutes of Health (NIH, R35-GM126945 to S.S.); Geoffrey Beene Cancer Research Center (to S.S.); Deutsche Forschungsgemeinschaft [394320208 to A.B.]; MSKCC structural biology core laboratory is supported by National Cancer Institute [P30-CA008748]; NE-CAT is funded by the National Institute of General Medical Sciences from the National Institutes of Health (P30 GM124165). The Eiger 16M detector on 24-ID-E is funded by a NIH-ORIP HEI grant (S10OD021527). This research used resources of the Advanced Photon Source, a U.S. Department of Energy (DOE) Office of Science User Facility operated for the DOE Office of Science by Argonne National Laboratory under contract no. DE-AC02-06CH11357.

[2] Ankan Banerjee[1], Shreya Ghosh[1], Yehuda Goldgur[2], and Stewart Shuman[1],* “Structure and two-metal mechanism of fungal tRNA ligase,” Nucleic Acids Res. **47**(3), 1428 (2019). DOI: 10.1093/nar/gky1275

Author affiliation: Sloan-Kettering Institute

Correspondence: * s-shuman@ski.mskcc.org

Funding was provided by the National Institutes of Health [R35-GM126945 to S.S.]; Geoffrey Beene Cancer Research Center (to S.S.); The MSKCC structural biology core laboratory is supported by National Cancer Institute [P30-CA008748. NE-CAT is funded by the National Institute of General Medical Sciences from the National Institutes of Health (P30 GM124165). The Eiger 16M detector on 24-ID-E is funded by a NIH-ORIP HEI grant (S10OD021527). This research used resources of the Advanced Photon Source, a U.S. DOE Office of Science User Facility operated for the DOE Office of Science by Argonne National Laboratory under Contract No. DE-AC02-06CH11357.

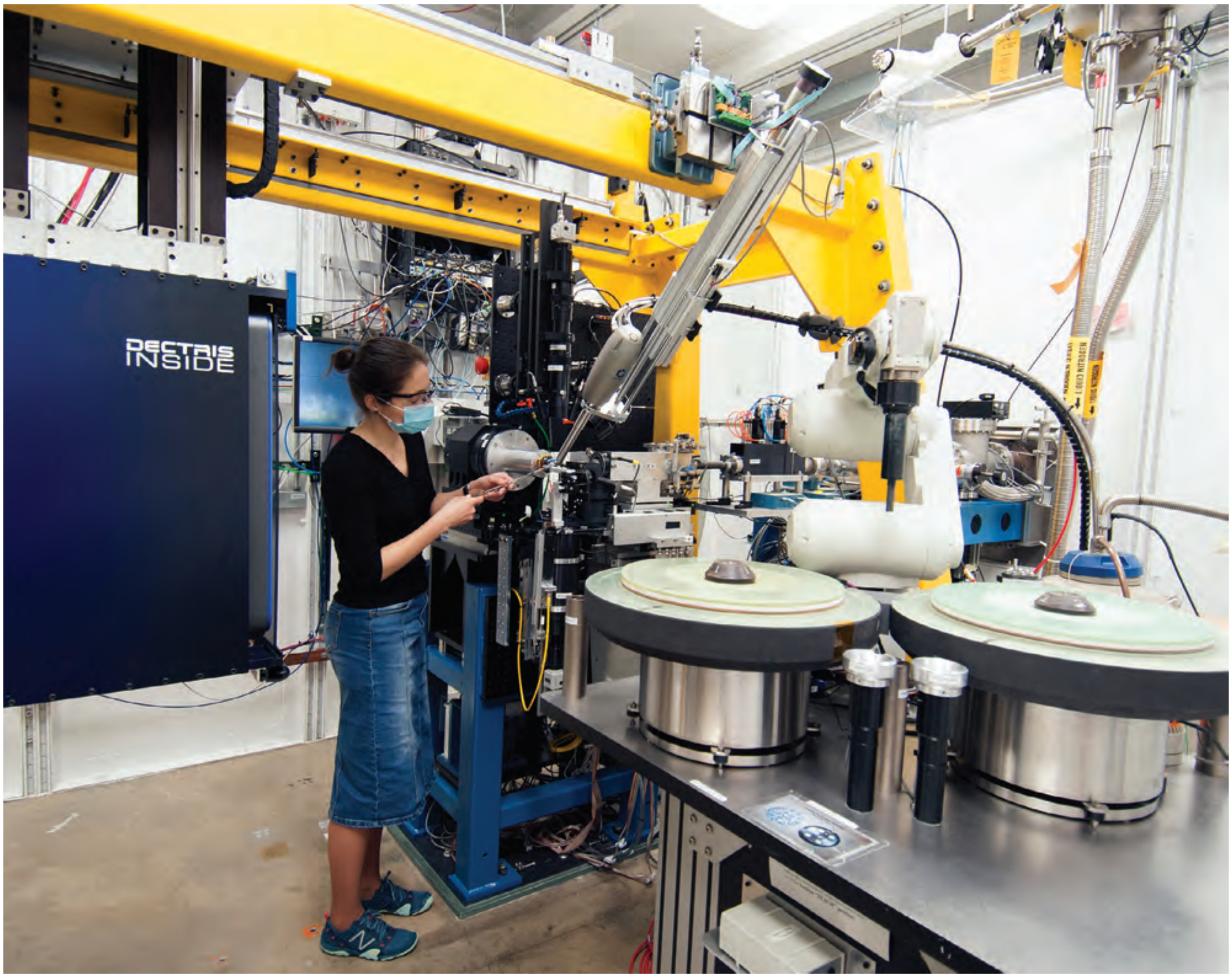

Robotic Sample-Handling for SARS-CoV-2 Studies at SBC-XSD Beamline 19-ID

Karolina Michalska, SBC-XSD physicist, checks the positioning of a unipuck containing an inert SARS-CoV-2 protein crystal in the 19-ID-D research station. The unipuck was mounted on a sample stage by the robot arm (center in the photo), which plucked it from one of the dewars in the right foreground. When the research station is cleared of occupants and the lead shielding door is closed, a beamline shutter will be opened, admitting high-brightness x-rays that will strike the crystal and create diffraction data to be collected by the detector at left in the photo, and transmitted to data collection software for later analysis.

Environmental, Geological, and Planetary Science

gsecars_pnas 116 19324

Using an Analog to Investigate the Interiors of "Super-Earths"

$MgSiO_3$ perovskite, also known as bridgmanite, is thought to be the most abundant mineral in the Earth's lower mantle. At the high pressures and temperatures of the lowermost mantle, about 150 km below the Earth's surface, bridgmanite undergoes a phase transition, or a rearrangement of its structure, into a phase known as post-perovskite (pPv). Although pPv is most likely the final silicate phase in the Earth's interior, other "post-post-perovskite" phases may exist in the interiors of much larger rocky planets ("super-Earths" up to ~10 Earth masses in size) recently discovered outside our solar system. Laboratory experiments to replicate the interior conditions of these giant planets (up to ~4000 GPa pressure, ~10,000 K temperature) are extremely challenging and generally beyond the reach of even state-of-the-art experimental techniques for static compression, so the predicted phases for $MgSiO_3$ have largely been based on quantum mechanical computations without experimental validation. One way to get around this conundrum is to perform experiments using analogs of bridgmanite that might display similar phase transitions but at lower pressures and temperatures. One of these suitable analogs is neighborite, or $NaMgF_3$. Scientists used the APS to probe the structural changes of neighborite *in situ* at extreme conditions. Their results show that neighborite undergoes multiple pressure-induced phase transitions and eventually decomposes into a mixture of binary fluorides. These results using neighborite as an analog could aid in understanding the possible phase transitions and their effects in the interiors of the super-Earths.

This page: Artist's rendering of Planet Nine alongside Earth. https://bit.ly/2B1BJpQ

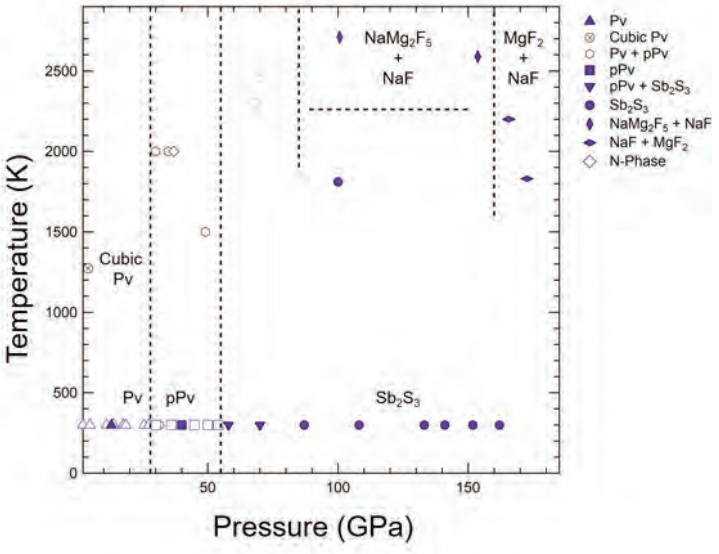

Fig. 1. Summary of constraints on the high-pressure-temperature phase diagram of $NaMgF_3$. The solid symbols (triangles: perovskite, star: post-perovskite, circles: Sb_2S_3, inverted triangle: pPv + Sb_2S_3, vertical diamonds: $NaMg_2F_5$ + NaF and horizontal diamonds: NaF + MgF_2) represent the present experimental data. Open symbols red, blue, and green show experimental literature data for the respective phases. The brown open circle indicates the high-temperature cubic phase. The dashed black lines are schematic phase boundaries. From R. Dutta et al., "Phase transitions beyond post-perovskite in $NaMgF_3$ to 160 GPa," Proc. Natl. Acad. Sci. USA **116** (39), 19324 (2019). ©2019 National Academy of Sciences

$NaMgF_3$ adopts the perovskite (Pv) structure at ambient pressure and undergoes a pressure-induced phase transition to a pPV form at only 19 GPa at room temperature, compared to ~125 GPa and 2000 K for bridgmanite. Determining what phase transitions neighborite undergoes as pressure and temperature increase could provide insight into bridgmanite's post-post-perovskite phases.

For these experiments, the researchers from Princeton University and The University of Chicago placed neighborite into a diamond anvil cell, a device that can generate extraordinarily high pressures. The researchers then ratcheted up the pressure to ~160 GPa, inducing high temperatures (~2710 K) with a laser toward the pressure peak to test the stability of the resulting phases, and collected x-ray diffraction (xrd) data at the GSECARS 13-ID-D x-ray beamline at the APS.

At room temperature and 13 GPa, the XRD patterns matched those of neighborite's Pv structure identified in previous studies. Upon further compression to 40 GPa, the diffraction pattern changed, indicating a pressure-induced phase transition. The researchers were able to index this pattern to a pPv structure identified in a previous study.

However, at 58 GPa, the diffraction pattern could not be indexed solely using results from previous studies. Any remnants of the known patterns completely faded at ~90 GPa, indicating the presence of a new phase. Theoretical predictions suggest that this phase is an Sb_2S_3-type, with a structure akin to the mineral stibnite. As the researchers continued to incrementally raise the pressure, they heated the sample with a laser to ~1810 K for 30 min and ~2710 K for 20 min, showing that this phase remained stable even under prolonged heating.

When the researchers maintained the pressure at ~90 GPa and raised the temperature to ~2590 K, an NaF peak appeared in the diffraction results, suggesting that the compound had at least partially dissociated. Indexing suggests that the other compound in the sample is $NaMg_2F_5$. This diffraction pattern remained stable at ~134 GPa, but changed again at ~162 GPa at ~1830 K, with indexing suggesting that this sample contained a mixture of NaF and MgF_2. Figure 1 shows the proposed phase diagram in $NaMgF_3$.

These findings from neighborite closely match theoretical studies of bridgmanite, which suggest that this perovskite also undergoes similar kinds of phase transitions that culminate into a two-stage breakdown into binary compounds.

The different bridgmanite phase transitions could significantly affect mantle dynamics, playing a key role in layering and viscosity, which in turn affect heat flow and long-term thermal evolution, and adding to our understanding of the super-Earths that lurk beyond our solar system.

– Christen Brownlee

See: Rajkrishna Dutta[1], Eran Greenberg[2], Vitali B. Prakapenka[2], and Thomas S. Duffy[1], "Phase transitions beyond post-perovskite in $NaMgF_3$ to 160 GPa," Proc. Natl. Acad. Sci. U.S.A. **116** (39), 19324 (2019). DOI: 10.1073/pnas.1909446116

Author affiliation: [1]Princeton University, [2]The University of Chicago
Correspondence: * rdutta@carnegiescience.edu

This work was funded by National Science Foundation (NSF) Grants EAR-1644614 and EAR-1836852. GeoSoilEnviroCARS is supported by NSF Earth Sciences Grant EAR-1634415 and the U.S. Department of Energy (DOE) Geosciences Grant DE-FG02-94ER14466. The gas-loading facility at GSECARS is partially supported by the Consortium for Materials Properties Research in Earth Sciences under NSF Cooperative Agreement EAR-1606856. This research used resources of the Advanced Photon Source, a U.S. DOE Office of Science User Facility operated for the DOE Office of Science by Argonne National Laboratory under Contract No. DE-AC02-06CH11357.

Oil Blob Imagery for Assessing Surfactant-Enhanced Aquifer Remediation

Oil pipelines and fracking operations frequently make headlines because of their potential for, and past history of, groundwater contamination, an enormous public safety hazard. Remediation processes exist but aren't necessarily well-understood. One such process, surfactant-enhanced aquifer remediation, injects surfactants – substances that lower the surface tension between liquids – into the contaminated soil or aquifer and then relies on flushing to displace and extract the hopefully modified, more-mobile oil-phase contaminant from the system. But how exactly do oil drops, wetting agents, and soil make-up interact on the scale at which this technique works? Recent research at the APS provides images of the oil distribution and how it changes throughout the flushing process, continuing to characterize the circumstances under which this technique is most effective.

In many cases, significant effort is required to remove crude oil from soil and groundwater because it is a non-aqueous phase liquid resistant to mixing with or dissolving in water. As such, these high-viscosity, low-solubility oil phases can essentially become trapped within pore spaces, making it difficult to mobilize when flushing with water alone. Surfactant-enhanced aquifer remediation techniques assume the surfactant will sufficiently lower the interfacial/surface tension of the oil (between aqueous solution and solid media), allowing it to more easily mobilize through the pore networks and/or mix with water (during flushing events), thereby enabling the oil phase to be transported through the sand/soil and removed from the aquifer more expeditiously. A multinational team of researchers assessed the surfactant-enhanced aquifer remediation process on the pore scale to quantify how the distribution of oil trapped in soil is dependent on the size of the physical characteristics of the oil-water-sand system, and how it changes with each flushing event.

To study the effect of these characteristics, the team constructed three experimental setups, added heavy crude oil to them, and flushed them with water several times, taking measurements after each flushing. The setups differ by the amount of unconsolidated sand-size fraction used to define three distinct pore (permeability) configurations: a homogeneous sand (homogeneous), a heterogeneous sand (mildly heterogeneous), an extremely heterogeneous sand (highly heterogeneous). The team's experimental process was to pack columns with the appropriate sand, saturate the column with liquid, add the heavy oil, flush the system with the surfactant, and image the resulting sand and oil network using novel synchrotron x-ray microtomography (SXM) performed at the GSE-CARS 13-BM-D beamline at the APS. The three-dimensional microtomography images allowed the team to measure oil distribution, blob volume, and the number of blobs before and after each surfactant flushing event.

The team's image results showed that the size of an individual oil blob, blob distribution, and the total volume of oil present in the columns were different due to both the specific sand (porous media) configuration in the experimental set-up and the flushing events (Fig. 1).

The oil distribution within the homogenous sand-packed column was predominantly comprised of a single large, interconnected ganglion of oil and progressive surfactant flushing did not do much to fragment distribution (or impart enough interfacial tension reduction effect for removal), so a negligible fraction of the oil was removed during the flushing process.

The oil distribution in the mildly heterogeneous sand-packed column was comprised of many discrete blobs of oil; the percentage of oil saturation was an order of magnitude smaller than in the homogeneous column under the same preparation and experimental conditions. The team found that although progressive surfactant flushing events caused some blob fragmentation and re-distribution, only a negligible relative fraction of heavy oil phase was removed from the system.

The oil distribution in the highly heterogeneous sand-packed column also was initially comprised of many discrete blobs prior to surfactant flushing, under a low oil saturation condition. However, a more pronounced enhanced blob fragmentation resulted after progressive flushing events. In this particular experiment, the flushing events acted first on large blobs, having a greater control on blob fragmentation into smaller blobs and enhanced interfacial reduction effect, leading to the greatest relative oil recovery (percentage of oil removed) for all the flushing experiments.

The team concluded that the heavy crude oil removal efficiency observed in the highly heterogeneous sand-packed column may have occurred due to the higher pH value of the system (a greater percentage of carbonate sand fraction that may have contributed to greater reduction of interfacial effects, i.e., interfacial tension, and more effective fragmentation and relative removal of oil blobs from the system. Conversely, the high permeability of the homogeneous column allowed the oil droplets to stay in contact with one another, thus resisting wetting that may exist under a more oil-wet condition (whereby surface cohesion with solid grains would be greater) and a larger connected oil ganglion that would require exceedingly (unrealistic) high viscous forces to mobilize as a single unit through the porous system, leading to negligibly relative oil removal during progressive surfactant flushing events.

The team was able to evaluate the relative importance of characteristics of the sand-oil system. Their effort demonstrated that an imaging procedure and ability for fluid-fluid quantification, using novel synchrotron x-ray microtomography, can be used to assess how amenable a particular physical environment or condition (such as porosity, permeability, porous media type, pH value, and contaminant type/properties, etc.) would be to surfactant-enhanced aquifer remediation. — Mary Alexandra Agner

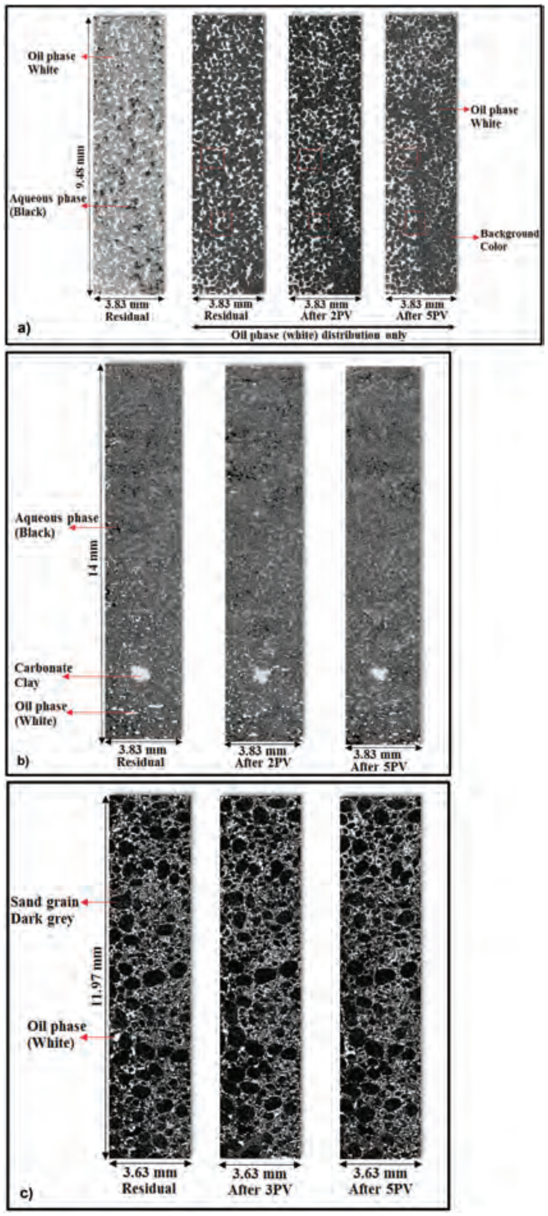

Fig. 1. SXM images of vertical sections of columns along the X-Z direction showing the distribution/saturation of heavy crude oil pre- (initial residual) and post-surfactant flushing: a) homogeneous (H-sand) porous medium (40/50 Accusand, $C_U = 1$) showing trapping of a continuous oil phase. Note, that the first image shows both the aqueous and NAPL (oil) phases for the residual saturation condition and second image shows only NAPL (oil) phase for residual saturation condition. The equilibrium pH over the duration of surfactant flushing ranged between 3.6 and 3.9. b) mildly heterogeneous (MH-sand) porous medium (Accusand/carbonate-fine mix, $C_U = 5.8$) showing discrete fragmentation of oil blobs. The equilibrium pH over the duration of surfactant flushing was approximately 8.13; c) highly heterogeneous (HH-sand) porous medium (Accusand/carbonate-fine mix, $C_U = 10.6$) showing discrete fragmentation of oil blobs. The equilibrium pH over the duration of surfactant flushing was approximately 8.31. The aqueous and oil (NAPL) phases were separated as binary images and then overlain as gray scale images. From J. Ghosh et al., J. Contam. Hydro. **223**, 103471 (2019).

See: Jaydeep Ghosh[1,2], Geoffrey R. Tick[1*], Nihat Hakan Akyol[3], and Yong Zhang[1], "A pore-scale investigation of heavy crude oil trapping and removal during surfactant-enhanced remediation," J. Contam. Hydro. **223**, 103471 (2019).
DOI: 10.1016/j.jconhyd.2019.03.003

Author affiliations: [1]The University of Alabama, [2]Chiang Mai University, [3]Kocaeli University
Correspondence: * gtick@ua.edu

Acknowledgment is made to the donors of the American Chemical Society Petroleum Research Fund for support (or partial support) of this research (Grant PRF# 46670-G8) and collaboration with TUBITAK Project No: 117Y140 and 115Y117. GeoSoilEnviroCARS is supported by the National Science Foundation-Earth Sciences (EAR - 1634415) and U.S. Department of Energy (DOE)-GeoSciences (DE-FG02-94ER14466). We also acknowledge Mark Rivers at GSECARS for providing his invaluable guidance and assistance (i.e., training, image processing, computer code development, etc.). This research used resources of the Advanced Photon Source, a U.S. DOE Office of Science User Facility operated for the DOE Office of Science by Argonne National Laboratory under Contract No. DE-AC02-06CH11357.

When Argonne entered minimum safe operations status in order to minimize on-site personnel in response to the COVID-19 pandemic, a rotating number of APS technical staff were among those who came on site to keep the APS operational in support of the critical novel coronavirus-related research ongoing at the beamlines. Here are a few of the people who kept the light on at the APS.

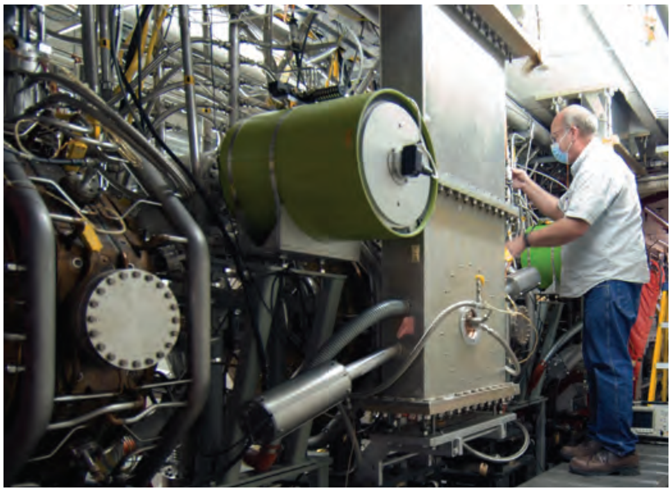

Roy Agner, ASD Radio Frequency Group Technician Senior : “I’m conducting tuner maintenance on the storage ring radio frequency cavity. Cavity tuner maintenance is essential to ensure proper cavity response under beam loading.”

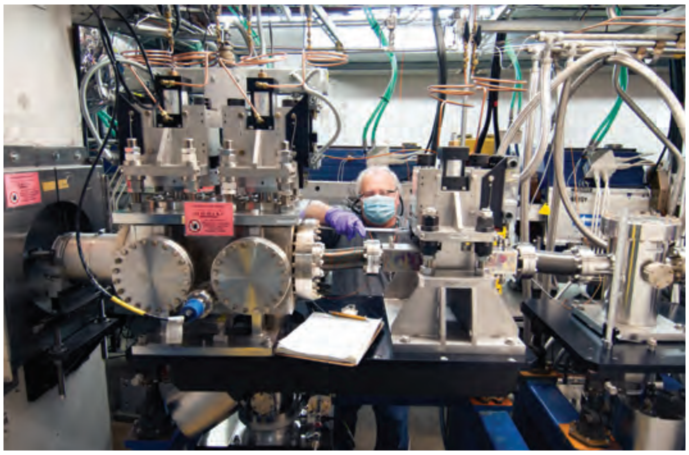

Scott Petersen, AES Survey & Alignment Group Technician Senior: “I’m aligning the Sector 22 second photon shutter in the insertion device front-end line for proper quality control, placing this component in the proper orientation to the electron beam. This component is one of many inside the storage ring that receives the beam off the insertion devices and is a part of the radiation safety system.”

> Brian Pruitt, AES Information Technology Group Senior Computer Specialist: “I’m changing out a failed module in a network switch that supplies network connectivity for the Sector 22 Southeast Regional Collaborative Access Team beamline so that staff of that beamline can continue to run experiments for their users.”

Arista Thurman III, AES Information Technology Group Principal Computer Engineer: “I’m replacing a failed cache module on an SAS disk controller in a DL380 G8 server in the injector control room after component failure resulted in a server being disabled/off-line.”

Debra Curry, AES Mechanical Operations and Maintenance Group Technician Senior: “One of my tasks is to twice a month record and document vibration and temperature readings from multiple Gould and SPX accelerator-system pumps. These recordings are then analyzed to determine what pumps are failing or near failing, to subsequently be rebuilt or replaced.”

Nanoscience

Keeping a Close Eye on Gene Activation in the Plant World

Transportation, heating, and electric generation fuels made from plants, collectively called biofuels, are promising alternative energy sources. But for biofuels to be economically competitive, plants grown for biofuel must yield more fuel per acre than they currently do. One potential way to increase crops' biofuel production is to increase the growth of the plant in its juvenile stage. Allowing the plant to grow more before flowering would increase the total amount of biomass, and thus fuel, the plant creates. To do this most effectively, biologists need a way to observe the activation of genes that regulate maturation in a living, growing plant. A team of researchers have now demonstrated that such a technique — developed at Duke University — using tiny, star-shaped nanoprobes made of gold could provide the tool to monitor gene activation in whole plants without the need for traditional complicated procedures of sample extraction. The APS played an important role in the project, determining the exact locations and amounts of the gold nanoprobes in the plants and confirming that the nanoprobes were indeed the source of the signals detected.

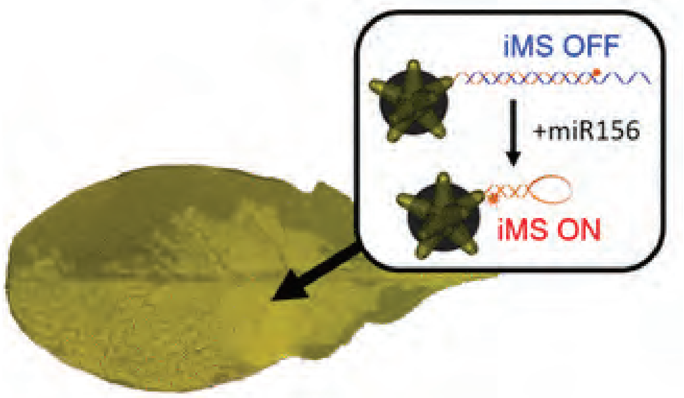

Fig. 1. Gold nanostars with spiral strings of DNA attached to their points probe for micro-RNAs that regulate plant growth (miR156) inside a leaf. Each string of DNA has a Raman label (orange dot) that triggers an amplified signal when miR156 is detected. Figures from B.M. Crawford et al., "Plasmonic Nanoprobes for in Vivo Multimodal Sensing and Bioimaging of MicroRNA within Plants," Appl. Mater. Interfaces **11**, 7743 (2019). © 2019 American Chemical Society

Understanding exactly which genes turn on inside a plant, and when, would be enormously useful to scientists trying to fine-tune plant growth for biofuel production. Usually, biologists have to take a sample of the plant and chemically analyze the ribonucleic acids (RNAs) the plant is producing to figure out which genes are active. Small RNAs that do not code for proteins, called microRNAs, regulate gene expression in plants. In particular, microRNA 156 (miR156) negatively regulates expression of several key genes that promote the beginning of the flowering phase of a plant's life. Annual plants such as corn and many other grasses stop vegetative growth when they flower, and redirect their energy into making seeds. That's undesirable for a biofuel crop, which ideally produces as much leaf and stalk as possible during the growing season. If biologists could see exactly when and where in a living plant miR156 levels begin to change, they could select plants with preferred growth patterns and examine their genes to learn how to induce those growth patterns in other biofuel crops.

Researchers at Duke University and Argonne teamed up to find such a method to observe miR156 in living plants. They injected probes into plants, in the form of star-shaped gold nanoparticles. Each tiny gold star, about 50 nm across, had unique sensors on its surface and on the tip of its points. The sensor was made of a double strand of DNA. One of the DNA strands was shorter than the other, and had a special molecular label attached to the end. The other, longer, strand extended out in a "toehold," a sticky end. The extended toehold-strand perfectly complemented the miR156. When the toehold encountered a miR156 molecule, the two locked together, unraveling the strand from the shorter DNA strand in the process. The left-behind shorter strand then coiled back on itself, bringing the label molecule in contact with the point of the gold nano star (Fig. 1). That label gave off a signal, which was amplified by the point of the star and then detected by the researchers.

Under illumination with laser light, the specific signal given off by the nanoprobe is called a Raman signal, which are a type of scattering of light. The signals are on very specific frequencies and are unmistakable when detected, but they are also very weak. The star shape of the

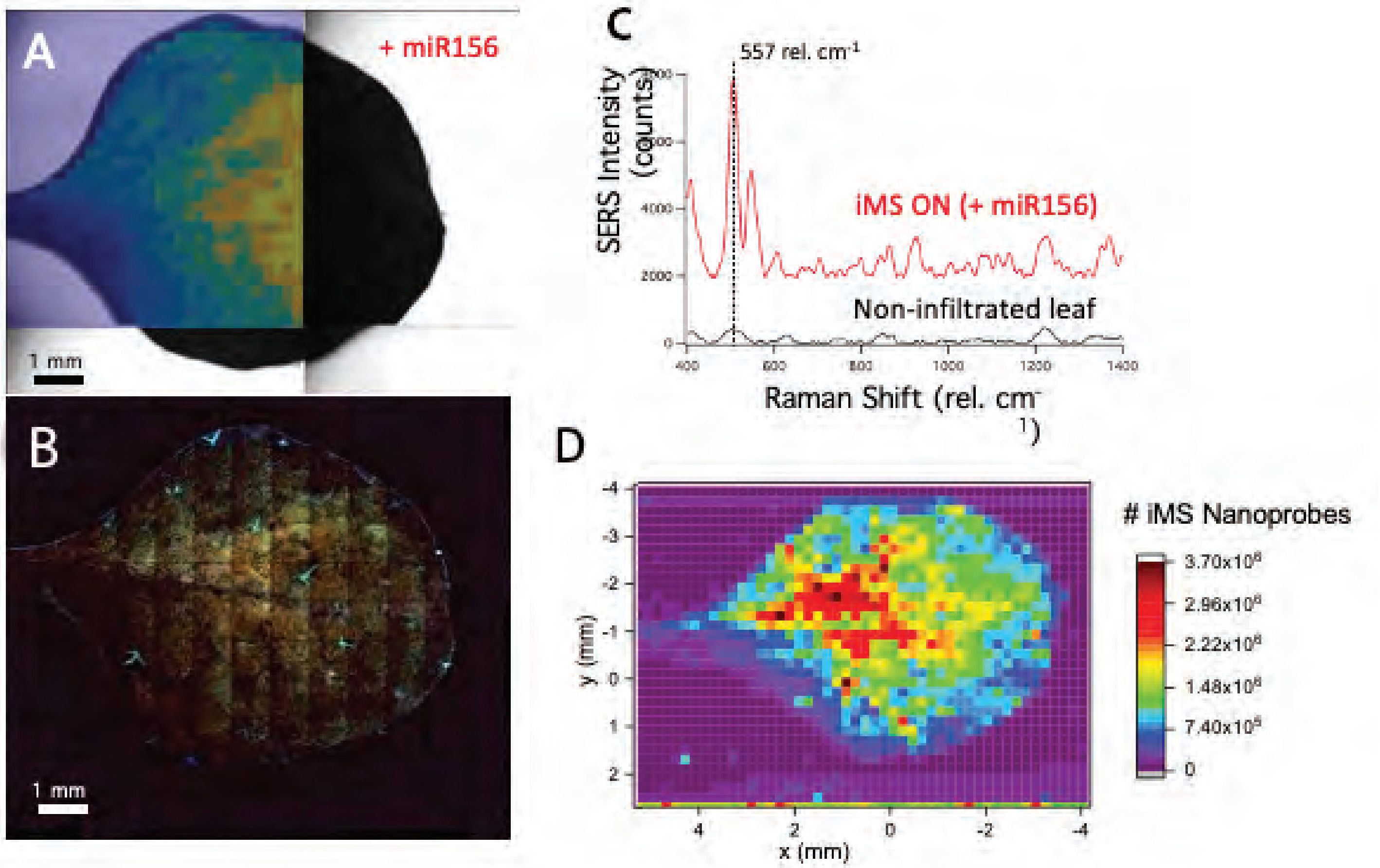

Fig. 2. Gold star-shaped nano probes for detection of miR156 infiltrate an *Arabidopsis thaliana* leaf. (A) Raman intensity map of the signal from nano probes detecting miR156 in the leaf. (B) Two-photon luminescence map of the infiltrated leaf (nano probes appear gold.) (C) Two different Raman spectra from the intensity map in A. The red spectrum is from an area infiltrated with the nano probes detecting miR156, the black spectrum is from an area without nano probes. (D) A gold x-ray fluorescence image shows location and quantity of nanoprobes within the leaf.

nano probe amplifies Raman signals a million-fold, making them easier to detect.

The probes worked, attaching to miR156 in the living plants and giving off detectible Raman signals. But the researchers needed to localize and confirm that the gold nanoprobes really were in the proper compartment of the plant cell giving off the signal. To prove that, the team used the MR-CAT insertion device beamline 10-ID-B at the APS. The MR-CAT insertion device beamline has the unique capability to detect elements spread diffusely through a biological sample. The team used x-ray fluorescence to confirm the presence of the gold nanoprobes within the plant tissue, both in the presence of the target microRNA and in its absence (Fig. 2).

Now that the researchers have proven that their gold nano stars equipped with microRNA sensors do indeed work in living plants, they are excited by the possibilities. The sharpness of the Raman signals generated by the nanoprobes means they are easily distinguished from one another. Unlike fluorescent labels for molecules, which have only a few possible colors, many different microRNAs could be detected simultaneously by different nano probes all using differently "colored" Raman signals. The technique will make it easy to observe gene expression in living plants and, the researchers hope, revolutionize research in biofuels and beyond. – Kim Krieger

See: Bridget M. Crawford[1], Pietro Strobbia[1], Hsin-Neng Wang[1], Rodolfo Zentella[1], Maxim I. Boyanov[2,3], Zhen-Ming Pei1[1] Tai-Ping Sun[1], Kenneth M. Kemner[3], and Tuan Vo-Dinh[1*], "Plasmonic Nanoprobes for in vivo Multimodal Sensing and Bioimaging of MicroRNA within Plants," Appl. Mater. Interfaces **11**, 7743 (2019). DOI: 10.1021/acsami.8b19977

Author affiliations: [1]Duke University, [2]Bulgarian Academy of Sciences, [3]Argonne National Laboratory

Correspondence: * tuan.vodinh@duke.edu

This material is based upon work supported by the U.S. Department of Energy (DOE) Office of Science, under Award Number DE-SC0014077. B.M.C. acknowledges the support of the National Science Foundation Graduate Research Fellowship under Grant No. 1106401. MR-CAT operations are supported by the U.S. DOE and the MR-CAT member institutions. The authors thank the MR-CAT beamline staff for assistance during data collection at the synchrotron. This research used resources of the Advanced Photon Source, a U.S. DOE Office of Science User Facility operated for the DOE Office of Science by Argonne National Laboratory under Contract No. DE-AC02-06CH11357.

A Matter of Size: A Closer Look at Molybdenum Oxide Nanoparticles

Cutting a piece of paper into halves or quarters or smaller isn't expected to change the paper's underlying structure, but things start to get strange down at the nanoscale. With the explosion of nanoparticle research and novel applications, scientists are beginning to acknowledge that the structure of a material in bulk quantities may not reflect the structure of that same substance in nanoparticle form. What's more, nanoparticles can have different structures depending on their size, suggesting that a single material may arrange itself into multiple configurations. Scientists are exploring molybdenum oxide nanoparticles as a long-lasting and robust anode material for lithium-ion batteries. But how size impacts the material's structure hasn't been clear, limiting the ability to improve the material. To better understand the impact of nanosizing on atomic structure, a research team working at the APS gathered x-ray scattering data on a series of molybdenum oxide nanoparticles. These data, combined with electron microscopy images, provides a deeper understanding on how size impacts atomic structure and also on how structure impacts a material's properties. Such insights pave the way to more sophisticated applications for nanoparticles.

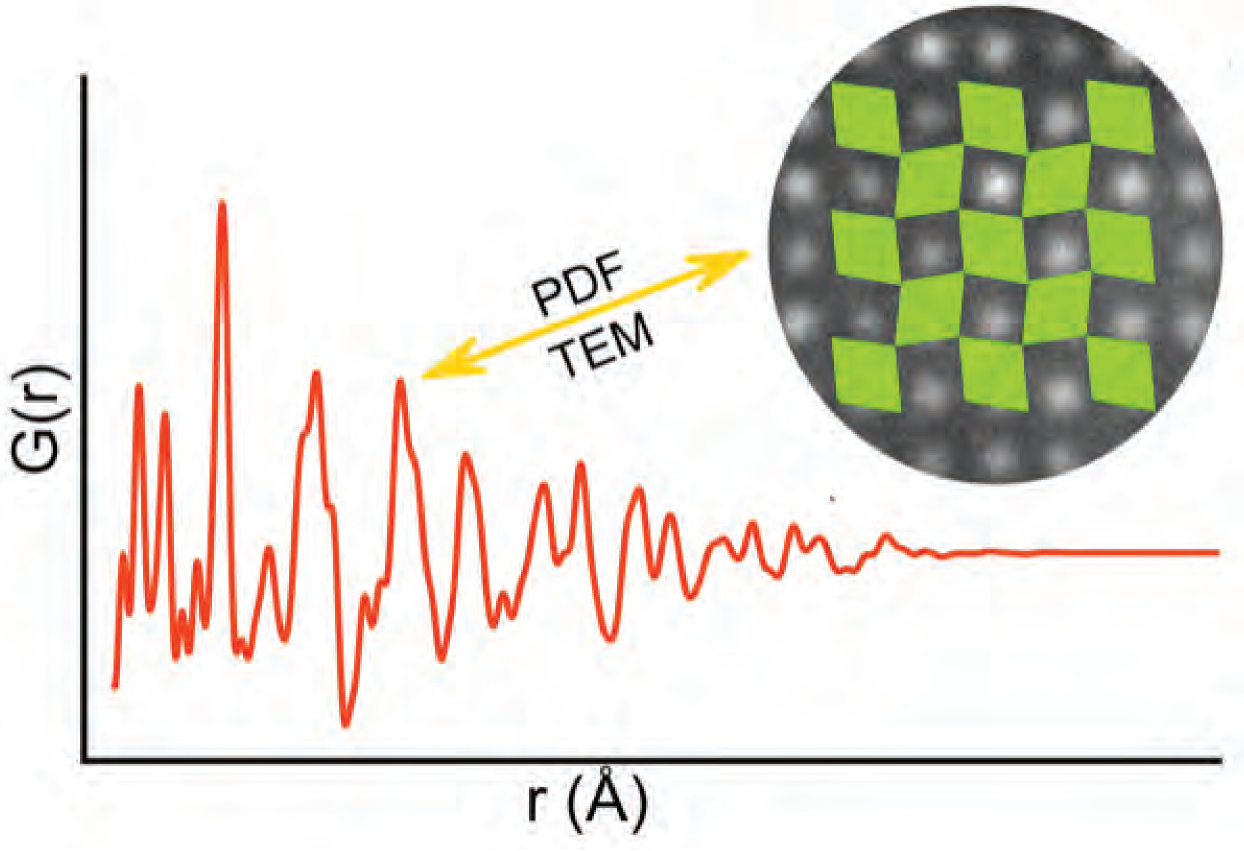

Garnering structural information about nanoparticles is no easy task. The most common approach to structure determination is x-ray crystallography, but that method, as the name suggests, relies on a crystal. A crystal is regular pattern of atoms which repeats itself in three dimensions. This long-range atomic order is not seen in nanoparticles because of their small size, and they only give rise to broad and diffuse features in their x-ray scattering patterns. This so-called "nanostructure problem" means that researchers need alternative techniques to get a handle on the atomic structure of nanoparticles.

In this study, the researchers from the University of Copenhagen (Denmark) and Monash University (Australia) synthesized molybdenum oxide nanoparticles of different sizes (from >5 nm to 50-100 nm) by preparing them under a range of conditions, altering the ratio of oleylamine to ethanol in the solvent from 0% to 80%. Then, the researchers headed to the XSD 11-ID-B beamline at the APS; and beamline P02.1 at PETRA III, DESY (Germany) to collect total scattering x-ray data on the samples.

Based on the samples' powder x-ray diffraction patterns, they grouped the resultant nanoparticles into three categories: amorphous (80% oleylamine), nanostructured (40%, 50%, and 60% oleylamine), and crystalline (0% and 20% oleylamine). For additional structural data, the researchers characterized the samples via scanning electron transmission microscopy. These images, taken together with the x-ray data, supported the categorization of the samples' nanoparticles as amorphous, nanostructured, or crystalline (Fig. 1). The combined data indicated significant variation in the particle size and atomic structure of the samples based on the solvent composition in the synthesis.

To gain further insights, the researchers turned to pair distribution function (PDF) analysis. This technique can help characterize amorphous and nanostructured samples by fully utilizing the x-ray scattering data, rather than only taking into account Bragg scattering, the type associated with crystalline materials. Using detailed PDF analysis and the microscopy data, the team created a model for the nanostructured molybdenum oxide particles ranging in size from 3 to 5 nm. They found significant defects, including differences in thickness, surface structure, and buckling that impacted the overall three-dimensional structure. They found similar defects in the larger crystalline molybdenum oxide nanoparticles (50-150 nm in diameter), but at lower concentration, so the average structures were unaffected. Such defects are more important than might be expected; similar defects in titanium oxide nanoparticles are associated with improvements in electrical conductivity.

< Fig. 1. MoO_2 nanoparticles show a structure that is distinct from the bulk distorted rutile structure and which has not yet been determined. Here, we present a model for nanostructured MoO_2 obtained through detailed atomic pair distribution function analysis combined with high-resolution electron microscopy. From T. Christiansen et al., ACS Nano **13**, 8725 (2019). © 2019 American Chemical Society

Previous research has shown that decreasing the size of molybdenum oxide crystallites leads to an improvement in the materials' performance as an anode in lithium-ion batteries. This study, the authors argue, provides a structural basis for those improvements, and suggests that such defects should be taken into account in similar nanoscale materials. – Erika Gebel Berg

See: Troels Lindahl Christiansen[1], Espen D. Bøjesen[2], Mikkel Juelsholt[1], Joanne Etheridge[2], and Kirsten M. Ø. Jensen[1]*, "Size Induced Structural Changes in Molybdenum Oxide Nanoparticles," ACS Nano **13**, 8725 (2019). DOI: 10.1021/acsnano.9b01367
Author affiliations: [1]University of Copenhagen, [2]Monash University
Correspondence: * kirsten@chem.ku.dk

We are grateful to the Villum Foundation for financial support through a Villum Young Investigator grant (VKR00015416). K.M.Ø.J. acknowledges funding from the Danish Research Council under the Sapere Aude Research Talent Program. E.D.B. acknowledges financial support through a research grant (VKR023371) from the Villum Foundation. J.E. acknowledges funding from the Australian Research Council Discovery Project No. DP150104483. The authors acknowledge use of the facilities and the assistance of A/Prof. Matthew Weyland at the Monash Centre for Electron Microscopy. We acknowledge DESY (Hamburg, Germany), a member of the Helmholtz Association HGF, for the provision of experimental facilities. Parts of this research were carried out at P02.1, and we would like to thank Martin Etter for assistance in using the beamline. This research used resources of the Advanced Photon Source, a U.S. Department of Energy (DOE) Office of Science User Facility operated for the DOE Office of Science by Argonne National Laboratory under Contract No. DE-AC02-06CH11357.

Making a Safer Coating for Gold Nanoparticles

Gold nanoparticles possess unique electronic and optical properties, making them popular for many biomedical applications. But the safety of gold nanoparticles often depends on the organic molecules attached to and coating them. Different coatings can change how cells recognize and interact with nanoparticles, and some coatings can cause inflammation and cell death. A team of researchers used the APS to examine how two common types of chemicals used to coat gold nanoparticles, surfactants and polyelectrolytes, interact with cells. The research reveals why surfactant-coated nanoparticles tend to cause inflammation, and how nanoparticles used in biomedicine could be designed to be safer.

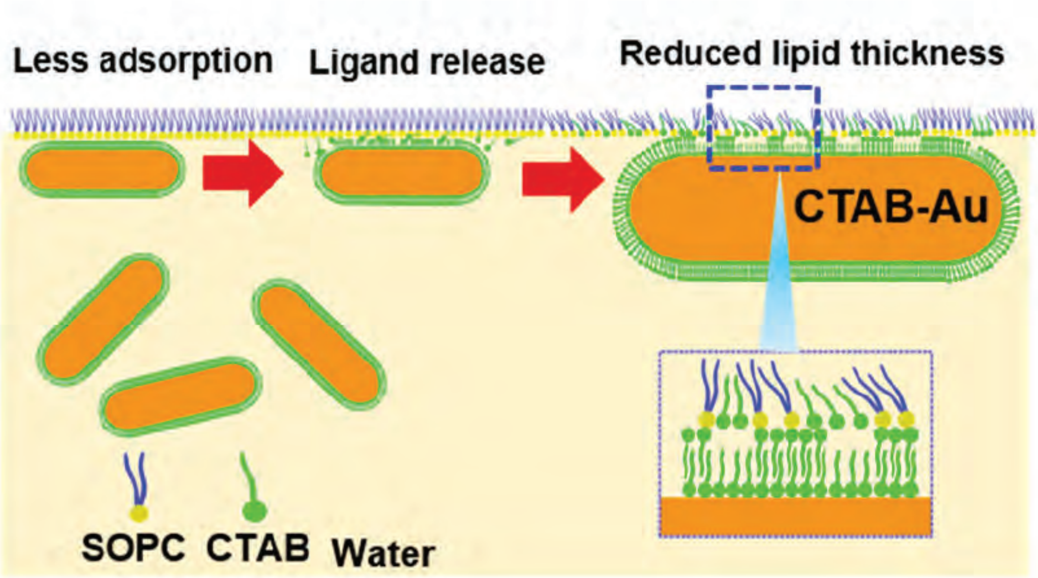

Fig. 1. The image shows gold nanorods (orange lozenges) coated with the surfactant CTAB (green). Instead of being adsorbed onto the phospholipid membrane (SOPC), the surfactant is released into solution and inserts itself in-between the molecules of SOPC forming the membrane, distorting the membrane's shape and integrity and causing it to thin.

Surfactants are molecules with one end that likes to mix in water and another end that prefers fats. They can help nanoparticles pass through cell membranes, which are made of layers of fatty molecules called lipids. Polyelectrolytes, another potential coating molecule for biomedical nanoparticles, are often used as drug delivery systems.

A team of researchers studied how the coated rod-shaped gold nanoparticles with either the surfactant cetyltrimethylammonium bromide (CTAB) or the polyelectrolyte poly(diallyldimethylammonium chloride) (PDDAC) interact with cell membrane. Neither coating molecule was attached to the nanorods with a strong chemical bond. Instead, as is commonly done with gold nanoparticles, the coatings clung to the nanorods due to the somewhat weaker van der Waals interaction (surfactant), or via hydrophobic and electrostatic attractions (polyelectrolyte).

To see how the two types of coated nanoparticles might affect living cell membranes, the researchers made a layer of the phospholipid 1-octadecanoyl-2-(9Z-octadecanoyl)-sn-glycero-3-phosphocholine (SOPC) in a trough of water. SOPC is one of the major building blocks of biological cell membranes. Floating on water, a monolayer–a layer one molecule thick–of SOPC acts as a pretty good proxy for a cell membrane.

The researchers used the techniques x-ray reflectivity (XRR) and grazing incidence x-ray off-specular scattering (GIXOS) to determine the thickness of the SOPC layer. Both XRR and GIXOS were performed at the ChemMatCARS 15-ID-C beamline at the APS. The beamline's facilities allow researchers to use APS's exceptionally brilliant, high-energy x-rays to examine liquid interfaces at the molecular level.

After measuring the thickness of the SOPC alone, the researchers added gold nanorods coated with either surfactant or polyelectrolyte to the troughs. After adding the coated nanorods, the teams measured the thickness of the SOPC layer again. They found that gold nanorods coated with the surfactant CTAB caused the SOPC layer to thin significantly.

The team suspected that the surfactant's weak van der Waals attachment to the gold nanorods allows it to easily detach and insert itself into the SOPC membrane. They noticed that the higher the concentration of surfactant-coated particles, the larger the surface area of the SOPC became, another clue that the surfactant was slipping into the membrane.

Using data from the XRR and GIXOS analyses, the researchers could see the reason the membrane thins out when surfactant is added to the mix: the heads of the SOPC molecules try to align with the lipid-loving heads of the surfactant. But the surfactant molecule is shorter than SOPC, so the longer SOPC molecules bend and push each other out of alignment, thinning the layer (Fig. 1.)

In contrast, the polyelectrolytes do not insert themselves into the SOPC, as they're more securely attached to the nanorod. They do not cause the SOPC membrane to thin. The thinning cell membranes are more apt to break and release the nanoparticles and their coating molecules into the cell's interior. This causes inflammation, and if it happens enough, can also lead to cell death.

The researchers suggest that in the future, biomedical nanoparticles should be carefully engineered to have more stable attachments to their coating molecules. The type of analysis they performed at ChemMatCARS will be very helpful in this effort, as it allows researchers to see how nanoparticles, coatings, and biological membranes interact. – Kim Krieger

See: Liming Wang[1,2], Peiyu Quan[1,2,6], Serena H. Chen[4], Wei Bu[3], Yu-Feng Li[1], Xiaochun Wu[5], Junguang Wu[1,2], Leili Zhang[4], Yuliang Zhao[1], Xiaoming Jiang[1], Binhua Lin[3]*, Ruhong Zhou[4,6]**, and Chunying Chen[1,2]***, "Stability of Ligands on Nanoparticles Regulating the Integrity of Biological Membranes at the Nano–Lipid Interface," ACS Nano **13**, 8680 (2019).
DOI: 10.1021/acsnano.9b00114

Author affiliations: [1]Chinese Academy of Sciences and National Center for Nanoscience and Technology of China, [2]University of Chinese Academy of Sciences, [3]The University of Chicago, [4]IBM Thomas J. Watson Research Center, [5]CAS Key Laboratory of Standardization and Measurement for Nanotechnology and CAS Center for Excellence in Nanoscience National Center for Nanoscience and Technology, [6]Columbia University
Correspondence: * lin@cars.uchicago.edu,
** ruhongz@us.ibm.com,
*** chenchy@nanoctr.cn

This work was supported by the Ministry of Science and Technology of China (2016YFA0201600, 2016YFA0203200), Key Program for International S&T Cooperation Projects of China (2016YFE0133100), the National Natural Science Foundation of China (91543206, 11435002, 11574224), Science Fund for Creative Research Groups of the National Natural Science Foundation of China (11621505), the National Science Fund for Distinguished Young Scholars (11425520), CAS Key Research Program for Frontier Sciences (QYZDJ-SSW-SLH022), and the CAS Interdisciplinary Innovation Team. B.L. acknowledges the support from the University of Chicago MRSEC under grant number NSF/DMR-1420709. R.Z. acknowledges the support from IBM Blue Gene Science Program (W125859, W1464125, and W1464164). A part of this work was supported by ChemMatCARS, which is supported by the Divisions of Chemistry (CHE) and Materials Research (DMR), National Science Foundation, under grant number NSF/CHE-1834750. Use of the Advanced Photon Source, an Office of Science User Facility operated for the U.S. Department of Energy (DOE) Office of Science by Argonne National Laboratory, was supported by the U.S. DOE under Contract No. DE-AC02-06CH11357.

Controlling Nanoparticle Crystallization

The formation of supercrystalline structures from nanoparticles dispersed in a solvent is a crucial step in the preparation of a variety of novel materials and devices. Allowing solvent to evaporate from a nanoparticle solution typically leaves behind a film-like periodic structure, whereas adding a miscible non-solvent to destabilize the solution tends to create discrete super-crystals. Using a combination of small-angle and wide-angle x-ray scattering (SAXS and WAXS) at the APS, along with small-angle neutron scattering (SANS), researchers have explored how the formation of supercrystals depends on the interaction between ligands that coat the nanoparticles and the surrounding solution. The results should help guide design methods for nanoparticle super-crystals and improve quantum dot devices such as light-emitting diodes, photovoltaics, photodetectors, lasers, and field-effect transistors.

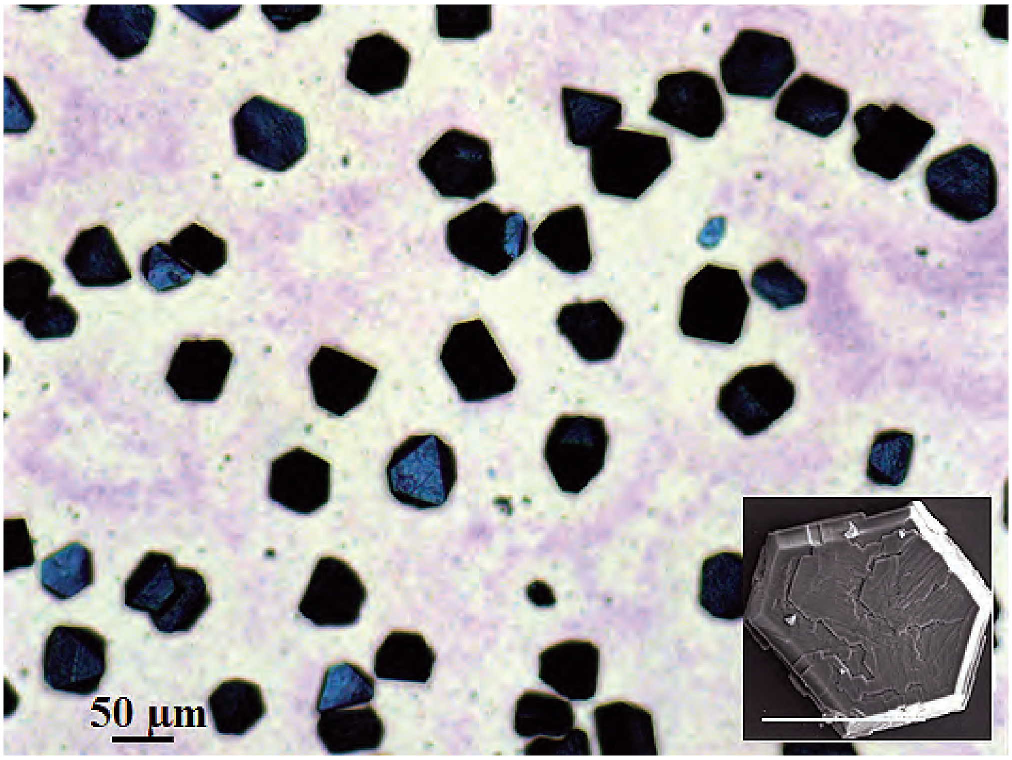

Fig. 1. Optical microscope image of super-crystals created by adding ethanol to a solution of lead-sulfur nanoparticles in toluene. Figures adapted from B. Lee et al.," J. Am. Chem. Soc. **141**, 16651 (2019). © 2019 American Chemical Society

Coating nanoparticles with a suitable ligand molecule allows them to disperse in a solvent. As the solvent evaporates, the nanoparticles assemble in a way that depends on their shape, either to maximize their packing density or to minimize the interstitial space that will cost surface energy. Spherical or near-spherical nanoparticles, if they are much larger than their ligand shell thickness, form a face-centered cubic (fcc) structure, their closest packing arrangement. This is the same arrangement that allows the most oranges to be packed in a box, for example, and minimizes interstitial volume between hard spheres. Smaller nanoparticles with a relatively thicker ligand shell, on the other hand, assemble into a body-centered cubic (bcc) structure. This is because spheres that are softer due to the higher relative volume of the ligands can fill interstitial space by being deformed, and the gaps in a bcc structure can be filled with much less shell deformation than those in a fcc structure. If you don't mind squeezing oranges to pack them tightly, then bcc packing is denser than fcc.

To bring some clarity to this complex state of affairs, the researchers in this study performed a series of experiments on lead-sulfur (PbS) nanoparticles with two sizes, 4.14 and 5.60 nm, coated in oleic acid, which were synthesized and characterized at the Center for Nanoscale Materials (CNM), at Argonne. The hydrocarbon ends of the ligands project outward, allowing the nanoparticles to dissolve in toluene, a non-polar liquid. To destabilize that solution and encourage the nanoparticles to form supercrystals, the researchers carefully added three different al-

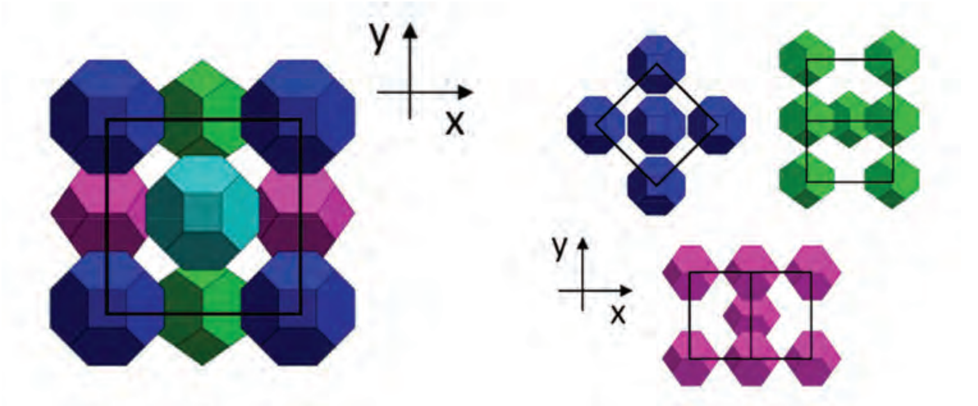

Fig. 2. Packing structures and nanoparticle alignments inferred from SAXS/WAXS studies. Left: fcc structure formed by 5.60-nm nanoparticles, with colors indicating the three different orientations of the truncated octahedra. Right: bcc structures formed by 4.14-nm nanoparticles, showing how the different orientations of the nanoparticles in the initial fcc structure transform into consistent overall alignments within the bcc arrangement.

cohols—methanol, ethanol, and isopropanol—to solutions of the nanoparticles in a test tube that also contained a glass slide on which crystallization occurred. The alcohols mixed with the toluene, but in doing so changed the interaction between the nanoparticles and their liquid environment (Fig. 1).

The team tracked the crystallization process *in situ* and also characterized the full three-dimensional reciprocal space of the super-crystals using SAXS and WAXS at XSD beamline 12-ID-B at the APS. If the shape of core particles governs their packing structure, the PbS nanoparticles, which are truncated octahedra, should pack into a bcc structure. The results confirmed that the 4.14-nm nanoparticles assembled into bcc crystals, but showed that the 5.60-nm nanoparticles adopted a fcc structure (Fig. 2). The fcc formation suggests that the ligand shell "screens" the true shape of the larger nanoparticles, causing them to behave like spheres. However, the shape of the cores still influenced the assembly. The SAXS/WAXS reciprocal space mapping technique revealed that the truncated octahedral nanoparticles in the final fcc super-crystals did not orient themselves randomly, as spheres would, but aligned themselves so that their faces were parallel to their neighbors' faces.

The researchers explain that the nanoparticles begin to arrange themselves into a fcc structure when there are still plenty of solvent molecules around, allowing the particles to take up random orientations. But as the solvent dries out, the larger particles settle into orientations restricted by their neighbors, and so are unable to reorganize themselves into their ideal bcc packing structure. Crystallization of the smaller particles likewise begins with fcc packing, suggesting they also behave like spheres, but those structures transform to bcc arrangements during later stages of solvent evaporation. In this case, a bcc packing structure is ideal considering both the particles' core shape and their relatively higher ligand volume. In the bcc super-crystals, the nanoparticles have a higher probability of all lining up the same way, providing structural evidence of the fcc-to-bcc phase transformation that was caught by the reciprocal space-mapping technique.

The team also conducted SANS studies at the High Flux Isotope Reactor, a DOE Office of Science user facility operated by Oak Ridge National Laboratory, enabling them to see how the ligand shell interacts with the pure and mixed solvents.

Putting all the evidence together, the researchers conclude that the different super-crystal structures form not because ligand molecules are removed in various ways, as had been previously suggested, but because the three alcohols influence ligand-solvent interactions in different ways. In particular, toluene has a greater affinity toward oleic acid than toward methanol, so when methanol is added, toluene concentration in the ligand shell rises, making it expand. Adding isopropanol does the reverse, shrinking the ligand shell by drawing toluene out. The study heightens our understanding of the complexity of influences on nanoparticle assembly, but also suggests ways to control the process to produce desired results.

– David Lindley

See: Byeongdu Lee[1*], Kenneth Littrell[2], Yuchen Sha[1,3], and Elena V. Shevchenko[1*], "Revealing the Effects of the Non-solvent on the Ligand Shell of Nanoparticles and Their Crystallization," J. Am. Chem. Soc. **141**, 16651 (2019). DOI: 10.1021/jacs.9b06010

Author affiliations: [1]Argonne National Laboratory, [2]Oak Ridge National Laboratory, [3]Wuhan University
Correspondence: * blee@anl.gov, ** eshevchenko@anl.gov

A portion of this research used resources at the High Flux Isotope Reactor, a supported by the U.S. Department of Energy (DOE) Office of Science User Facility operated by the Oak Ridge National Laboratory. Work at the Advanced Photon Source and at the Center for Nanoscale Materials at Argonne National Laboratory was supported by the U.S. DOE Office of Science-Basic Energy Sciences, under Contract No. DE-AC0206CH-11357.

Measuring Heat and Light

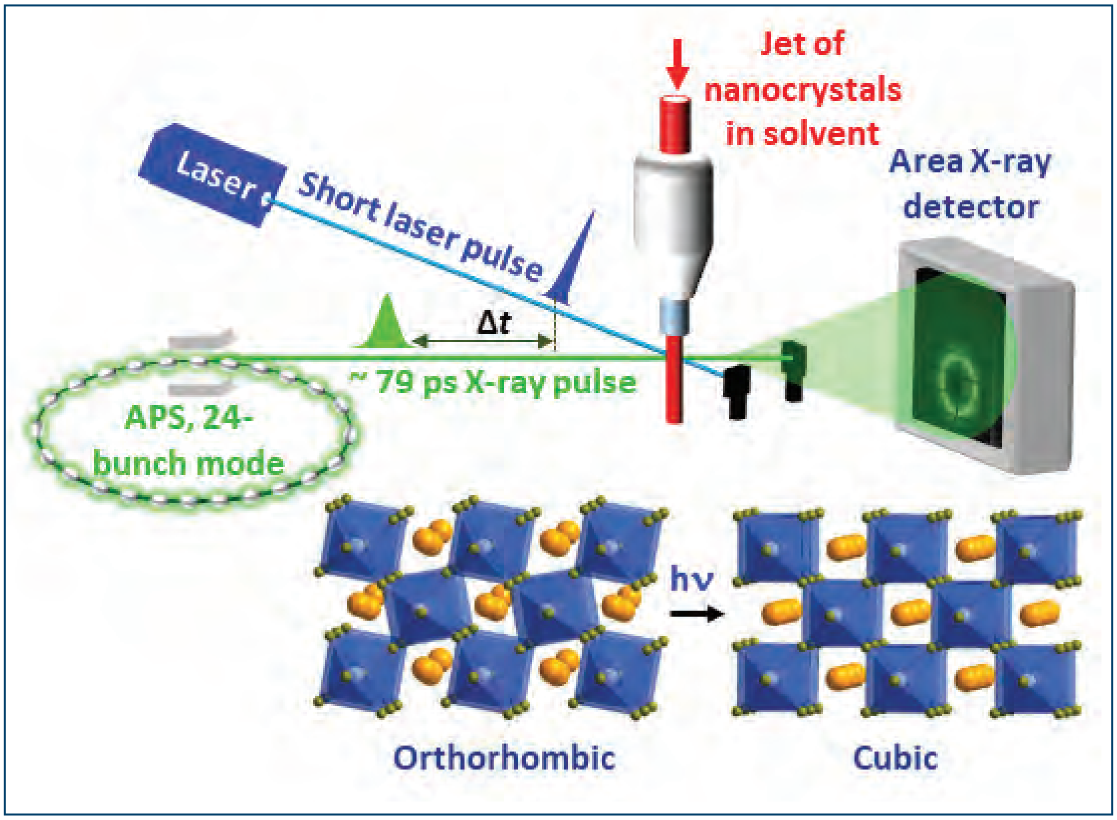

Fig. 1. An x-ray beam passing through a jet of nanocrystals detects how the energy from a laser pulse causes the crystal structure to change from orthorhombic to cubic.

A class of materials known as halide perovskites has become increasingly popular in some optoelectronic applications, including solar cells, light-emitting diodes (LEDs), and certain types of lasers. In addition to being inexpensive and straight-forward to manufacture, the crystalline structure of perovskites gives them superior electronic properties, leading to highly efficient light emission or, in the case of solar cells, collection. However, passing energy through such materials heats them up, which can change their properties and cause their light to dim. Now a group of researchers using the APS has measured how much the heating caused by light can alter structure of the crystal.

These materials are often characterized at room temperature and treated as if their properties remain constant in operation. Standard methods of measuring thermal transport in materials are designed for use on large crystals with flat surfaces, so they don't work well on tiny nanocrystals of the type the researchers were studying.

The team created nanocrystals approximately 11 nanometers wide made of cesium lead bromide, one of many formulations of perovskite that is particularly promising for use in bright LEDs and lasers. They then performed time-resolved x-ray diffraction on their samples, using XSD beamline 11-ID-D at the APS. They placed the nanocrystals into a solution, which they streamed past the x-ray beam and hit with short pulses of x-rays, lasting about 79 ps, and laser light, about 1.6-ps long. The x-rays passing through the nanocrystal produced a diffraction pattern on the detector, based on the crystalline structure. Hitting the sample with an x-ray pulse first, followed by the laser pulse, produced one set of diffraction patterns. But when the laser pulse hit first, and therefore heated the crystal, the patterns altered, with the diffraction peaks changing to lower angles of diffraction as the crystal heated up.

A certain level of heating caused the crystal to change from an orthorhombic phase, in which units of the crystal are tilted with respect to one another, to a cubic phase, in which the units are all in the same orientation (Fig. 1). It took approximately 510 ps for the heat to dissipate and the crystal to recover its original form. At higher laser powers, above 2.5 mJ/cm^{-2}, the change in diffraction showed the crystal becoming amorphous, the start of melting, though it still returned to its original form when it cooled. Above 18 mJ/cm^{-2}, some of the change was irreversible.

To calculate how the temperature of the crystal was changing as it heated and cooled, the team performed static, temperature-depended x-ray diffraction at the DND-CAT 5-ID beamline also at the APS. Instead of streaming the nanocrystals in solution past the beam, they performed these measurements on a thin column of nanocrystals suspended in a polymer matrix, and determined the diffraction peaks for a series of temperatures. That allowed them to match the known temperature patterns with the changes they observed versus time.

The researchers say other perovskites with different combinations of elements may behave differently. Knowing how different compositions affect the photoelectronic properties of the materials could help in improving devices. For instance, in an LED it would be better to shed heat quickly, allowing more electrical energy to be pumped in to create higher brightness without degrading performance. On the other hand, thermoelectric materials, which convert heat to electricity, would benefit if the heat remained in the material longer. Being able to tune those properties by altering the composition of the materials could prove beneficial. – Neil Savage

See: Matthew S. Kirschner[1], Benjamin T. Diroll[2], Peijun Guo[2], Samantha M. Harvey[1], Waleed Helweh[1], Nathan C. Flanders[1], Alexandra Brumberg[1], Nicolas E. Watkins[1], Ariel A. Leonard[1,2], Austin M. Evans[1], Michael R. Wasielewski[1], William R. Dichtel[1], Xiaoyi Zhang[2], Lin X. Chen[1,2], and Richard D. Schaller[1,2]*, "Photoinduced, reversible phase transitions in all-inorganic perovskite nanocrystals," Nat. Commun. **10**, 504 (2019).
DOI: 10.1038/s41467-019-08362-3

Author affiliations: [1]Northwestern University, [2]Argonne National Laboratory
Correspondence: * schaller@anl.gov or
schaller@northwestern.edu

We acknowledge support from the Ultrafast Initiative of the U.S. Department of Energy (DOE) Office of Science-Basic Energy Sciences, through Argonne National Laboratory under Contract No. DE-AC02-06CH11357. Use of the Center for Nanoscale Materials, an Office of Science user facility, was supported by the U.S. DOE Office of Science-Basic Energy Sciences, under Contract No. DE-AC02-06CH11357. This work made use of the Jerome B. Cohen X-Ray Diffraction Facility supported by the MRSEC program of the National Science Foundation (DMR-1720139) at the Materials Research Center of Northwestern University and the Soft and Hybrid Nanotechnology Experimental (SHyNE) Resource (NSF ECCS-1542205). DND-CAT is supported by Northwestern University, E.I. DuPont de Nemours & Co., and The Dow Chemical Company. N.C.F was partially supported by Basic Energy Sciences, CBG Division, U.S. DOE, and resources at the Advanced Photon Source were funded by the National Science Foundation under Award Number 0960140. This work was supported by the U.S. DOE Office of Science-Basic Energy Sciences under Award DE-FG02-99ER14999 (M.R.W.). This material is based upon work supported by the National Science Foundation Graduate Research Fellowship Program under Grant No. DGE-1324585 (S.M.H., A.B., A.M.E. and N.E.W.). This research used resources of the Advanced Photon Source, a U.S. DOE Office of Science User Facility operated for the DOE Office of Science by Argonne National Laboratory under Contract No. DE-AC02-06CH11357.

A Novel Organic Dye Nanoassembly Harnesses Light To Drive Chemical Changes

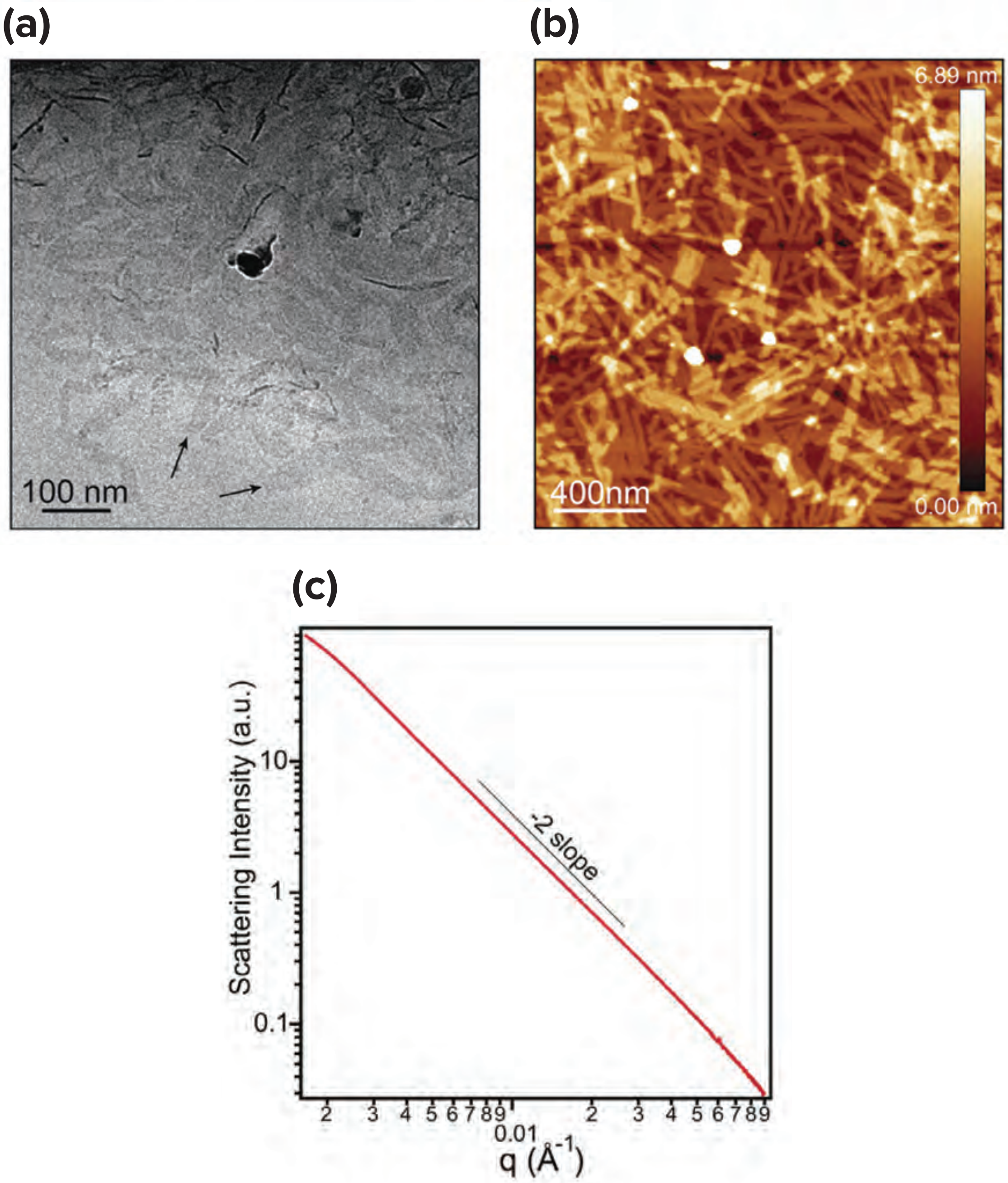

Fig. 1. Morphology of supramolecular nanoscale ribbons observed using cryo-TEM (a) and AFM (b), and SAXS patterns (c).

Supramolecular structures are complex arrays of molecules held together by comparatively weak intermolecular bonds. The study of these nano-assemblies can help us learn more about the fundamentals of chemistry and physics, and they also have significant applications in medicine and energy science. In experimentation at the APS, a research team made an important discovery directly pertinent to nano and clean energy science. By chemically modifying a photosensitive organic dye (perylene monoimide), the authors of this study created a supramolecular system that is water soluble and can be controlled by altering the acidity (i.e., pH) of this system's environment. They additionally showed that these assemblies can be used to drive light-induced reactions, suggesting exciting possibilities for the future of renewable energy.

Perylene monoimides are a type of organic dye that is capable of absorbing visible light. An "imide" is an organic functional group possessing the structure (—CONHCO—) built around a central nitrogen atom. In contrast, perylene is a unique structure compromised of multiple different carbon rings. Its chemical formula is $C_{20}H_{12}$ and its official chemical type is a polycyclic aromatic hydrocarbon. Thus, a perylene monoimide dye is a dye that contains both a multi-ringed structure (i.e., the perylene hydrocarbon) and a unique chemical group that contains nitrogen and oxygen (i.e., the imide). Imides are well known for their presence in high-strength commercial polymers while perylene has been utilized in research as a probe to measure the presence of fat molecules.

In this study, the researchers from Northwestern University investigated a unique, water-soluble perylene monoimide system that was carboxylated, meaning that a carboxyl group (R–COOH) was added to the dye. Additionally, the authors functionalized the core of the perylene molecule with a hydroxyl group (a molecule with oxygen and hydrogen bonded together). This made the entire supramolecular assembly ionizable, meaning that hydrogen atom of the hydroxyl group can be reversibly exchanged off and onto the perylene core in response to the solutions acidity level. The pH level of a given environment can range from 0 (most acidic) to 14 (most basic). The authors showed that these assemblies could be used as photosensitizers: they can harness and transfer energy from light to produce chemical changes. Specifically, they demonstrated that the photocatalytic production of hydrogen (combination of two protons to create a molecule of hydrogen gas) was possible at a pH of 4. This system was also capable of converting carbon dioxide to higher value products at a more alkaline pH of 9-10.

A significant portion of this work required the APS. More specifically, solution x-ray experiments were conducted at the DND-CAT 5-ID-B,C,D and XSD 8-ID-E beamlines at the APS. X-ray scattering was performed to characterize the nanostructure morphology of the customized perylene monoimide supramolecular system. The researchers used solution phase wide-angle x-ray scattering to probe differences in the internal structure of the nanoassemblies as a function of pH. Cryogenic transmission electron microscopy (cryo-TEM) and atomic force microscopy (AFM) helped reveal the morphology of the supramolecular nanoscale ribbons. Small angle x-ray scattering (SAXS) was then used to confirm the ribbon morphology observed by microscopy. The data for these studies are shown in Fig. 1.

While there are several different theoretical applications for this work, the most cogent application is relevant to the fields of energy science and renewable energy. The ability to utilize light to drive chemical reactions (photosynthesis) is the basis of life on our plant, and the ambitious goal of splitting water into hydrogen to generate energy is longstanding. This edifying work has helped to showcase another potential source of renewable solar energy, which puts us collectively one-step closer to a greener, safer planet. – Alicia Surrao

See: Adam Dannenhoffer, Hiroaki Sai, Dongxu Huang, Benjamin Nagasing, Boris Harutyunyan, Daniel J. Fairfield, Taner Aytun, Stacey M. Chin, Michael J. Bedzyk, Monica Olvera de la Cruz, and Samuel I. Stupp*, "Impact of charge switching stimuli on supramolecular perylene monoimide assemblies," Chem. Sci. **10**, 5779 (2019). DOI: 10.1039/c8sc05595e

Author affiliation: Northwestern University
Correspondence: * s-stupp@northwestern.edu

This work was supported as part of the Argonne-Northwestern Solar Energy Research (ANSER) Center, an Energy Frontier Research Center funded by the U.S. Department of Energy (DOE) Office of Science-Basic Energy Sciences under Award # DE-SC0001059. Determination of Electronic Energy levels and DFT calculations were supported by the U.S. DOE Office of Science-Basic Energy Sciences, under award no. DE-FG02-00ER45810. Molecular dynamic simulations were possible thanks to the generous support from the U.S. DOE, under award no. DE-FG02-08ER46539. DND-CAT is supported by Northwestern University, E.I. DuPont de Nemours & Co., and The Dow Chemical Company. The authors thank Dr. J. Strzalka for help with GIWAXS setup and measurements at Argonne National Lab. This research used resources of the Advanced Photon Source, a U.S. DOE Office of Science User Facility operated for the DOE Office of Science by Argonne National Laboratory under Contract No. DE-AC02-06CH11357.

X-RAY AVAILABILITY AND RELIABILITY

In fiscal year 2019*, the APS x-ray source continued to function as a highly reliable delivery system for synchrotron x-ray beams for research. Several factors support the overall growth in both the APS user community and the number of experiments carried out by that community. But there is a direct correlation between the number of x-ray hours available to users; the success of the APS experiment program; and the physicists, engineers, and technicians responsible for achieving and maintaining optimum x-ray source performance. Below are definitions of important measures for the delivery of x-ray beam to users (latest data shown graphically).

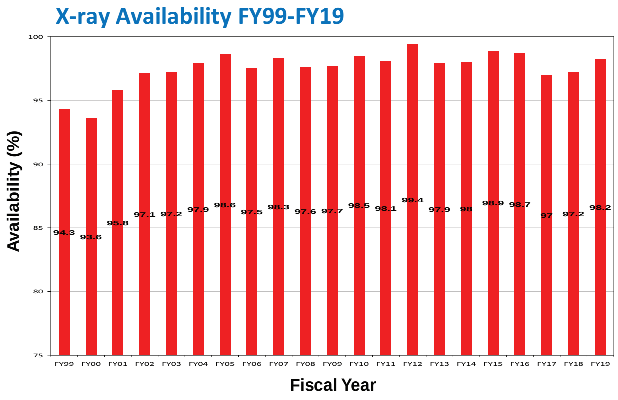

X-ray Availability: The number of hours that beam is available to users divided by the number of hours of scheduled beam delivery prior to the beginning of a run. The specific definition of available beam is that the APS main control room has granted permission to users to open shutters, and there is more than 50-mA stored beam in the storage ring.

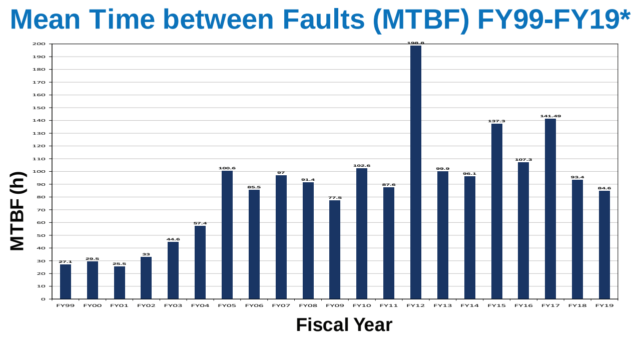

Storage Ring Reliability: A measure of the mean time between beam losses (faults), or MTBF, calculated by taking the delivered beam and dividing by the total number of faults. The APS targets, and routinely exceeds, 70 h MTBF. A fault is defined as complete unavailability of beam either via beam loss or removal of shutter permit not related to weather. A fault also occurs when beam has decayed to the point where stability and orbit can no longer be considered reliable (50 mA).

* While the highlights in, and title of, this report cover calendar year 2019, data on accelerator performance and user statistics are measured on the basis of fiscal years.

TYPICAL APS MACHINE PARAMETERS

LINAC

Output energy	425 MeV
Output beam charge	0.3–3 nC
Normalized emittance	5–20 mm-mrad
Frequency	2.856 GHz
Modulator pulse rep rate	30 Hz
Gun rep rate	2–26 Hz
(1-13 pulses, 33.3 ms apart every 0.5 s)	
Beam pulse length	8–15 ns
Bunch length	1–10 ps FWHM

PARTICLE ACCUMULATOR RING

Nominal energy	425 MeV
Circumference	30.66 m
Cycle time	0.5 s or 1 s
Fundamental radio frequency (RF1)	9.77 MHz
12th harmonic RF frequency (RF12)	117.3 MHz
RMS bunch length (after compression)	0.34 ns

INJECTOR SYNCHROTRON (BOOSTER)

Nominal extraction energy	7.0 GeV
Injection energy	425 MeV
Circumference	368.0 m
Ramping rep rate	2 Hz or 1 Hz
Natural emittance	132 nm-rad (nominal) 87 nm-rad (actual)
Booster RMS bunch length	100 ps
Radio frequency	351.935 MHz

STORAGE RING SYSTEM

Nominal energy	7.0 GeV
Circumference	1104 m
Number of sectors	40
Length available for insertion device	5.0 m
Nominal circulating current, multibunch	100 mA
Natural emittance	2.5 nm-rad
RMS momentum spread	0.096%
Effective emittance	3.1 nm-rad
Vertical emittance	0.040 nm-rad
Coupling (operating)	1.5%
Revolution frequency	271.555 kHz
Radio frequency	351.935 MHz
Operating number of bunches	24 to 324
RMS bunch lengths	33 ps to 25 ps
RMS bunch length of 16 mA in hybrid mode	50 ps

Novel Accelerator and X-ray Techniques and Instrumentation

Removing the Uncertainty of Flame-Sampling with X-ray Fluorescence Spectroscopy

Similar to the uncertainty principle of quantum physics is the observer effect, in which measuring or observing a phenomenon changes it. It's a principle with important implications for one of the most important tools of combustion chemistry, the flame-sampling experiment, in which chemical reactions are observed and studied within the dynamic environment of a laminar flame using a quartz-tipped sampling probe. The probe, however, affects the flame, thus inevitably altering the flow and temperature fields and thus, the measured data. The precise effects of the distortions created by the sampling probe, and how to minimize and compensate for them in experimental results and models are vital questions. Researchers sought to provide more definitive insights through x-ray fluorescence spectroscopy observations of probe-perturbed flames carried out at the APS. Rather than refuting the value of flame-sampling due to the unavoidable perturbations caused by sampling probes, these experiments and the resulting data promise to improve the utility and accuracy of flame-sampling analyses and models.

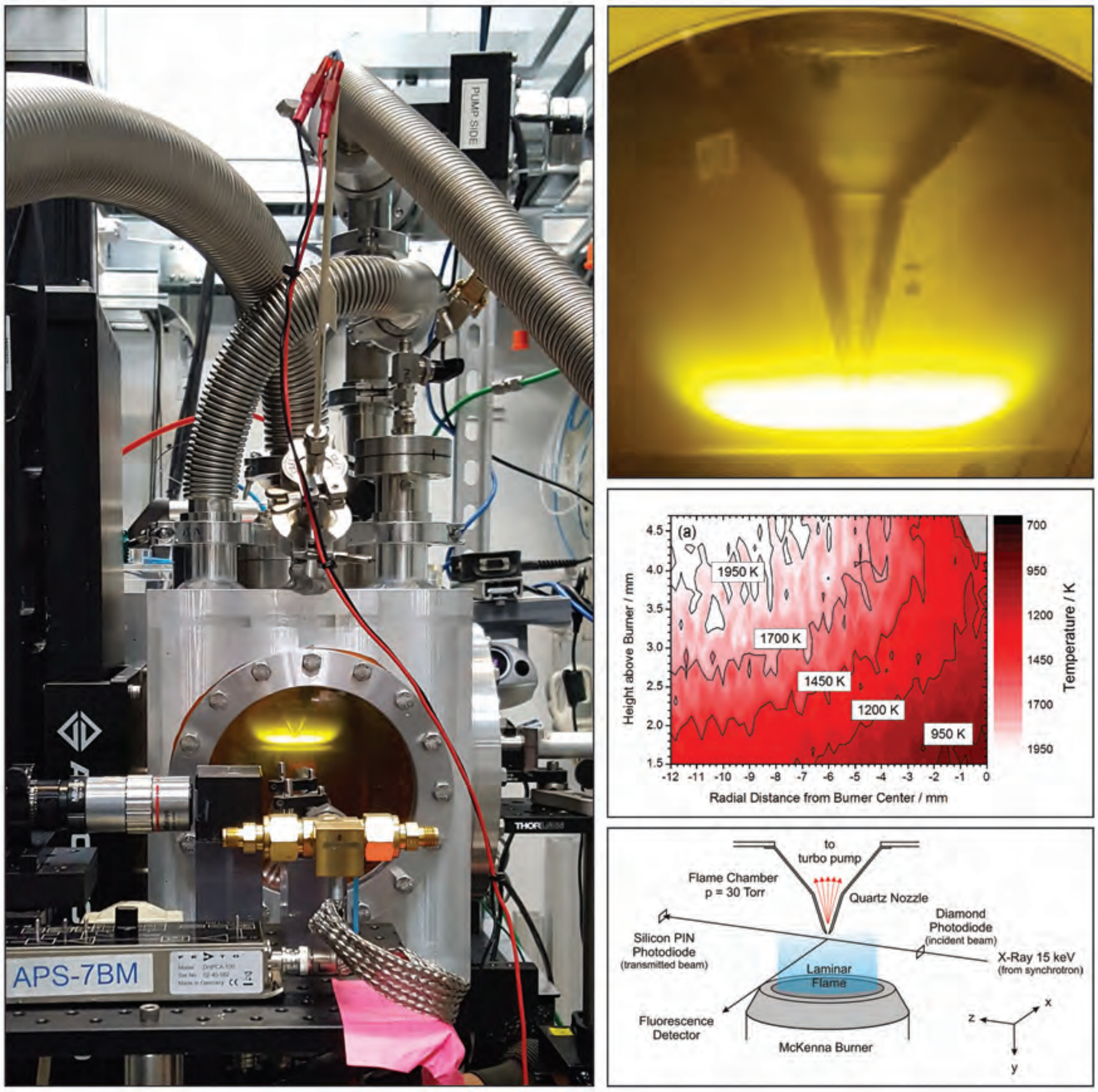

Following previous work, which accurately imaged the two-dimensional temperature field around a quartz probe in a low-pressure laminar pre-mixed C2H4/O2/Kr/Ar flame, the research team from the Sandia and Argonne national laboratories examined how the geometry of four different sampling probes affects the temperature field. Using storage ring-based x-ray fluorescence spectroscopy at the XSD 7-BM beamline at the APS, the investigators collected fluorescence signals of Kr atoms added to the flame and converted these into temperature measurements using methods developed in their earlier studies (Fig . 1).

The measurements were made in three dimensions: flame temperature, radial distance from the flame centerline, and probe distance from the burner, along with centerline temperature measurements of both perturbed and unperturbed flames. This allowed the creation of three-dimensional plots to provide an accurate picture of a broad range of temperature fields. The quartz probes, made in the Glass Workshop at Argonne, had various opening angles from 15° to 45° at 10° increments, each with a 400-µm aperture. The precision of the probe shapes was important for interpreting the differences among the observed effects.

At burner-probe separations of 4 mm and 7 mms along the centerline, temperature differences in the flame were clearly evident among the various probe geometries, with a difference of over 1000 K between perturbed and unperturbed flames with the 15° and 45° probes. The tip of the 15° probe was also 300 K higher than the tip of the 45° probe at the same burner separation. The 22-mm burner-probe separation measurements were in the post-flame zone and showed little temperature difference between perturbed and unperturbed flames. The experimenters note that the sampling probe acts as a heat sink at all separations, affecting the flame more significantly at shorter burner-probe distances by physically distorting the flow field, which does not occur at larger separation distances.

< Fig. 1. Left: Photograph of the experimental set-up. Top right: photograph of the flame and the quartz sampling probe through the Kapton window. Middle right: Two-dimensional experimental temperature profile determined using x-ray Kr fluorescence. Bottom right: schematic of the experimental set-up.

Measurements at different burner-probe separations and distances in the radial axis conducted up to 20 mm from centerline displayed similar effects. At 0-mm radial distance, temperatures were essentially identical between the 15° and 45° probes in the post-flame region and only began to show up when the burner-probe separation was reduced to 7 mm. At a separation of 3.8 mm in the bottom of the flame zone, temperature differences were more apparent, with the 45° probe causing flow perturbations out to 15-mm radial distance, with a temperature drop of about 1200 K.

The investigators note some intriguing effects when plotting temperature differences against the 15° and 45° probe geometries. The maximum difference between the two probes is seen not along the centerline, but 4 mm outward, and temperatures 3 mm below the probe tip show even greater differences. When the tip is moved closer to the burner in the pre-heat zone at 1.87 mm, very large flow perturbations are seen with all probes. Fluid dynamics calculations may be needed to fully interpret these phenomena.

Based on this work, the experimenters recommend a greater standardization of sampling probe design, or at least greater emphasis on clearly specifying its parameters when reporting experimental and modeling results. This will only facilitate both the useful comparison of experimental data among different research groups and of data with theoretical models, reducing experimental uncertainties. – Mark Wolverton

See: N. Hansen[1]*, R.S. Tranter[2], J.B. Randazzo[2], J.P.A. Lockhart[2], and A.L. Kastengren[2], “Investigation of sampling-probe distorted temperature fields with X-ray fluorescence spectroscopy,” P. Combust. Inst. **37,** 1401(2019). DOI: 10.1016/j.proci.2018.05.034

Author affiliations: [1]Sandia National Laboratories, [2]Argonne National Laboratory
Correspondence: * nhansen@sandia.gov

This material is based upon work supported by the U.S. Department of Energy (DOE) Office of Science-Basic Energy Sciences. The work at Argonne was performed under Contract No. DE-AC02-06CH11357. Sandia National Laboratories is a multi-mission laboratory managed and operated by National Technology and Engineering Solutions of Sandia, LLC., a wholly owned subsidiary of Honeywell International, Inc., for the U.S. DOE National Nuclear Security Administration under contract DE-NA0003525. This research used resources of the Advanced Photon Source, a U.S. DOE Office of Science User Facility operated for the DOE Office of Science by Argonne National Laboratory.

The APS Upgrade Will Enable Improved Bragg Coherent Diffraction Imaging

Coherent x-ray diffraction imaging (CDI) is an important non-destructive imaging technique available at the APS. When probing crystalline materials in three dimensions, the technique is called Bragg coherent diffraction imaging (BCDI). Scientists currently use BCDI to reveal nanoscale properties of crystals, including strain and lattice defects. The APS Upgrade (APS-U) will provide highly coherent x-rays at far greater energies than are now available at the APS, allowing BCDI to reveal crystalline imperfections in even greater detail throughout a far larger volume. Unfortunately, current reconstruction algorithms have difficulty coping with the diffraction patterns resulting from substantially higher x-ray energies. Theoretically, these limitations can be overcome by shrinking detector pixel size, enlarging the dimensions of the experiment, or recording many more diffraction patterns. But each of these options entails significant design drawbacks. A research team has now demonstrated a signal processing method that yields high-resolution BCDI images derived from high-energy x-rays using standard experimental parameters. The new processing method was confirmed through simulations and experimentally at the APS. These results promise unprecedented imaging of complex crystalline materials and polycrystalline interfaces, as well as nanocrystals embedded within a bulk matrix, for instance nanocrystals dispersed within catalytic systems. More generally, the new processing method will encourage broader use of flexible CDI experiments at fourth-generation x-ray light sources.

BCDI involves diffracting a coherent beam of monochromatic x-rays off a crystalline lattice. Monochromatic means the x-rays possess a single frequency, while coherent means they share the same relative phase, with their individual peaks and troughs moving in sync. During a typical BCDI experiment, a nanocrystal is incrementally rotated under an x-ray beam. At certain angles, the diffraction patterns are brightest; these patterns are Bragg peaks. X-ray detectors measure the intensities of each peak, which are recorded and later computer-processed. Figure 1a shows the basic experimental concept. Note the central bright spot in yellow and the surrounding interference fringes.

By employing BCDI at x-ray energies around 10 keV, scientists have measured properties like lattice defects and strain in nano-sized crystals embedded in a polycrystalline matrix. However, penetration is relatively limited for larger samples (micrometer-range and above).

With the advent of the APS-U, highly-coherent x-rays with energies of 50 keV and above will become available, allowing imaging of previously-inaccessible crystals residing deep within polycrystalline materials. However, higher-energy BCDI is challenging when using standard experimental setups because the fringe pattern associated with each Bragg peak gets compressed on the detector as the x-ray energy increases, which effectively means that data is lost and image resolution suffers.

In order to achieve high-resolution imaging for next-generation BCDI experiments without radically changing experimental equipment, dimensions, or run times, the research team from Argonne and Aix Marseille University (France) developed a computer processing technique based upon a newly-designed algorithm. This algorithm borrows heavily from standard algorithms used for current BCDI experiments, but is modified for the data compression of higher-energy BCDI. This data compression results from a phenomenon called pixel binning.

Just like a digital camera, x-ray detectors have many individual pixels (picture elements). Capturing the broader Bragg peaks of high-energy BCDI using standard detectors results in binning of the diffraction pattern, in which several adjacent pixels are effectively treated as a single, larger pixel. However, this degrades image resolution. Binning, while often useful in scientific imaging and consumer

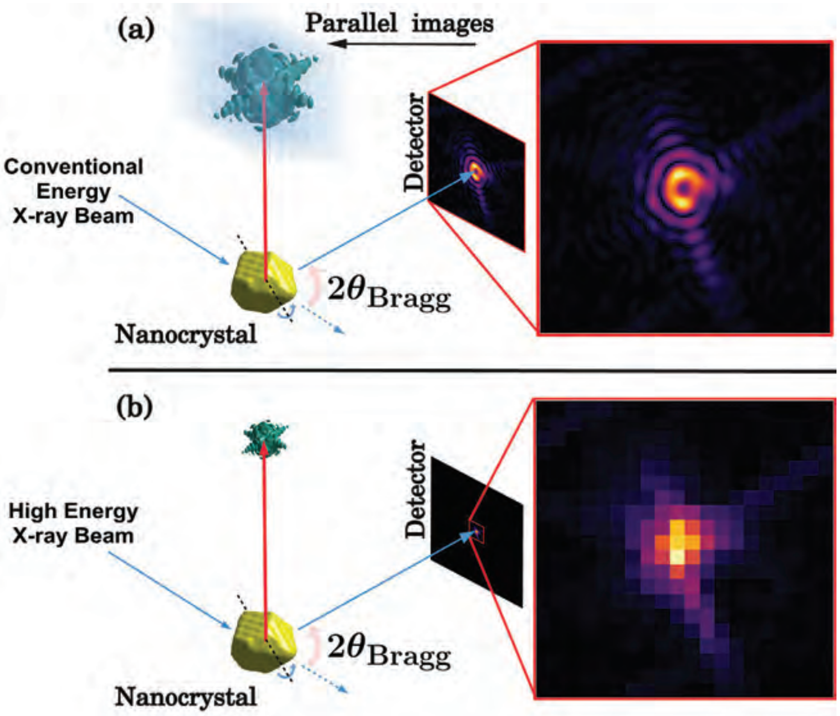

Fig. 1. Comparison of x-ray diffraction patterns obtained from conventional and high-energy BCDI experiments. In both instances, a gold nanocrystal is rotated in tiny increments under a highly-coherent x-ray beam. Using x-ray energies that are currently available at the APS for BCDI experiments results in well-defined diffraction patterns, as seen in panel (a). Using an identical experimental setup and the higher-energy x-rays available following the APS upgrade, the diffraction pattern becomes pixelated as depicted in panel (b). Figures from S. Maddali et al., "Phase retrieval for Bragg coherent diffraction imaging at high x-ray energies," Figures from S. Maddali et al., Phys. Rev. A **99**, 053838 (2019). ©2019 American Physical Society

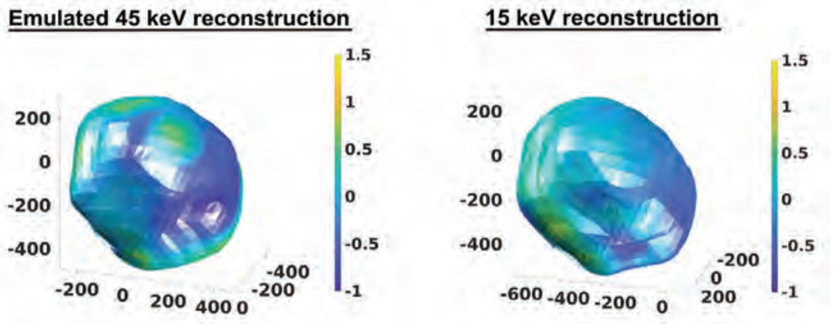

Fig. 2. Two image reconstructions of a gold nanocrystal derived from BCDI experiments. The right-hand image is based on diffraction data gathered from a conventional 15 keV BCDI experiment. The left-hand image is based on data gathered from a BCDI experiment designed to emulate high energy x-rays of 45 keV. The two images achieve similar detail. Nanocrystal size is displayed in nanometers along horizontal and vertical axes. Surface color depicts the relative phase of the diffracted x-rays, as indicated by the vertical color bars.

digital cameras, is undesirable here. The new reconstruction technique takes the highly pixelated data (Fig. 1b) and largely reverses the binning effect by reinterpreting the data as a virtual, high-resolution image with smaller pixels.

To confirm the efficacy of the new reconstruction technique, two experimental sessions were run at XSD beamline 34-ID-C of the APS. The first session utilized highly coherent, 15-keV x-rays. A second experiment mimicked x-rays three times as energetic (45 keV). Although the APS can currently produce 45-keV x-rays, they are not sufficiently coherent for BCDI experiments. To get around this limitation, the sample/detector distance was reduced by one-third while utilizing the same highly coherent 15-keV x-rays, which effectively emulated the highly coherent 45-keV x-rays that will become available with the APS-U.

Figure 2 compares images of the same gold nanoparticle derived from the two experiments. The two images are quite similar, indicating that the new processing technique can obtain good images from a higher-energy BCDI experiment. Computer simulations corroborated these findings. The researchers note that the methods demonstrated in this study are applicable to other imaging techniques, such as two-dimensional transmission coherent diffraction imaging. – Philip Koth

See: S. Maddali[1*], M. Allain[2], W. Cha[1], R. Harder[1], J.-S. Park[1], P. Kenesei[1], J. Almer[1], Y. Nashed[1], and S. O. Hruszkewycz[1], "Phase retrieval for Bragg coherent diffraction imaging at high x-ray energies," Phys. Rev. A **99**, 053838 (2019).
DOI: 10.1103/PhysRevA.99.053838

Author affiliations: [1]Argonne National Laboratory, [2]Aix Marseille University
Correspondence: * smaddali@anl.gov

Design and simulation of the phase-retrieval framework for high-energy coherent x-ray diffraction was supported by Laboratory Directed Research and Development funding from Argonne National Laboratory, provided by the Director, Office of Science, U.S. Department of Energy (DOE) under Contract No. DE-AC02-06CH11357. Experimental demonstration of the method was supported by the U.S. DOE Office of Science-Basic Energy Sciences, Materials Science and Engineering Division. This research used resources of the Advanced Photon Source, a U.S. DOE Office of Science User Facility operated for the U.S. DOE Office of Science by Argonne National Laboratory under Contract No. DE-AC02-06CH11357.

Beam Dynamics in the APS Upgrade Storage Ring

The APS Upgrade (APS-U) Project storage ring lattice [1] is designed to reduce the horizontal emittance nearly two orders of magnitude compared to the APS today, providing far brighter x-ray beams. Because of the strong link between lower emittance and challenging beam dynamics, a critical factor in confidently taking this step is high-fidelity simulation of beam dynamics.

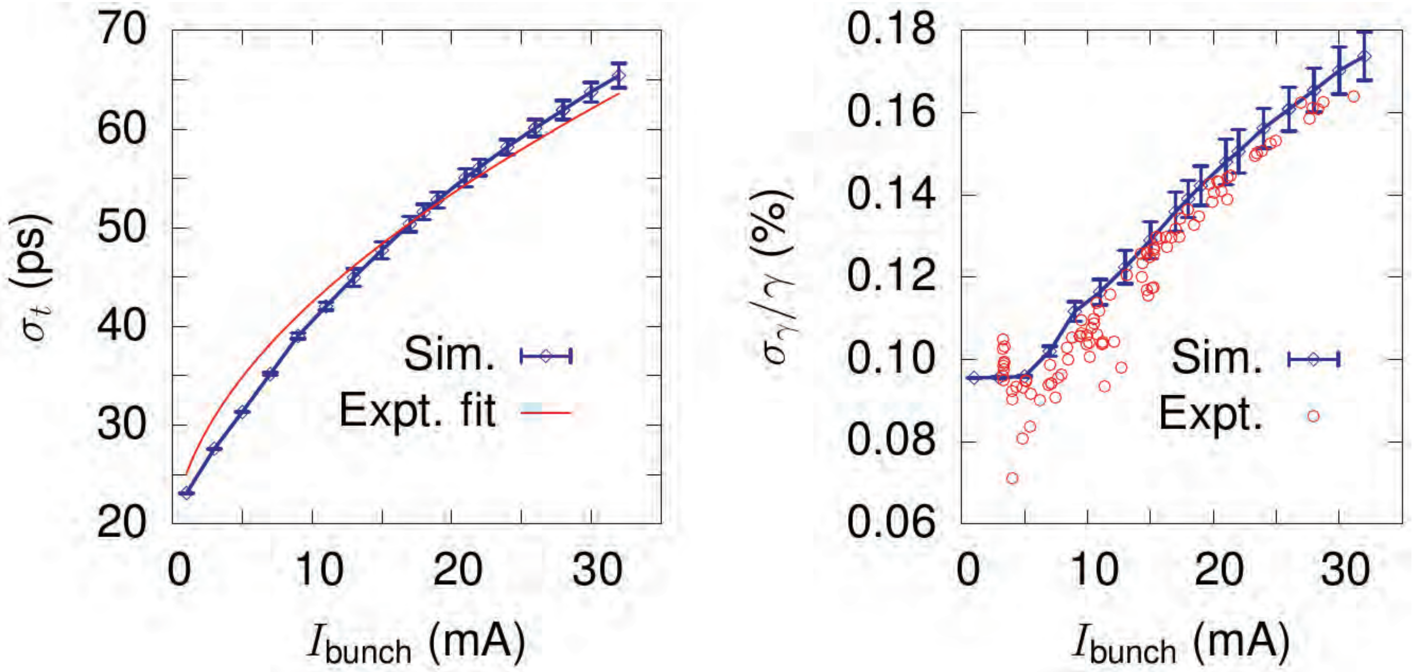

Fig. 1. Comparison of modeling of longitudinal beam instabilities in the present APS storage ring with experimental measurements [6]. The same modeling tools and techniques are used to predict instabilities in the APS-U ring.

Comprehensive modeling of electron beam dynamics must cover three aspects. First, we must model the behavior, including long-term stability, of single electrons in the external fields created by the accelerator magnets and radio-frequency (rf) systems. Second, we must understand the mutual interactions of the electrons in the beam, which includes intra-beam scattering and interaction via collective electromagnetic fields. Third, we must model the interaction of electrons with matter, such as (possibly ionized) residual gas or a beam dump. For APS-U, this modeling relies on the APS-developed code ELEGANT [2,3] and other codes.

Single-particle dynamics determines the beam emittance and lattice functions, but also the dynamic acceptance and local momentum acceptance. The dynamic acceptance determines the injection aperture and thus affects injection efficiency, while the local momentum acceptance strongly affects the beam lifetime, particularly for timing-mode operation. The dynamic acceptance and lifetime are optimized in simulation using a multi-objective genetic algorithm that adjusts elements of the magnetic lattice [4]. To ensure a robust solution, the APS-U Project has developed a detailed simulation of the commissioning process [5], which provides a set of possible configurations of the new machine after commissioning. For every significant design update, 100 such configurations are evaluated for injection efficiency, beam lifetime, and other characteristics [1].

Mutual interactions of electrons in the beam can result in inadequate lifetime and low instability thresholds. Intra-beam scattering, which occurs within a single electron bunch, can inflate the emittances and reduce the beam lifetime, both of which can be mitigated by lengthening the electron bunch. Toward this end, the APS-U incorporates a passive higher-harmonic rf cavity [6], whereby the electron beam creates fields that lengthen the electron bunches, a process that is simulated in a self-consistent fashion. Because of resistivity and unavoidable variations in the vacuum chamber cross-section, electron bunches produce electromagnetic wakes, which affects the behavior of the bunch itself and the following bunches. As the bunch charge increases, these effects become more severe, producing instability. Following methods used for the existing APS, detailed modeling was performed for the APS-U to ensure adequate stability margin for timing mode operation [7] (Fig. 1). Modeling of stability at injection [8] was an important factor in the final lattice selection.

Scattering from residual gas is a significant lifetime-limiting mechanism that has been carefully modeled [9], including predicting where electrons are lost. The electron beam can also ionize gas atoms, leading to a potentially unstable collective interaction with an ion cloud, particularly for 324-bunch operation. Modeling [10] has allowed developing countermeasures, namely, introducing a number of symmetric gaps into the 324-bunch train. These countermeasures were tested in experiments in the APS that involved deliberate injection of gas into the vacuum chamber.

Inevitably, every injected electron eventually impacts some part of the vacuum vessel. In the most dramatic example, a trip of one of the rf systems will promptly produce a full beam loss. Experience with the APS and modeling for the APS-U [11] indicate that the lost beam can cause catastrophic chamber damage. As a result, a series of beam dumps will be present in the APS-U to absorb the beam and localize the damage.

By modeling the new storage ring at this unprecedented level of detail, the APS-U beam-physics team hopes to speed the commissioning of the new ring, facilitating a rapid return to x-ray operations and full realization of the potential of the new design.

Contact: Michael Borland (mborland@anl.gov),
Ryan Lindberg (lindberg@anl.gov)

References

[1] M. Borland et al., “Lower emittance lattice for the Advanced Photon Source using reverse bending magnets,” Proc. NAPAC16, WEPOB01 (2017).

[2] M. Borland, “elegant: a Flexible SDDS-Compliant Code for Accelerator Simulation,” ANL/APS/LS-287 (2000).

[3] Y. Wang et al, “Pelegant: A Parallel Accelerator Simulation Code for Electron Generation and Tracking”, AIP Conf. Proc. 877, 241 (2006).

[4] M. Borland et al., “Multi-objective direct optimization of dynamic acceptance and lifetime for potential upgrades of the Advanced Photon Source,” ANL/APS/LS-319 (2010).

[5] V. Sajaev, “Commissioning simulations for the Argonne Advanced Photon Source upgrade lattice,” Phys. Rev. Accel. Beams **22**, 040102 (2019).

[6] S. H. Kim et al., “Design study of the higher harmonic cavity for the Advanced Photon Source,” Proc. IPAC15, TUPJE076 (2015).

[7] R. R. Lindberg et al., “Instability thresholds for the Advanced Photon Source multi-bend achromat upgrade,” Proc. IPAC15, TUPJE077 (2015).

[8] R. R. Lindberg et al., “Collective effects at injection for the APS-U MBA lattice,” Proc. NAPAC16, WEPOB08 (2017).

[9] M. Borland, “Parallel tracking-based modeling of gas scattering and loss distributions in electron storage rings,” Proc. NAPAC19, WEPLE08 (to be published).

[10] J. Calvey et al., “Modeling ion effects for the Argonne Advanced Photon Source upgrade,” Phys. Rev. Accel. Beams **22**, 114403 (2019).

[11] M. Borland, “Simulation of beam aborts for the Advanced Photon Source to probe material-damage limits for future storage rings,” Proc. NAPAC19, MOPLM07 (to be published).

A New High-Throughput HEDM Instrument at APS Beamline 6-ID-D

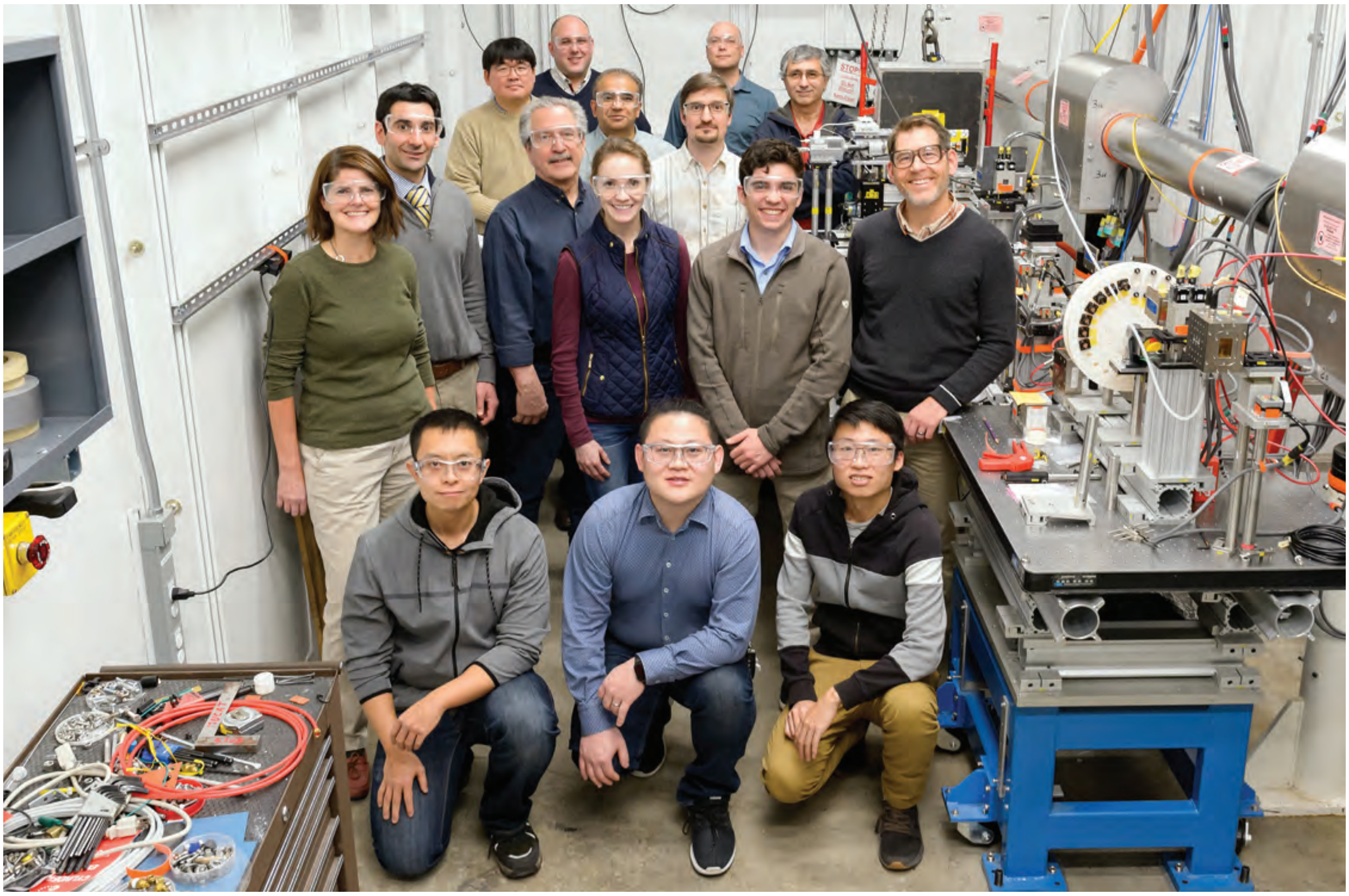

HT-HEDM team members inside the extended 6-ID-D hutch during initial commissioning of the instrument in December 2019, with NSF principal investigators denoted by *. Left to right, first row: Chen Zhang (CMU/CSM), Zhou Quan (Purdue/Utah), He Liu (CMU); second row: Erika Benda (XSD), Michael Sangid* (Purdue), Robert Suter* (CMU), Ashley Spear* (Utah), Robert Zampino (CSM), Jon Almer (XSD); third row: Jun-Sang Park (XSD), Sarvjit Shastri (XSD), Peter Kenesei (XSD), Ali Mashayekhi (XSD); fourth row: Aaron Stebner* (CSM) and Brandon Kappes (CSM).

A first-of-its-kind high-throughput, high-energy diffraction microscopy (HT-HEDM) instrument was installed at the XSD 6-ID-D end station in 2019. This instrument is funded through a National Science Foundation (NSF) Major Research Instrumentation grant with four partners: Carnegie Mellon University (CMU), Purdue University, the Colorado School of Mines (CSM), and the University of Utah. The APS is providing support to house the instrument; it will be operated by the XSD Materials Physics and Engineering Group. The instrument will allow both *ex situ* and limited *in situ* measurements (with a high-temperature furnace) of diffraction quantities on the grain-scale. The instrument leverages HEDM techniques development over the last two decades, including at the XSD 1-ID beamline of the APS. Key hardware includes focusing optics, a high-resolution sample manipulation system, and several detectors. Bluesky is being used for data collection, with a data reduction and analysis pipeline developed in collaboration with APS data scientists for the large data volumes. In order to accommodate this instrument, the 6-ID-D end station was extended downstream by 5 m and a control area with a mezzanine was constructed adjacent to it. This construction allows the HT-HEDM and existing high-energy x-ray program (operated by the XSD Magnetic Materials Group) to share space and beam time. Commissioning and initial experiments using the HT-HEDM instrument are ongoing. Contact; Jon Almer (almer@anl.gov)

Detector and Data Pipeline Developments for XPCS at APS Beamline 8-ID-I

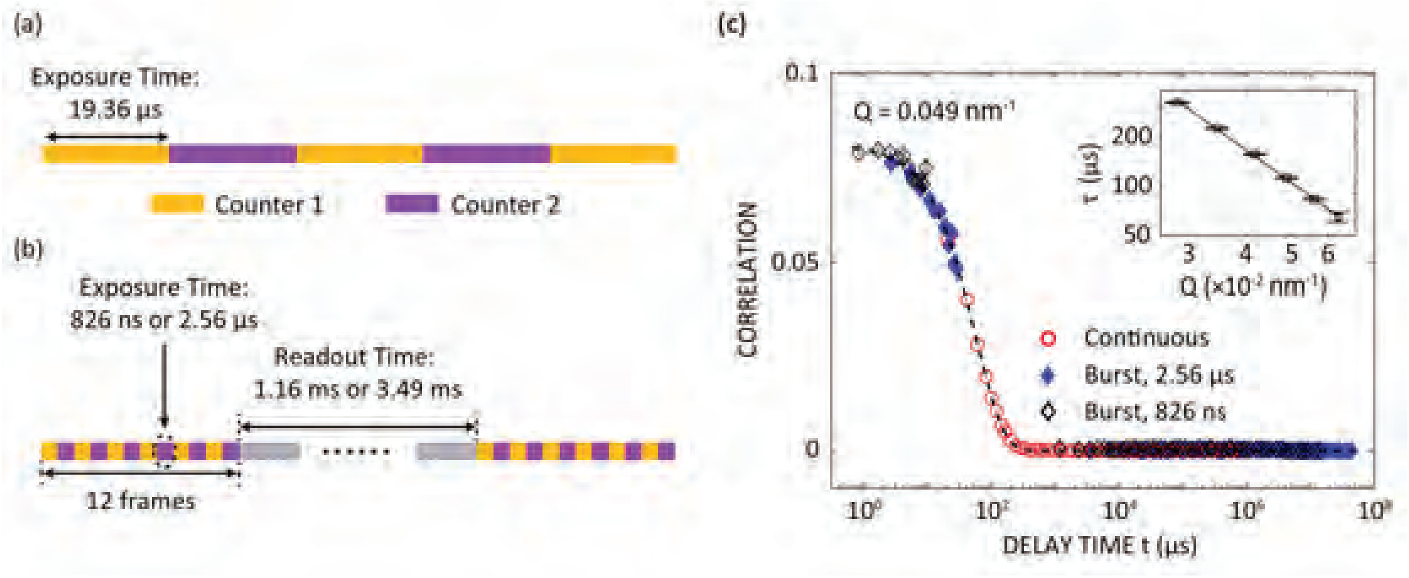

Fig. 1. Illustration of the frame acquisition sequence in the (a) continuous 50-kHz operation and (b) burst-mode operation. The acquisition time and the readout time can be either 826 ns/1.16 ms or 2.56 µs/3.49 ms depending on the clock frequency. (c) Intensity autocorrelation function g2 measured on a 100-nm-diameter silica nanoparticle in water showing the stitching of the 826-ns burst mode, 2.56-µs burst mode, and the 50-kHz continuous mode. The inset shows the characteristic time τ extracted from the exponential fitting g2 plotted as a function of the momentum transfer Q. The black solid line is the fit of τ vs. Q-2 dictated by the Einstein-Stokes equation describing the Brownian motion of the silica nanoparticles.

A large number of dynamical processes with chemical or biological relevance, such as the diffusion of nanoparticles, proteins, viruses, and micelles in aqueous environments occur on a spatial scale of 1 nm to 100 nm, leading to a dynamical time scale on the order of microseconds. While the 100-fold coherence enhancements to be delivered by the APS Upgrade Project will enable such novel science to be carried out routinely, commensurate developments in the detector frame rates and high-throughput data handling are critical for its realization.

With collaboration from AGH University in Poland, the team at XSD beamline 8-ID-I has demonstrated the first sub-microsecond, resolved x-ray photon correlation spectroscopy (XPCS) using an area detector and an ultrafast x-ray camera (UFXC) with continuous coverage from 826 ns to 10 s [1]. The detector can acquire frames continuously at a frame rate of 56 kHz (Fig. 1a), resulting in a sequence of frames separated by ~20 µsec. A shorter time resolution is achieved in a "burst mode" of operation whereby either 12 or 24 frames are acquired with an acquisition time as short as 826 ns, reading them out in 1 msec (Fig. 1 b). A combination of the two measurements using the same sample yields a gapless coverage of the XPCS correlation function from 826 ns to over 10 sec (Fig. 1 c). The detector has enabled successful dynamics measurements of gelation, liquid-liquid phase separation [4] and biophysical systems [2,3]. In 2018, Rigaku Corporation, Inc., purchased the UFXC technology from AGH University and built a larger detector, the X-ray Seamless Pixel Array, with a 56-kHz frame rate and a 1024 x 512-pixel array, which is currently deployed at 8-ID-I.

In order to handle and process the data from such detectors at high frame rates, the team at 8-ID-I has pioneered the high-performance computing (HPC) implementation of XPCS data reduction. Since initial deployment in 2013 [5], the team has been continually improving the performance of this system to keep the data reduction time within that required to collect data. The first implementation was developed in the "Hadoop Map Reduce" framework. To keep pace with the highly increased data rates, the group migrated the implementation to OpenMP, which supports multithreaded computation in a multi-core

"XPCS" cont'd. on page 127

Deployment of a Transition Edge Sensor Detector at APS Beamline 1-BM

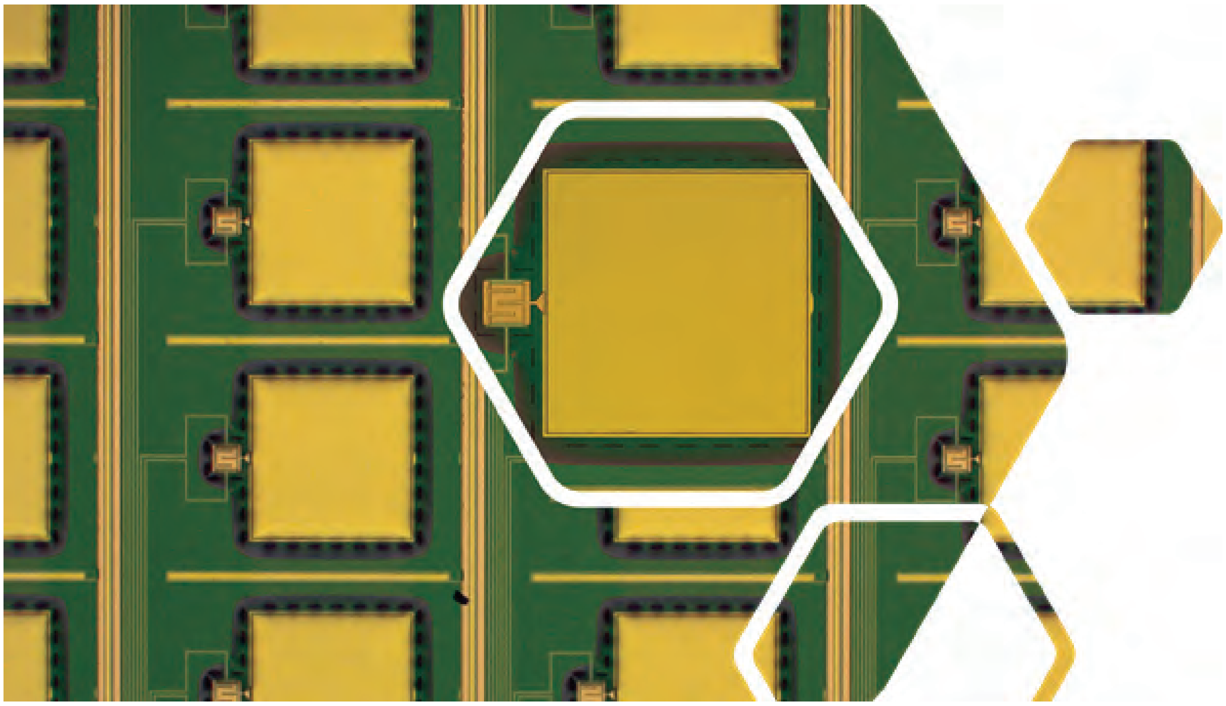

Fig. 1. Photo of an array of TESs. The insert shows a blown-up picture of a single pixel. On the left of the pixel the superconducting bilayer (which represent the thermal sensor) is visible, while on the right-hand side is the photon absorber, in this case made only of gold. The dark green shadow is the suspended SiN_x membrane that provides the thermal isolation.

X-ray fluorescence (XRF) is a powerful technique for identification of the elemental makeup of unknown samples, and for the quantification of their abundances. Hard x-rays (> 2 keV) are especially useful as they can probe all elements of the periodic table above phosphorus (Z = 15). However, the K-shell photon emission lines of common 3*d* and 4*d* transition metal elements like iron, nickel, and copper are in the 5-keV to 15-keV energy range, as are the L-shell lines of the 5*d* elements. In samples containing certain combinations of these metals, such as integrated circuits with hafnium oxides and copper, or organometallic complexes relevant to biological processes, semiconductor-based x-ray energy-resolving detectors cannot resolve these overlapping lines. Silicon drift detectors (SDDs) ,under ideal conditions, achieve an energy resolution of 125 eV, for example. Failing to properly resolve lines can result in an uncertainty in composition determination, or even completely missing the presence of a dilute element. In partial fluorescence yield x-ray absorption measurements, where the fluorescence yield of a particular emission line is monitored as the incident beam energy is scanned, the inability to measure the flux from one emission line alone limits the usable energy range. Superconducting energy-resolving photon detectors such as transition edge sensors (TESs) provide an order of magnitude better energy resolution than semiconductor-based detectors, while still maintaining the advantages of an energy-dispersive measurement. A TES is in essence a quantum-limited thermal sensor, capable of determining with great precision the energy of the absorbed photon by measuring the induced temperature rise. A TES-based spectrometer with an energy resolution of ~ 10 eV at 10 keV can easily resolve the emission lines of neighboring elements, allowing consistent identification of all peaks in XRF spectra, and extended x-ray absorption fine structure measurements over a very large range.

The XSD Detectors Group at the APS, in collaboration with the National Institute of Standards and Technology, is developing an instrument composed of ~ 100 pixels with a saturation energy of ~ 25 keV, an energy resolution of ~ 10 eV, and a total count rate of ~ 1000 counts/sec. The TES pixel is a superconducting bilayer square, which represents the thermal sensor, with a sidecar photon absorbe composed of a bilayer of gold and bismuth, all on a

"Transition" cont'd. on next page

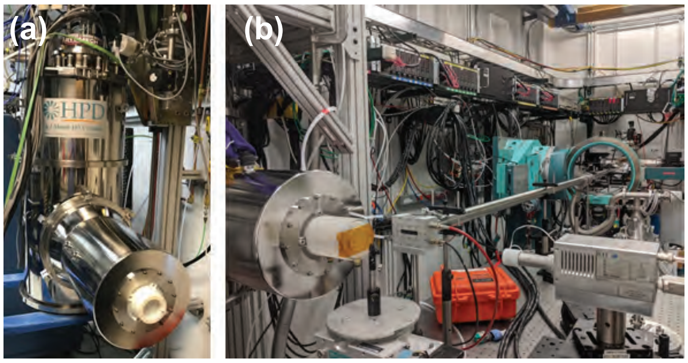

Fig. 2. (a) Photo of the TES spectrometer cryostat with snout. (b) Photo of the 1-BM-C experiment station prepared for x-ray fluorescence experiments.

"Transition" cont'd. from previous page

thin SiN_x membrane providing the thermal isolation for the correct measurement of the temperature evolution (Fig. 1). These sensors operate at very low temperatures (~ 100 mK), therefore a complex cryogenic environment is needed.

The Detectors Group in collaboration with the XSD Beamline Instrumentation Group developed a novel cryogenic setup that, building upon a commercial cryostat, brings the sensor close to the sample under examination for improved detection efficiency (snout, Fig. 2). In the current state, the instrument achieves resolutions on the order of ~ 10 eV at few counts/sec/pixel with an array of ~ 20 pixels. With this setup, a series of wide-band, high-resolution fluorescence experiments have been run at XSD beamline 1-BM-C. The group was able to study complex systems containing transition metals with overlapping x-ray emission lines, which would be impossible to separate with a silicon detector. In Fig. 3, the spectrum of the main emission lines from an integrated circuit fabricated with a 350-nm complementary metal-oxide semiconductor technology is shown together with the corresponding spectrum measured with a commercial silicon detector. The enhanced resolution of the TES spectrometer enables the identification of various composing metals, which would otherwise be indistinguishable. The group is currently developing a new generation of sensors based on an array of ~ 100 pixels and with enhanced count rates, of the order of tens of counts/sec/pixel, which will greatly increase experiment speed.

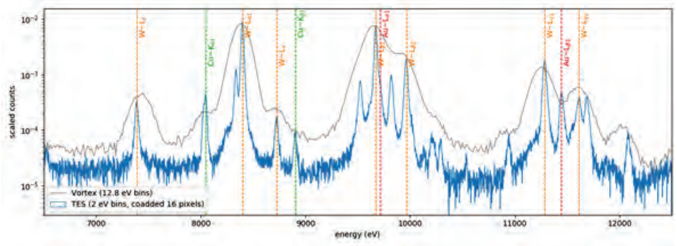

Fig. 3. X-ray fluorescence spectra of an integrated circuit fabricated in 350-nm complementary metal-oxide semiconductor technology, measured with a TES spectrometer (blue) and a commercial silicon detector (gray).

Contact: Orlando Quaranta (oquaranta@anl.gov)

Reference

"Hard X-ray Fluorescence measurements with TESs at the Advanced Photon Source," Tejas Guruswamy, Lisa M. Gades, Antonino Miceli, Umeshkumar M. Patel, John T. Weizeorick, Orlando Quaranta, https://arxiv.org/abs/1909.05919

"XPCS" cont'd. from page 125

CPU architecture (limited to a single node). The OpenMP implementation is built using a custom and highly efficient sparse implementation for the primary Multitau algorithm and a standard Eigen library is used for vectorized computation wherever applicable.

In the last three years, the detector frame rate at 8-ID-I has increased 500-fold from 100 Hz to 50,000 Hz. The workhorse detectors are a Medipix-based LAMBDA 750K (2 kHz) and a Rigaku 500K (56 kHz). To continue to process the data in near real-time with the data coming at the above rates, the APS developed Data Management (DM) and Workflow system has been implemented [5,6,] to provide a detector agnostic automated data processing pipeline with low latency.

The data from the XSD Dynamics & Structure Group's beamlines are archived to the DM system, which is built around a 2-PB data storage system [7]. General users of the APS can access their data remotely using their APS user credentials via Globus (http://www.globus.org/).

With the current coherent flux, for samples with low scattering rate, the ultrafast measurements need to be repeated hundreds of times to accumulate sufficient signal to noise ratio, which is all done seamlessly using the above developments.

Contact: Suresh Narayanan (sureshn@anl.gov)

References

[1] Q. Zhang et al., "Sub-microsecond-resolved multi-speckle X-ray photon correlation spectroscopy with a pixel array detector," J. Synch. Rad. **25**, 1408 (2018).
[2] D. Sheyfer et al., "Nanoscale critical phenomena in a complex fluid studied by x-ray photon correlation spectroscopy (submitted)
[3] P. Vodnala et al., "Hard-sphere-like dynamics in highly concentrated alpha-crystallin suspensions," Phys. Rev. E **97**, 020601 (2019).
[4] P. J. Chung et al., "α-Synuclein Sterically Stabilizes Spherical Nanoparticle-Supported Lipid Bilayers," ACS Appl. Bio Mater. **2**, 1413 (2019).
[5] F. Khan et al., J. Synchrotron Rad. (2018). 25, 1135-1143
[6] S. Veseli et al., "APS Data Management System," J. Synch. Rad. **25** 1574 (2018)
[7] J-S. Park et al., "Data management and processing workflow for the Materials Physics and Engineering group beamlines at the Advanced Photon Source," J. Synch. Rad. **26** 373 (2019).

Toward *In Situ* and *Operando* Structural Analysis of Functional Thin Films Via Grazing-Incidence Total X-ray Scattering

The precise structural analysis of interlayers and ultrathin films is of high importance for the understanding and development of functional devices. X-ray Science Division beamline 11-ID-B is dedicated to structural investigations of amorphous and nano-crystalline materials through pair distribution function (PDF) analysis of total x-ray scattering data, operating at photon energies of 59 keV and 87 keV. The technique provides quantitative structural insights over a wide length scale – from the nearest-neighbor atoms up to nanometers. The maximum obtainable momentum transfer Q_{max} ultimately determines the real-space resolution of the PDF function. Thus, modern measurements of PDF-suitable data take place at high-energy synchrotron light sources where a combination of bright, intense high-energy x-rays and large, highly sensitive area detectors positioned at a short sample-to-detector distance allows for collection of high-quality data with large Q_{max} on a time scale in the order of seconds.

Utilization of high-energy photons, with their inherent large penetration power, enables measurements on a wide range of materials and within complex sample environments under operating conditions, i.e., *in situ* and *operando*, but can significantly hamper measurements on a highly important and interesting subset of materials and samples, namely thin films and interlayers. The extremely small amount of sample in the path of a highly-penetrating x-ray beam (often significantly less than 1-µm thick) and strong contributions from the substrate (whose thickness often exceeds that of the film by a factor of 10^4) during conventional, transmission-based experiments lead to an extremely unfavorable sample-to-background ratio. This in turn requires extremely long collection times (up to one hour) and often still yields data of a quality that can significantly hinder and make often a reliable PDF extraction impossible for amorphous materials.

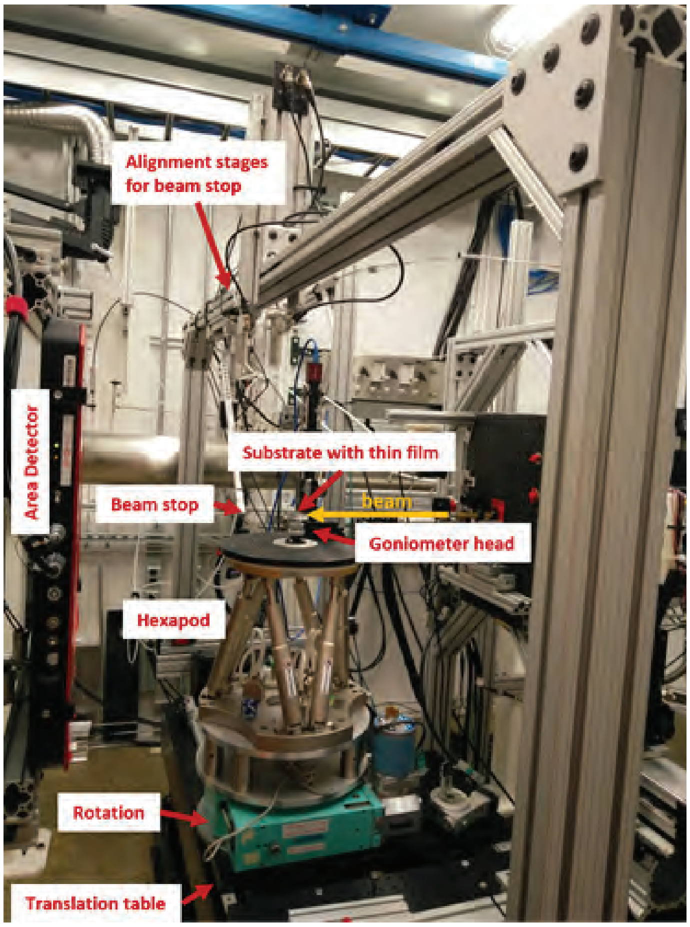

Fig. 1. Grazing-incident experimental setup within XSD beamline 11-ID-B. The beam is coming from the right. The sample is mounted on a goniometer head on the hexapod. The rotation below the hexapod enables alignment and sample studies in all directions. The stage below can support two experimental setups at the same time. The beam stop and the area detector can be translated along the beam path for best resolution.

The signal of an ultrathin film can be significantly enhanced, however, by performing the measurement under grazing incidence geometry close to the critical angle, minimizing the penetration of the x-ray into the substrate. The critical angle is linear to the wavelength of the photons, and it is approximately 0.02° for glass – a common thin film substrate material – at the photon energy of 87 keV. The best enhancement of the film signal is expected barely below this angle, which requires a very precise alignment of the substrate. Therefore, this type of measurement presents certain nontrivial technological challenges and equipment requirements. Essential for successful measurement is a highly stable stage assembly capable of sample positioning with extreme precision in

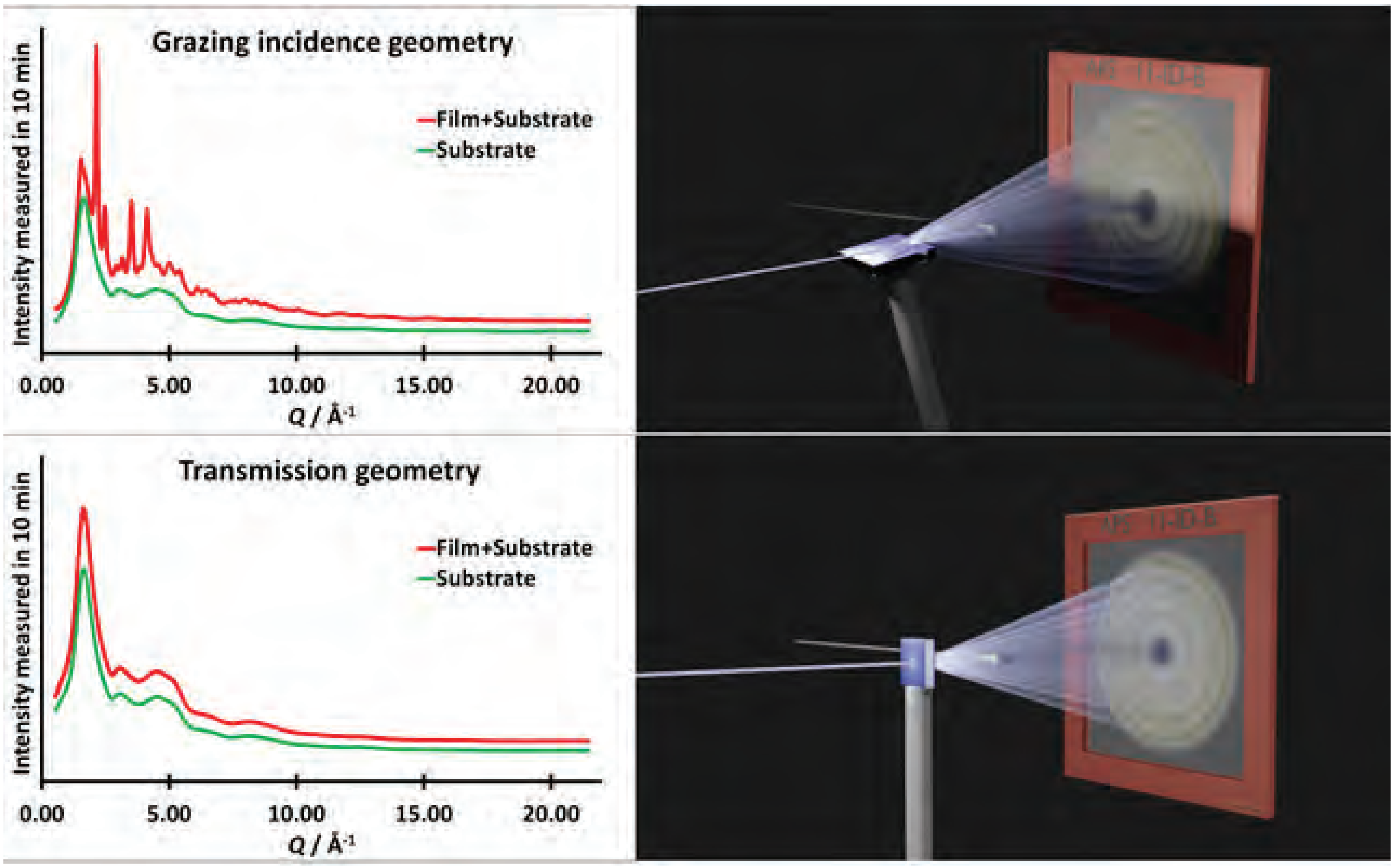

Fig. 2. Comparison of integrated scattering data collected at beamline 11-ID-B on the same 100-nm-thin indium oxide films in grazing incidence geometry (top) and transmission geometry (bottom) measured in the same time of 10 min. The measured intensity in transmission geometry is dominated by the substrate. In grazing incidence geometry, the diffraction pattern from the thin film is easy to distinguish from the substrate.

respect to height and incident angle as well as a focused x-ray beam of a few micrometers in height.

The instrumentation in XSD beamline 11-ID-B was completely redesigned in 2019-2020 to accommodate a broader variety of experimental setups. One of these setups, capable of collecting grazing-incidence high-energy total x-ray scattering data suitable for PDF analyses (GI-PDF), was commissioned last year at beamline 11-ID-B. A newly acquired Physik Instrumente H-840 hexapod has enabled sample positioning with precise sub-micrometer positioning and an angular resolution of better than 0.001° (Fig. 1). Vertical one-dimensional x-ray focusing yielding a beam height of less than 5 µm (by 400 µm) at 87 keV has been achieved with APS-produced compound reflective lens structures etched into a silicon wafer. The thin-film signal enhancement over the substrate signal resulting from GI-PDF geometry (Fig. 2) provides superior data quality from measurements with substantially reduced collection times (on the order of several minutes), enabling measurements and analysis of even amorphous thin films. The expansion of the current GI-PDF setup is planned for measurements under variable temperature (-150° C to 1000° C) and controlled atmosphere (various gases), opening up new research avenues including *in situ* growth and annealing as well as *operando* measurements of functional thin films and interlayers.

Contact: Uta Ruett (uruett@anl.gov) and
Olaf Borkiewicz (borkiewicz@anl.gov)

Reference

[1] A.-C. Dippel, M. Roelsgaard, U. Boettger, T. Schneller, O. Gutowski. U. Ruett, "Local atomic structure of thin and ultrathin films via rapid high-energy X-ray total scattering at grazing incidence," IUCRJ **6**, 290 (2019). DOI: 10.1107/S205225251900051

This research used resources of the Advanced Photon Source, a U.S. Department of Energy (DOE) Office of Science User Facility operated for the DOE Office of Science by Argonne National Laboratory under Contract No. DE-AC02-06CH11357.g incidence" IUCRJ **6**, 290 (2019). DOI: 10.1107/S205225251900051

Temperature-Jump Method Reveals Protein Shape Dynamics

At the cellular level, biological processes are geometry-dependent, like the plastic stars and rectangles of brightly-colored children's toys that only pass through the slots if you pair the correct shapes. The shape of a molecule, called its conformation, dictates what it can do and with which other molecules it can interact. But macromolecules – such as proteins, plastics, and even carbon nanotubes – aren't fixed; they bend, rotate, and even walk. Macromolecules shift shapes due to environmental factors, such as temperature or light, and as part of biological processes as varied as the movement of fuel through cell walls and skin cell response to pressure, plus the use of enzymes to speed up biological processes. Because a protein's shape is a function of the temperature of its solvent, a team of scientists chose to pair temperature-jump perturbations with x-ray scattering experiments carried out at the APS to measure molecular structures directly, currently an underutilized combination of techniques. Their results establish the applicability and success of this combined process to determine the conformational dynamics of an important protein.

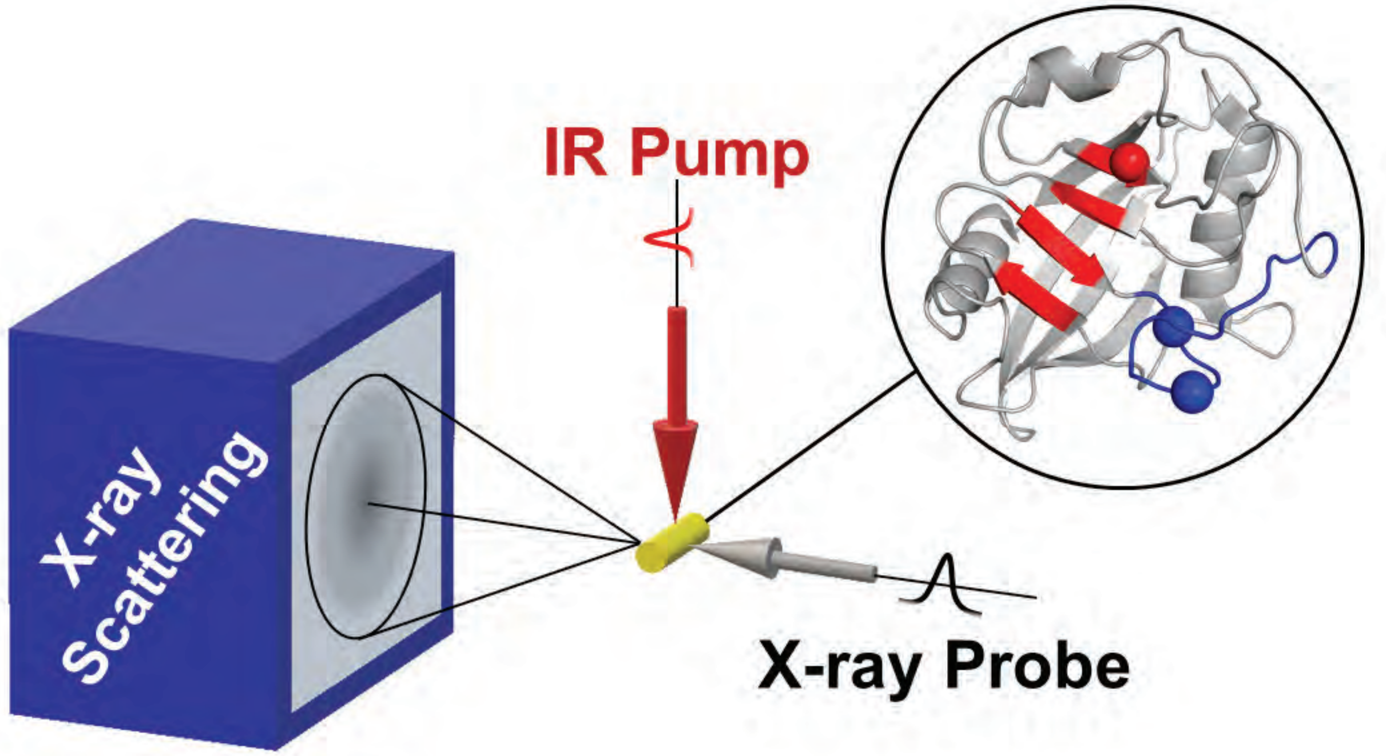

Scientists employ a number of tools that allow them to determine the conformations of proteins, such as molecular crystallography and solution scattering. However, these techniques typically focus on static structures found under equilibrium conditions and so don't assess intermediate shapes that may arise during conformational change. Using time-resolved x-ray scattering and diffraction could address this, but they have mostly been used to characterize molecules with a light-sensitive component, which excludes many fundamental proteins. The team of researchers from the University of California, San Francisco, and the National Institutes of Health demonstrated the wide applicability of the combination of temperature jumps with x-ray scattering by scrutinizing a significant protein, human cyclophilin A, a molecular chaperone which aids in the folding of proteins and plays a role in signaling between cells.

The study focused on the most common genetic variant, or wild-type, of the protein. The conformation of human cyclophilin A includes a “loops” region and a “core” region, both of which participate in different biological processes. The team used an infrared laser to increase the temperature of the solvent containing human cyclophilin A. At regular time intervals, while the protein relaxed to a new equilibrium shape, the team measured its structure using x-ray solution scattering, as depicted in Fig. 1. They measured both small- and wide-angle x-ray scattering data using the BioCARS 14-ID beamline at the APS. The team collected the x-ray scattering images in pairs in order to associate the imagery immediately before and after an increase in temperature. The results of the team's investigations included both dynamic information about human cyclophilin A and the efficacy of this new process to the understanding of other macromolecules.

The team found that temperature perturbations changed the scattering profile of the protein. From the two-part change in scattering, the team concluded that a two-part model was necessary to explain their results. To further investigate the specifics of the two-part change, the team also measured the conformational changes of two human cyclophilin A mutations. The rates and frequencies of changes in the loops and core regions differed between the wild-type protein and the mutants. From these differences, the team was able to draw conclusions about the dynamics of each variant of the protein. They were also able to associate each part of their model with one of the two conformational regions. Unlike existing methods which focus on static protein structure, this combination of temperature jump and x-ray scattering allowed the team to determine protein motions as a function of time.

< Fig. 1. A simplified version of the experimental setup during the combined temperature-jump and x-ray scattering technique.

The success of the team's investigations into the conformational change of human cyclophilin A illustrates how this combined method can describe macromolecular dynamics that occur at different rates and structural characteristics that are unavailable using techniques that temporally average structural information. This combination of temperature jumps and x-ray scattering could yield information about those macromolecules not well-characterized by today's widely-used techniques, enabling not only more refined basic science but novel medicines and other biotechnologies. – Mary Alexandra Agner

See: Michael C. Thompson[1], Benjamin A. Barad[1], Alexander M. Wolff[1], Hyun Sun Cho[2], Friedrich Schotte[2], Daniel M. C. Schwarz[1], Philip Anfinrud[2]*, and James S. Fraser[1]**, “Temperature-jump solution X-ray scattering reveals distinct motions in a dynamic enzyme,” Nat. Chem. **11**, 1058 (November 2019).
DOI: 10.1038/s41557-019-0329-3

Author affiliations: [1]University of California, San Francisco, [2]National Institutes of Health
Correspondence: * anfinrud@nih.gov, ** jfraser@fraserlab.com

We thank the staff at BioCARS (I. Kosheleva, R. Henning, A. DiChiara, and V. Srajer) for assistance. This work was supported by the National Science Foundation (STC-1231306), the National Institutes of Health (GM123159 and GM124149), a Packard Fellowship from the David and Lucile Packard Foundation, the U.C. Office of the President Laboratory Fees Research Program LFR-17-476732 (to J.S.F.), the Intramural Research Program of the National Institute of Diabetes and Digestive and Kidney Diseases (to P.A.) and a Ruth L. Kirschstein National Research Service Award (F32 HL129989 to M.C.T.). The use of BioCARS was supported by the National Institute of General Medical Sciences of the National Institutes of Health under grant number P41GM118217. The time-resolved setup at Sector 14 was funded in part through a collaboration with P.A. (NIH/NIDDK). This research used resources of the Advanced Photon Source, a U.S. DOE Office of Science User Facility operated for the DOE Office of Science by Argonne National Laboratory under Contract No. DE-AC02-06CH11357.

RIXS to the Forefront in the Study of Strongly Correlated Materials

It is now clear that novel materials exhibiting surprising or even revolutionary physical properties are necessary for critical advances in technologies that markedly affect people's everyday lives. Iridium oxides have attracted growing attention due to the unique consequences of their rare interplay of on-site Coulomb repulsion, crystalline fields, and strong spin-orbit coupling (SOC) interactions. The most profound manifestation of that competitive environment is the $J_{\mathrm{eff}} = 1/2$ Mott state, which serves as the building block for a host of fascinating proposed and observed states, including those of frustrated magnets, topological insulators, and possibly even unconventional superconductors. The strong competition between Coulomb repulsion and electron hopping can lead to hopping between neighboring IrO_6 octahedra in, for example, the face-sharing iridate $Ba_5AlIr_2O_{11}$, delocalizing the electrons and possibly heavily modifying or even destroying the $J_{\mathrm{eff}} = 1/2$ Mott state. An international team of researchers used the APS to show that it is possible to directly probe such states to understand orbital dimerization between neighboring pairs of IrO_6 octahedra in $Ba_5AlIr_2O_{11}$.

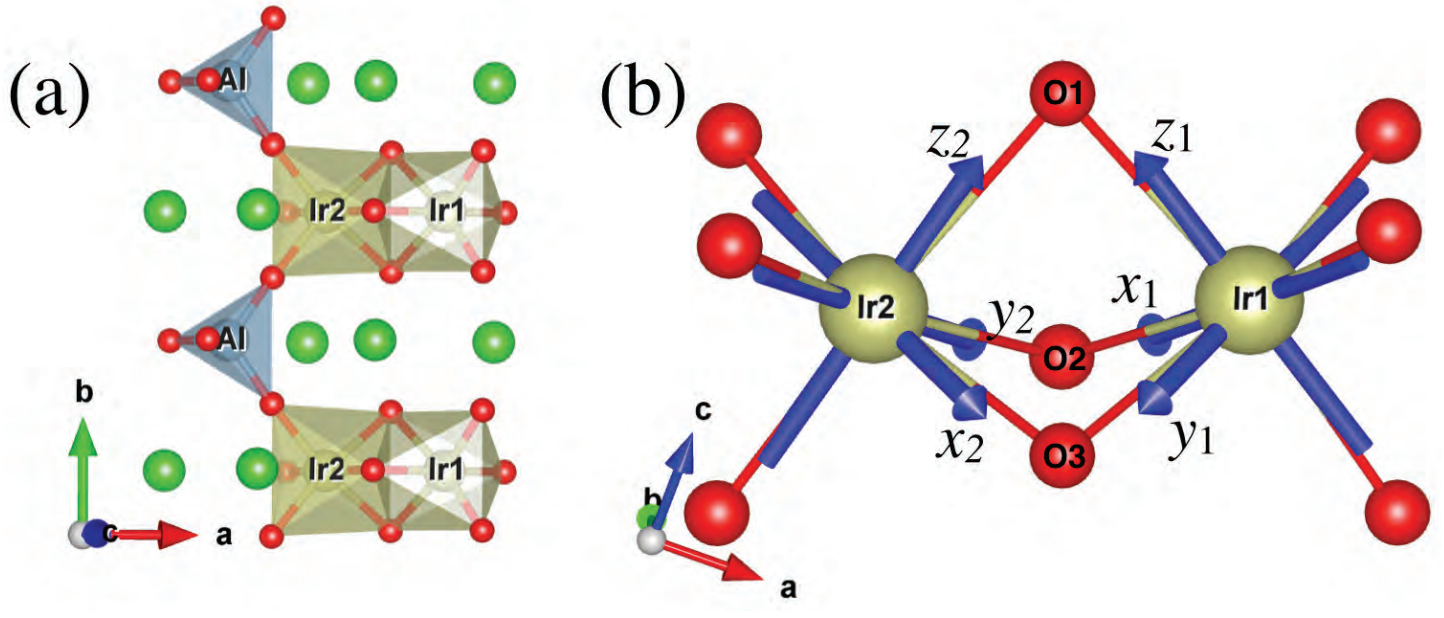

Fig 1. (a, b) Crystal structure of $Ba_5AlIr_2O_{11}$. The two inequivalent IrO_6 octahedra are labeled Ir1 and Ir2 and colored in dark yellow. Quasi-one-dimensional Ir chain structures occur via the connection of these octahedra through AlO_4 tetrahedra along the b axis.

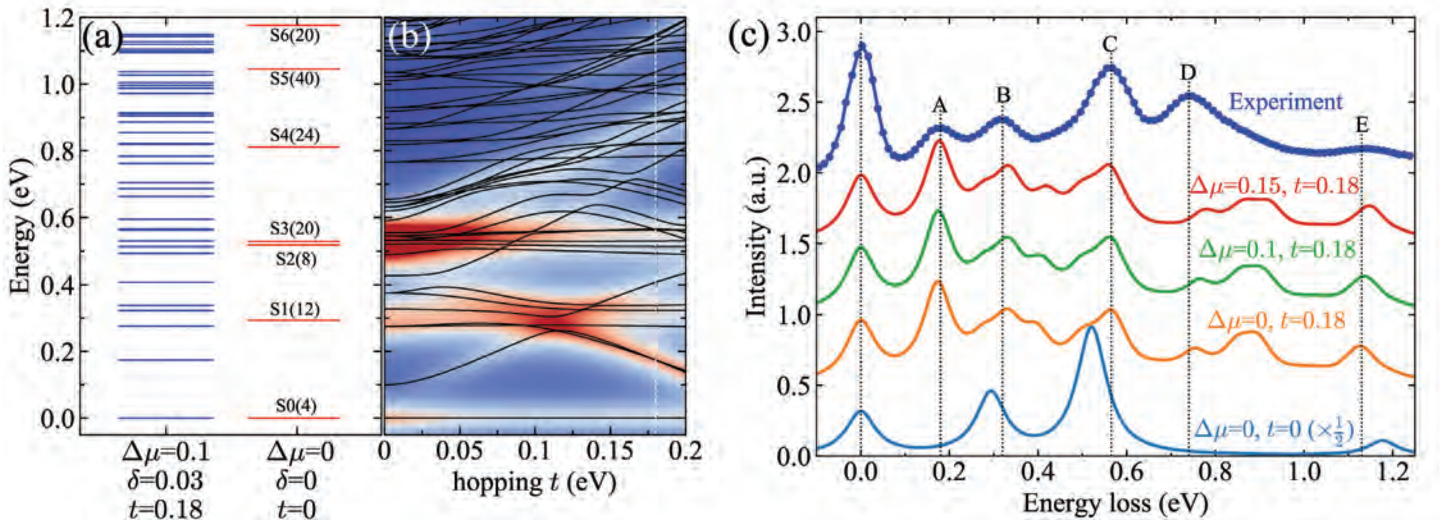

Fig. 2. (a) Illustration of the splitting of the trivial direct product states after turning on the hopping t between the two Ir sites. (b) The solid lines are the energy spectra of the Ir-Ir cluster model as a function of hopping t at the change in chemical potential $\Delta\mu$ = 0.1 eV and the crystal field splitting δ = 0.03 eV; the color map indicates the corresponding simulated RIXS intensity, while the vertical dotted line indicates t = 0.18 eV. (c) The simulated RIXS spectra at several chosen parameters are compared with the experimental result; δ = 0 for the bottom light blue curve and δ = 0.03 for all others.

The researchers performed resonant inelastic x-ray scattering (RIXS) experiments at the Ir-L_3 edge using the RIXS spectrometer at XSD beamline 27-ID at the APS and established that RIXS can directly measure peaks associated with orbital dimerization and that a quantitative description of the dimer electronic configuration can be extracted using density functional theory (DFT) calculations and multiplet modeling.

The team of researchers began by surveying incident-energy-dependent RIXS peaks at room temperature to see whether the five distinct peaks in the spectra exhibited dispersive behavior at various momentum transfer values. A more detailed incident energy dependence was then mapped at 40 K with 80-meV energy resolution. Understanding the polarization dependence of the scattering at resonance is crucial, which is why the RIXS spectrometer was designed to scatter x-rays both vertically and horizontally. In the end, data were collected with a horizontal scattering geometry with the incident x-ray polarization being parallel to the scattering plane, which included the [010] Ir chain direction and the [101] sample surface normal. The lack of appreciative dispersive behavior in the five RIXS peaks suggested that the excitations were confined within the dimer and that coupling through the $\mathrm{AlO_4}$ tetrahedra could be neglected (Fig. 1).

The researchers used a two-site cluster model for the two inequivalent Ir1 and Ir2 octahedra. The EDRIXS toolkit developed in the COMSCOPE project was used to simulate the RIXS spectrum, with the real experimental geometry and polarization applied. To understand the electronic structure that gave rise to the observed excitations, the researchers started with the nonphysical condition in which the Ir1-Ir2 hopping and the non-cubic crystal field were set to zero. With the octahedra decoupled, the electronic structure was determined by the SOC, the on-site Coulomb repulsion, and Hund's J_H interactions. With J_H = 0.3 eV and SOC = 0.345 eV values taken from previous research, the simulated RIXS spectrum exhibited only three peaks (Fig. 2c).

To estimate the hopping and the non-cubic crystal field, the researchers performed a first-principles DFT calculation using the Vienna *ab initio* Simulation Package. After turning on the hopping, the two peaks that were missing when the hopping was turned off appeared in the simulated RIXS spectrum as excitations between delocalized dimerized states. The calculated RIXS spectrum agreed well with experimental observations in other respects as well (Fig. 2c). The DFT calculations and the RIXS simulations confirmed that the hopping strength between Ir1 and Ir2 in $\mathrm{Ba_5AlIr_2O_{11}}$ is indeed strong enough to form dimer orbitals and that the electronic structure of $\mathrm{Ba_5AlIr_2O_{11}}$ needs to be described by partially delocalized dimer orbitals, rather than J_{eff} = 1/2 atomic states in the strong SOC limit.

The dimerization process was found to significantly change the magnetic properties of $\mathrm{Ba_5AlIr_2O_{11}}$. The calculated effective local moment per dimer was about 1 μB,

"RIXS" cont'd. on page 135

Results Using the Superconducting Helical Undulator at the APS

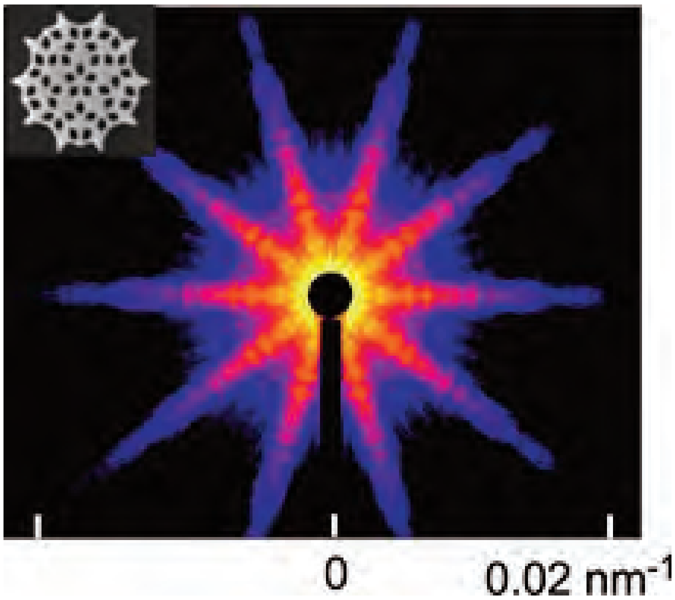

Fig. 1. Coherent diffraction imaging of a microscopic test sample (inset) using the HSCU white beam at the XSD 7-ID beamline. The high-contrast speckle patterns clearly show that the unfiltered beam can be used for imaging non-periodical structures. The resolution is sufficient to resolve structures of micrometers (equivalent to a q-resolution of 10^{-3} nm^{-1} at the 6-keV fundamental photon energy) with the white beam. The q-range marked also corresponds to the value at 6 keV. An Eiger 500K detector was used to record the scattering pattern.

Coherence-Driven Experiments Using the APS Helical Superconducting Undulator

A first-of-its-kind insertion device (ID), a 1.2-m-long helical superconducting undulator (HSCU), has been designed, assembled, installed at the XSD 7-ID beamline of the APS, and is now in operation [1]. The magnetic field in the HSCU is generated and tuned by its helical superconducting coils in which the current can be adjusted to tune the x-ray energy. Thanks to the helical magnetic field, the HSCU has the unique property of producing circular polarized hard x-ray photons that are best-in-principle for probing magnetic materials. However, there are less-known properties in the HSCU compared to a linear undulator. These include (1) a stronger magnetic field resulting in a more intense x-ray flux in the first harmonic, (2) lower high-harmonics contents in on-axis radiation, and (3) lower heat load in the center cone of the beam. The spectral distribution of the x-ray beam indicates the HSCU is closer to an ideal undulator than a conventional undulator that uses permanent magnets. While the photon flux values are comparable to the APS full-length (2.5-m) Undulator A, for example, at 6-keV photon energy, the high-harmonics radiation is significantly lower in the HSCU beam. On the other hand, the power in the central cone is measured to be about five times lower in the HSCU beam than in Undulator A. Coherent x-ray imaging/scattering in both real and reciprocal spaces has been developed at the APS using unfiltered white HSCU beam, which are technically difficult, if not impossible, with the conventional Undulator A.

Ultrafast X-ray Phase-Contrast Imaging with the HSCU White Beam

It has been demonstrated that it is possible to image fluid droplets with single x-ray pulses of about 100-ps duration, during which the motion and structure of the droplets are frozen. While both the HSCU and Undulator A yield enough x-ray flux for this technique, the HSCU spectrum is much cleaner, with weaker high-order harmonics. By combining multi-pulse exposure or consecutive frames, it is possible to get a clear picture of how the droplets evolve in three-dimensional space and time.

White-Beam Coherent Diffraction Imaging

Coherent diffraction imaging (CDI) is a lens-less imaging method using monochromatic x-rays. Theoretically, its reconstruction resolution is only limited by diffraction angle and x-ray wavelength. To achieve the ultimate resolution, CDI requires high transverse-coherence flux. With Undulator A, due to the intense high-order harmonics, it is necessary to have a set of filtering optics (e.g., reflection mirror and monochromator) to select monochromatic x-rays from a single undulator radiation harmonic. However, all optics can inadvertently distort the x-ray wave front and degrade coherence. The unfiltered HSCU beam, with a much lower number of x-ray photons in the high-order harmonics, makes white-beam-based CDI possible, as shown in Fig. 1. In this case, the highest x-ray flux can be achieved without compromising the transverse coherence

"Helical" cont'd. on next page

"Helical" cont'd. from previous page

of the beam, thanks to the wide energy spectrum. In the meantime, with minimal optics in the beam, the x-ray wave front is preserved to the greatest extent. In addition, the coherent scattering signal from higher orders can in principle be removed or separated by energy thresholding on the detector, while speckle smearing due to the finite bandwidth of the fundamental can be tackled by advanced algorithms during reconstruction.

White-beam X-ray Photon Correlation Spectroscopy

X-ray photon correlation spectroscopy (XPCS) has been developed at third-generation synchrotron sources such as the APS as an important coherent technique for studying the dynamics of microstructures and nanostructures. In addition to the coherence requirement of the x-ray beam, a successful XPCS experiment requires the beamline to be stable during the measurement. Vibrations on the order of a fraction of the beam size, or 1 µm, will degrade the XPCS signal. It has been demonstrated that the HSCU white beam, with no major optics between the source and the sample, can be readily used for XPCS measurements of fast dynamics in a nanoparticle colloidal suspension. Thus, major sources of vibration are removed in such an optics-free beamline.

To summarize, at the XSD 7-ID beamline, unfiltered and high-intensity white beam from the newly installed HSCU was used for coherence-driven experiments that normally use a monochromatic x-ray beam. At the current APS, the high coherent flux can be used to achieve better time resolution for the measurements. The HSCU-equipped beamline can also be used as an APS Upgrade Project test ground to validate new coherence-based experimental ideas and methods. Although the longitudinal coherence length has an intrinsic limit when probing dynamics in the high momentum-transfer regime, studies demonstrate satisfactory speckle contrast in the ultra-small-angle and small-angle regimes, well suited for a wide range of science cases of non-periodical micro- and nanostructures and their dynamics. Contact: Jin Wang (wangj@anl.gov)

This research used resources of the Advanced Photon Source, a U.S. Department of Energy (DOE) Office of Science User Facility operated for the DOE Office of Science by Argonne National Laboratory under Contract No. DE-AC02-06CH11357.

"RIXS" cont'd. from page 133

which was consistent with the experimental results but much smaller than the 1.732 µB value expected for two isolated Ir sites. This indicated that the symmetry of the magnetic order parameter deviated from the ideal spherical symmetry due to the intersite hopping and the extended orbitals.

The research established RIXS as a spectroscopic tool fully able to probe the formation of delocalized dimer orbitals and characterize their microscopic properties, which may open new directions in the study of delocalization in other dimerized strongly correlated materials by RIXS with widespread potential applications in molecules, oxide heterostructures, and even ultrafast transient states.

– Vic Comello

See: Y. Wang[1]*, Ruitang Wang[2,3,7], Jungho Kim[4], M. H. Upton[4], D. Casa[4], T. Gog[4], G. Cao[5], G. Kotliar[1,6], M. P. M. Dean[1]**, and X. Liu[2]***, "Direct Detection of Dimer Orbitals in $Ba_5AlIr_2O_{11}$," Phys. Rev. Lett. **122**, 106401 (2019). DOI: 10.1103/PhysRevLett.122.106401

Author affiliations: [1]Brookhaven National Laboratory, [2]ShanghaiTech University, [3]Chinese Academy of Sciences, [4]Argonne National Laboratory, [5]University of Colorado, Boulder, [6]Rutgers University, [7]University of Chinese Academy of Sciences
Correspondence: *yilinwang@bnl.gov, ** mdean@bnl.gov,
*** liuxr@shanghaitech.edu.cn

Work at ShanghaiTech University was supported by the ShanghaiTech University startup fund and partially supported by MOST of China under Grant No. 2016YFA0401000 (experiment, data analysis, and leading writing). R. W. was supported by the international partnership program of the Chinese Academy of Sciences under Grant No. 112111KYSB20170059 (experiment and data analysis). Work at Brookhaven National Laboratory was supported by the U.S. Department of Energy (DOE) Office of Science-Basic Energy Sciences, as a part of the Computational Materials Science Program through the Center for Computational Design of Functional Strongly Correlated Materials and Theoretical Spectroscopy (calculations, software development, and data interpretation), Basic Energy Sciences, Early Career Award Program under Award No. 1047478 (writing), and the U.S. DOE Office of Science-Basic Energy Sciences, under Award No. DE-SC0012704. Work at Argonne National Laboratory was supported by the U.S. DOE Office of Science, under Award No. DE-AC-02-06CH11357 (synchrotron user facility instrumentation). Work at the University of Colorado, Boulder, was funded by National Science Foundation Grant No. DMR-1712101 (materials synthesis). This research used resources of the Advanced Photon Source, a U.S. DOE Office of Science User Facility operated for the DOE Office of Science by Argonne National Laboratory under Contract No. DE-AC02-06CH11357.

APS Users by Institutional Geographic Distribution (FY 2019)

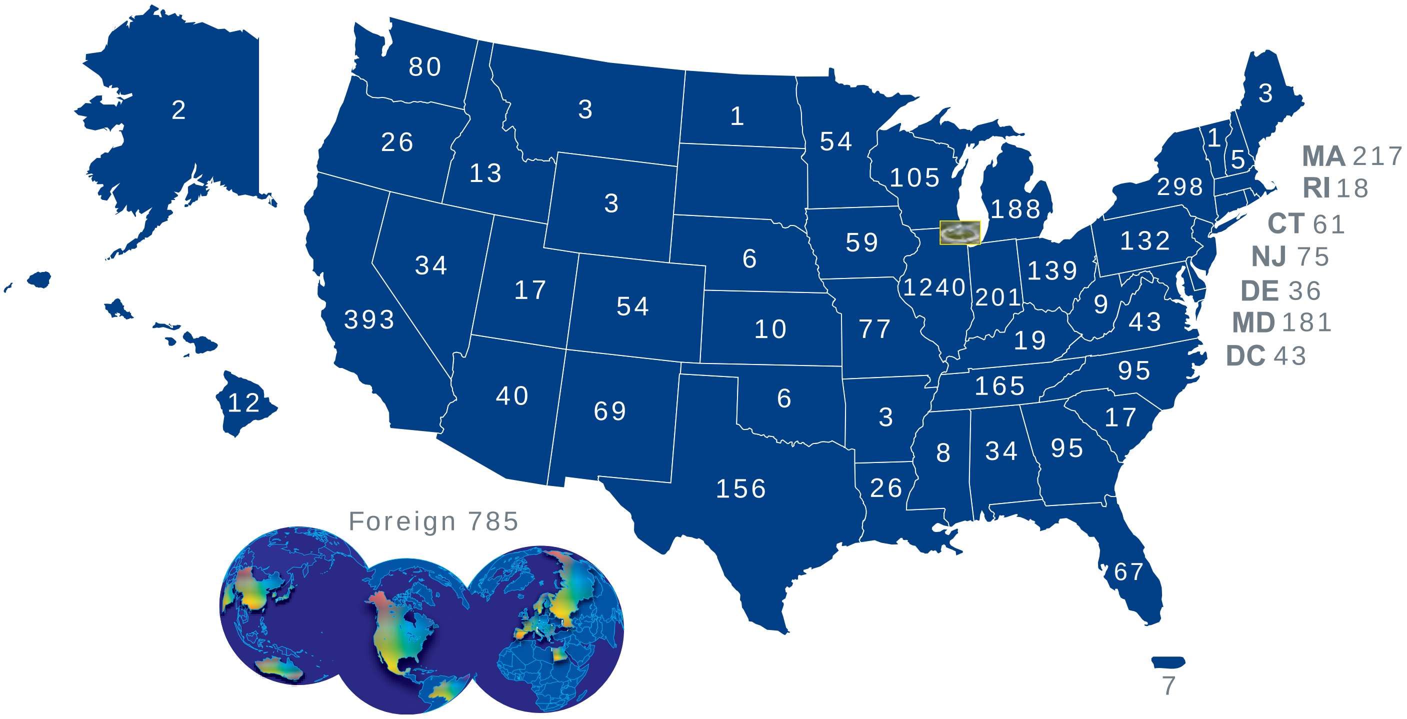

A new algorithm has been applied so that only 1 unique user is associated with mail-in and remote proposals.

APS Funding (FY 2006-FY 2019)

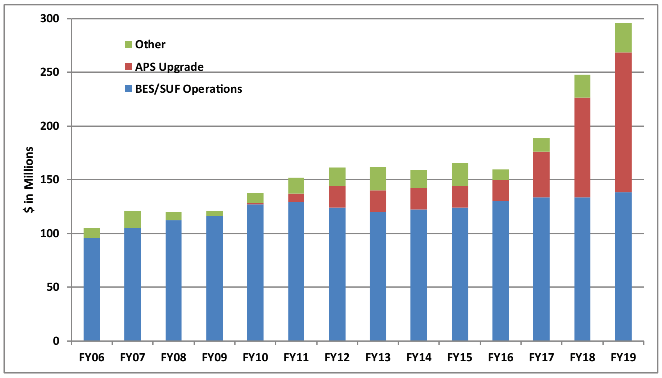

APS Staffing (FY 2007-FY 2019)

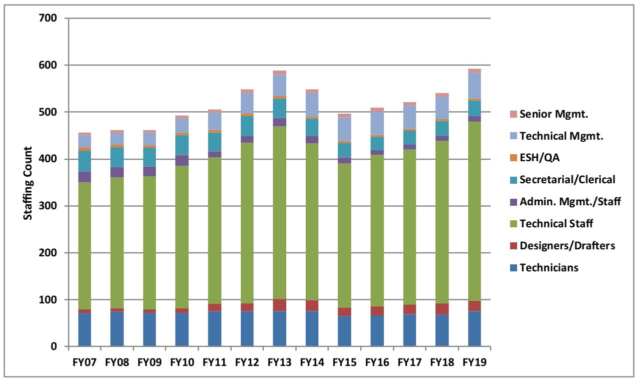

Photon Sciences Directorate Organization Chart

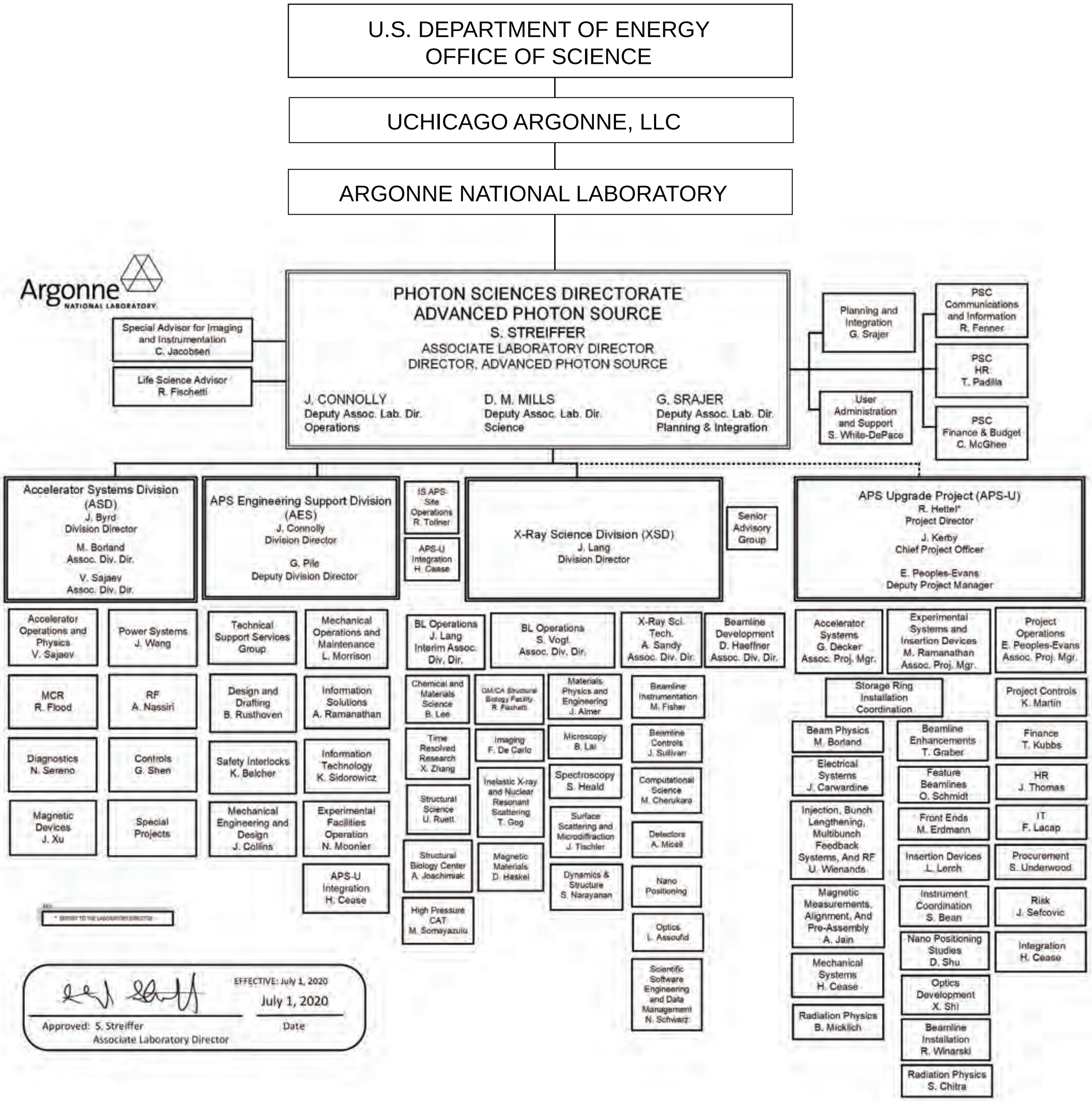

APS Source Parameters

Undulator A (31 insertion devices [IDs] in 25 sectors)

Period: 3.30 cm
Length: 2.1 m in sectors 16, 21, 23, 24, 28, 34; 2.3 m in Sector 6; 2.4 m in sectors 1, 2, 5, 7, 8, 9, 10, 11, 15, 17, 18, 19, 20, 22, 26, 28, 31, 32, 33
Minimum gap: 10.5 mm
B_{max}/K_{max}: 0.892 T/2.75 (effective; at minimum gap)
Tuning range: 3.0–13.0 keV (1st harmonic)
3.0–45.0 keV (1st–5th harmonic)
On-axis brilliance at 7 keV (ph/s/mrad^2/mm^2/0.1%bw):
4.1 x 10^{19} (2.4 m), 4.0 x 10^{19} (2.3 m), 3.3 x 10^{19} (2.1 m)
Source size and divergence at 8 keV:
Σ_x: 276 μm Σ_y: 11 μm
$\Sigma_{x'}$: 12.7 μrad (2.4 m), 12.8 μrad (2.3 m), 12.9 μrad (2.1 m)
$\Sigma_{y'}$: 6.7 μrad (2.4 m), 6.8 μrad (2.3 m), 7.1 μrad (2.1 m)

2.30-cm Undulator (2 IDs in sectors 11, 14)

Period: 2.30 cm Length: 2.4 m
Minimum gap: 10.5 mm
B_{max}/K_{max}: 0.558 T/1.20 (effective; at minimum gap)
Tuning range: 11.8–20.0 keV (1st harmonic)
11.8–70.0 keV (1st-5th harmonic, non-contiguous)
On-axis brilliance at 12 keV (ph/s/mrad^2/mm^2/0.1%bw): 6.9 x 10^{19}
Source size and divergence at 12 keV:
Σ_x: 276 μm Σ_y: 11 μm
$\Sigma_{x'}$: 12.3 μrad $\Sigma_{y'}$: 5.9 μrad

2.70-cm Undulator (5 IDs in sectors 3, 12, 14, 35)

Period: 2.70 cm
Length: 2.1 m in Sector 12; 2.4 m in sectors 3, 14, and 35
Minimum gap: 10.5 mm
B_{max}/K_{max}: 0.698 T/1.76 (effective; at minimum gap)
Tuning range: 6.7–16.0 keV (1st harmonic)
6.7–60.0 keV (1st-5th harmonic, non-contiguous)
On-axis brilliance at 8.5 keV (ph/s/mrad^2/mm^2/0.1%bw):
5.7 x 10^{19} (2.4 m), 4.7 x 10^{19} (2.1 m)
Source size and divergence at 8 keV:
Σ_x: 276 μm Σ_y: 11 μm
$\Sigma_{x'}$: 12.7 μrad (2.4 m), 12.9 μrad (2.1 m)
$\Sigma_{y'}$: 6.7 μrad (2.4 m), 7.1 μrad (2.1 m)

3.00-cm Undulator (8 IDs in sectors 12, 13, 16, 21, 23, 27, 34)

Period: 3.00 cm
Length: 2.1 m in sectors 12, 13, 16, 21, 23, 34; 2.4 m in Sector 27
Minimum gap: 10.5 mm
B_{max}/K_{max}: 0.787 T/2.20 (effective; at minimum gap)
Tuning range: 4.6–14.5 keV (1st harmonic)
4.6–50.0 keV (1st-5th harmonic)
On-axis brilliance at 8 keV (ph/s/mrad^2/mm^2/0.1%bw):
4.8 x 10^{19} (2.4 m), 3.9 x 10^{19} (2.1 m)
Source size and divergence at 8 keV:
Σ_x: 276 μm Σ_y: 11 μm
$\Sigma_{x'}$: 12.7 μrad (2.4 m), 12.9 μrad (2.1 m)
$\Sigma_{y'}$: 6.7 μrad (2.4 m), 7.1 μrad (2.1 m)

3.50-cm SmCo Undulator (Sector 4)

Period: 3.50 cm Length: 2.4 m
Minimum gap: 9.75 mm
B_{max}/K_{max}: 0.918 T/3.00 (effective; at minimum gap)
Tuning range: 2.4–12.5 keV (1st harmonic)
2.4–42.0 keV (1st-5th harmonic)
On-axis brilliance at 7 keV (ph/s/mrad^2/mm^2/0.1%bw): 3.7 x 10^{19}
Source size and divergence at 8 keV:
Σ_x: 276 μm Σ_y: 11 μm
$\Sigma_{x'}$: 12.7 μrad $\Sigma_{y'}$: 6.7 μrad

3.60-cm Undulator (Sector 13)

Period: 3.60 cm
Length: 2.1 m
Minimum gap: 11.0 mm
B_{max}/K_{max}: 0.936 T/3.15 (effective; at minimum gap)
Tuning range: 2.2–11.8 keV (1st harmonic)
2.2–40.0 keV (1st-5th harmonic)
On-axis brilliance at 6.5 keV (ph/s/mrad^2/mm^2/0.1%bw): 2.8 x 10^{19}
Source size and divergence at 8 keV:
Σ_x: 276 μm Σ_y: 11 μm
$\Sigma_{x'}$: 12.9 μrad $\Sigma_{y'}$: 7.1 μrad

1.72-cm Undulator (3 IDs in sectors 30, 35)

Period: 1.72 cm
Length: 4.8 m (2 x 2.4 m) in Sector 30; 2.4 m in Sector 35
Minimum gap: 10.6 mm
B_{max}/K_{max}: 0.330 T/0.53 (effective; at minimum gap)
Tuning range: 23.7–26.3 keV (1st harmonic)
On-axis brilliance at 23.7 keV (ph/s/mrad^2/mm^2/0.1%bw):
1.0 x 10^{20} (4.8 m), 4.4 x 10^{19} (2.4 m)
Source size and divergence at 23.7 keV:
Σ_x: 276 μm Σ_y: 11 μm
$\Sigma_{x'}$: 11.6 μrad (4.8 m) 11.9 μrad (2.4 m)
$\Sigma_{y'}$: 4.3 μrad (4.8 m), 4.9 μrad (2.4 m)

1.80-cm Undulator (Sector 32)

Period: 1.80 cm
Length: 2.4 m
Minimum gap: 11.0 mm
B_{max}/K_{max}: 0.244 T/0.41 (effective; at minimum gap)
Tuning range: 23.8 - 25.3 keV (1st harmonic)
71.4 - 75.9 keV (3rd harmonic)
On-axis brilliance at 23.8 keV (ph/s/mrad^2/mm^2/0.1%bw): 2.8 x 10^{19}
Source size and divergence at 23.8 keV:
Σ_x: 276 um Σ_y: 11 um
$\Sigma_{x'}$: 11.9 urad $\Sigma_{y'}$: 4.9 urad

IEX 12.5-cm Quasi-Periodic Polarizing Undulator (Sector 29)

Period: 12.5 cm
Length: 4.8 m

Circular polarization mode:
Max. currents: horizontal coils 34.4 A, vertical coils 20.7 A
K_{max}: 2.73 (effective; at max. currents)
B_{max}: 0.27 T (peak; at max. currents)
Tuning range: 0.44–3.5 keV (1st harmonic)
On-axis brilliance at 1.8 keV (ph/s/mrad^2/mm^2/0.1%bw): 1.4 x 10^{19}

Linear horizontal polarization mode:
Max. current: vertical coils 47.6 A
K_{max}: 5.39 (effective; at max. current
B_{max}: 0.54 T (peak; at max. current)
Tuning range: 0.24–3.5 keV (1st harmonic)
0.24–11.0 keV (1st–5th harmonic)
On-axis brilliance at 2.1 keV (ph/s/mrad^2/mm^2/0.1%bw): 1.1 x 10^{19}

Linear vertical polarization mode:
Max. current: horizontal coils 50.3 A
K_{max}: 3.86 (effective; at max. current)
B_{max}: 0.37 T (peak; at max. current)
Tuning range: 0.44–3.5 keV (1st harmonic)
0.44–11.0 keV (1st–5th harmonic)
On-axis brilliance at 2.1 keV (ph/s/mrad^2/mm^2/0.1%bw): 1.1 x 10^{19}

Fast polarization switching not required
Source size and divergence at 2 keV:
Σ_x: 276 μm Σ_y: 13 μm
$\Sigma_{x'}$: 13.9 μrad $\Sigma_{y'}$: 8.8 μrad

12.8-cm Circularly Polarizing Undulator (Sector 4)

Period: 12.8 cm
Length: 2.1 m
Circular polarization mode:
Max. currents: horizontal coils 1.34 kA, vertical coils 0.40 kA
K_{max}: 2.85 (effective; at max. currents)
B_{max}: 0.30 T (peak; at max. currents)
Tuning range: 0.4–3.0 keV (1st harmonic)
On-axis brilliance at 1.8 keV (ph/s/mrad^2/mm^2/0.1%bw): 3.1 x 10^{18}
Linear horizontal polarization mode:
Max. current: vertical coils 0.40 kA
K_{max}: 2.85 (effective; at max. current)
B_{max}: 0.30 T (peak; at max. current)
Tuning range: 0.72–3.0 keV (1st harmonic)
0.72–10.0 keV (1st–5th harmonic)
On-axis brilliance at 2.1 keV (ph/s/mrad^2/mm^2/0.1%bw): 2.3 x 10^{18}
Linear vertical polarization mode:
Max. current: horizontal coils 1.60 kA
K_{max}: 3.23 (effective; at max. current)
B_{max}: 0.34 T (peak; at max. current)
Tuning range: 0.58–3.0 keV (1st harmonic)
0.58–10.0 keV (1st–5th harmonic)
On-axis brilliance at 2.1 keV (ph/s/mrad^2/mm^2/0.1%bw): 2.3 x 10^{18}
Switching frequency (limited by storage ring operation): 0–0.5 Hz
Switching rise time: 50 ms
Source size and divergence at 2 keV:
Σ_x: 276 μm Σ_y: 12 μm
$\Sigma_{x'}$: 16.7 μrad $\Sigma_{y'}$: 12.7 μrad

1.80-cm Superconducting Undulator (2 IDs in sectors 1, 6)

Period: 1.80 cm
Length: 1.1 m
Gap: 9.5 mm (fixed)
Max. current: 450 A
B_{max}/K_{max}: 0.962 T/1.61 (effective; at maximum current)
Tuning range: 11.2–24.7 keV (1st harmonic)
11.2–150.0 keV (1st-13th harmonic, non-contiguous)
On-axis brilliance at 13 keV (ph/s/mrad^2/mm^2/0.1%bw): 3.2 x 10^{19}
Source size and divergence at 13 keV:
Σ_x: 276 μm Σ_y: 11 μm
$\Sigma_{x'}$: 13.2 μrad $\Sigma_{y'}$: 7.5 μrad

3.15-cm Helical Superconducting Undulator (Sector 7)

Period: 3.15 cm
Length: 1.2 m
Coil winding diameter: 31.0 mm
Max. current: 450 A
B_{max}/K_{max}: 0.413 T/1.213 (B_x=B_y effective; at maximum current)
Tuning range: 6.0-13.0 keV (1st harmonic)
On-axis brilliance at 6.0 keV (ph/s/mrad^2/mm^2/0.1%bw): 2.2 x 10^{19}
Source size and divergence at 6 keV:
Σ_x: 276 μm Σ_y: 11 μm
$\Sigma_{x'}$: 14.7 μrad $\Sigma_{y'}$: 10.0 μrad

APS Bending Magnet

Critical energy: 19.51 keV
Energy range: 1–100 keV
On-axis brilliance at 16 keV (ph/s/mrad^2/mm^2/0.1%bw): 5.4 x 10^{15}
On-axis angular flux density at 16 keV (ph/s/mrad^2/0.1%bw): 9.6 x 10^{13}
Horizontal angular flux density at 6 keV (ph/s/mradh/0.1%bw): 1.6 x 10^{13}
Source size and divergence at the critical energy:
Σ_x: 92 μm Σ_y: 31 μm
$\Sigma_{x'}$: 6 mrad $\Sigma_{y'}$: 47 μrad

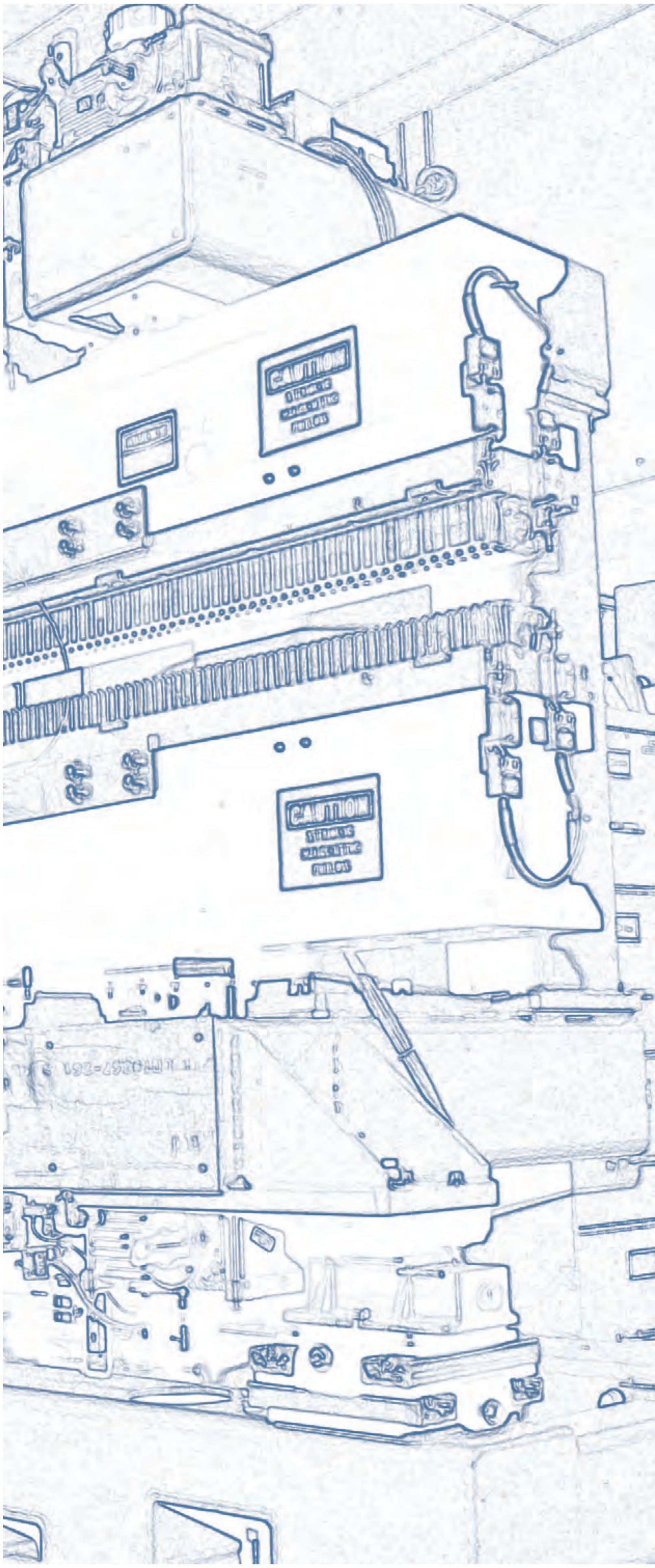

Acknowledgments

APS Science 2019 Editorial Board:

John Byrd (ANL-ASD), John Connolly (ANL-AES), Robert Fischetti (ANL-PSC), Robert Hettel (ANL-PSC), Jim Kerby (ANL-PSC), Jonathan Lang (ANL-XSD), Dennis Mills, (ANL-PSC), George Srajer (ANL-PSC), Stephen Streiffer (ANL-PSC), Stefan Vogt (ANL-XSD)

Reviewers:

Vukica Srajer (BioCARS); Thomas Irving (Bio-CAT); Binhau Lin (ChemMatCARS); Yogendra Gupta, Sheila Heyns, and Paulo Rigg (DCS), Denis Keane (DND-CAT); Michael Becker, Robert Fischetti, and Janet Smith (GMCA-XSD); Mark Rivers, Vitali Prakapenka, Steve Sutton, and Yanbin Wang (GSECARS); Maddury (Zulu) Somayazulu (HPCAT-XSD); Lisa Keefe (IMCA-CAT); Jordi Benach (LRL-CAT); Keith Brister (LS-CAT); Carlo Segre (MR-CAT); Kay Perry (NE-CAT); Andrzej Joachimiak (SBC-XSD); John Rose and Bi-Cheng Wang (SER-CAT); Ralph Bechtold, Jeffrey Collins, Leonard Morrison (AES); Kathleen Carrado Gregar, Elena Shevchenko (NST); Paul Rossi (WSH); Ahmet Alatas, Jonathan Almer, Vincent De Andrade, Francesco De Carlo, Thomas Gog, Daniel Haskel, Steve Heald, Jan Ilavsky, Ivan Kuzmenko, Barry Lai, Byeongdu Lee, Suresh Narayanan, Uta Ruett, Alec Sandy, Jon Tischler, Xiaoyi Zhang, Hua Zhou (XSD)

Unless otherwise noted, the research highlights in this report were written by:

Mary Alexandra Agner (marymary@alum.mit.edu)
Christen Brownlee (christenbrownlee@gmail.com)
Erika Gebel Berg (erikagebel@gmail.com)
Vic Comello ANL-CPA - retired (vcomello@anl.gov)
Dana Desonie (desonie@cox.net)
Sandy Field (sfield@fieldscientific.com)
Philip Koth (philkoth@comcast.net)
Kim Krieger (mskrieger@gmail.com)
David Lindley (dxlindley@gmail.com)
Tien Nguyen (tmnguyen5@gmail.com)
Chris Palmer (crpalmer2009@gmail.com)
Nicola Parry (nicola@parrymedicalwriting.com)
Neil Savage (neil@stefan.com)
Alicia Surrao (alicia@untoldcontent.com)
Stephen Taylor (stephen@untoldcontent.com)
Mark Wolverton (exetermw@earthlink.net)

Aerial photograph of the APS: John Hill (Tigerhill Studio, http://www.tigerhillstudio.com)
Business Manager & Data: Christine McGhee (ANL-PSC)
Publications, contracts, rights and permissions, circulation: Jessie L. Skwarek (ANL-PSC)
Printing oversight: Brian Pifer, John Schneider (ANL-CPA)
Editorial, project coordination, design, photography: Richard B. Fenner (ANL-PSC)

Our thanks to the corresponding authors and others who assisted in the preparation of the research highlights, to the users and APS personnel who wrote articles for the report, and our apologies to anyone inadvertently left off this list. To all: your contributions are appreciated.

U.S. DEPARTMENT OF ENERGY | Office of Science

Advanced Photon Source
Argonne National Laboratory
9700 S. Cass Ave.
Lemont, IL 60439 USA
www.anl.gov • www.aps.anl.gov